Supernova remnants' interactions with the inter-stellar medium

Parkinson, Michael Lawrence

SUPERNOVA REMNANTS' INTERACTIONS
with the
INTER-STELLAR MEDIUM

by

MICHAEL LAWRENCE PARKINSON

November, 1987

An account of work done at the Department of Physics and submitted to the University of Durham in accordance with the regulations for admission to the degree of Doctor of Philosophy.

To my parents.

ABSTRACT

All-sky data at a number of different wavelengths are used to examine the Giant Radio Loops. The x-ray emission of Loop I is modelled as being due to a Supernova Remnant (SNR) that has evolved in a hot, homogeneous, quasi-isotropic medium. The shock is found to weaken towards higher latitudes, and this is attributed to an increase in the ambient gas temperature away from the galactic plane. Other evolutionary possibilities are examined. Radio spectral index maps from 38 to 1420MHz of the northern celestial hemisphere are produced, and the spectra of loops I and III are modelled on the assumption that the energy distribution of electrons accelerated in the shocks will have an upper energy cut-off due to the finite age of the remnants. It is found that the steepening spectra can be fitted by such a model. The electron distribution below the cut-off of order 10GeV is found to fit best if a flatter spectrum than predicted by simple shock theory is assumed. The idea that shocks interacting with clouds can explain this flatter spectrum and enhance the soft x-ray emission is put forward as an alternative evolutionary possibility, bringing together the two separate x-ray and radio emission mechanisms. Other galactic SNR are examined to support this idea, including a newly discovered SNR that exists inside the error circle of the COS-B source 2CG342-02. Although this remnant's association with the γ-ray source cannot be excluded, no firm evidence is found to identify it as the source.

PREFACE

The work presented in this thesis was carried out during the period 1983-87 whilst the author was a research student under the supervision of Dr. John L. Osborne in the Physics Department of the University of Durham.

Some of the work contained in this thesis was carried out in collaboration with Dr. J.L. Osborne, but the calculations are those of the author.

Parts of the work are published as follows:

Parkinson, M.L. and Osborne, J.L., 1885. Space Sci. Rev., **40**, 503.

Lawson, K.L., Mayer, C.J., Osborne, J.L. and Parkinson, M.L., 1987. M.N.R.A.S., 225, 307.

CONTENTS

CHAPTER 5 MODELLING AND ANALYSIS OF THE LOOPS

CHAPTER 1

INTRODUCTION

1.1 THE GIANT RADIO LOOPS

Since the first continuum radio maps of the sky were produced the most noticeable feature other than the concentration of emission defining the galactic plane was the occurrence of a number of 'Spurs' coming out of the plane. These are traceable up to high latitudes where they fade out. Some of these have been found to fit the arcs of small circles reasonably well, and have become known as loops. Of these, four of the largest and most prominent are simply termed Loop I to Loop IV.

Loop I, also known as the North Polar Spur, is the most obvious single continuum feature in the radio sky. For this reason and its associated x-ray emission it is also the most studied (see Salter, 1983 and references therein). It is easily traceable along a continuous 100° arc of a small circle. Rising northwards out of the galactic plane at l~30°, it reaches a maximum latitude of +80° at l~329°. Loops II and III are much less intense

in their brightest regions, and fade out at much lower latitudes, ~45°, away from the plane. Unlike Loop I, both of these loops are seen as 2 arcs. The arcs of Loop II are unconnected but a faint connection is seen between the arcs of Loop III. Loop II differs from the others in that the spurs extend southwards from the plane. One notable feature that all these three have in common is that although the calculated small circles cross the galactic plane the majority of the emission is concentrated in one hemisphere only. Loop III is the only loop that shows some emission on both sides of the plane, but the spur in the southern hemisphere is considerably smaller and fainter. A fourth feature, much smaller than the others, is situated just south of the North Polar Spur's northern-most reach, and is designated Loop IV. This loop is different from the other three in that its completed circle lies entirely in the northern galactic hemisphere. The 408MHz survey of Haslam et al. (1982) is given in figure 1.1. Overlaid on this map are the small circles defined by the loops. Berkhuijsen et al. (1971) calculated the best fit small circles to each loop, and these positions are given in table 1.1. She also examined the polarization of stars of known distance in the direction of the NPS (Berkhuijsen, 1973). A distance at which there was enhanced polarization was looked for, and on the basis of these results the size of Loop I was calculated, assuming it to be a spherical object. By comparison with Loop I, and fitting the brightness of the

other loops with a Van der Laan (1962) model of Spoelstra (1972), a distance to the other three loops was estimated. The relevant parameters are also shown in table 1.1.

LOOP	l(deg)	b(deg)	diam(deg)	dist(pc)	diam(pc)
I	329 ±1.5	17.5 ±3	116 ±4	130 ±75	230 ±135
II	100 ±2	-32.5 ±3	91 ±4	110 ±40	175 ± 65
III	124 ±2	15.5 ±3	65 ±3	150 ±50	200 ± 65
IV	315 ±3	48.5 ±1	39.5±2	250 ±90	210 ± 75

TABLE 1.1

Size and location of the Radio Loops (Berkhuijsen, 1973)

The errors quoted are very large, and it is noted that there is some discrepancy in the relative magnitudes of these errors. Loop I is the only one for which direct observations have yielded information as to its distance, yet the errors quoted for this are larger than for those loops fitted with a model that is far from reliable given the huge variability of SNRs. Thus, when these sizes are quoted in this and other papers they should be taken as rather unreliable estimates.

The only tenable explanation for radio features with intensities and spectra such as these spurs, showing over 70% polarization (Spoelstra, 1971, 1972), is synchrotron radiation from relativistic electrons in a weak galactic magnetic field. Over the years a number of ideas have been put forward to explain the radio loops. Amongst others, these include galaxy collisions (Johnson, 1957);

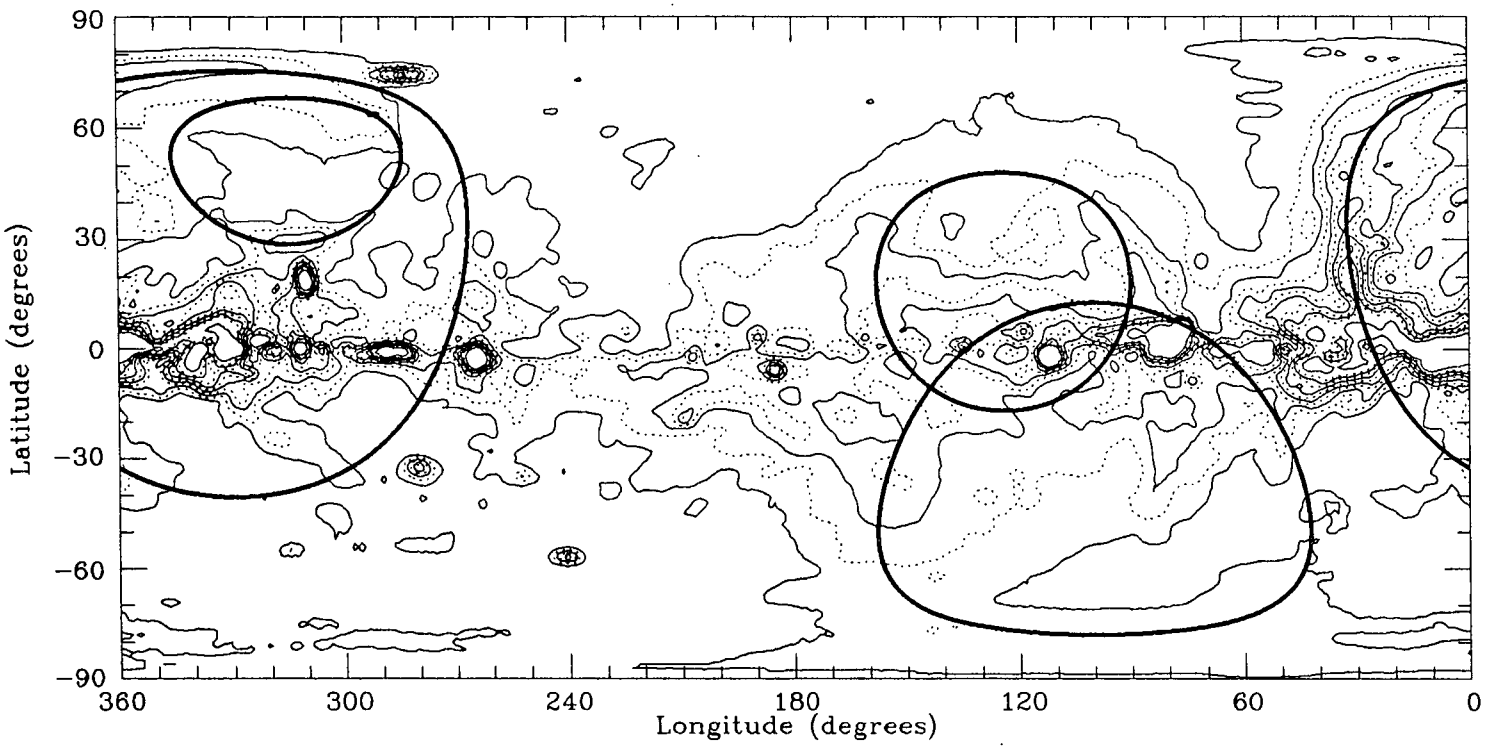

Fig. 1.1 Map at 408 MHz smoothed to 3 degrees
with the loops as defined by Berkhuijsen (1971) overlaid.

Kelvin

——————— 2 10 18 26 34 48

..... 6 14 22 30 38

inter-spiral arm links (Brown et al., 1960; Sofue, 1973, 1976), a magnetic helical structure linking all the loops as one object (Rougoor, 1966; Mathewson, 1968), and Parker instabilities (Parker, 1965) whereby cosmic ray pressure leads to instabilities in the magnetic field which causes it to expand out of the galactic plane (Bingham, 1967).

Brown et al. (1960) also suggested that the North Polar Spur (NPS) might be a bright section of a supernova remnant (SNR). All of the loops are now widely believed to be very large, old, SNRs, the relativistic electrons having acquired their high energies via shock acceleration (Axford, 1981, and references therein) at the interface of the SNR blast wave and the Inter-stellar medium (ISM).

The radio spurs do not exhibit a smoothly varying intensity across their width or along their arc, but show much small scale structure. The spurs are made up of many ridges of emission which generally follow the line of the arc, but are not individually continuous for its whole length. Specifically for Loop I, which is not only the brightest of the loops but also the largest and therefore best resolved, many such short concentric ridges have been noted (Large et al., 1966; Holden, 1969). Another example of small scale structure was pointed out by Haslam et al. (1964). The spur, which for the most part is greater than 10° across, becomes a single bright ridge for $11° < b < 16°$ of the order 1° wide, which they term a 'narrow neck'. As well as the ridging within the main continuum arc there

are a number of sub-arcs that branch from the main spur. These branches are all on the inside, giving it a somewhat feather-like appearance, whilst the outside of the spur remains smooth, with a well defined and abrupt edge. Possible explanations for the origin of this side branching will be proposed and discussed later in this thesis.

More recently than the radio detection of the loops, x-ray data has become available to confirm the idea that at least Loops I and IV are of supernova origin. X-ray surveys below 6keV (Bunner et al., 1972; Korte et al., 1974; McCammon et al., 1983) have revealed gas of the order 10^6 K associated with these loops, particularly with the NPS. This is the expected result after the passage of a high velocity shock. Loops II and III are completely devoid of any x-ray enhancement, but their similarity to Loop I suggests that they have similar origins.

Models of the gas and temperature distribution of a spherical blast wave indicate that the most intense x-ray emission should appear in the form of a spherical shell just inside the shock front, which will appear circular when seen in projection (see chapter 3). The x-ray emission associated with Loop I has just such a bright ridge of emission inside the arc of the NPS, and this is thus strong evidence for the theory that Loop I is a SNR.

As well as the x-ray surveys such as McCammon et al. (1983) that will be examined in later chapters, there have been a number of single scans taken across the x-ray ridge. The general conclusion is that the emission is from a hot plasma at a few 10^6K, but finer details of each observation vary. Using 4 scans, Cruddace et al. (1976) noted a spectral hardening of the x-ray ridge with increasing distances away from the radio spur. From data at mid-latitudes Borken and Iwan (1977) split the emission into two 'concentric' x-ray ridges, but only attributed the spectral hardening to the outer ridge. The term concentric has to be misleading since the area surveyed was small in comparison to the NPS, and the term probably arrives from the assumption that the ridges must form part of a spherical feature. SNR models of Loop I vary with each observation, the location of the scan on the NPS probably being a major factor. Davelaar et al. (1980) deduce an age as little as 75,000yrs, whilst Cruddace et al. (1976) arrive at an age of 4.10^5yrs, the latter value being more in line with other estimates. The deduced size has been as low as 45pc, (Hayakawa et al. 1979), but most authors manage to arrive at values close to that given in table 1.1.

A possibility that has been considered is that Loop I is a re-heated SNR. Iwan (1980) suggest Loop IV as a candidate for the new source of energy in the old cavity. The existence of an H_I shell outside the radio spur suggests that there was such a pre-existing cavity since,

if the radio spur is closely associated with the SNR shock, anything ahead of this must be of different origin. Heiles et al. (1980) believe that it is the existence of the H_I shell that is responsible for the NPS. They argue that it is the confinement of cosmic ray electrons in a highly ionized medium, in conjunction with the poor confinement provided by the neutral gas region that leads to such a well defined outer edge to the spur. In chapter 5 it will also be argued that it is the pre-existence of this gas shell that is largely responsible for shaping the NPS, both radio and x-ray, but the arguments and model will be somewhat different.

Such is the variety of interstellar space that one might expect the evolution of any remnant to be totally different from any other; dependent on the nature of its local environment. Knowledge of the nature of a remnant's environment may be able to help explain the observed state of that remnant, but it should not be overlooked that the reverse may also be true, the remnant acting as a probe of the interstellar medium. It is thus necessary to study the local ISM as well as the loops to help give an acceptable model of their origin.

Many studies of the radio loops or general SNR modelling have tended to concentrate on one aspect, eg. either radio or x-ray observations. In this thesis an attempt is made to bring together both radio and x-ray models of the loops, together with a knowledge of the

local ISM. Of the four loops, much of the analysis and discussion will relate primarily to Loop I and Loop III, and Loop II will not be examined at all. There is the initial assumption that the loops are probably all of a similar nature and that analysis of one gives clues as to the origin of them all. However, it should be acknowledged here that it is not coincidental that Loops I and III are the most studied. These two loops are the most interesting, particularly Loop I with its bright radio and x-ray emission. Excluding Loop II from the study restricts deductions about the local ISM to the Northern galactic hemisphere.

In chapter 2 of this thesis, the general features of the interstellar medium will be outlined, with particular reference to the matter distribution within 200pc of the Sun. Chapter 3 briefly reviews the models devised to explain the evolution of aspects of a SNR under a variety of conditions, introducing some of the equations that will be used later to model the loops. Chapter 4 presents the survey maps at radio, infra-red and x-ray wavelengths, along with detailed explanation of how the data has been cleaned and prepared prior to analysis of the loops. Chapter 5 uses this data to model the loops in terms of old SNR, both for the cosmic ray and the thermal gas components. Other SNR are discussed in chapter 6, and new observations of a possible SNR that may be associated with a COS-B γ-ray source are presented.

CHAPTER 2

INTER-STELLAR MEDIUM

The Interstellar Medium has been observed throughout the electromagnetic spectrum, and the evidence points to it being very complex, inhomogeneous, non-isotropic and multi-component; with structure on all scales from galactic downwards. It appears to be a long way from the ideal substrate that could be easily fitted into a general model that could explain the evolution of supernova remnants. In this chapter the various components that make up the ISM will be described, and the observational evidence for each component will be briefly outlined. We start with data obtained at the long wavelength end of the electromagnetic spectrum and progress through to high energies, and then review observations of the local ISM.

2.1 GENERAL OBSERVATIONS OF THE INTER-STELLAR MEDIUM

2.1.1 Radio

Broad-band radio all-sky maps show two main components. Thermal emission from the gas component of

the ISM, and synchrotron emission due to relativistic electrons spiraling around a magnetic field. With magnetic fields at $3\mu G$ the latter shows evidence for the presence of cosmic ray electrons up to 10GeV.

Emission line observations reveal that much of the interstellar matter is gaseous neutral hydrogen radiating at 21cm due to a spontaneous change of spin state within the atom. Detailed maps (see Burton et al. 1987, and references therein.) of H_I distribution have been produced. There are large scale fluctuations, primarily in the z-dependence (distance away from the galactic plane) with an approximate local scale height of 120pc (Burton et al. 1987), but also the clumping of gas into spiral arms. The latter has been deduced by observing the doppler shift of the emission. In conjunction with a model for the rotation curve of the Galaxy the distance to the source of the emission can be obtained. It can also be deduced that some regions of gas have velocities that are discrepant with their positions, indicating a very turbulent ISM. This large scale structure can be seen in many other external galaxies.

If the sky away from the galactic plane is examined smaller scale detail is revealed. Here there is no confusion due to a very strong background emission, and only the local gas within 100pc of the Sun is of significant column density. The gas can be seen to be clumped into 'clouds' of column densities typically 10^{18}

to $10^{20}\,cm^{-2}$. The clouds tend to be filamentary, or at least very elongated, when seen projected onto the 2-D sky; but it is probable that many of these filaments are sheets of gas seen edge on. Evidence suggest that there is clumping of the gas on scales smaller than can be resolved at 21cm (Greisen and List, 1986).

Other emission line observations reveal a second gas component: molecular hydrogen, H_2. Unfortunately, H_2 is a symmetrical molecule and does not have a suitable easily detectable transition. Local H_2 clouds can be observed in UV emission bands, but the carbon monoxide molecule can be relatively easily detected and can act as a tracer for the much more abundant (and therefore more dynamically significant) H_2. Provided that the ratio between the two types of molecule is constant and is a known value, and the spin temperatures are predictable, then the amount and distribution of H_2 can be deduced. The correct conversion factor to use is not certain and is under continual revision, (see Bhat et. al. 1985a), but some things can be said regardless of this conversion factor. The molecular gas is confined more to the galactic plane than the atomic gas, with a scale height of 60pc (Burton et al., 1987), the clouds tend to be much more massive, and have a different distribution with respect to galactic radius. This latter gas component is not important for the evolution of the loops.

2.1.2 Infra-Red

Infra-red radiation is generally accepted to be due to thermal emission from dust grains, though alternatives have been suggested to account for some of the emission (Harwit et al., 1986). The latest IR data comes from IRAS (Infra-Red Astronomical Satellite). This has shown the dust to be very well correlated with the gas, and at high latitudes this means H_I. The filamentary detailed structure of the ISM can again be seen.

The dust is thought to consist of silicate and graphite grains going down to polyatomic sizes (Draine and Anderson, 1985) with number density $n \propto a^{-3.5}$, where a is the mean grain radius (Mathis et al., 1977). The grains heat/cool until they are in equilibrium with the interstellar radiation field (Cox et al., 1985; Mathis et al., 1983). The emissivity of the grains is such that their cooling rates are proportional to T^5 or T^6, and the variation in temperature of the grains in different regions of space is thus small, except where there is a strong enhancement to the radiation field, such as in an H_{II} region.

2.1.3 Optical and Ultra-Violet

There is optical/UV emission from H_{II} regions closely associated with young stars and from young SNR. From the general ISM, though, there is little evidence for optical emission, and diffuse far UV at high latitudes

(Holberg, 1987) can be explained by interplanetary scattering. One can, however, use the optical/UV emission from stars as a probe of the intervening space between us and the star.

Much starlight is seen to be polarized. Stars in similar positions on the sky often have similar angles of linear polarization and the degree of polarization is correlated to distance, with nearby stars being only very slightly polarized. This suggests that the mechanism for producing the polarization is not intrinsic to each star, but is symptomatic of the ISM. It is indicative of a an all pervading galactic magnetic field. Within the field are elongated dust grains which will preferentially align themselves with respect to the magnetic field lines so as to rotate with minimum energy. The result is that one angle of polarization is preferentially absorbed/scattered. The direction and magnitude of the observed polarization is thus a guide as to the mean field strength and direction.

Absorption by dust grains will also reduce the overall flux from a star. This process is wavelength dependent, increasing in strength from the red part of the spectrum through to the Ultra-Violet. This is interstellar reddening. The difference between the observed 'colour' of the star and what one would expect for a star of its spectral type gives an indication of the amount of absorbing dust.

Some UV lines have been detected in the ambient ISM, and may well have similar origins to some x-ray emission which we will now discuss.

2.1.4 X-Rays

X-rays from 0.1keV up to 100keV are seen in all directions and have been termed 'The X-Ray Background'. The hard X-ray sky is very uniform, and thus much of it may be extragalactic in origin, or from a hot diffuse halo around The Galaxy. The softer X-rays have to be of local galactic origin or else they would be absorbed before they reached us, though at high galactic latitudes it may be possible for a more distant contribution. There are suggestions that this 'background' is not truly diffuse in origin, but is due to the summation of a great many sources unresolved by any detectors. Extrapolating the known bright sources down to supposed fainter more numerous sources would indeed suggest that there may be such undetected sources. Above 1keV this may be as high as 50% (Giocconi and Zamorani, 1987; Hamilton and Helfand, 1987). However, this would still leave a great deal that can only be explained by truly diffuse, interstellar, thermal emission.

At very soft x-ray energies ($E < 0.8keV$) we have to assume a source of emission very local to the Sun. At these energies the x-rays will be absorbed by as little as $10^{20}\,cm^{-2}$ H_I column densities. With a mean gas

density of $1cm^{-3}$ sources further away than 30pc would be absorbed. The detected x-ray spectrum is not readily compatible with a picture of simple absorbtion by an intervening uniform density gas. If the gas was clumped its average 21cm emission would be unchanged but its absorbing properties would change to allow some soft x-rays to travel further by passing around clouds. As noted in section 2.1.1, the gas shows structure right down to the resolution of the detectors, so there is no reason to suppose that clumping of the correct size and density to fit the x-ray background does not exist.

The importance of the X-rays is that they indicate the presence of gas with temperatures in the region of a million Kelvin. Although the densities of these regions are very low ($n \simeq 10^{-3} cm^{-3}$) they occupy as much as 90% of interstellar space. Since the gas is radiating and hence cooling, we need to invoke an energy source to keep so much gas at such a high temperature. The most obvious explanation, and of relevance to this thesis, is that it is the energy of supernovae transferred to the ISM in the form of supernova remnants.

In some directions X-UV absorption lines have been detected, O_{VI}, (York and Frisch,, 1984) indicating very local regions at a few 10^5 K and very low column densities of H_I.

There is a general anti-correlation of H_I with respect to x-rays, and this can be put down to two factors. Firstly, where there is H_I between us and the source region, there will be a reduction in observed flux. Thus, even a uniform x-ray emitting sky would appear anti-correlated with H_I. Secondly, where there are large regions of H_I there may be less x-ray emission and vice-versa. It would appear that observations are best fitted with a degree of displacement of one region by the other, rather than having a good small scale mixing of the two components (Tanaka and Bleeker, 1977).

2.1.5 Gamma Rays and Cosmic Rays.

These final two observations are very closely related since many gamma rays are created by the interaction of cosmic rays with the interstellar gas. The latter are also very relevant to the main topic considered in this work, since a large number of them may owe their very existence to the interaction of SNRs with the ISM.

Cosmic rays, ie. high energy particles, can be detected directly by satellites; intentionally or as contamination of other observations (X-ray, γ-ray), or indirectly on the ground via air showers. They can be considered to reach the Earth uniformly from all directions, the interstellar magnetic field destroying any directionality they may have possessed close to their source. The best means of detecting a cosmic ray source

is the observation of γ-rays.

The COS-B satellite showed that nearly all the γ-rays come from a region very close to the galactic plane. Of the 'point' sources detected, some have been associated with giant clouds, the ρOph cloud being the most positive of such identifications. The association may be due to the interaction of the ambient Cosmic ray flux with the cloud, rather than being an indication of the presence of a cosmic ray source or enhancement. Some recent possible identifications (2CG078+01 & 2CG006-00, Pollock, 1985) have suggested that the cosmic ray flux in these γ source regions is enhanced, this being attributed to nearby SNR. Bhat et al. (1985b) have shown gamma rays to emanate from a region with no obvious large gas density, implying an enhancement of cosmic rays. This latter result is of great interest since the enhancement is attributed to the North Polar Spur, Loop I.

The cosmic rays mentioned above are of atomic nuclei. The evidence for cosmic ray electrons is in the form of radio synchrotron emission. This is usually associated with supernova remnants and forms the basis for the identification of such objects.

2.1.6 Summary

The gas components are clumped on all scales, from giant H_2 regions of up to a few 10^6 solar masses, $n \simeq 10^3\,cm^{-3}$, to small H_I cloudlets unresolved by

detectors, $n \simeq 1 cm^{-2}$. These smaller clouds are usually filamentary rather than spherical. Mixed in with the gas is dust, showing mean temperatures of order 25K. There are also large volumes of very hot, 10^6K, very diffuse, $10^{-3} cm^{-3}$, gas. Each of these components has a different degree of confinement to the plane.

Permeating the whole of the galaxy is a magnetic field of $\simeq 3\mu G$, through which diffuse cosmic ray protons (and other ions) and electrons.

Modelling all these different components simultaneously has not been successfully done, however, a self consistent model that at least brings together the different gaseous components is that of McKee and Ostriker (1977). Their model requires standard clouds that are spherical, 2.1pc in radius. The properties of this theoretical ISM are reproduced in table 2.1. Clearly

	Cloud Core	Cloud Halo		Inter-Cloud
	Cold Neutral	Warm Neutral	Warm Ionized	Hot Ionized
H density (cm^{-3})	42	0.37	0.25	0.0035
ionization fraction	0.001	0.15	0.68	1.00
Temperature (K)	80	8000	8000	$4.5.10^5$
Mean Radius (ρ^c)	1.6		2.1	-
filling factor	0.024	0.05	0.23	0.7

Table 2.1

Typical cloud and typical inter-cloud medium of McKee and Ostriker (1977)

the model is unrealistic, the true clouds of the ISM are

obviously non spherical. It does, however, give a working basis, and gives a reasonable representation of the densities and filling factor of the different components.

2.2 THE SOLAR NEIGHBOURHOOD

The previous sections have noted the general features of the interstellar medium, as they apply to the galaxy as a whole. In this section, in an attempt to draw a more detailed picture of the solar neighbourhood, published observations that relate specifically to the local part of the Milky Way are examined.

2.2.1 Gas Distribution

Some authors (eg. Cox and Anderson, 1982; Innes and Harquist, 1984) have suggested that the Sun is embedded in an unusually low density, fully ionized region, perhaps excavated by a SNR. Evidence to support this local bubble theory comes from observations of Ultra-Violet absorption of emission from stars. Having calculated the $E_{(V-B)}$, use of a suitable conversion factor will give the column density of H_I in the direction of the star. If this is done for many stars, all of known distances, a 3-dimensional picture of local space can be built up. Observations at 21cm are unable to give sufficiently accurate information, lacking sensitivity and, for such local gas, any distance information.

Using $N_H = 5.5 \times 10^{21} E_{(v-B)} cm^{-2}$ and a sample of 82 local stars, Paresce (1984) has produced a contour map of H_I (reproduced in figure 2.1) out to 200pc from the Sun, projected onto the galactic plane. Perhaps the most striking feature of this map is the almost complete absence of any H_I in the longitude range $200° < l < 270°$, ie. the lowest marked contour lies beyond the edge of the map.

Frisch and York (1983) have produced a similar map from a sample of 140 stars (Fig 2.2). These indicate that in this same direction the $5.10^{18} cm^{-2}$ and the $5.10^{19} cm^{-2}$ contours are as far away from the Sun as 300pc and 500pc respectively. This is in contrast to other directions where the contours are much closer and are comparatively circular around the Sun. Here, Frisch and York have placed their $5.10^{19} cm^{-2}$ contour as close as 100pc, and Paresce draws the $10^{19} cm^{-2}$ at a distance of 20pc.

Comparing volume densities of H_I: the mean density $\langle n_{HI} \rangle$ out to 500pc in the direction $l=230°$ is $0.03 cm^{-3}$, whilst at $l=50°$, out to 10pc $\langle n_{HI} \rangle = 0.3 cm^{-3}$; and out to 150pc $\langle n_{HI} \rangle = 4.4 cm^{-3}$.

The maps of Frisch and York are projected perpendicular to the galactic plane, as well as onto it. The relative lack of contouring is, perhaps, more realistic than the map of Paresce. In order to produce maps that can be considered anything more than best guess sketches one would need a far larger sample of stars than

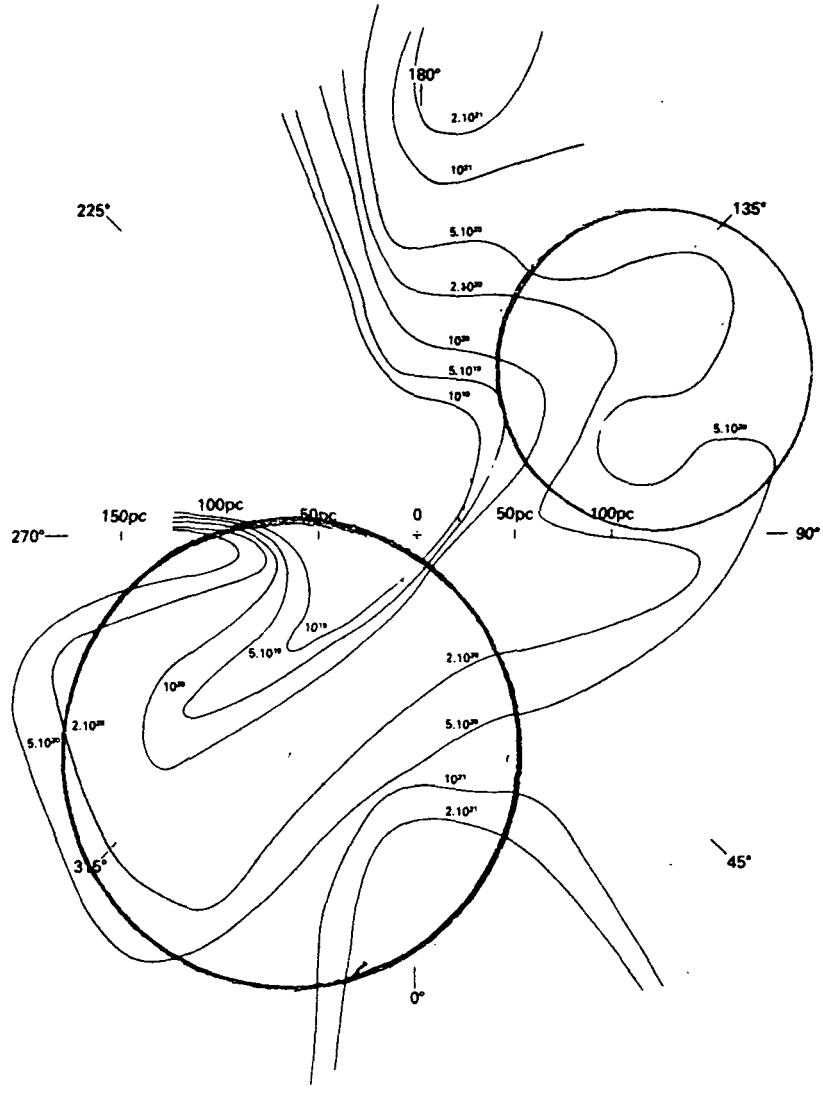

Figure 2.1
UV synthesis map (Paresce, 1984) of H_I column densities projected onto the galactic plane. The Sun is at the centre with galactic longitude marked around the edge. Loops I and III are also shown projected onto the plane.

were used to produce these maps. The sky needs to be sampled not only in many directions but also over a range of distances, with two or more physically nearby stars being used to confirm measurements at each point. Of the stars used by Paresce, 25% are more than 20° away from the plane of the galaxy, and it is unrealistic to assume

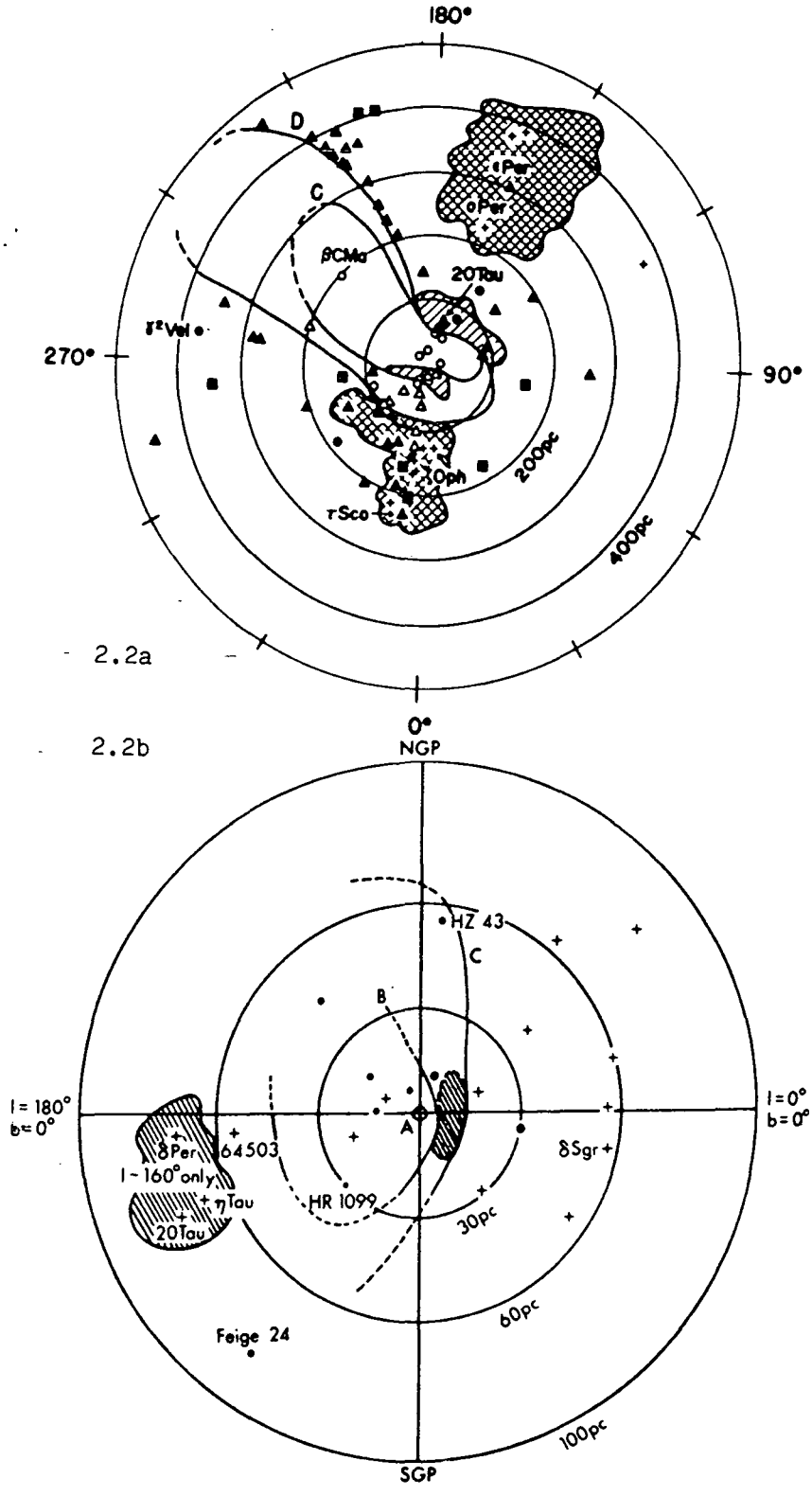

Figures 2.2a and 2.2b.
UV synthesis maps (Frisch and York, 1983) of H_I column densities projected onto:
a.) the galactic plane
b.) perpendicular to the plane (not to the same scale)
Contours of column densities are: A, $5.10^{17}cm^{-2}$; B, $25.10^{17}cm^{-2}$; C, $5.10^{18}cm^{-2}$; D, $5.10^{19}cm^{-2}$. Shaded areas are clouds. Symbols mark the positions of stars used.

that stars at all latitudes can be reliably used to produce a map which when projected onto the plane is 2-dimensional. However, with some confidence it can be said that the Sun appears to be at the edge of a low density 'hole', probably just inside it. The very local gas having temperatures of 10^4K and being 50% ionized with densities of ~0.06cm^{-3} (Paresce 1984) supports this. The Cox and Anderson, (1982); Innes and Harquist, (1984) suggestion may thus be correct.

It has been argued that we are inside the cavity due to Loop I, folds in the dense shell and distortions from a perfect sphere allowing us to see the North Polar Spur at the same time. However, whilst not ruling out the possibility that we are inside the Loop I cavity, the 'hole' that is shown in the maps (figs. 2.1 and 2.2) is likely to be of some other origin, since the positional information on Loop I (if due to a single supernova event) is discrepant with the 'hole'. Only if the NPS is not part of a sphere may it be possible for it to be directly related to this huge H_I free region.

In contrast to these observations, Vidal-Madjar et al. (1978) have suggested that the Sun may be embedded at the edge of a very small cloud. Although giving no positive proof of being inside such a cloud, they do show that the H_I that does exist close to the Sun is clumped on a very small scale, detecting 2 discrete velocity components in absorbtion lines towards λSco, only 15pc

distant. A later observation (Ferlet et al., 1986) revealed very small clouds towards αAri, a star only 5pc from the Sun. A total detectable column density of under $10^{16}cm^{-2}$ ($n=0.0005cm^{-3}$) agrees with the idea of the Sun being in an unusually low density region. However, the fact that this can be resolved into 3 velocity components with sufficient separation between them to exclude turbulent components of the same cloud is evidence to suggest that the clumping of gas can take place on very small scales indeed. This will be an important factor to consider when the X-ray sky is examined in chapter 5.

The above section gives some indication of the neutral gas distribution, but what of other components? The nearest major molecular, H_2 cloud in the solar neighbourhood is ρOph, ~1kpc away,. This particular gas component appears to be of little significance locally. The final gas component, H_{II}, is more important and is evident in a very bright x-ray sky. The detection of x-rays at energies below 0.5keV shows that this emission is very close to the sun. With $n\sim1cm^{-3}$, 10^6 K sources more than 30pc distant would be over 90% absorbed. X-ray data will be examined in some detail later, but with regard to the H_I 'hole', one might expect to see a soft x-ray bright spot in this direction. One might guess that there could be more x-ray emitting gas here, on the assumption this component has displaced the neutral one. Even if the mean volume emissivity was the same as in other directions, the low mean density of absorbing

material ($0.03cm^{-3}$) should allow us to 'see' very soft x-rays of 0.5keV out to 900pc, or at least to the far edge of the hole, before 90% absorption of a source. The absence of such an enhancement would therefore suggest that this 'hole' is also lacking in $H_{I\,I}$ with $T>10^6 K$. There is, however, some evidence of a cooler $H_{I\,I}$ component. At $10^5 K$ the gas will not emit x-rays, but measurements made of O_{VI} in the X-UV are slightly stronger (Jenkins, 1978) in this direction than any other. These are not intense enough to suggest that this region has a large density component of hot gas, but is merely indicative of the long line of sight without absorbtion. At these temperatures the cooling takes place very rapidly, resulting in recombination to neutral gas. It would appear that this 'hole' is genuinely very short of matter.

2.2.2 The Giant Radio Loops

Also shown in figures 2.1 and 2.2 are the positions of the loops. If the loops are the edges of spherical cavities excavated by supernovae blast waves then one might expect there to be a depletion in the H_I column density through these regions, and possibly an increase at the edge. When comparing these figures one should bear in mind the above mentioned reservations as to the reliability of the contours (Paresce's in particular) and bias towards zero galactic latitude, the remnants being centred some distance from the plane and showing no

sign of crossing it. However, given these reservations, one might argue that there is some slight evidence for the existence of loops I and III. Although the contours do not closely follow the outer edge of the supposed cavity, there is some displacement of the contours in fig 2.1 towards greater distances in the direction of l=310°. The 2.10^{20} contour at l=90° could be associated with a build up of gas at the edge of Loop III. Similarly, the large number of contours at l=270° could mark the edge of Loop I, though this is quite likely to be a positional coincidence and simply denotes the edge of the 'hole'. The most interesting feature in the Paresce map may turn out to be the proximity of the $10^{20}cm^{-2}$ contour in the l=45° direction. This is not perfectly coincident with the outline of Loop I, but this is near to the NPS, and when we examine 21cm data later in chapter 5, the morphology of this H_I will show it to be of major importance.

CHAPTER 3

SUPERNOVA REMNANTS

3.1 EVOLUTION

3.1.1 Birth of a Remnant.

Towards the end of the life of large stars of a few Solar masses it is believed that instabilities in the centre of the star can cause a rapid collapse of the core, leading to the release of large amounts of energy and the ejection at high velocities of the outer part of the star. The star may then be observed as a Supernova, radiating intensely over the entire electromagnetic spectrum for a period of a several days. If the star is in a distant galaxy then the object will eventually fade and become undetectable. However, if the supernova event is sufficiently local, in our own galaxy or the associated Magellanic clouds, then we may be able to observe the continued evolution of the ejecta as the resultant blast wave expands into the environment surrounding the site of the initial explosion. Many such Supernova Remnants (SNR) have been identified, but for only a few of these do we

have a historical record of their birth (eg. Tycho, Kepler, Crab).

Remnants can be sorted into two main groups, classified by the spatial distribution of their radio emission; Radio synchrotron being the means of identifying the remnant as such. The classical remnant exhibits a 'shell' structure, with most of the emission taking place near the surface of the 'sphere' as defined by the expanding blast wave. The other type is the centre filled remnant. Here the emission appears to come from the entire volume of the object, and the shape is often far from spherical. A complicating factor is that the supernova may leave behind an object such as a pulsar, injecting large quantities of energy into the centre of the remnant over a prolonged period of time. Clearly, if this energy is comparable to that of the initial explosion then the evolution is likely to progress along somewhat different lines.

Since the giant radio loops are (if they are SNR) shell type remnants, the filled remnants need not be considered further. It is possible that an old shell type remnant may have been centre filled in its youth. One cannot be confident that an established shell structure was not once filled, however, once a shell type structure has been established the evolution should proceed as will be described below.

3.1.2 Outline of the Life and Death of a Remnant.

Early in the life of a remnant the expansion will be independent of the nature of the surrounding ISM. The ejecta will be free to expand at a constant velocity, sweeping up the ambient material before it. For a typical supernova of energy 10^{51} ergs, this will be of the order a few 10^{4} km.s^{-1}. As long as this is greater than the speed of sound in the ISM this will cause a shock wave to be produced at the interface of the advancing ejecta and the ambient ISM. This shock will heat up the gas crossing the shock to temperatures of 10^{6} to 10^{8} K. Not until the blast wave has swept up as much matter as comprised the initial ejecta will the expansion show significant signs of slowing.

That is, when

$$\frac{4}{3}\pi\rho_0 R^3 \simeq M_0 \qquad 3.1$$

where ρ_0 is the density of the ISM, R the radius of the SNR sphere, and M_0 the mass of the ejecta.

Once this stage has been reached the remnant is said to have entered the adiabatic phase. The evolution can then be represented by a simple similarity solution (Sedov 1959), hereafter referred to as the Sedov solution. These equations, which relate to an initial massless point injection of energy into a uniform medium, will be examined in more detail later in this chapter.

Eventually the remnant will enter the cooling phase. As the expansion velocity falls to a few 100km.s^{-1} the temperature of the gas behind the shock front falls and starts to radiate more readily. This cooling allows the density to increase well beyond that predicted by the Sedov solution, and the rate of cooling increases further. Neutral gas starts to condense out and the blast ceases to be supersonic. A cold dense shell continues to expand outward at less than 100km s^{-1} (the snow-plough phase) and then loses its identity as it merges with the ISM.

3.2 EVOLUTION OF THE ADIABATIC PHASE

The adiabatic phase is of most interest when studying shell remnants and their interactions with the ISM. The free expansion phase lasts for only a relatively small fraction of the remnant's lifetime. In the final stages of the radiative cooling phase the remnant starts to fade from view and become indistinguishable from the ISM. Most known remnants are in the adiabatic phase of their evolution, and this is thought to be the most likely stage of the remnants that will be considered later. The rest of this chapter will, therefore, examine in some detail theories of varying complexity as to how this stage of an SNR develops.

3.2.1 Explosion in a Uniform Medium

3.2.1.1 Cold, Pressureless ISM. -

Sedov (1959) produced a similarity solution to explain the expansion of a blast wave. The treatment concerns the case of a large release of energy at a point, and is applicable to the explosion of supernovae. The solution does not include the injection of additional mass at the sight of the explosion, but once the swept up mass is well in excess of that initial mass (equation 3.1), then the remnant can be adequately described by the Sedov solution.

Equations relating the conservation of mass, momentum and energy across the shock can be written thus,

$$V_s = \frac{2}{\gamma+1} U_s \left[1+(a_o/U_s)^2\right] \qquad 3.2a$$

$$\rho_s = \frac{(\gamma+1)}{\gamma-1}\rho_o \left[1+\frac{2}{\gamma-1}(a_o/U_s)^2\right]^{-1} \qquad 3.2b$$

$$P_s = \frac{2}{\gamma+1}\rho_o \left[1+\frac{\gamma-1}{2\gamma}(a_o/U_s)^2\right] \qquad 3.2c$$

where V_s, ρ_s, p_s refer to the velocity, density and pressure, respectively, of the gas immediately behind the shock front. γ is the ratio of the specific heats of the gas, which from here on we shall assume to be 5/3. This is thought to be the most likely case for the majority of interstellar space which is fully ionized. ρ_o and a_o are the mass density of and the sound velocity in the undisturbed ambient medium ahead of the shock, and U_s is the velocity of the shock. Subscripts o and s will always

refer to parameters in the ambient medium and immediately behind the shock respectively. The frame of reference is that of the undisturbed gas, ie. $V_o = 0$.

As long as $a_o < U_s$ the blast wave will propagate as a shock rather than a sound wave. If $U_s >> a_o$ then we can use the strong shock approximation. In the limit as $a_o \to 0$ one has a zero pressure ambient medium, and equations 3.2 become:

$$V_s = \frac{3}{4} U_s \qquad 3.3a$$

$$\rho_s = 4\rho_o \qquad 3.3b$$

$$P_s = \frac{3}{4} \rho_o U_s^2 \qquad 3.3c$$

From dimensional analysis one can relate the energy of the explosion E_o, the radius of the shock r_s, the time t, and the ambient density. For the case of a spherical blast wave one gets

$$r_s = \frac{(2E_o)^{1/5} t^{2/5}}{\rho_o^{1/5}} \qquad 3.4$$

where the factor 2 is deduced for the case where $\gamma = \frac{7}{5}$.

Sedov goes on to deduce the value of parameters describing the gas with respect to all radii from the centre to the shock. The equations will not be reproduced here, but figure 3.1 shows the results graphically.

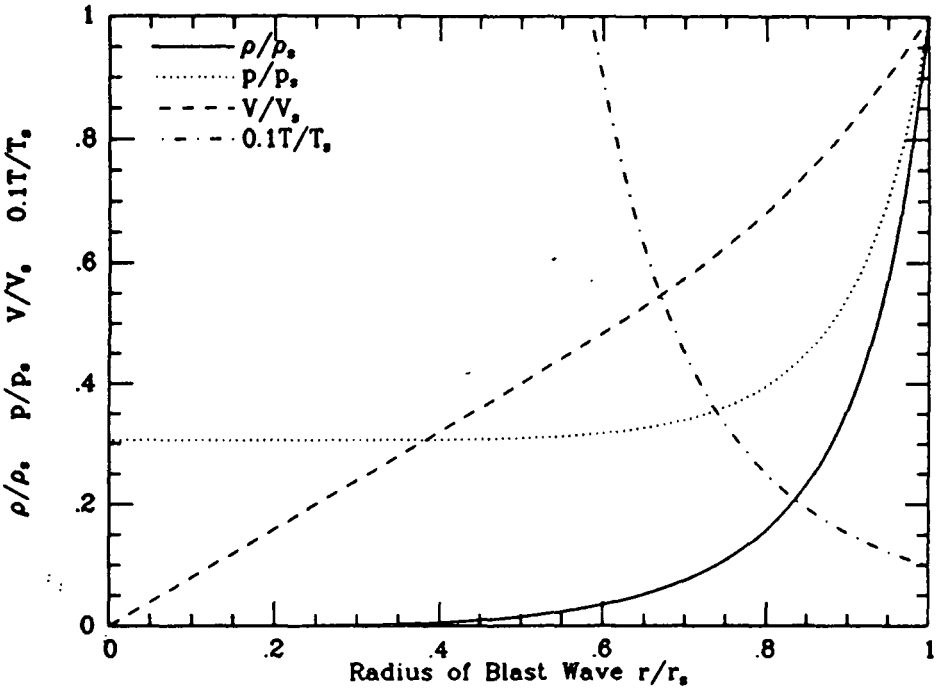

Figure 3.1 Sedov Solution
Density, pressure, velocity & temperature wrt shock values

T_r , P_r , V_r , are all normalized to unity at ρ_s , T_s , P_s , V_s . The point to note is the concentration of matter just behind the shock front. One may also note that the pressure is fairly constant and the velocity of the gas decreases to zero towards the centre. However, as these parameters cannot be directly observed they are of relatively minor importance. On the other hand, the temperature of an SNR can be deduced from the spectrum of the emission, and the density distribution will determine where the emission will be seen.

Shock velocities of a few 100km.s^{-1} will lead to temperatures of a few million Kelvin ($T_s \simeq 12 U_s^2$ Kelvin; from equations 3.3b and 3.3c with U_s in km.s^{-1}). With thermal emission proportional to ρ^2 , figure 3.1

indicates that SNRs will be brightest at their outer edges, and can be detected as x-ray spherical shells.

3.2.1.2 Hot ISM -

The Sedov solution will suffice so long as the shock velocity is high enough for the strong shock approximation to hold. However, as the remnant gets older the velocity decreases. Differentiating equation 3.4 gives:

$$U_s \propto t^{-3/5} \qquad 3.5$$

There will come a time when the speed of sound in a hot ambient medium will become a sizable fraction of the shock velocity, and this may greatly affect the subsequent evolution.

Gaffet (1978) relates the shock velocity to pressure and density thus:

$$U_s^2 = (P_0 + 4P_s)/3\rho_0 \qquad 3.6$$

which includes the effect of the ambient pressure. Comparing this with equations 3.3a and 3.3b, one finds that $U_s^2{}_{Gaffet} = U_s^2{}_{Sedov} + P_0/3\rho_0$ ie. the shock proceeds slightly faster in the warmer medium.

Hayakawa (1979) uses this and

$$E = \frac{4}{3}\pi r_s^3 \frac{3}{2} P_0 \qquad 3.7$$

(Gaffet 1978) to deduce,

$$r_s = 21 (E_{50}/n_0)^{1/5} t_5^{2/5} \qquad 3.8$$

which is of the same form as equation 3.4, deduced from the Sedov solution, E_{50} being the energy of the explosion in units of 10^{50} ergs, n_0 the gas number density in cm^{-3} and t_5 the age in units of 10^5 years.

Substitution of U_s from equation 3.6 into the equations for conservation of mass and momentum,

$$\rho_0 (V_0 - U_s) = \rho_s (V_s - U_s) \qquad 3.9a$$

$$\rho_0 (V_0 - U_s)^2 + P_0 = \rho_s (V_s - U_s)^2 + P_s \qquad 3.9b$$

will yield the ratio of the shocked and ambient, temperatures and pressures in terms of the density jump across the shock.

$$\frac{\rho_s}{\rho_0} = \eta \qquad 3.10a$$

$$\frac{P_s}{P_0} = \frac{4\eta - 1}{4 - \eta} \qquad 3.10b$$

$$\frac{T_s}{T_0} = \frac{4\eta - 1}{4 - \eta} \cdot \frac{1}{\eta} \qquad 3.10c$$

If we approximate the density distribution as

$$\rho_r = \eta \rho_0 \left(\frac{r}{r_s}\right)^{\nu} \qquad 3.11a$$

$$\nu = 3\eta - 3 \qquad 3.11b$$

which, when $\eta=4$, gives a similar distribution of gas to the Sedov solution in the important region close to the shock, and if the pressure behind the shock is assumed to be in approximate equilibrium, the temperature distribution can be also be found from 3.11a. Thus the parameters that are important for interpreting the observation of the thermal gas, namely the density and temperature distributions, can be expressed purely in terms of the density jump, η, which is dependent on the temperature or sound speed of the ambient gas. This is given in equation 3.2b which becomes

$$\rho_s / \rho_0 = \eta = 4(1+3a_0^2/U_s^2)^{-1} \qquad 3.12$$

with $1<\eta<4$ for shock velocities ranging from the sound speed a_0 to infinity.

3.2.2 Explosion in a Non-Uniform Medium

3.2.2.1 Plane Stratified Medium -

Old SNR can be seen to have radii that are of the same order of magnitude as the scale height of the gas in the disk of the galaxy. Clearly, they can no longer be considered to be expanding into a uniform medium, since they will experience a considerable variation in the nature of the ambient medium as a function of z. An SNR of radius 100pc in a gas of scale height 100pc might experience a density at z=200pc of one tenth of that which it found in the galactic plane.

Numerical models (Chevalier and Gardner, 1974) have shown that in such a medium, although one would expect to find that a remnant's evolution would be greatly affected, the resultant shock front need not be too far from being spherical. However, the apparent centre of the sphere will not mark the site of the progenitor supernova. For an explosion above the plane, the blast travelling towards the plane will progress more slowly than that travelling in the opposite direction into less dense regions. The result will be that the centre of the cavity will be further above the plane than the site of the explosion. The models also predict that the greatest shell densities (not surprisingly) are towards the galactic plane, and one might therefore expect a remnant to be more visible in this region. A small point worth mentioning here is that; in addition to variation in gas distribution, Chevalier and Gardner have also taken into account an additional complication, that of gravity. The cavity will experience a degree of buoyancy against the gravitational pull towards the galactic plane, which will tend to push it to still larger z.

3.2.2.2 Spherically Symmetric Models -

It is possible that the ISM surrounding a pre-supernova object can be affected by stellar winds from the progenitor star, or on a greater scale by a group of nearby early type stars in an OB association. These winds might result in a density distribution such that $\rho_0 \propto r^{-\xi}$

(-ξ is used for consistency with previous authors).

Chevalier and Messina (1976) examined this for decreasing densities with radius, choosing ξ such that the blast wave would still experience some deceleration, ie. $0<\xi<3$. Stellar winds near to stars appear to have such a density distribution, but for volumes of space on the scale of old SNR one might expect the stellar winds to have excavated a cavity with respect to the density of the more distant ISM. An increasing density with respect to radius might, therefore, be more appropriate.

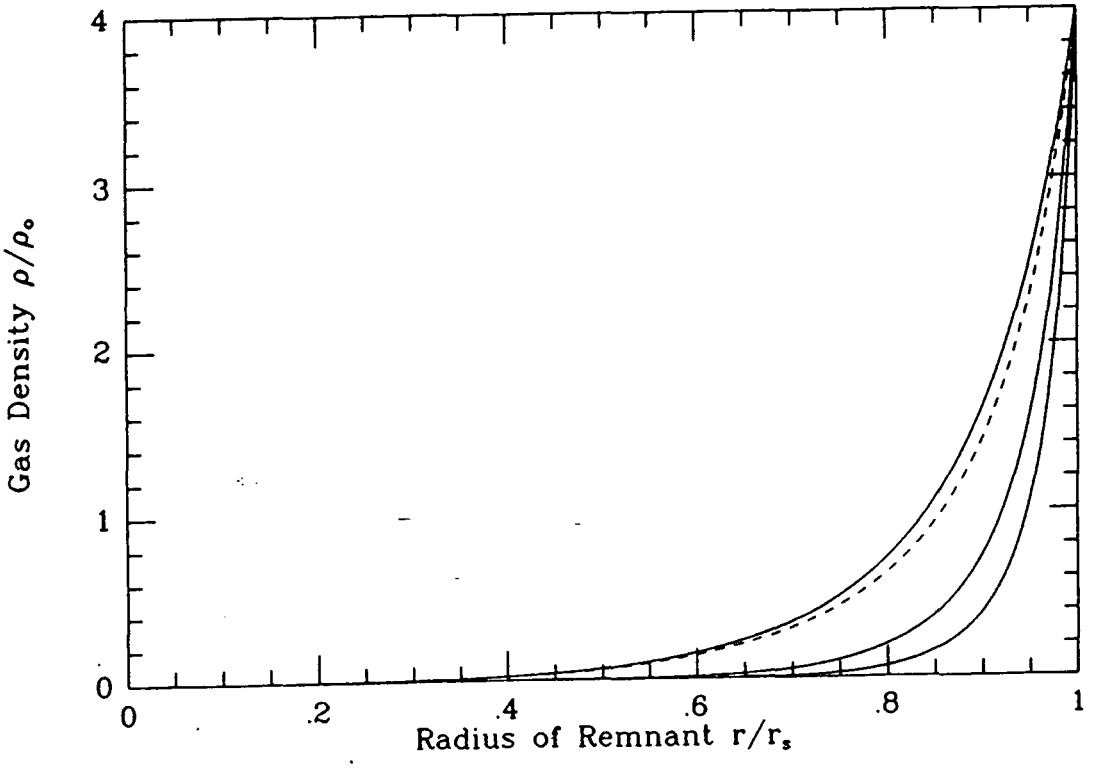

Figure 3.2
Gas density distribution behind a strong SNR shock for evolution inside a spherical cavity with ξ=0,2,4. The Sedov solution is shown as the dashed line.

Cox and Franco (1981) have analyzed numerical models for ξ=0,-1,-2,-3,-4, where ξ=0 is the equivalent of the Sedov solution. The relative internal pressure of the

remnant does not vary much from model to model. However, the density profile shows an increasing proportion of matter concentrated just behind the shock as ξ becomes more negative. This is not surprising, as this is simply a reflection of the ambient density distribution. The value of the parameters at the shock are still as for the Sedov solution (equations 3.3), with the value of the constant ambient density ρ_0 being replaced by the instantaneous density just ahead of the shock. Figure 3.2 shows densities relative to the shock density, ρ_s, for some models.

3.2.2.3 Inhomogeneous ISM -

Unfortunately, as noted in the previous chapter, models which assume a smooth uniformity of matter in space are not representative of the true nature of the ISM. A simplified model would consist of neutral gas clouds of quasi-random size and distribution, embedded in a much hotter fully ionized medium. The models of Cox and Smith (1974), and of McKee and Ostriker (1977) do this in a self consistent manner. The results of the latter paper being summarised in table 2.1

How these clouds affect the evolution of a remnant has been studied both analytically (McKee and Ostriker, 1977), and numerically (Cowie, McKee and Ostriker, 1980). For a standard small cloud the bulk of the shock is not directly affected by the interaction. The blast

propagating in the hot, low density component of the ISM will simply pass around the sides of the cloud. The 'hole' that is punched in the shock surface will be filled in after the cloud has passed. However, the cloud itself will have a shock driven into it, and this coupled with the thermal conduction from the very hot gas now surrounding the cloud will lead to heating which will 'evaporate' material from the outer edges. If the cloud is small it may be completely obliterated. Both heating processes will extract some of the energy from the remnant, reducing the temperature, but increasing the density as cloud material becomes part of the inter-cloud medium. During a period of large evaporation, McKee and Ostriker find that $r_s \propto t^{3/5}$, rather than the $r_s \propto t^{2/5}$ of the Sedov solution. As the evaporation decreases with age and cooling starts to set in, the evaporation rate decreases and the derived expression for the expansion reduces to the same form as the Sedov solution. An assumption used in this model is that thermal conduction will take place within the interior of the remnant. The process of thermal equalization will be aided by the evaporation. Away from the shock front the temperature and density of the cavity will be much more uniform with respect to radius, unlike the infinitely hot (and therefore unrealistic) centre of the Sedov model. Cowie, McKee and Ostriker (1980) present radial cuts through their models for several evolutionary ages of a remnant, and these show that the gas distribution and temperature

may be very different from the Sedov type model, being far more complex and variable with time.

3.2.2.4 Magnetic Fields -

None of the models mentioned so far have included magnetic fields. This is partly due to the lack of understanding of the nature of the magnetic field, and is largely due the complexity of trying to include such a parameter in an already difficult model. It is not due to an *a priori* assumption that the effects of the magnetic field will be of only minor importance.

Chevalier (1974) has attempted to take account of magnetic fields, and has considered them as being extremely tangled on the scale of the remnant, and, therefore, essentially homogeneous and isotropic. He shows that SNR can evolve fairly independently of such a field B, provided the field's pressure does not dominate that of the ram pressure of the shock. However, observations show that the interstellar magnetic field is not so simple, showing considerable structure on scales comparable to a typical remnant in the adiabatic phase. A remnant's evolution may thus be dependent on the orientation of the field lines with respect to the shock, and a remnant might, therefore, be expected to evolve differently in different directions. If B is of significant magnitude then it will reduce the degree of compression, thus less energy will be transferred to the

bulk velocity of the gas behind the shock, and the expansion will be able to proceed at a greater rate.

Another factor that will work in conjunction with the magnetic field to smooth out the shock is the action of cosmic rays. These can excite Alfven waves in the magnetic field which will travel at the Alfven velocity ahead into the ambient medium and help to reduce the strength of the shock still further.

This brings us to part of a remnant's evolution so far neglected: the production of cosmic rays.

3.3 EVOLUTION OF THE SYNCHROTRON EMISSION

The Sedov solution and all the previously mentioned related models have been concerned with distribution and temperature of the ambient non-relativistic gas. However, the one thing that most clearly identifies a SNR is its non-thermal radio emission due to the interaction of relativistic particles with the interstellar magnetic field.

One of the most important questions in cosmic ray astronomy is 'where do they come from?'. Some means of accelerating the particles to their high energies is required, and one of the possible mechanisms is shock acceleration. This effect can be seen in the Solar Wind's bow shock at the Earth, and possible explanations for the observed cosmic ray flux have come from the idea of

termination shocks at the edge of stellar winds, spiral arm shocks, and intergalactic shocks. Webb et al. (1985) suggest that stellar winds may account for a sizeable fraction of the observed cosmic ray flux, but one of the most promising sources for the creation of relativistic particles is supernovae and the shock fronts of remnants. The strength of the non-thermal radio emission from SNR is clear evidence of an enhancement of high energy electrons.

3.3.1 Van der Laan Model

Van der Laan (1962) considered the supernova blast and ejecta as a piston compressing the ambient medium before it. Using the Rankine-Hugoniot relations of conservation of mass, momentum and energy, he derives the compression ratio of the gas at the interface. Thus far the approach is as for the Sedov solution, and the results $1<\eta\leq 4$ for $\gamma=\frac{5}{3}$ are therefore the same. He then replaces the terms for the pressure and internal energy of the gas with those for the sum of the gas, the magnetic field and the relativistic particles; the latter two components tending to reduce η below its maximum attainable value of 4. Assuming flux freezing, ie. the gas and magnetic field are well coupled (which should be good for the fully ionized hot phase of the ISM), the compression of the gas will lead to a similar compression of the magnetic field, and hence an increase in the number density of the cosmic rays. However, as well as the relativistic gas being compressed, each individual

particle within that gas will receive an increase in its energy by a mechanism that is now described.

Van der Laan shows that a particle crossing the shock will receive an increase in the component of its momentum p' perpendicular to the shock of $\chi^{1/2}$ (ie. $p_s' = \chi^{1/2} p_o'$) and he goes on to show that $\chi = \eta$. The increase in emissivity for an ambient spectrum of cosmic rays of the form $N_{(E)}dE = KE^{-\gamma}dE$ is

$$\varepsilon_\nu / \varepsilon_{o\nu} = (K/K_o)(B/B_o)^{\alpha+1} \chi^{(2\alpha+1)/2} I \qquad 3.13$$

which is strictly true only for the one dimensional case. Here $(K/K_0) = \eta$ is the compression of the relativistic gas, $(B/B_0) = \eta$ is that for the magnetic field, $\alpha = (\gamma-1)/2$ is the radio synchrotron spectral index for an $E^{-\gamma}$ electron energy spectrum. I is an integral function of χ, α and θ, where θ is the pitch angle the particle makes with the shock.

If magnetic irregularities scatter the cosmic rays equation 3.13 loses its θ dependence and becomes

$$\varepsilon_\nu / \varepsilon_{o\nu} = (K/K_o)(B/B_o)^{\alpha+1} [1 + (\chi/(\chi-1)^{1/2}) \sin^{-1} \{((\chi-1)/\chi)^{1/2}\}] \qquad 3.14$$

For $\alpha = 0.5$ and $K/K_0 = B/B_0 = \chi = \eta = 2, 3, 4$ $\quad \varepsilon/\varepsilon_0 = 7.3, 24, 55$. Generally $K/K_0 \neq B/B_0 \neq \chi \neq \eta$.

The Van der Laan model obtains the enhanced emission simply by compressing the magnetic field and a pre-existing cosmic ray gas. However, as mentioned earlier, shocks may be able to accelerate particles, and

it could be that SNR shocks 'create' cosmic rays in situ, and it is these 'new' relativistic particles that give rise to the observed synchrotron emission. The most likely mechanism for increasing the energy of cosmic rays is First Order Fermi acceleration. (Bell 1978, Axford 1981)

3.3.2 Particle Acceleration

In a scatter-free medium although a cosmic ray will travel around its Larmor ring many times before the ring is completely engulfed by the shock, it will effectively cross the shock only once. In order to accelerate a particle up to very high energies it is necessary for many crossings to take place. This can be achieved by having a scattering medium which will allow cosmic rays to diffuse back upstream across the shock front. Scattering can occur off any magnetic irregularity. These may be pre-existing, but the shock is able to create its own. Downstream of a shock these can be generated by the turbulence which is a natural consequence of the blast wave. Ahead of the shock, scattered cosmic rays will, generally, eventually be overtaken by the advancing shock. However, the acceleration process will be enhanced if there is increased scattering here as well. Upstream irregularities can be generated by the cosmic rays themselves, exciting Alfven waves in the magnetic field which travel ahead of the shock (Bell, 1978) and act as the scattering centres.

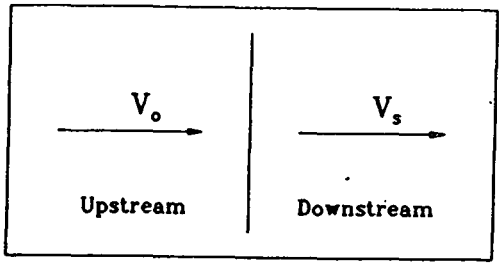

Figure 3.3 Gas Velocities wrt the Shock

If the scattering centres have velocities representative of the gas velocities on either side of the shock, a relativistic particle will 'see' these irregularities as a pair of mirrors converging towards the shock front. There will be a gain of energy each time a particle is reflected. The probability of a cosmic ray being scattered back across the shock from downstream to the upstream is less than unity,so many particles will be lost to the shock region. However, if a particle manages to travel back-and forth across a shock y times, then its probable energy gain is given by

$$\ln(E_y/E_0 \simeq 4y(V_1 - V_2)/3U_s \qquad 3.15$$

(Bell, 1978), and the resulting differential energy spectrum of an ensemble of cosmic rays is

$$N_{(E)}\,dE=(\gamma-1)(E/E_0)^{-\gamma}/E_0\;dE \qquad 3.16$$

$$\gamma=(2V_2+V_1)/(V_1-V_2) \qquad 3.17$$

(Subscripts 1 and 2 referring to parameters either side of the shock in the rest frame of the shock.) Strictly, V_1 and V_2 are the velocities of the upstream and downstream scattering centres with respect to the shock, figure 3.3, however, if we approximate these to be the same as the gas velocities then for a strong shock we have $4V_2=V_1$ and $\gamma=2$.

(For $\eta=2,\ 3,\ 4$: $\gamma=4,\ 2.5,\ 2$)

3.3.2.1 Magnetic Fields -

Magnetic fields exist and are essential to the acceleration process, but their precise influence on the evolution of the cosmic rays, as with their effects on the general dynamics of the SNR, are not well understood. Since they have directionality this property may be an important influence on the outcome of the acceleration. Shocks into a tangential, perpendicular or tangled field may produce different results. Webb, Dury and Völk (1986) have considered shocks occurring obliquely to a magnetic field. They have suggested that the shock acceleration efficiency (ie. the fraction of shock dissipated energy converted into cosmic ray energy) decreases for increasing angles of the magnetic field with respect to to the shock, though this only becomes significant for low Mach numbers. For high energy particles which have required long acceleration times,

they suggest that the efficiency will be related to the mean field direction.

3.3.2.2 Non-test Particle Modelling. -

The production of cosmic-rays in the shock (section 3.3.2) has only really been examined for the case of a single test particle. No full mathematical analysis to date has predicted what feedback effect there is from the production of numerous cosmic rays. In general terms, one effect already mentioned is the enhancement of scattering centres ahead of the shock through the production of Alfven waves. However, the fact that the particles and the resultant Alfven waves travel ahead of the shock may affect the nature of the shock itself. The likely simple result is that the shock in the thermal gas will be weakened, but the effect on the cosmic ray production efficiency may be different from the corresponding weak shock strength in the test particle model of Bell.

CHAPTER 4

OBSERVATIONS

4.1 X-RAY DATA

The data consists of observations made by McCammon et al. (1983), based at Wisconsin University. Using a number of rocket soundings almost the entire sky has been covered in the energy range 0.1keV to 6keV. Seven broad-band filters were used, and these are listed in table 4.1 and their frequency responses shown in fig 4.1. Contour maps of the seven bands are given in fig 4.2(a-g). The maps were considered too complex to have the contours labeled with their respective intensities. To assist the reader in establishing the intensity level of a given contour, alternate contours have been drawn in different styles. For the higher energy bands the area around l=150° is a minimum and is surrounded by the lowest defined contour in each map, but for the B and C bands the style of contouring has been changed at an intermediated intensity in order to clearly show the region of higher emission, and this gives the best starting point for anyone wishing

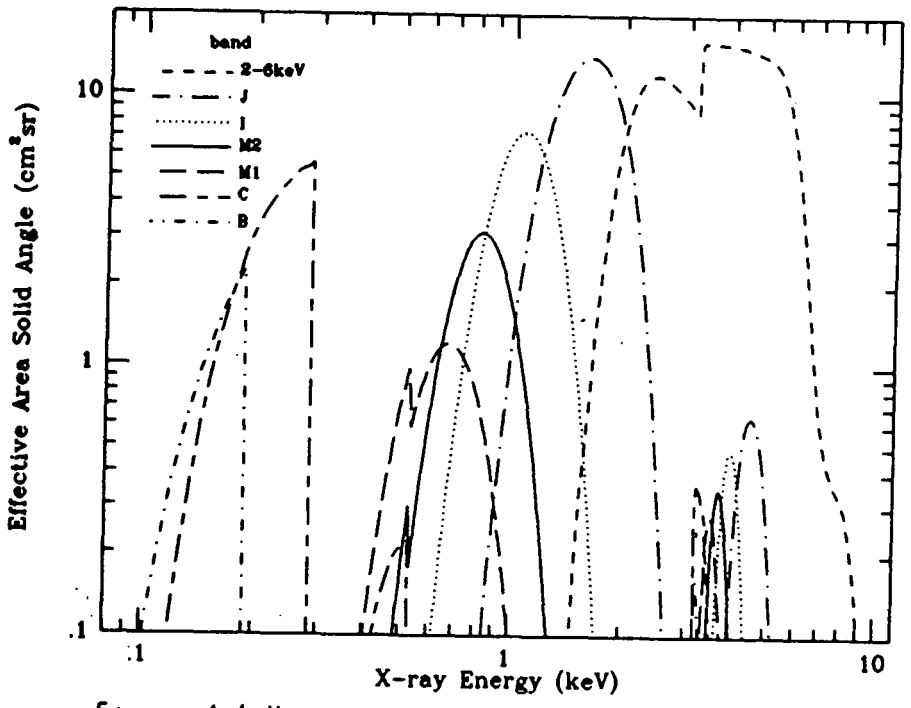

Figure 4.1 Wisconsin X-ray Bands

Band	B	C	M1	M2	I	J	2-6keV
lower limit (keV)	0.13	0.16	0.44	0.60	0.77	1.1	1.8
upper limit (keV)	0.188	0.284	0.93	1.1	1.5	2.2	6.3

Table 4.1 Energy ranges of Wisconsin x-ray bands

to label the contours.

The choice of contour levels is fairly arbitrary. The lowest was chosen so as to be high enough not to give a confused tangle of lines over the fairly uniform minimum around l=150° (Hence the lack of contours in the 2-6kev map.). Because of the similarity of the M1, M2 and I bands, the contours for these maps were chosen so as to be roughly comparable.

The data was provided on magnetic tape by the Wisconsin group in the form of Aitoff projection maps. However, in spite of gross distortions towards the polar

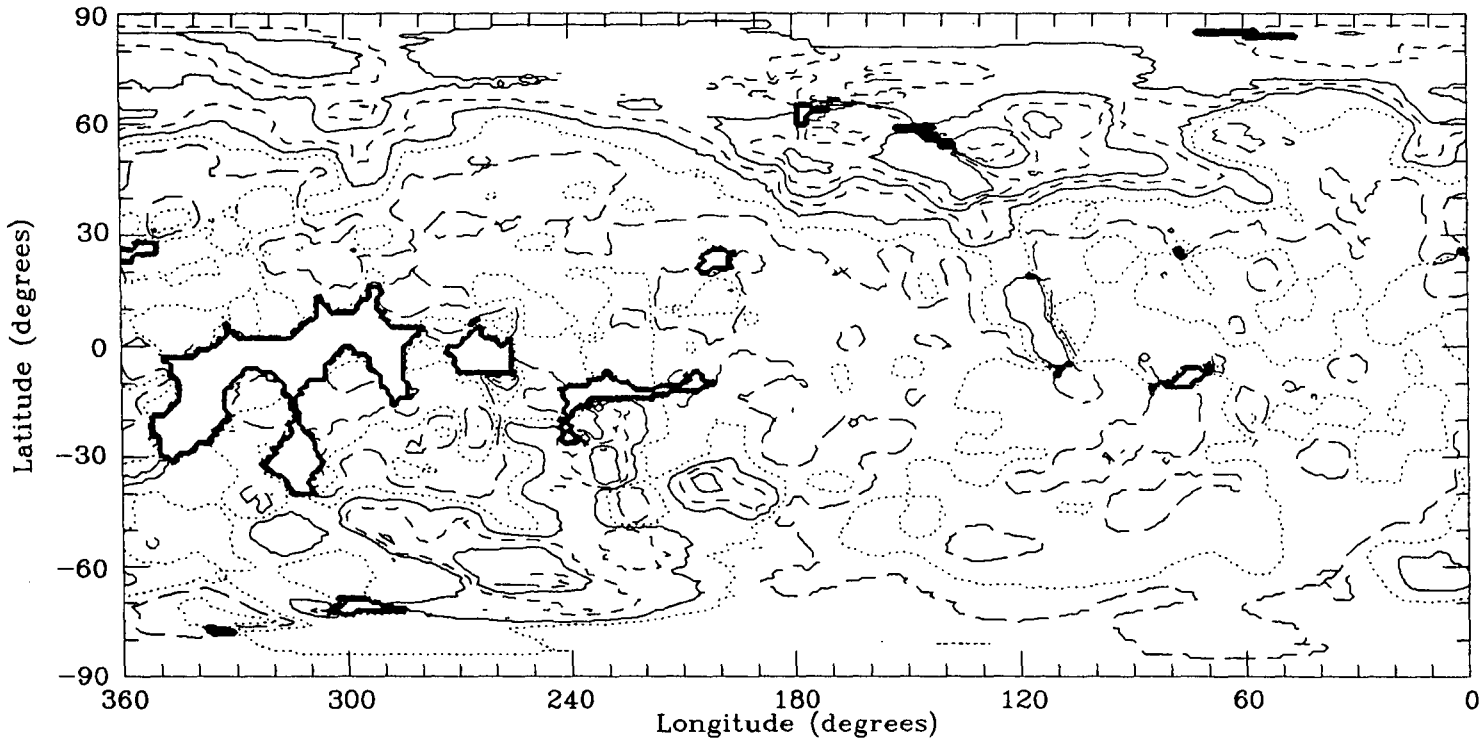

Fig. 4.2a B-band x-ray map in Galactic co-ordinates.

	Counts/sec
- - - - - - - - -	25, 45
.....	35, 55
———	65, 85, 105
- - - - - - - - - - -	75, 95

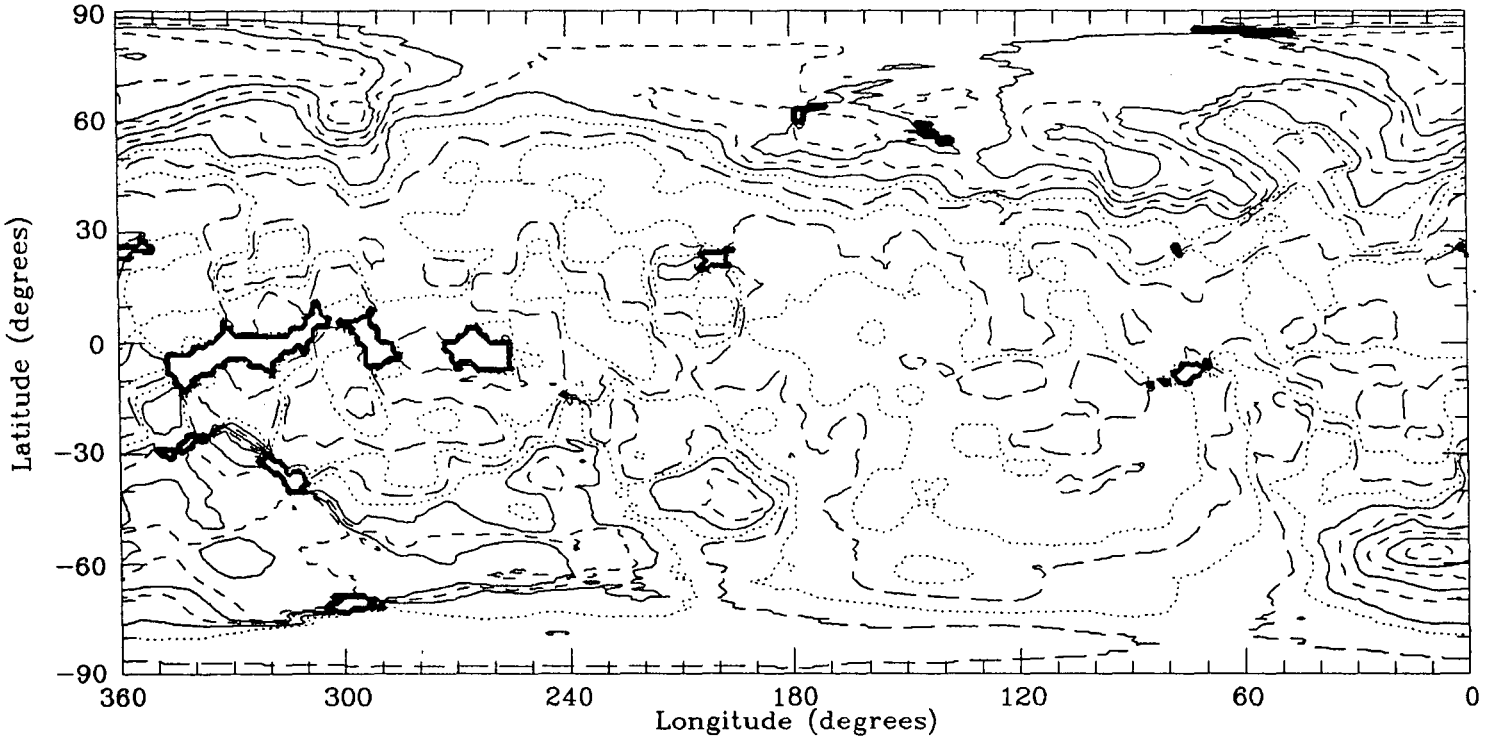

Fig. 4.2b C-band x-ray map in Galactic co-ordinates.

	Counts/sec
— — — — — — —	60, 100, 140
.....	80, 120, 160
———————	180, 220, 260, 300
- - - - - - - - - - - -	200, 240, 280

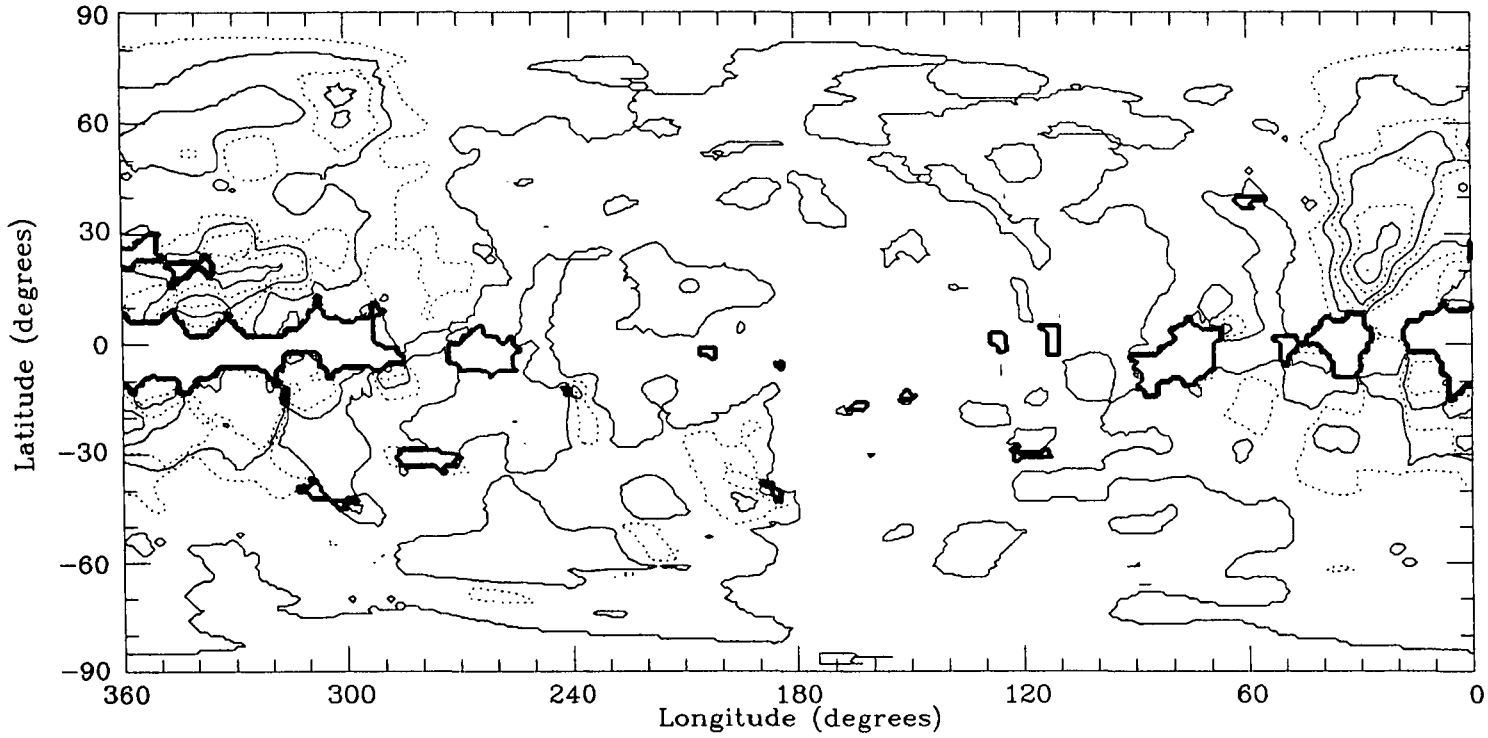

Fig. 4.2c M1-band x-ray map in Galactic co-ordinates.

Counts/sec
20, 40, 60, 80
30, 50, 70, 90

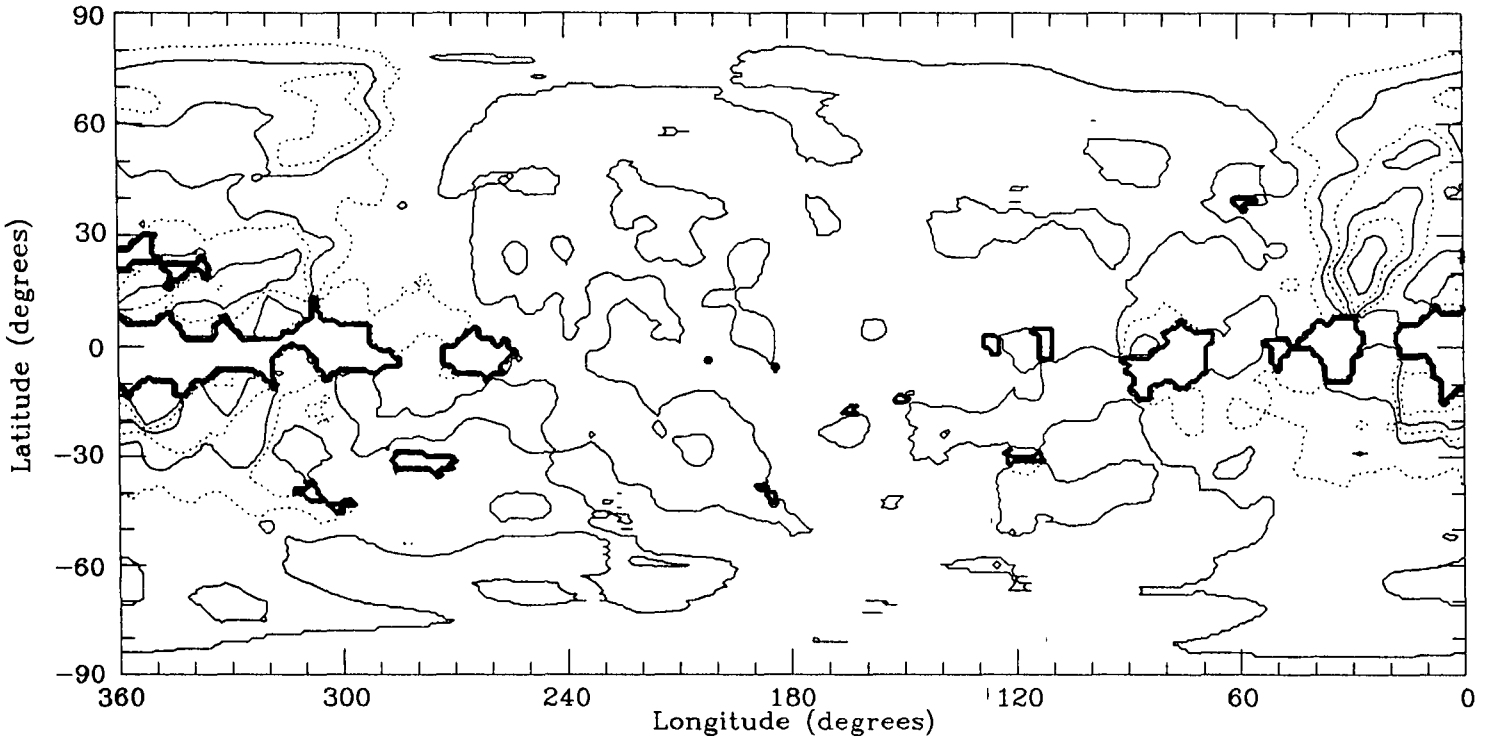

Fig. 4.2d M2-band x-ray map in Galactic co-ordinates.

Counts/sec
30, 63, 97, 130
47, 80, 113

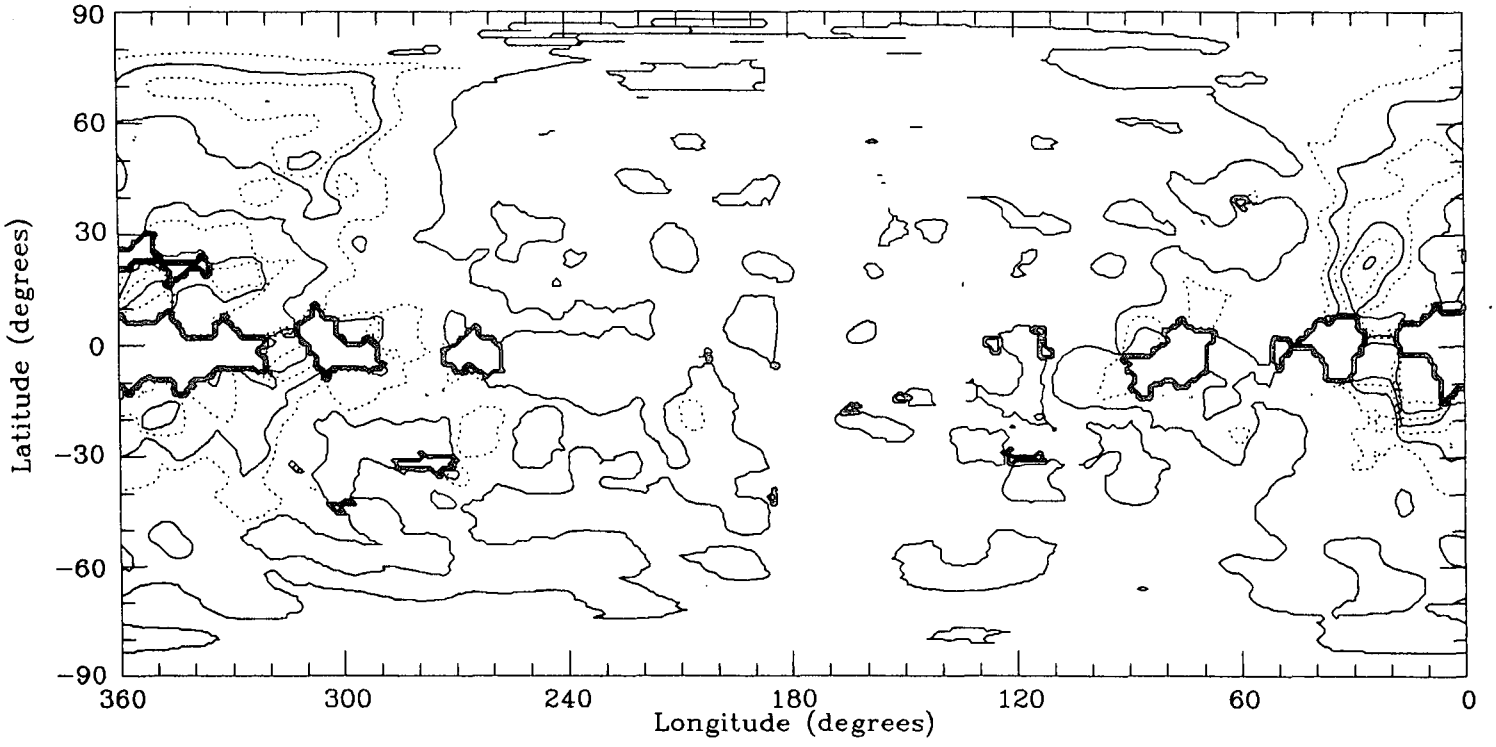

Fig. 4.2e I-band x-ray map in Galactic co-ordinates.

Counts/sec
50. 83. 117. 150
67. 100. 133. 167

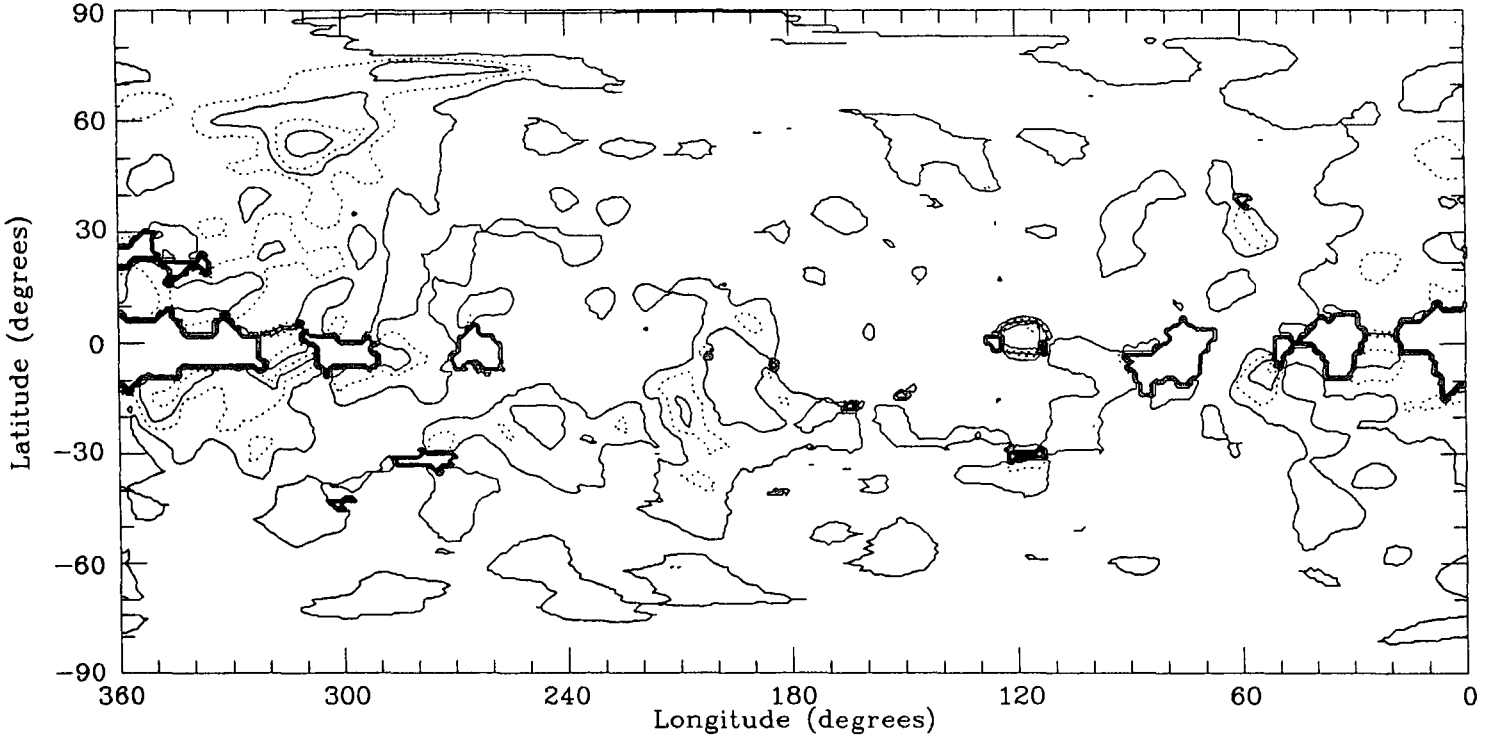

Fig. 4.2f J-band x-ray map in Galactic co-ordinates.

Counts/sec
75. 105. 135
90. 120. 150

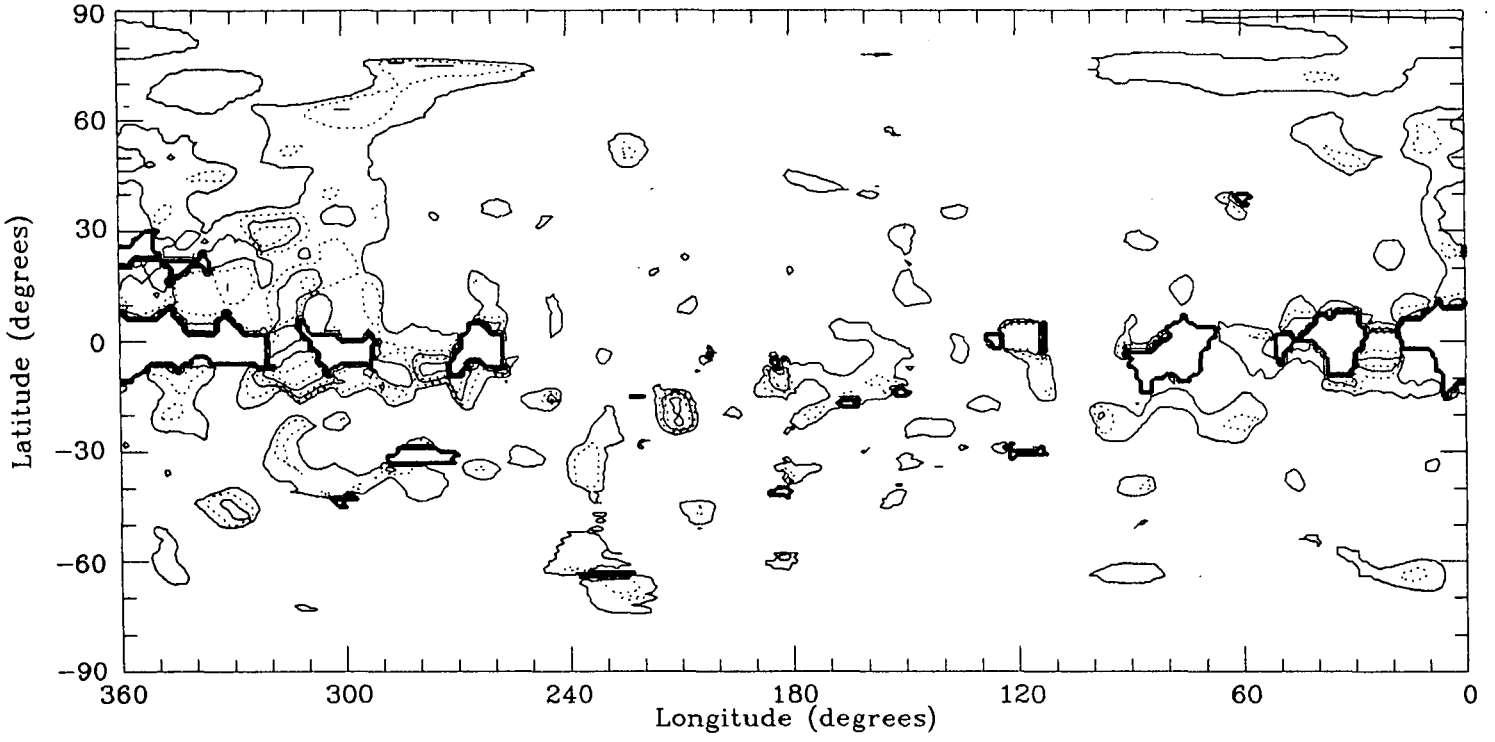

Fig. 4.29 2-6keV x-ray map in Galactic co-ordinates.

	Counts/sec
———	110, 130, 160
.....	120, 140, 180

regions, the maps given in figure 4.2 are in the form of a rectangular grid of latitude and longitude in order to give easier reference to co-ordinates without the need for an overlay on top of already confused contours. Although the Aitoff projection gives equal area maps it has not been used here because there is still considerable distortion and later maps will, in any case, show the regions of interest in greater detail.

The contours on each of these maps are in terms of counts/second. This is simply the number of counts observed divided by the effective time of the observation. The actual number of counts observed in each map is thus almost entirely dependent on the effective area/sensitivity of the band and a direct comparison of counts in different bands is relatively meaningless. Unfortunately, the large band width of the different filters makes it impossible to produce more meaningful maps in units of ergs.$s^{-1}cm^{-2}sr^{-1}$ without a reliable knowledge of the nature of the emission spectrum. As will be discussed later, the emission appears to be thermal in nature, with a temperature range of 1 to 100 million Kelvin. Appendix A gives conversion factors from counts/second for each band, to ergs.$s^{-1}cm^{-2}sr^{-1}$ between the defined photon energy limits, for a few temperatures of a thermal model. The final column gives the total expected integrated flux per emission measure at each temperature. In practice, each region of the sky will contain a number of source regions of varying

temperatures, thus preventing the production of intensity maps.

4.1.1 Point Source Subtraction

A number of point sources had already been subtracted by the Wisconsin group, 5 from the B and C bands, and 67 from the higher energy bands. (McCammon et al., 1983; Burrows, 1982). The criteria used for subtraction was that the source should have over 20 Uhuru counts in the 4th UHURU catalogue (Forman et al. 1978). Not all of the sources defined by this objective criteria and removed from the maps were actually observed, and conversely, there were some apparent source that were not removed. This could be due to a number of reasons. For example, possible variability of the source or an insufficiently well known spectrum to allow accurate extrapolation of the 4U source over the wide pass bands. Subsequent to the initial publication of these maps a catalogue of HEAO-II soft X-ray sources became available (Nugent et al., 1983). We attempted to see if the subtraction of these sources from some of the maps would make any significant changes.

Since the HEAO-II satellite was operating at energies within the range covered by some of the filters, it was thought possible to arrive at a better estimate of the contribution of each source to the detected flux than was possible with the 4U sources. Little spectral information was available for the sources, so an assumed E^{-2} power law

was used for the photon spectrum. This lack of knowledge as to the spectral form restricted the attempted subtraction to only the bands within which the HEAO observation was made. All the sources were used, and each was convolved down to the resolution of the appropriate map. Where only an upper limit flux was stated this upper limit was used in the subtraction.

The resultant maps were not significantly altered. The total flux from the brightest of the sources being only a small fraction of the background. Neither was there sufficient grouping of sources on the scale of the Wisconsin detector's beam size for combined fluxes to become important. In many places there was evidence of small localized maxima being subtracted, the high positional coincidence of the source suggesting that the maxima were indeed due to the source. Often, the correct magnitude of the subtraction indicated that the estimated flux was accurate. However, most sources did not coincide with maxima, and a few were located very close to minima. In these cases, if the estimated source strength was great enough there would be an easily discernable increase in the depth of the minima. We therefore decided that there was no reason to subtract any of the sources, and the maps as originally provided by Wisconsin University were used for all further analysis.

4.1.2 General Features

Two features are most striking. Firstly, there is a strong latitude dependence at the softer energies. There is a steady increase in intensity moving from the plane to either pole. This is almost certainly due to the absorbtion of the x-rays by the neutral hydrogen, the concentration of the cool gas at low latitudes absorbing all B-band x-rays save those that were emitted very locally. At higher latitudes the absorption length of the soft x-rays is much greater, and the resulting increase in the length of the contributing line of sight leads directly to an increase in the observable flux.

Secondly, there is the enhanced emission in the higher energy bands coming from the direction of the galactic centre. The region of enhancement is of large angular size and is mainly confined to the northern hemisphere, $270° < l < 40°$. The brightest and most obvious feature in the sky is the extended x-ray ridge that marks the easterly edge of this enhanced region in the M and I bands. Starting at $(l,b)=(30°,8°)$ this ridge can be easily traced round to $(300°,60°)$ There is thus a strong positional coincidence between this x-ray ridge and the radio continuum North Polar Spur. Later in this section on the x-ray data the evidence for this to be a physical relationship will be examined.

4.1.3 X-ray Maps

As can be seen from figure 4.2 there is no evidence of x-rays coming from loops II or III and these regions need not be examined in any greater detail. In order to show the x-ray region associated with Loop I in relation to the circular nature of the loops it is best to reproduce some of the maps in the form of a stereographic projection. This projection has the property of preserving angles, and thus a small circle on a sphere will be projected into 2-dimensions as a circle. Yaglom (1979) gives equations for the stereographic projection through the north pole. Combining this with a spherical co-ordinate transformation enables the projection to be centred on any radio loop, though it should be noted that it is not necessary for a small circle to be centred on the projection in order that it appear circular. Figure 4.3 shows all 7 bands as a stereographic projection of one hemisphere of the sky, centred on l=329°, b=17.5; ie. the centre of Loop I as defined by Berkhuijsen (1973). The radio spur at 408MHz is also given in the same projection for comparison. Figure 4.4 gives the detailed co-ordinates of these maps. The thick solid curves give the positions of the zero longitude and zero latitude, and the dashed lines are at 10° intervals. The North Galactic pole is near the top of the map with longitude increasing clockwise about it. The thick solid lines are the loops. The large centre circle being Loop I, enclosing the smaller Loop IV. Parts of loops II and III

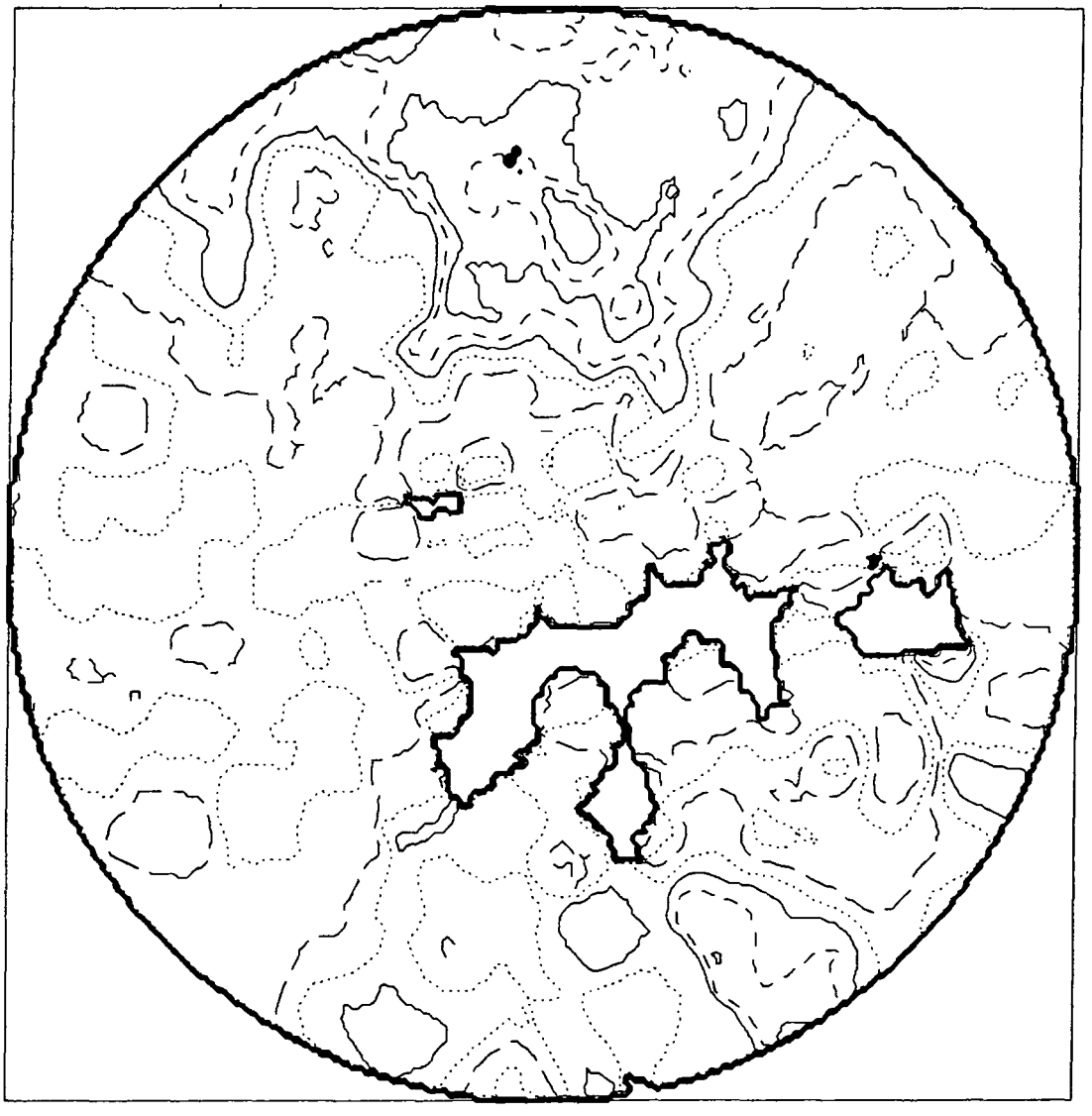

Fig. 4.3a Stereographic projection of B-band x-rays. centred on l=329 b=17.5

	Counts/sec
– – – – – –	25, 45
.....	35, 55
————	65, 85, 105
- - - - - - - - -	75, 95

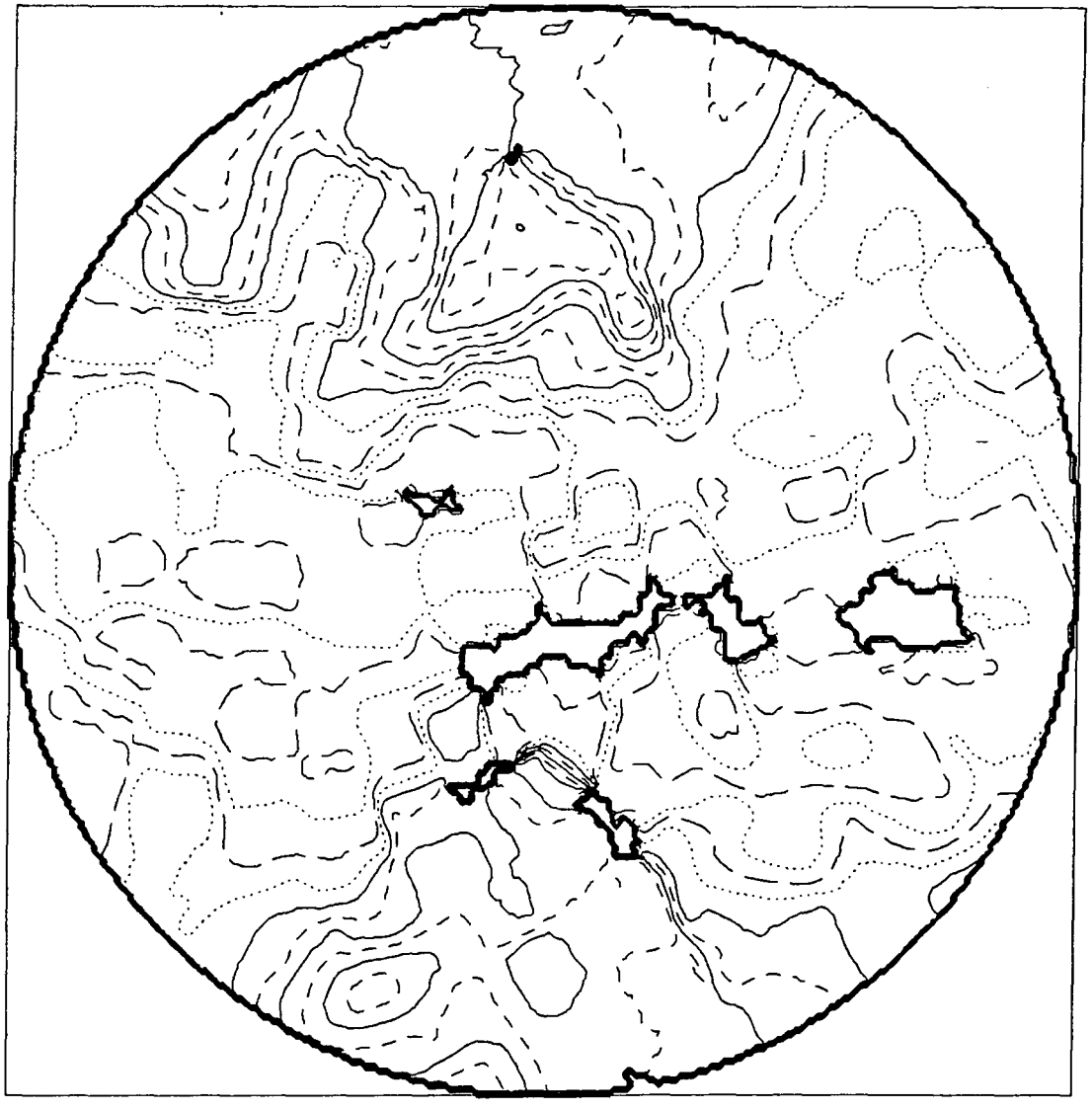

Fig. 4.3b Stereographic projection of C-band x-rays, centred on l=329 b=17.5

	Counts/sec
.— — — — — —	60, 100, 140
.....	80, 120, 160
————	180, 220, 260, 300
- - - - - - - -	200, 240, 280

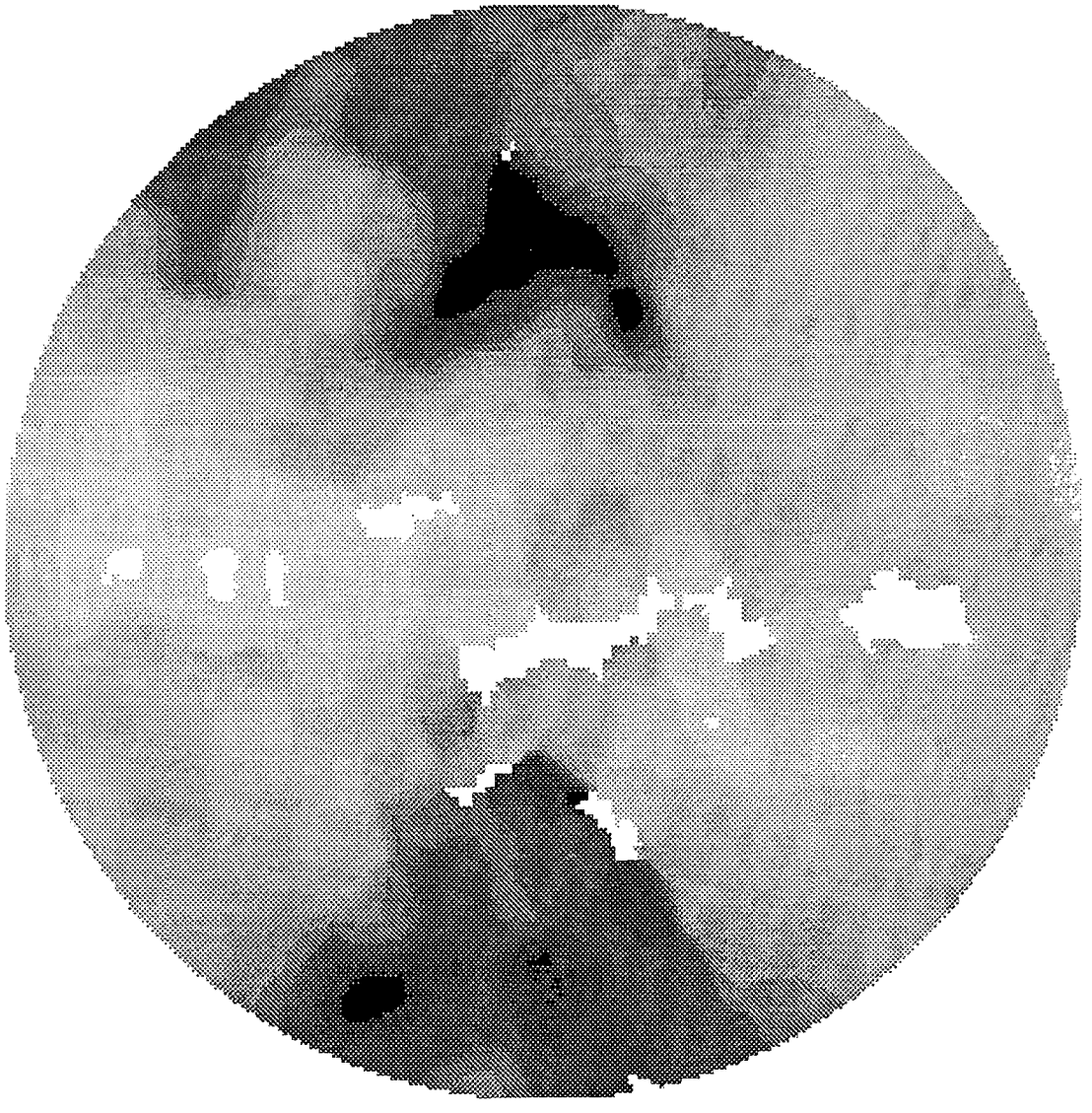

Figure 4.3bb Greyscale representation of figure 4.3b

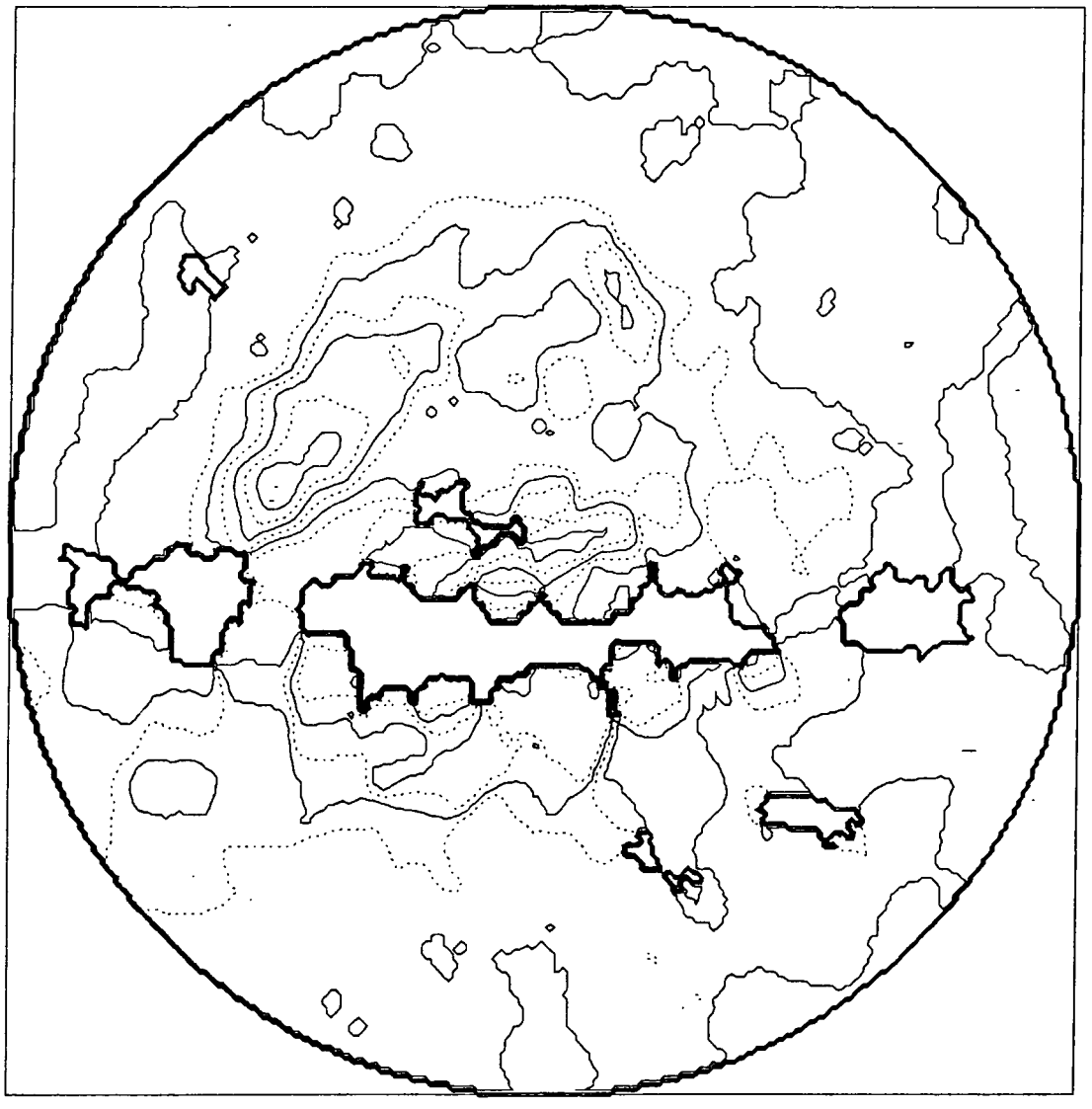

Fig. 4.3c Stereographic projection of M1-band x-rays, centred on l=329 b=17.5

Counts/sec

——— 20, 40, 60, 80

..... 30, 50, 70, 90

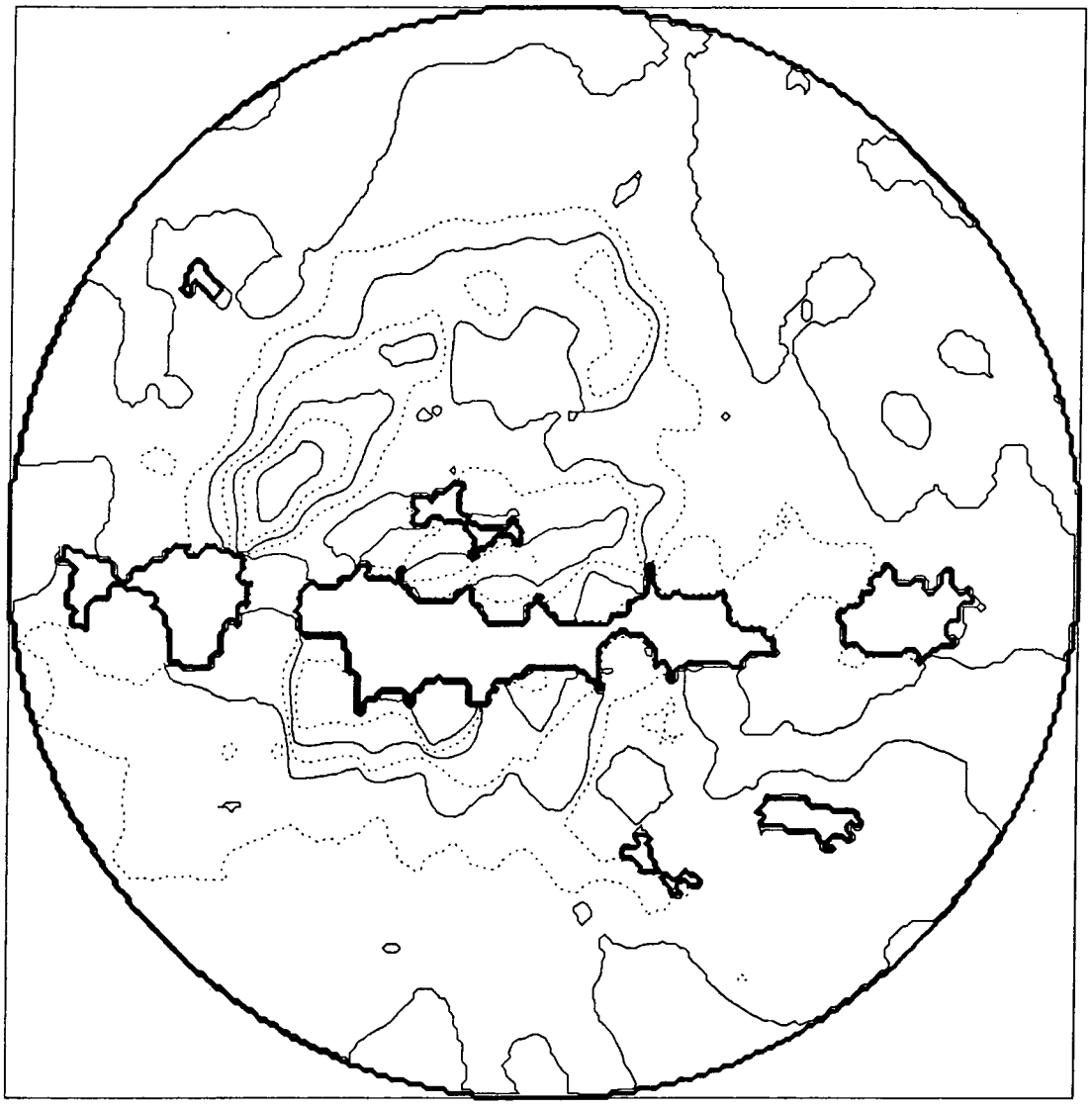

Fig. 4.3d Stereographic projection of M2-band x-rays, centred on l=329 b=17.5

Counts/sec

——————— 30, 63, 97, 130

..... 47, 80, 113

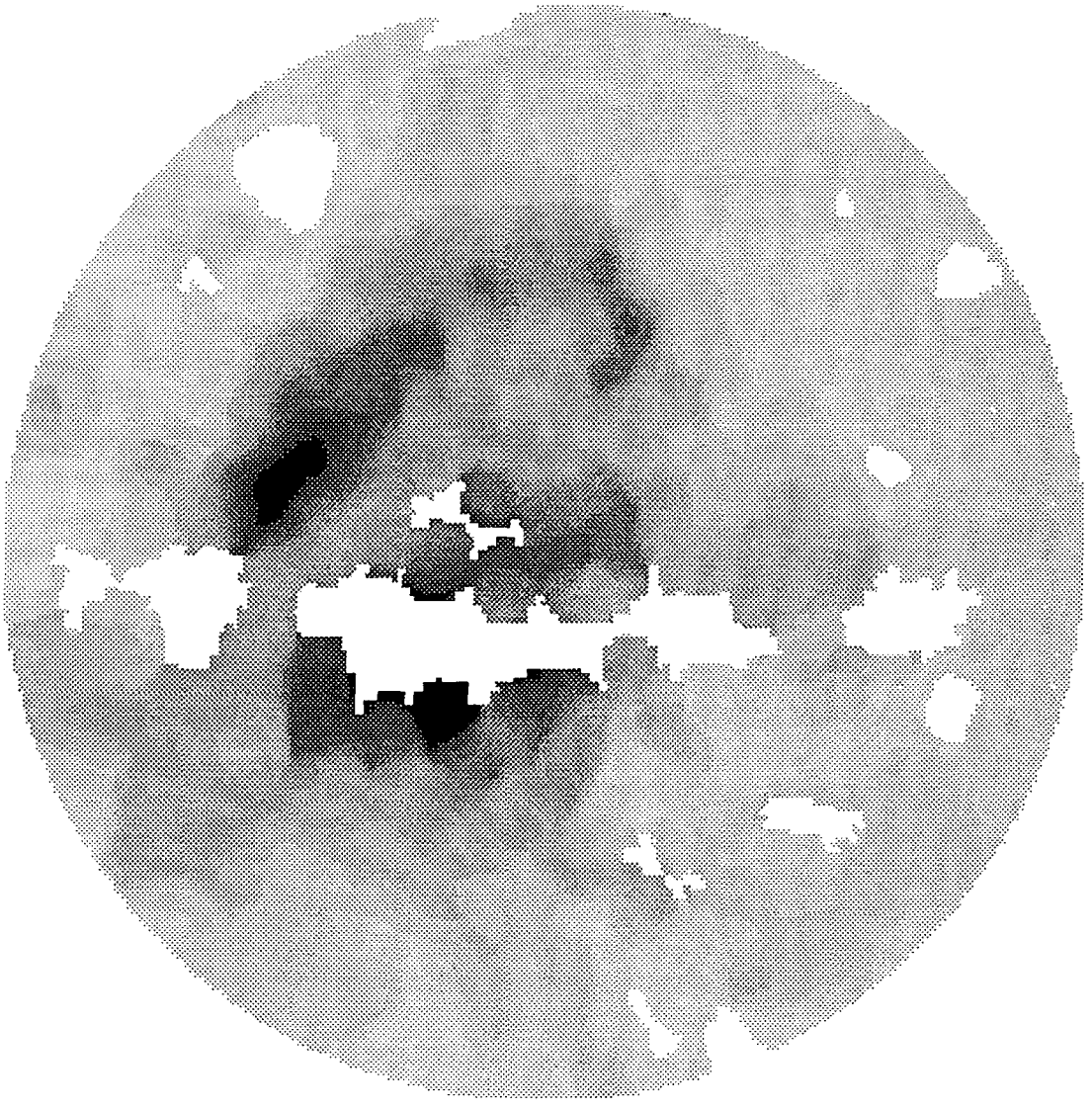

Figure 4.3dd Greyscale representation of figure 4.3d

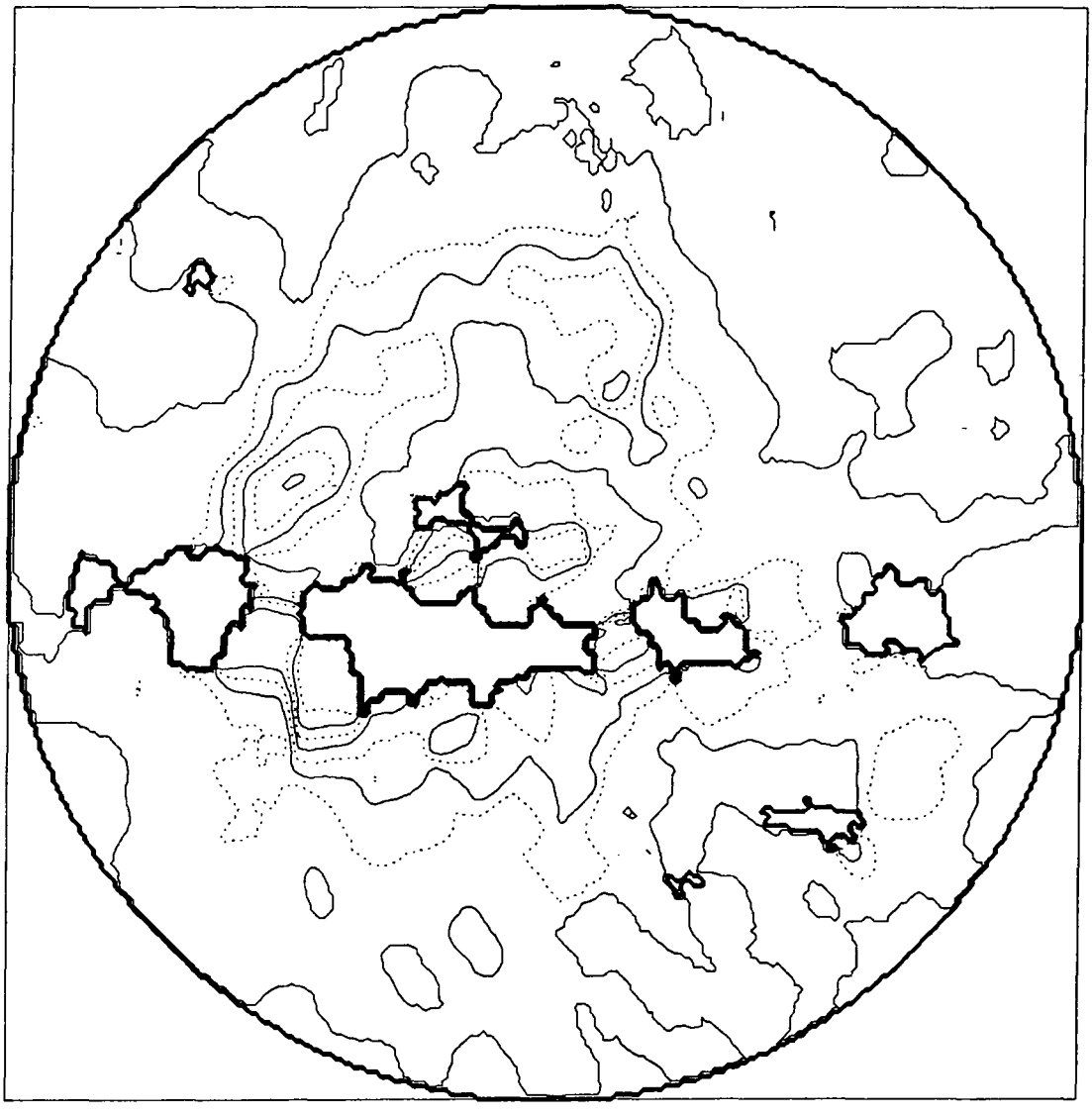

Fig. 4.3e Stereographic projection of I-band x-rays, centred on l=329 b=17.5

Counts/sec

——————— 50, 83, 117, 150

..... 67, 100, 133, 167

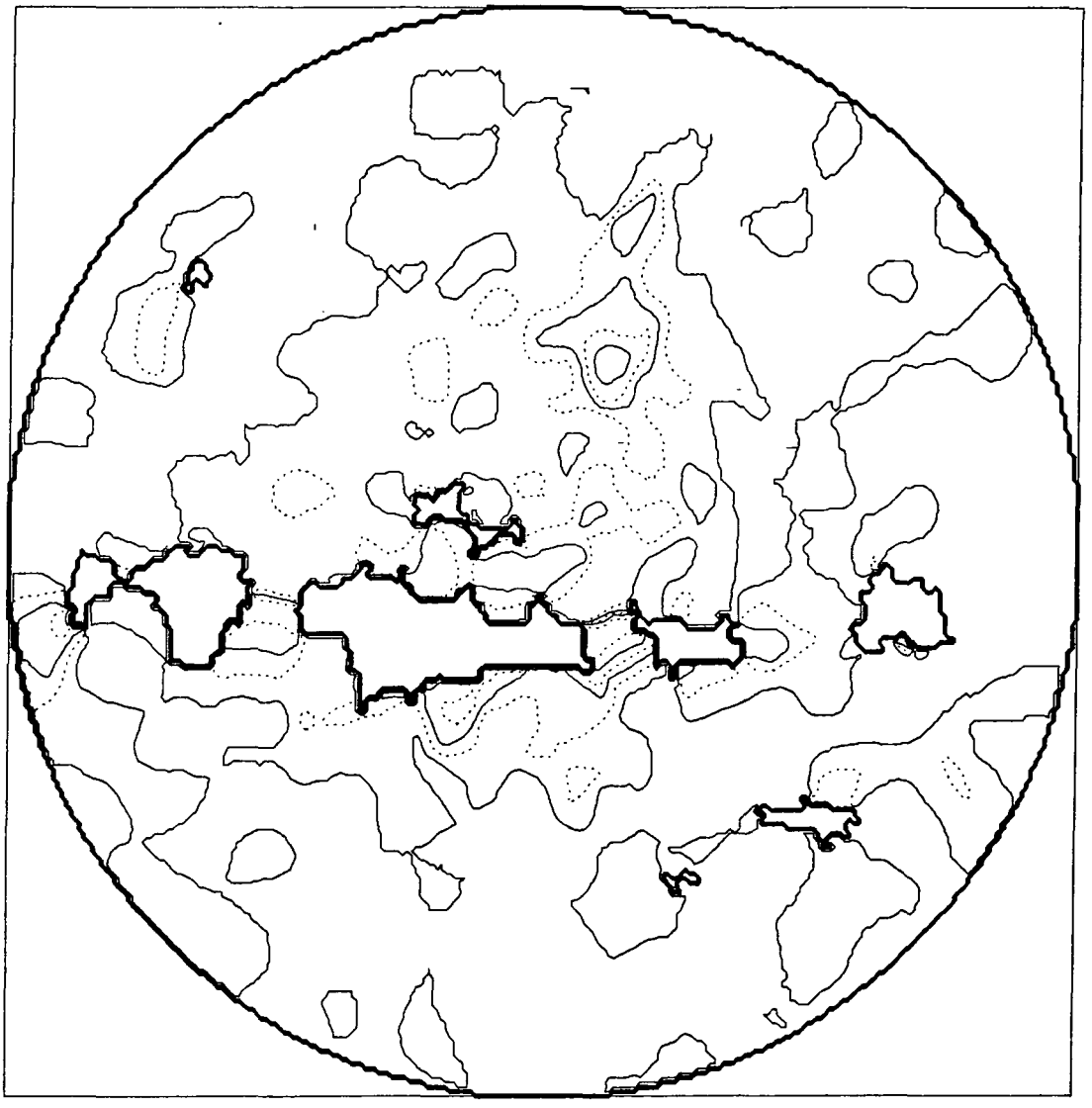

Fig. 4.3f Stereographic projection of J-band x-rays, centred on l=329 b=17.5

Counts/sec

——————— 75, 105, 135

..... 90, 120, 150

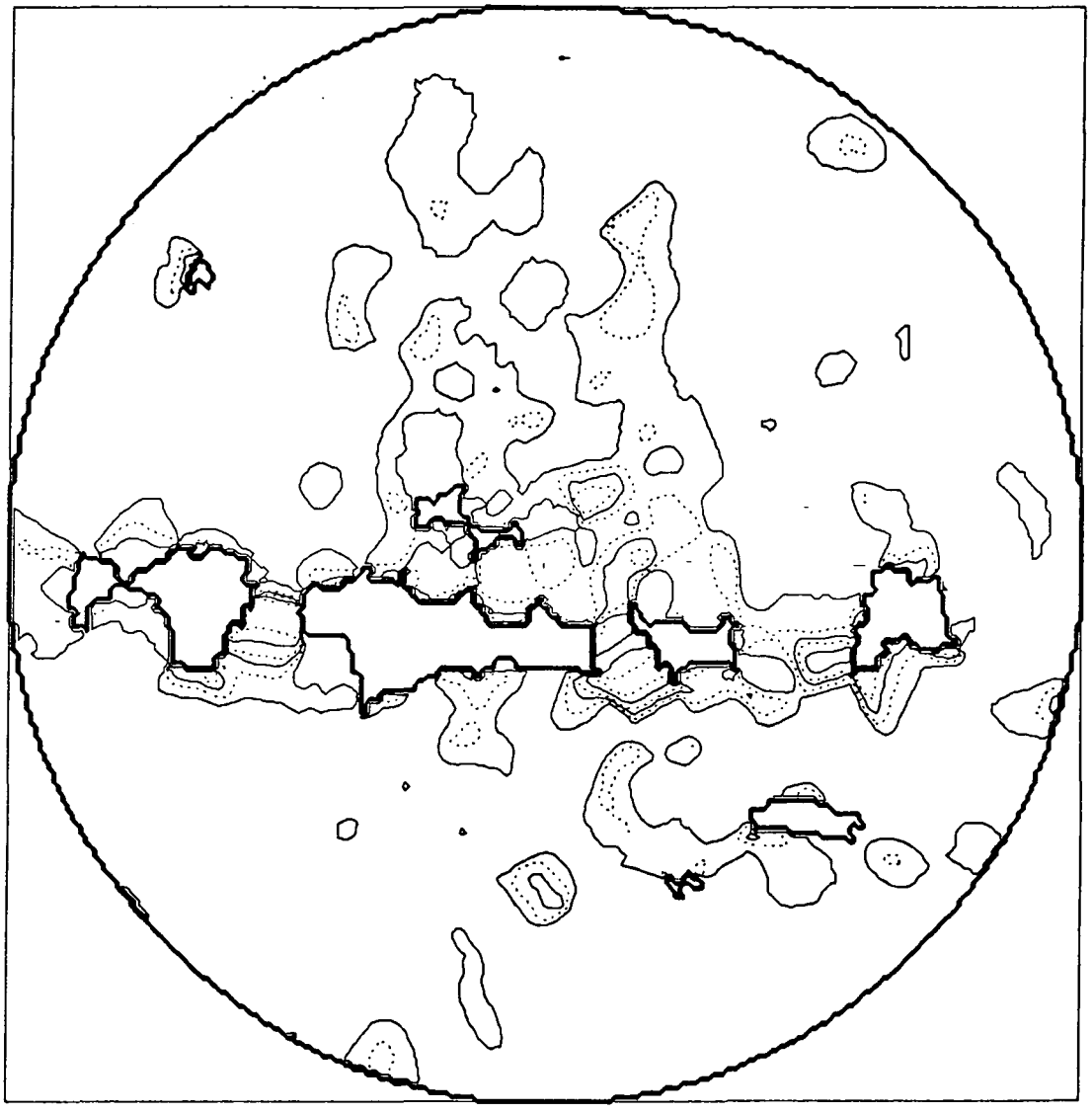

Fig. 4.3g Stereographic projection of 2-6 keV x-rays centred on l=329 b=17.5

	Counts/sec
———	110. 130. 160
.....	120. 140. 180

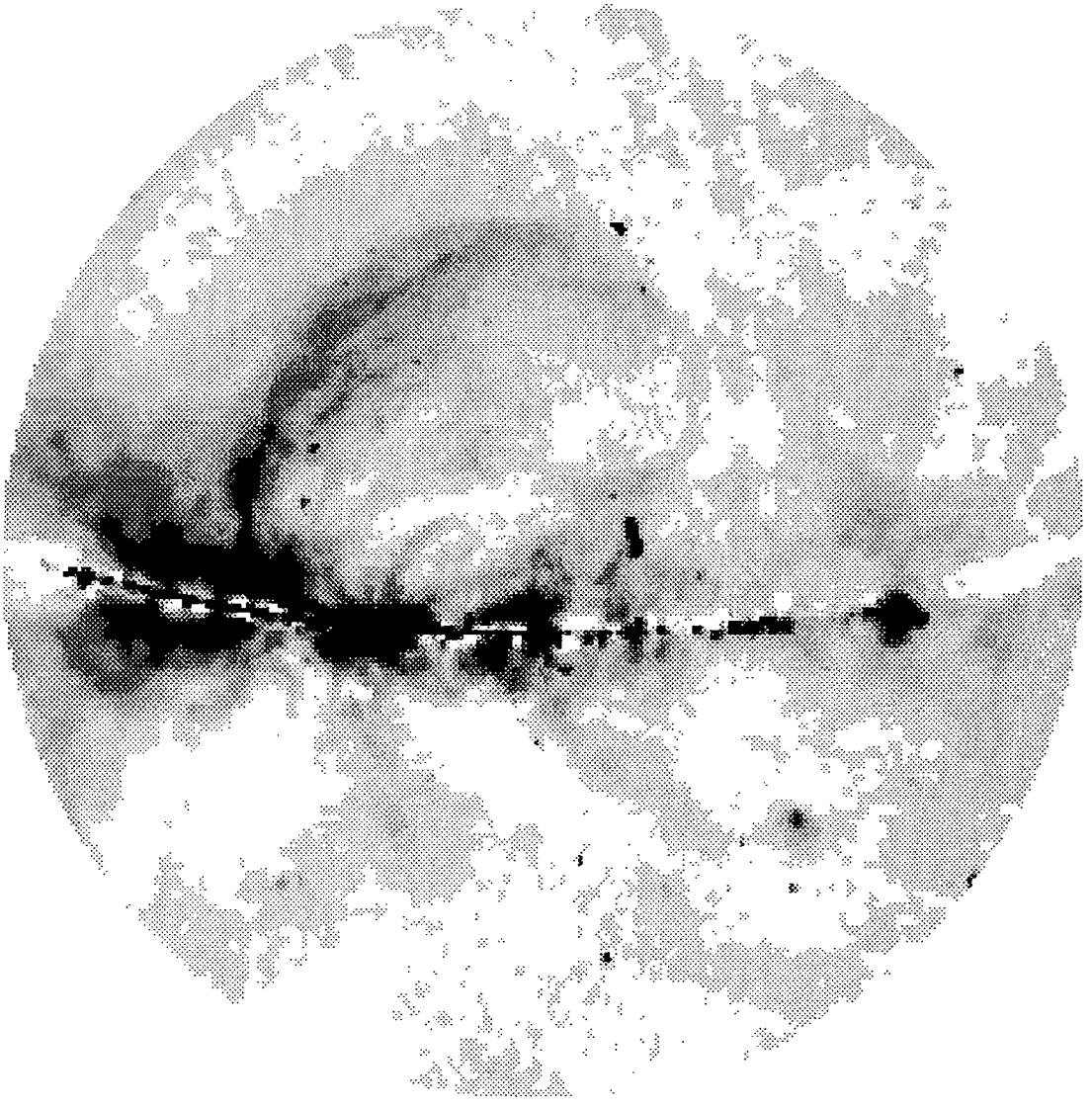

Figure 4.3h Greyscale representation of 408MHz data. Co-ordinates given by figure 4.4

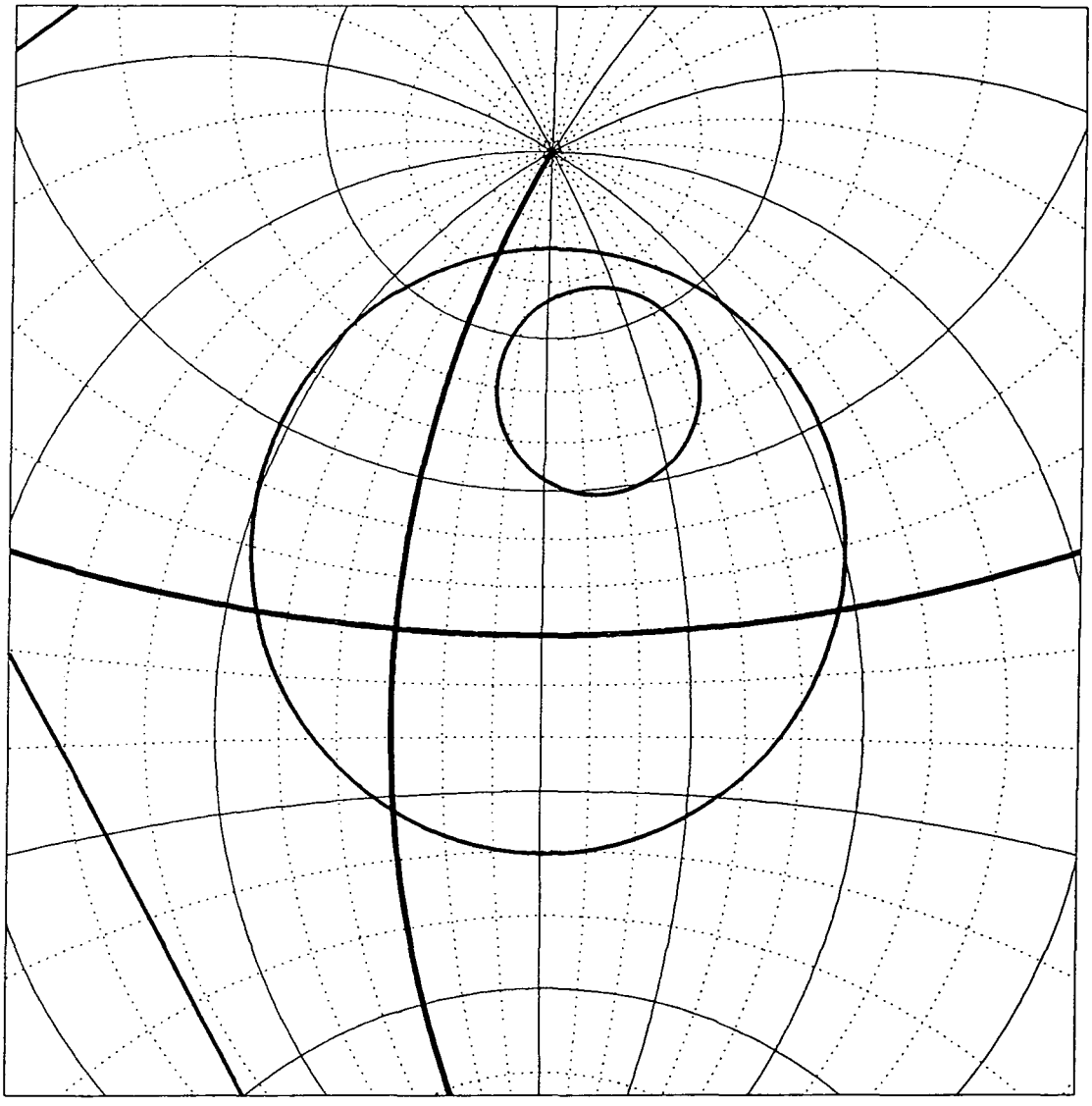

Figure 4.4 Co-ordinates for fig. 4.3 with the the radio loops as defined by Berkuijsen (1971). l=0 and b=0 are shown as bold lines.

are shown as arcs to the bottom left and top left. To assist the reader figure 4.4 has been reproduced a transparency overlay, and is enclosed on the inside of the rear cover of this thesis.

4.2 RADIO DATA

An all-sky map of the galactic radio emission has been presented in chapter 1. Figure 1.1 shows the radio continuum at 408MHz (Haslam et al. 1982). Due to the greater quantity of data from large scale surveys in the north celestial hemisphere, the best observed of the loops is Loop III, the centre of which lies close to the north celestial pole. Much of the North Polar Spur is also in the northern hemisphere, but the majority of the sky that is encircled by Loop I lies to the south of the equator. When examining the radio data the emphasis will therefore be on Loop III. There are 6 surveys covering the entirety of Loop III that will be mentioned here, ranging in frequencies from 38MHz up to 1420MHz. These are at 38MHz (Milogradov-Turin and Smith 1973, Milogradov-Turin 1984), 178MHz (Turtle and Baldwin 1962), 404MHz (Pauliny-Toth and Shakeshaft 1962), 408MHz (Haslam et al. 1982), 820MHz (Berkhuijsen 1972), and 1420MHz. (Reich 1982). Details and history of all of these surveys are given in Lawson et al. (1987) and references therein. Only four of these surveys will be considered here: 38, 408, 820 and 1420MHz. The 404MHz data and the 178MHz data will not be used. The former is essentially superseded by, and acted

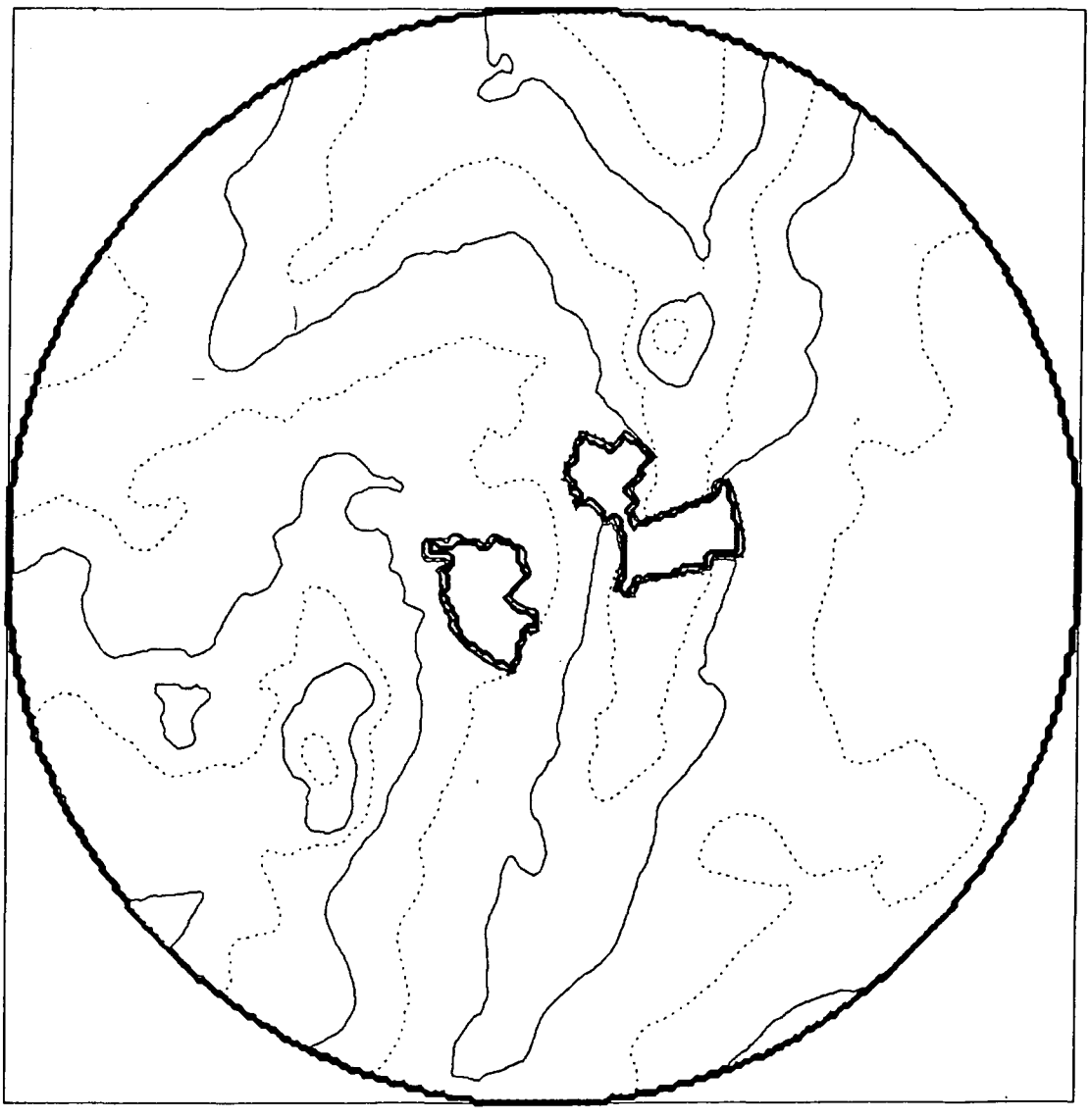

Fig. 4.5a Stereographic projection of 38MHz data centred on the North Celestial Pole

Kelvin

..... (4900), 6390, 9370, 15300, 30200

——— 5490, 7580, 12300, 21300, (60000)

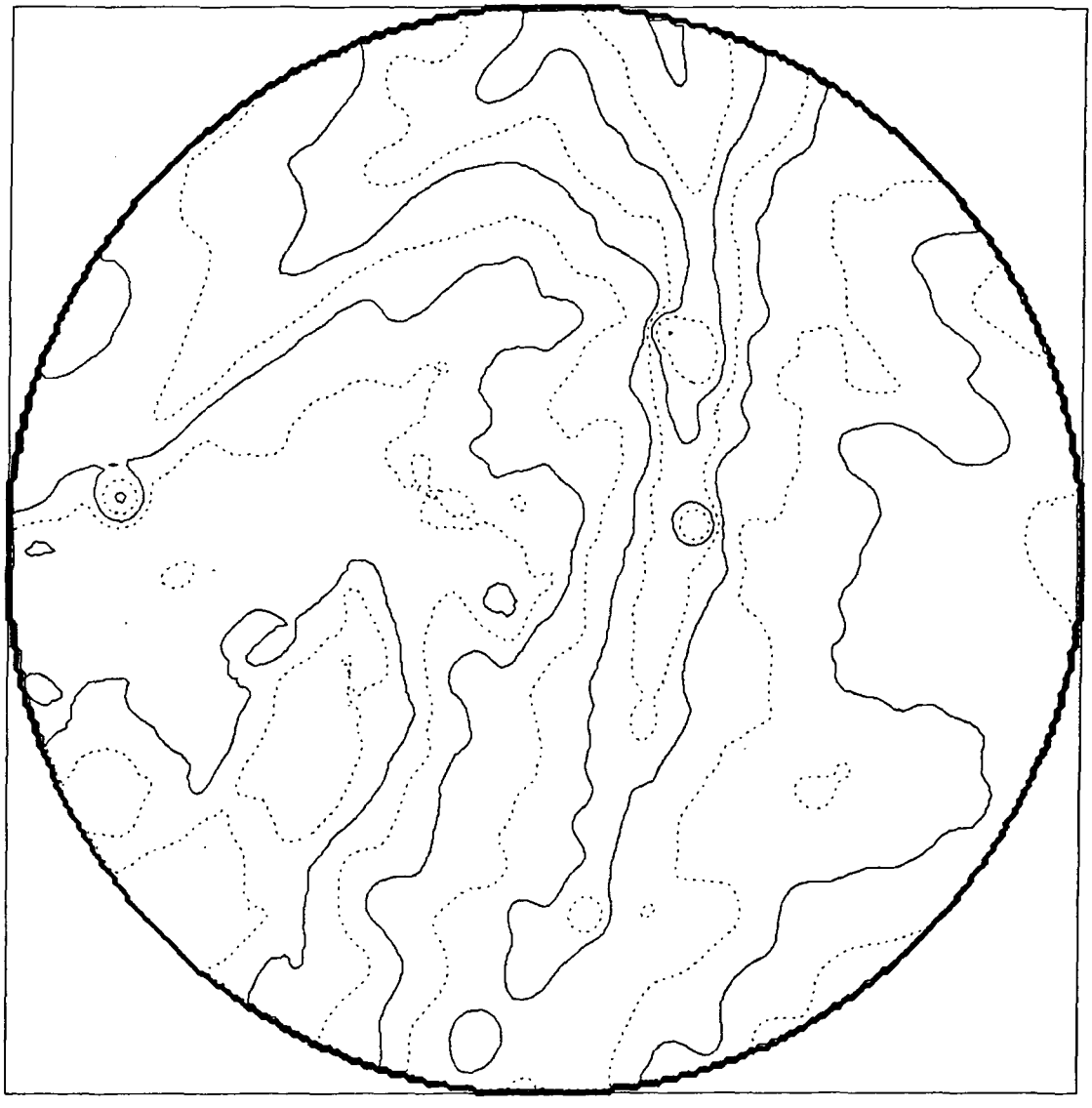

Fig. 4.5b Stereographic projection of 408MHz data centred on the North Celestial Pole

	Kelvin
.....	15, 20, 30, 50, 100
————	17, 24, 40, 70, 200

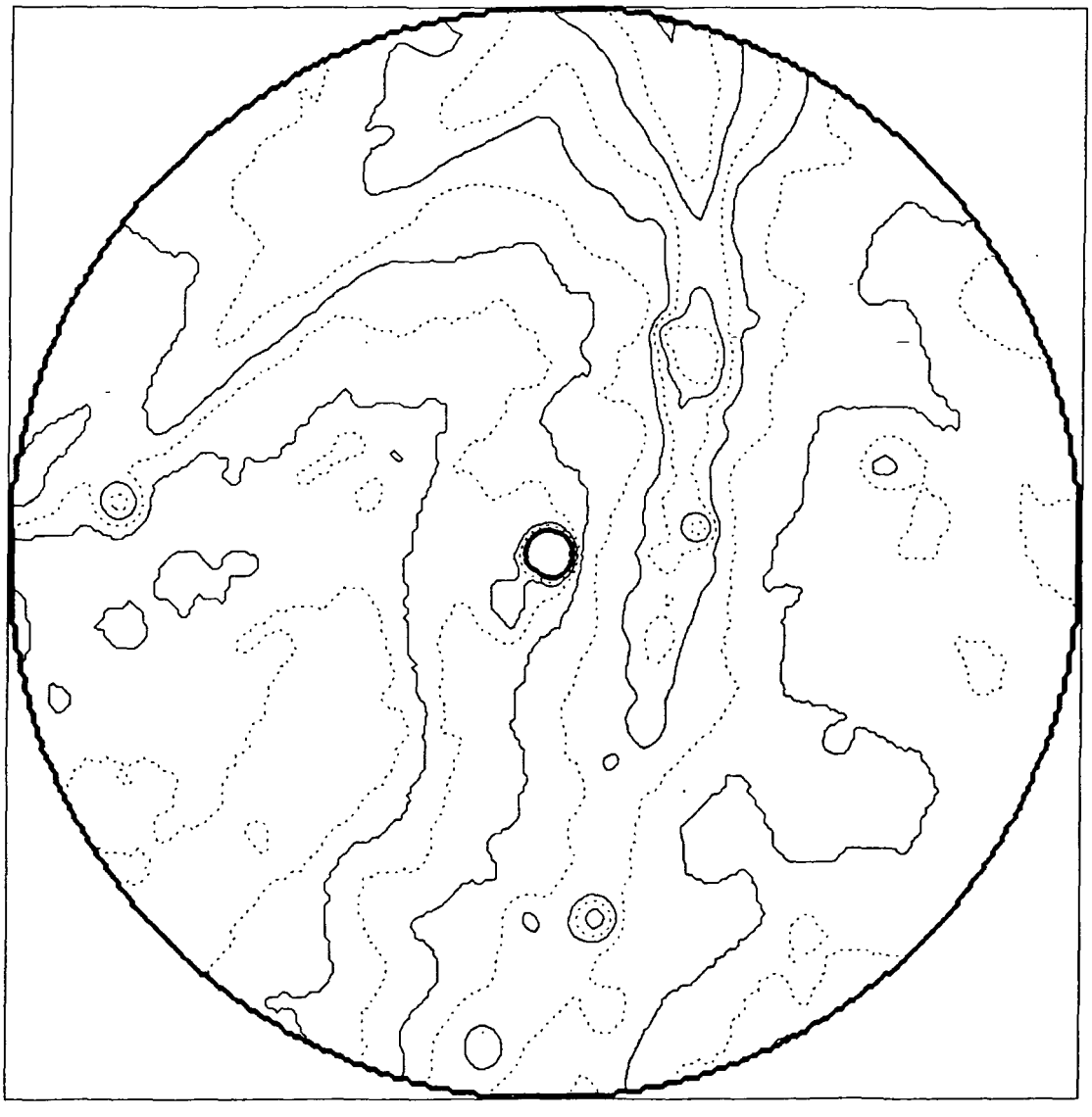

Fig. 4.5c Stereographic projection of 820MHz data centred on the North Celestial Pole

	Kelvin
.....	5.85, 6.78, 8.65, 12.4, 21.8
————	6.22, 7.53, 10.5, 16.1, 40.5

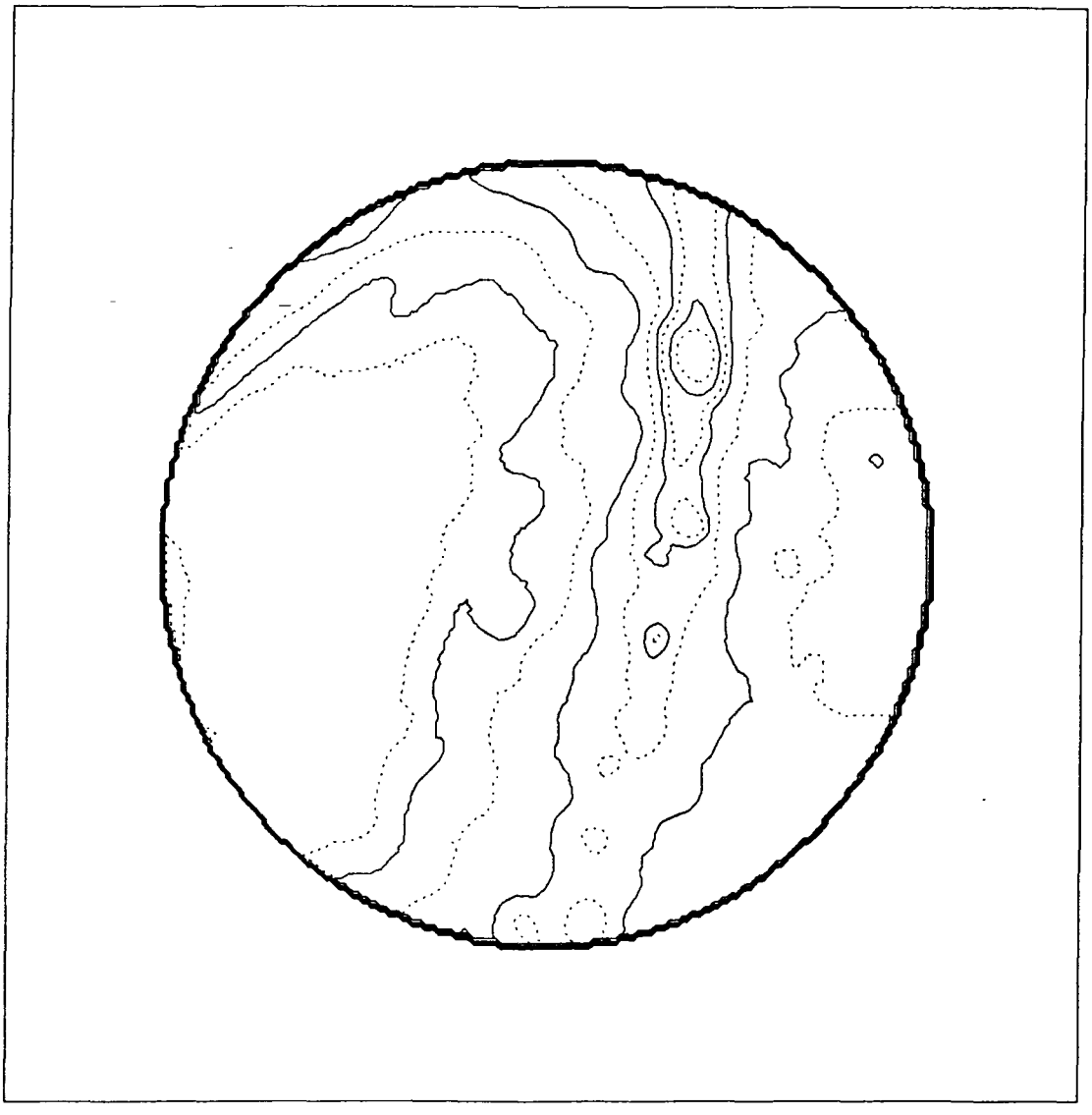

Fig. 4.5d Stereographic projection of 1420MHz data centred on the North Celestial Pole

	Kelvin
.....	3.39, 3.64, 4.14, 5.14, 7.65
————	3.49, 3.84, 4.64, 6.14, (12.7)

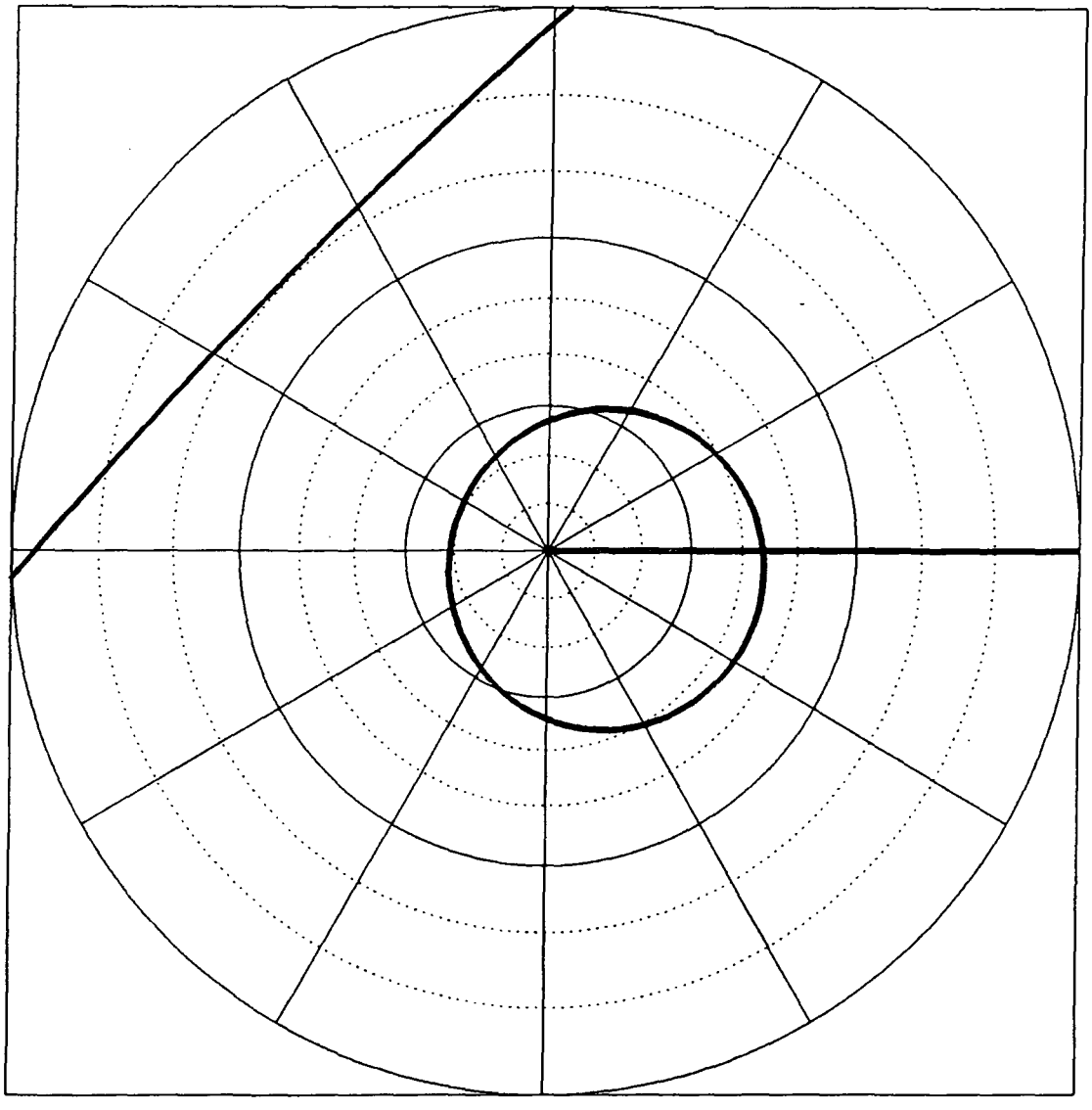

Fig. 4.6a Celestial co-ordinates for figs. 4.5 & 4.7
RA runs clockwise at 2hr intervals.
Declination is marked every 10°.
l=0° marked bold.
Loops I and III are outlined.

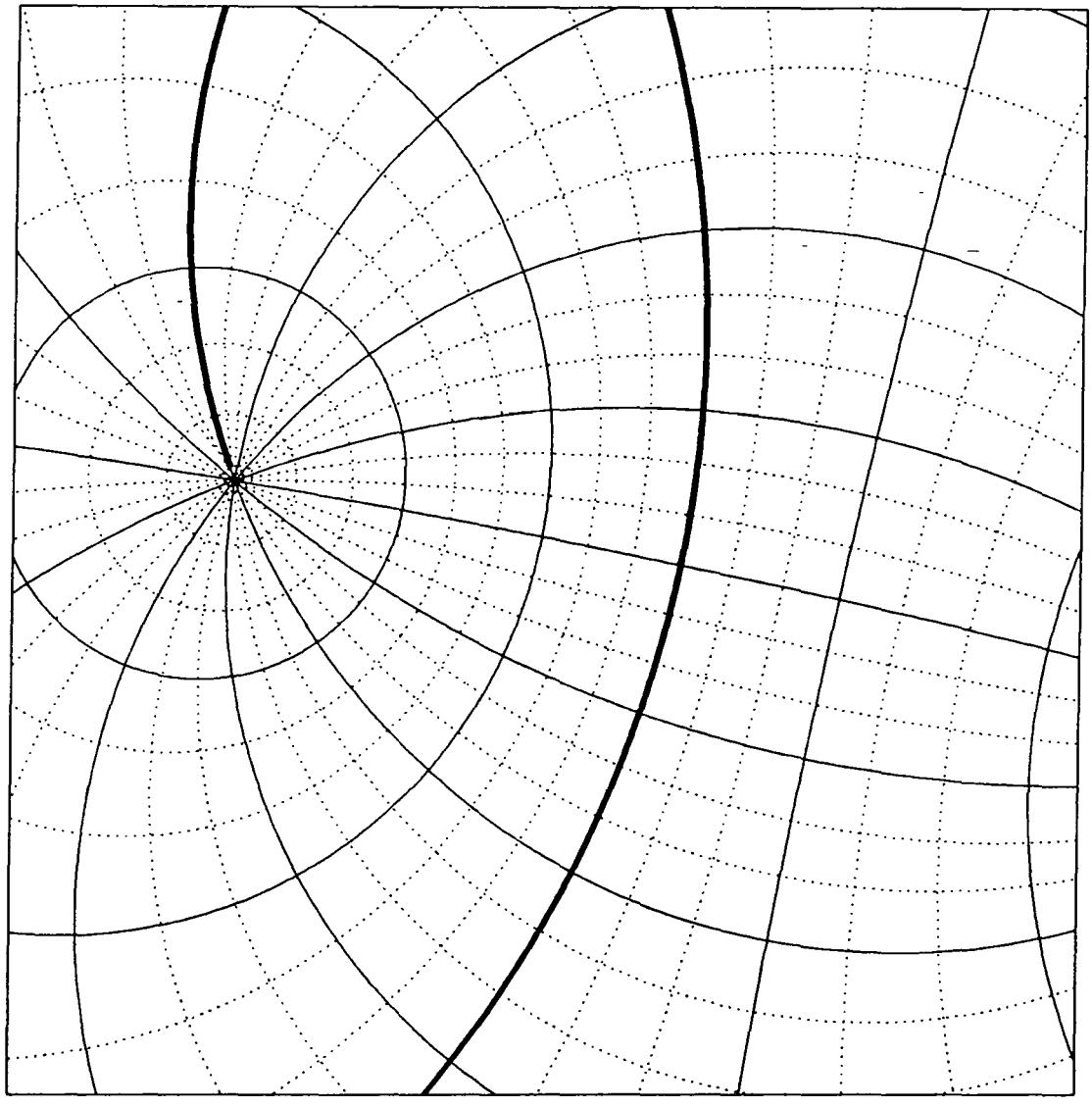

Fig. 4.6b Galactic co-ordinates for figs. 4.5 & 4.7
l and b marked every 10°. l runs clockwise about the N. Galactic Pole. l=0° and b=0° are bold.

as a calibrator for, the 408MHz survey. Anomalies in the way the latter was produced (see Lawson et al.) have made it difficult to correctly calibrate and convolve to the other surveys, and the large emission from side-lobes of the detector causes considerable error. The remaining four surveys are shown as contour maps of the Northern Celestial Hemisphere in figure 4.5. The projection is again stereographic, but is now centred on the North Celestial Pole. Figures 4.6a and 4.6b give the co-ordinate system in both celestial an galactic, and the latter is reproduced as an overlay enclosed inside the rear cover of this thesis.

4.2.1 Subtraction of Non-galactic Contributions.

Ideally, when studying any object one would want to remove all contributions to the observed intensity that come from background or foreground sources. As with the x-ray emission from the loops, this cannot be readily done for the loop's radio emission since the galactic background fluctuates unpredictably on scales that are smaller than the size of the loops. However, in the radio sky there is a uniform calculable contribution of non-galactic origin, and this can be subtracted.

Many measurements have been made of the microwave background radiation. Weis (1980) lists measurement that have been made in the Rayleigh-Jeans part of the spectrum. The weighted mean of the 12 observations made above 4 GHz,

and therefore likely to be free from galactic contamination, gives a temperature of 2.7 ±0.1K. Since this is a thermal spectrum, 2.7K can be subtracted from the brightness temperature of all the surveys.

Frequency	HPBW	Scale error	Base level error	Extragalactic background	Base Level correction	Sky minimum
MHz	Deg.	%	%	K	K	K
38	7.5	5	300	2185	-	3300
408	0.85	10	3	5.89	-	8.53
820	1.2	6	0.6	3.17	0.97	1.47
1420	0.6	5	0.5	2.80	0.13	0.37

Table 4.2 The 4 continuum surveys used.
Columns 1-4 give their characteristics as given in the relevant papers (see text). Column 5 gives the total extragalactic background subtracted from the maps as defined in the text. Column 6 gives the additional subtraction from the 820 and 1420MHz surveys to normalise the sky minium to a constant spectral index, and column 7 gives the resultant temperature of that sky minium.

There is also a contribution from the sum of all unresolved extragalactic 'point' sources. Willis et al. (1977) fit source counts at 610 and 1415MHz. Integrating over all the sources gives a spectral index between the two frequencies of 2.78, and a brightness temperature of 30K at 150MHz. Brindle (1967), using frequencies of 13.15 and 81.5MHz, attempted to deduce the contributions of the isotropic component. He arrived at a spectral index of 2.75, and a brightness temperature at 150MHz of 48±11K.

The background subtracted from the four surveys examined here assumes an unresolved extragalactic source contribution of 50K at 150MHz with a spectral index of 2.75, and a microwave background of temperature 2.7K. The total background subtracted at each frequency is given in table 4.2

4.2.2 Comparison of the Surveys.

The errors in all of the surveys can be split into two types. One being essentially random fluctuations with each survey, and the other being a systematic error that can be considered as an uncertainty in the setting of the zero level. Once the extragalactic contribution has been subtracted these errors can be a considerable fraction of the remaining brightness temperature. This is particularly true at the higher frequencies. It is important to eliminate these errors as far as is possible, since the nature of taking a spectral index is to highlight any small difference between two surveys.

If, in comparing say the 408 and 820MHz surveys, the higher resolution map is simply convolved to that of the lower, then the resultant spectral index map shows a great deal of noise due to the random fluctuations in the sensitivity/calibration of the two surveys. This noise is not truly random, but shows up as two overlaid patterns of striations that are artifacts of the scanning procedures used to track across the sky. Although convolving both

maps to a common low resolution loses some of the small scale detail, it is the simplest method for averaging out these fluctuations. It was found that smoothing the 3 higher resolution surveys to 4° HPBW was sufficient for most of the scanning effects to disappear. The 38MHz data already has an initial resolution substantially lower at 7.5°. This shows no sign of similar scanning effects and has not had to be smoothed further.

Having smoothed out the random errors one is still left with the uncertainties in the absolute base levels of the various surveys. A standard technique is to use a 'T-T' plot, where the brightness temperature at two different frequencies are plotted against one another. By choosing the points to be plotted from a sufficiently small region of the sky it is hoped that the spectral index over that area can be assumed to be constant. A least squares straight line fit will not only give the spectral index by its gradient, but the relative errors between the base levels of the two surveys can be deduced from the intercept. When the data is correctly calibrated the best fit straight line should pass through the origin. However, there is a major problem with this technique. As mentioned, it is necessary that the spectral index be uniform over the region plotted, but it is also desirable that there is a reasonable variation in intensities to give an accurate fit. In selecting points to give the latter one can no longer be confident of the former. An alternative method of re-calibration has thus been

adopted.

The most sensitive region to base level errors will be the region of least intensity. In the Northern hemisphere this 'Sky Minium' is located at approximately. $20° < \delta < 50°$, $130° < \alpha < 150°$. Taking the two surveys with the smallest fractional errors (38 and 408MHz) as being 'correct', a constant spectral index was assumed for this region and the absolute base levels of the higher two frequencies were fixed. There are problems with this method also. Firstly, it is not possible to re-calibrate the lower two frequency surveys, so one has to accept the originally quoted errors. Secondly, the spectral index of the region is unknown, so assuming a constant spectral index would appear to make the method unreliable. However, a justification of this assumption can be found if one has an understanding of the likely nature of any galactic spectral index. The sky minium region corresponds to lines of sight passing through the halo of the outer parts of the Galaxy. It is to be expected that in such a region the spectral index should be constant or increasing slowly with increasing frequency. A constant spectral index can therefore be thought of as the simplest assumption, and base level adjustments based on this will give a lower limit to the steepening of the spectral index in other parts of the sky. It is quite possible that the sky minimum has an increasing spectral index, in which case the base levels should be adjusted further. The effects of this on the spectra of the loops

will be mentioned in chapter 5.

There are clearly problems with both the 'sky minimum' and the 'T-T' plot methods. However, the above mentioned difficulties of the 'T-T' plot mean that there are many uncertainties in the final result and it is not clear what has actually been done. The advantage of the technique used here is that the location and nature of the uncertainties are more obvious, and limitations of the final results can more readily be assessed.

4.2.3 The Spectral Index Maps

After subtracting the background, smoothing and 'correcting' the base levels, spectral index maps were produced from maps of adjacent frequencies. Assuming a power law form for the emission spectrum, $T_{B(\nu)} \propto \nu^{-\beta}$ then between surveys at frequencies ν_1 and ν_2 and galactic brightness temperatures of $T_{B(1)}$ and $T_{B(2)}$ the spectral index will be given by

$$\beta_{(1/2)} = \log[T_{B(1)}/T_{B(2)}]/\log(\nu_2/\nu_1) \qquad 4.1$$

The resultant maps are shown in figures 4.7a-c and 4.7aa-cc in contour and greyscale representations.

4.3 INFRA-RED DATA

Supernova remnants, particularly older SNR, do not appear as emitters of infra-red radiation. However, observations in this part of the electromagnetic spectrum

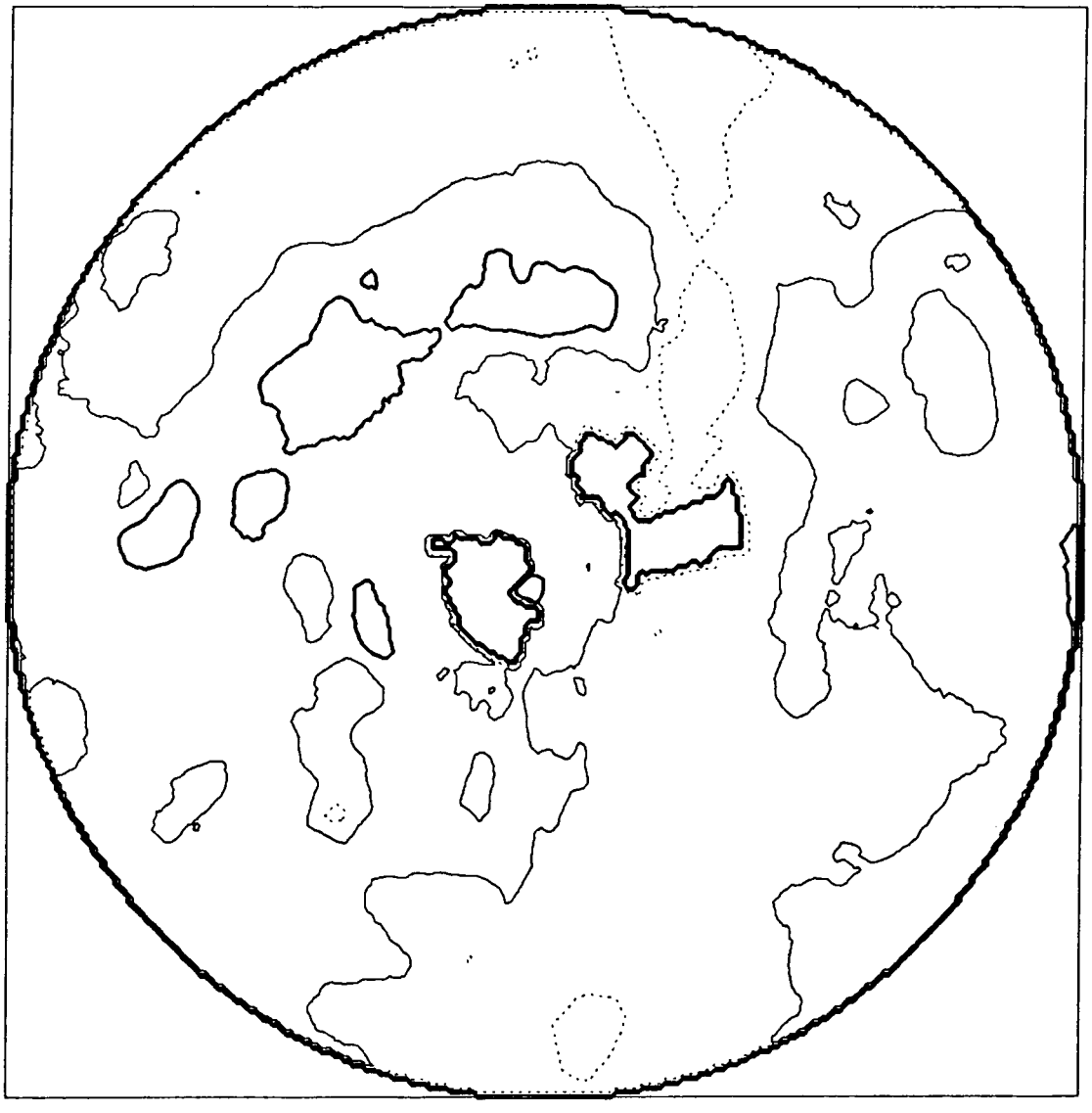

Fig. 4.7a Spectral Index Map 38MHz / 408MHz

β
2.4
2.5
2.6

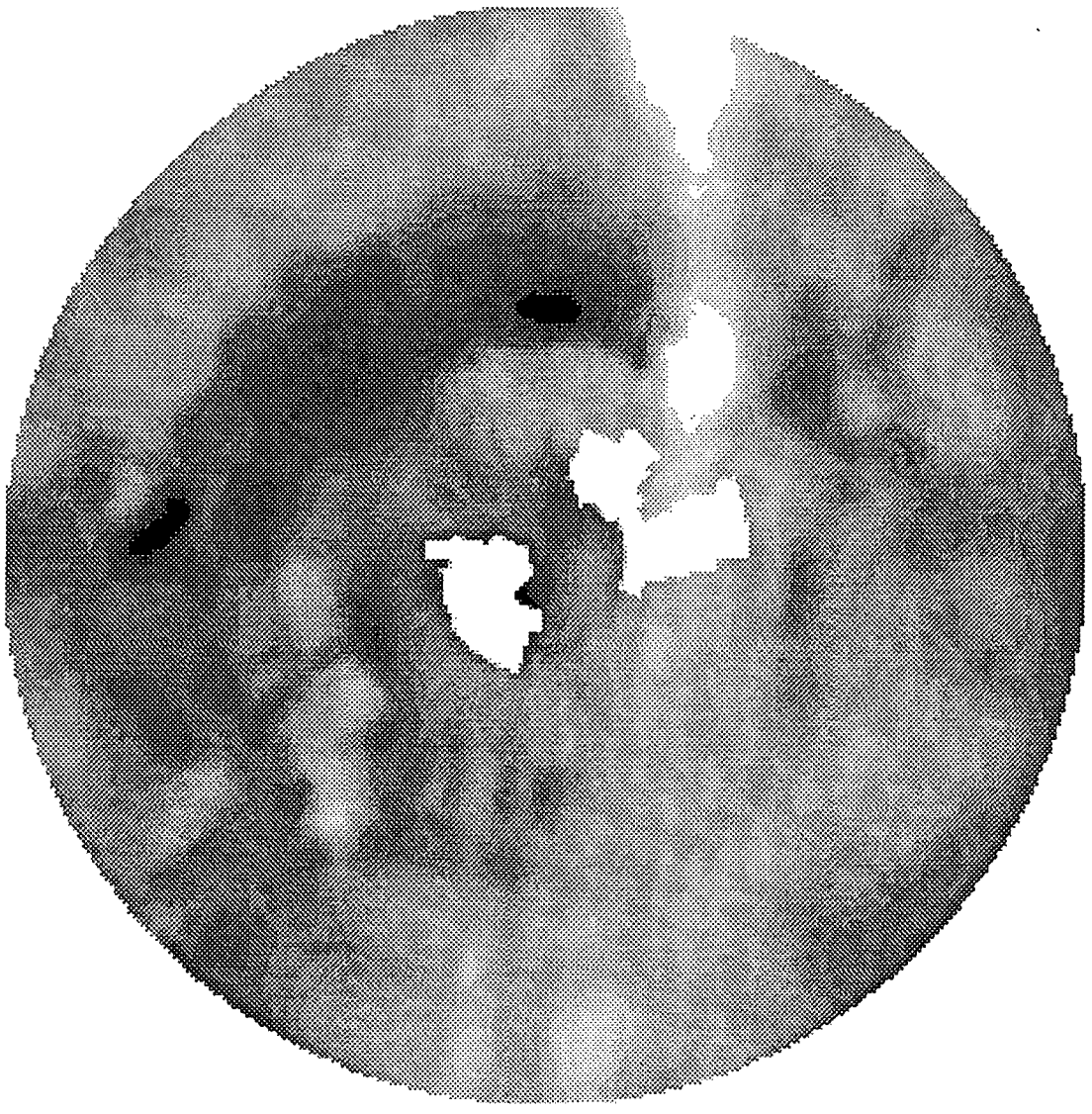

Figure 4.7aa Greyscale representation of figure 4.7a

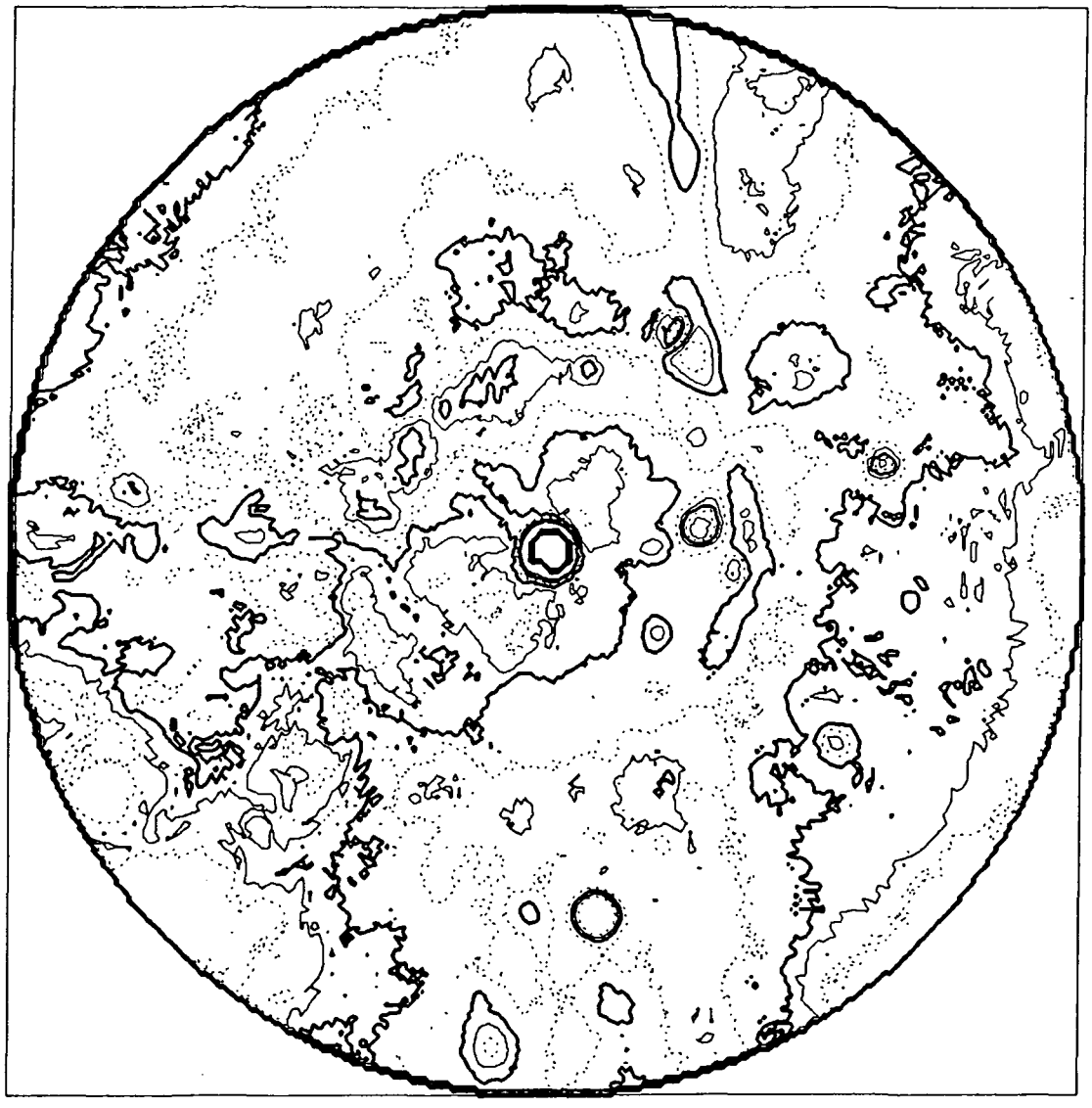

Fig. 4.7$_b$ Spectral Index Map 408MHz / 820MHz

	β
.....	2.4, 2.7, 3.0
———	2.5, 2.8, 3.1
———	2.6, 2.9

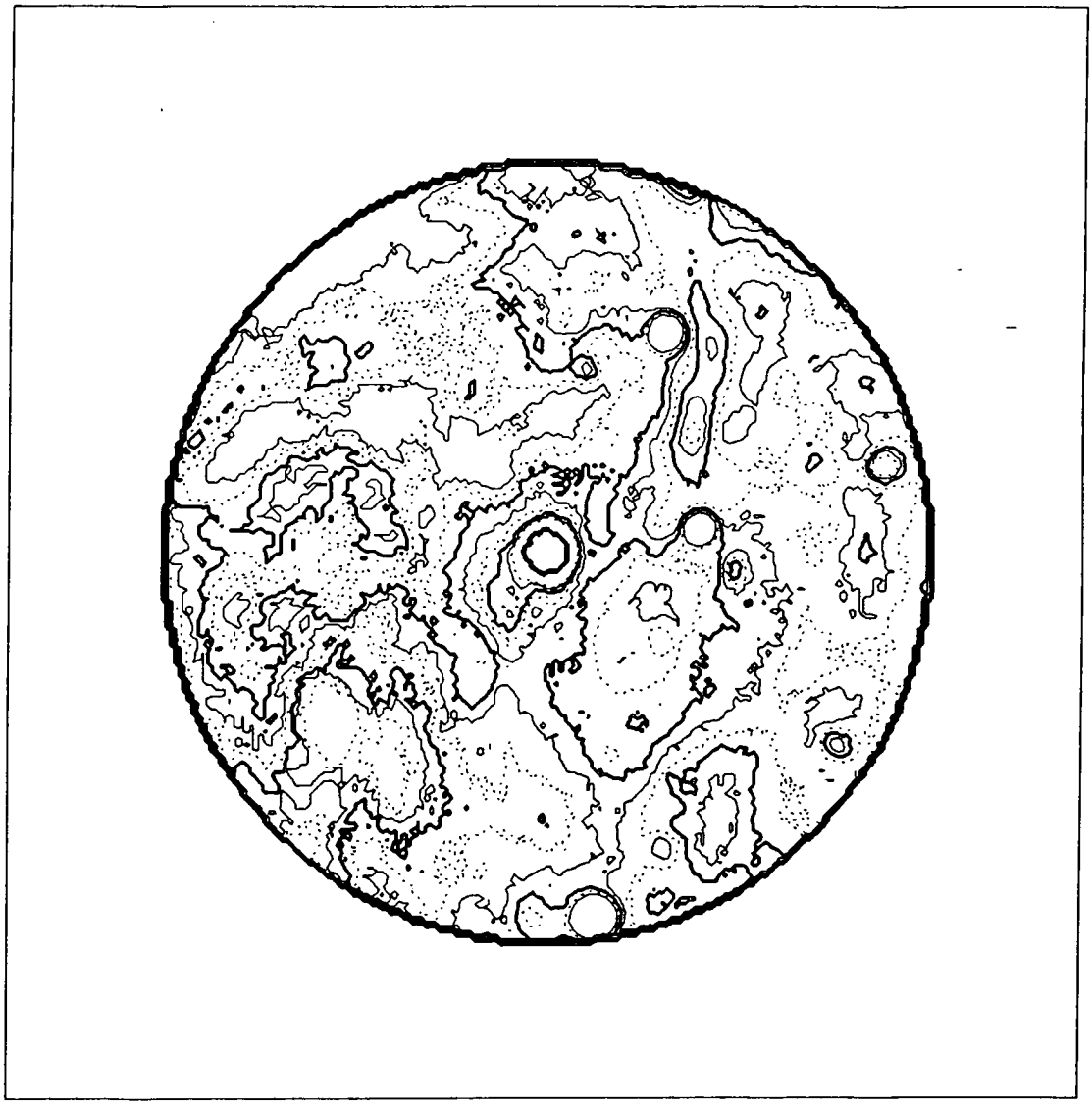

Fig. 4.7c Spectral Index Map 820MHz / 1420MHz

	β
.....	2.4, 2.7, 3.0
————	2.5, 2.8, 3.1
————	2.6, 2.9

Figure 4.7cc Greyscale representation of figure 4.7c

give evidence of the distribution of matter about the remnant; not only directly showing the presence of dust, but also implying the presence of gas. The correlation of dust with gas has been noted by a number of authors (Burton et al. 1987 and references therein), and shall be examined and confirmed later in this section. The infra-red data can thus help to explain the features of a SNR by giving an understanding of the nature of the medium into which the shock wave is expanding.

The recent IRAS (Infra-Red Astronomical Satellite) observations have yielded a vast quantity of data in the 12 to 100μm wavelength range. During the 9 months of operation, over 95% of the sky was surveyed with broad-band detectors nominally operating at 12, 25, 60, and 100μm. The IRAS data base provided maps in two resolutions. The higher resolution data consisted of 16.5° by 16.5° 'plates' of approximately 2' by 2' pixels at 4' resolution. This data was binned into 0.5° by 0.5° pixels to produce the low resolution all-sky maps.

4.3.1 Contamination of the IRAS Data

On the high resolution 'plates' there is a noise source evident as patterns of quasi-parallel striping of several arc minutes in width. These show the scan pattern of the satellite, and are the result of short term fluctuations in the calibration and sensitivity of the detector, often due to an 'after-glow' effect when a

bright source has recently crossed the field of view. In order to satisfactorily address this problem it would be necessary to start with the original telemetry and correct prior to the synthesis of the maps. Although it would be possible to do this for a small area of the sky it is not within the scope of this work to do this on the scale of the galactic radio loops. There is also an external source of contamination, the Zodiacal emission, evident on the plates as a background intensity gradient across the map. On most of these plates it is possible to subtract a simple 2-D inclined plane that approximates to the background emission, though some plates are more complex.

On the low resolution maps the fluctuations induced within the satellite are to a large degree averaged out within the half degree bins, except where the scans have crossed an infra-red bright section of the galactic plane. Here all adjacent scans suffer from the 'after-glow' effect, leading to a smearing of the galactic plane in the direction of the scans. The major source of contamination is now the zodiacal emission due to dust within the solar system. Although the quantity of this dust in the line of sight is minimal compared with the galactic dust, the larger mean grain size, the dust's proximity to the Sun making it much hotter, and the nature of thermal emission results in the zodiacal light being disproportionately intense.

Before these maps could be used it was necessary to remove from them some of this extraneous emission.

4.3.2 Removal of the Zodiacal Contamination

In the 12 and 25μm maps this zodiacal emission comprises almost all of the intensity more than 5° away from the galactic plane. The 100μm maps clearly show filamentary galactic emission that might be associated with galactic H_I. This structure is also visible in the 60μm band, but to a lesser extent and the zodiacal contamination is greater. The 100μm maps are therefore considered to be of greatest interest.

The simplest method for removing zodiacal emission from the 100μm map would fit it with a mathematical profile as a function of ecliptic latitude, a cosecant law giving quite a good approximation at ecliptic latitudes above 40° (Hauser et al., 1984). Another alternative would be to exclude all bright 100μm sources, including the entire region close to the galactic plane, and obtain a mean profile by averaging over all ecliptic longitudes. (Burton et al., 1987). The latter has the advantage over a simple mathematical formula as it will work at all latitudes (whereas a cosecant law breaks down at low latitudes) and will pick up second order effects such as the brightest zodiacal emission coming from two narrow bands a few degrees either side of the ecliptic.

However, neither of these methods was used here for the following reasons. The manner in which the data was collected results in a further source of confusion that cannot be thus accounted for. The need to avoid scanning directions that would cross the disk of the Moon made it impossible to keep the detector pointing at a constant solar elongation, ie. 90°. The scanning was advanced at a different rate than was necessary to keep pace with the apparent solar motion. When the moon moved to an inconvenient position the scanning of that strip of sky would cease, only to be resumed after the moon had moved on. The result is a discontinuously fluctuating intensity of zodiacal contamination on a scale of 10° to 15° of ecliptic longitude. Also, the slight inclination of the ecliptic to the plane of the zodiacal dust caused the detected emission to vary according to the time of the year of the observation.

Both of these problems might have been more readily overcome had all scans passed exactly through the ecliptic poles, enabling one model profile to be only slightly modified for each ecliptic longitude, as attempted by Burton et al. (1987). However, the satellite made many scans that did not even pass close to the poles, and the synthesised maps available for study are thus a patchwork of observations made at a variety of solar elongations and times of the year.

The method we have chosen was one that would to a large extent automatically take care of much of these complications. As mentioned earlier, after binning to a half degree pixel size the 12 and 25μm bands show very little other than the zodiacal emission. Since the four bands collected their data simultaneously, the 12 and 25μm maps should contain the same trend of zodiacal emission.

The 12 and 25μm maps were fitted with a thermal spectrum. The temperatures and derived intensities were calculated with the help of a program supplied by University College London, which took full account of the 'colour corrections' required to compensate for the detectors broad-band response. This was extrapolated to 100μm. An emissivity of of λ^{-1} gave a best fit. The calculated zodiacal dust temperature was within a few degrees of 185K over the entire sky. Close to the ecliptic plane the effective temperature is slightly lower than elsewhere due to dust further away from the sun. The lune banding effects were still visible, but the results were far superior to what could be achieved by subtraction of the same profile at all ecliptic longitudes.

The data as originally provided is collated into three separate maps, each giving hours confirmed coverage. The above procedure was performed on the first two sets of maps. The third set of maps were ignored since only two

thirds of the sky is covered and this data was taken towards the end of the satellite's life and shows signs of contamination due to loss of on-board coolant. The resultant 100μm maps from HCON1 and HCON2 (Hours CONfirmed) were then combined. The minimum values of the two maps were taken as this gave a much smoother final map than would have been achieved by simple averaging. This is because most of the residual noise had been due to high intensity glits, the result of 'after-glow' or insufficient subtraction of zodiacal emission at the bright edge of the lune bands. Where one of the maps had an absence of data the other map was used.

A first time glance at H_I maps and the 100μ map reveals a strong correlation between the two, particularly at high latitudes. As a guide to the effectiveness of the subtraction of the zodiacal emission figure 4.8 and table 4.3 shows how well the 100μm map correlates with the H_I column density maps of Cleary et al. (1979), Heiles and Habing, (1974) before and after the removal of the zodiacal emission.
The ratio at high latitudes of the 100μm intensity to the H_I column density is approximately 0.14×10^{-19} MJy.sr^{-1} cm^2, and appears to be constant over the sky to within 20%

For a region with a constant dust to gas ratio the best straight line should pass through through the origin. Any discrepancy can be put down to a constant background of extragalactic gas or dust. To correctly determine the

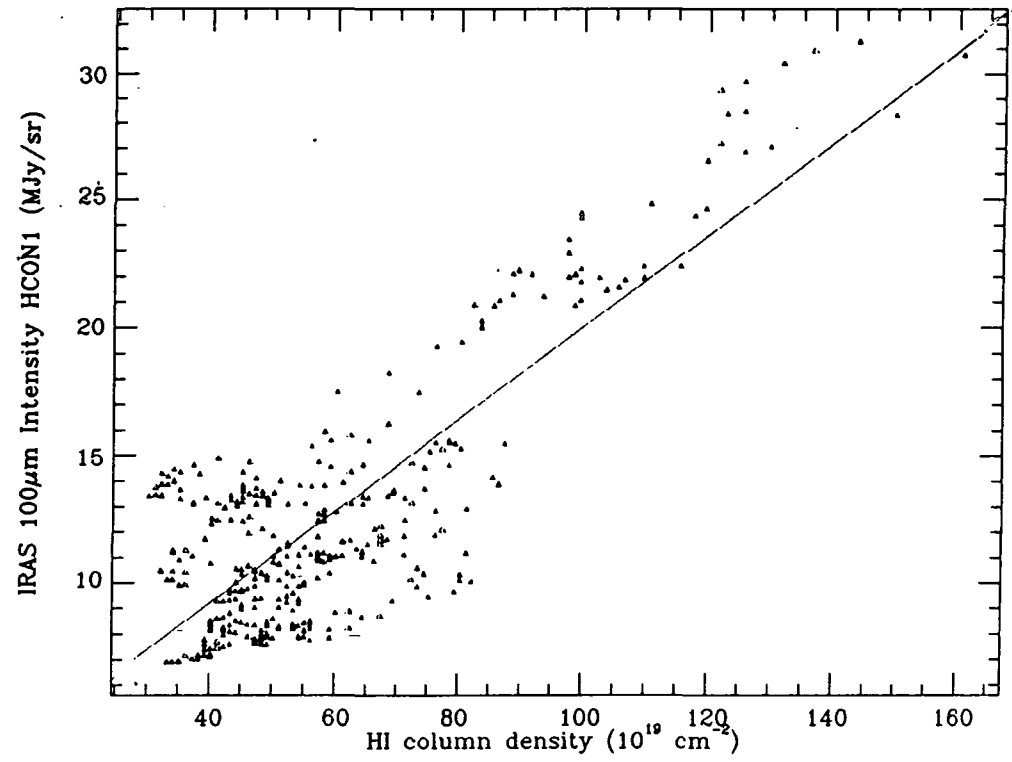

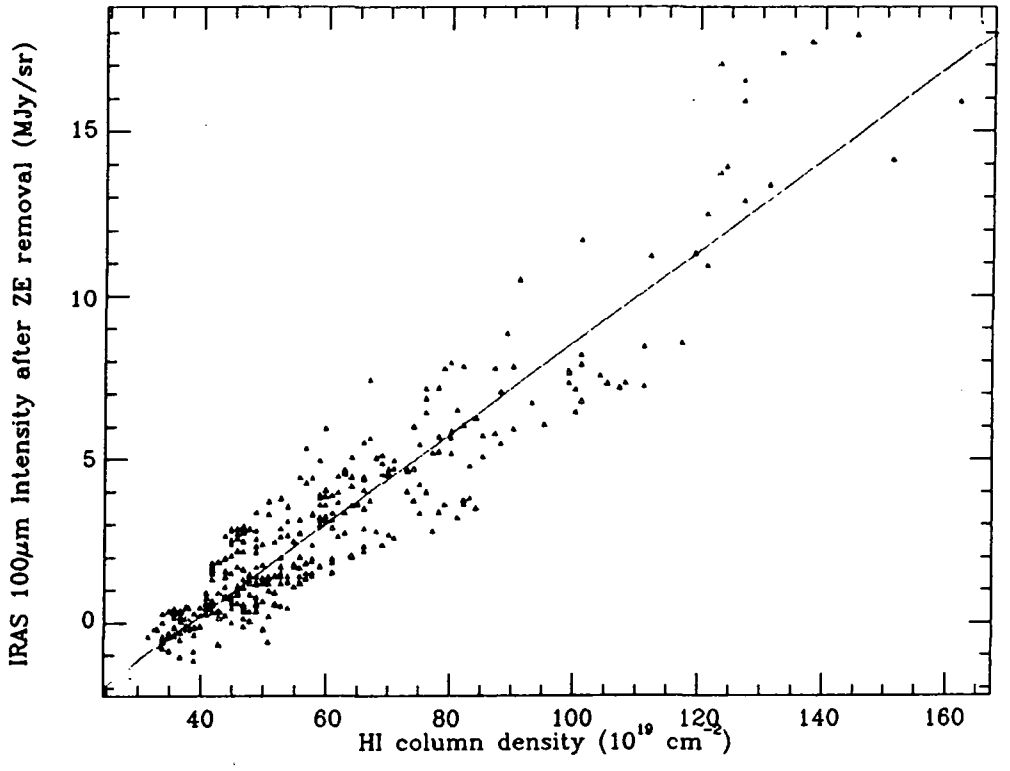

Figure 4.8 The correlation between HI and 100μm. along galactic latitude, b=30°

l^o	b^o	HCON1		Final Map	
1-136	+30	0.184±0.007	0.082	0.156±0.004	0.90
1-360	+60	0.213±0.02	0.52	0.120±0.008	0.94
300-360	+30	0.166±0.008	0.94	0.127±0.005	0.96

Table 4.3

Columns 1 and 2 give the galactic co-ordinates in degrees of the region of sky over which the IRAS 100μm and the HI data were fitted with a best straight line. Columns 3 and 5 give the gradient of the fit in 10^{-19} MJy.sr^{-1}cm^2 before and after removal of zodiacal emission. Columns 4 and 6 give the corresponding correlation coefficients.

amount of dust, and thus establish the dust to gas ratio, it should be necessary to determine the temperature of the dust by using the 60μm data in conjunction with the 100μm. Unfortunately, away from the galactic plane the diffuse 60μm intensity is only a small fraction of the zodiacal contribution. The noise level after zodiacal subtraction is thus very large, and a temperature determination is only possible in the brighter regions. However, due to the interstellar radiation field having a relatively uniform intensity (Mathis et al., 1983; Cox et al, 1985) and the dust cooling as a strong function of temperature (luminosity roughly proportional to T^5 or T^6 for silicon and graphite grains respectively) the diffuse high latitude dust varies only a few degrees from a mean of approximately 25K.

As fig 4.9 shows, at this temperature the 60 to 100μm

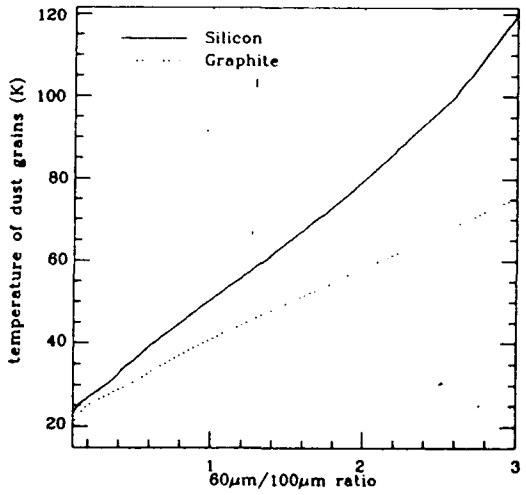

Figure 4.9 Temperature of dust deduced for silicon and graphite grain models.

emission ratio is roughly linear with temperature. With the total 100μm emission also roughly linear within this temperature range it would require a large variation in the 60μm emission with respect to 100μm in order to invalidate the assumption that the 100μm emission alone gives an accurate picture of the dust distribution. Hence the good correlation in fig 4.8. Close to the plain where there are numerous hot H_{II} regions and many cold dense clouds, the 60μm emission would need to be considered.

The reason for establishing that there is a good correlation of dust to gas is that although it is the gas distribution that will be of major importance in considering the evolution of the giant radio loops, the IRAS data is available in much higher resolution, and it would be opportune to take advantage of this, and assume the gas is comparably distributed.

CHAPTER 5

MODELLING AND ANALYSIS OF THE LOOPS

5.1 INTRODUCTION

In this chapter the data presented in the previous chapter will be used to examine the giant radio loops. Loop III contains little evidence of x-ray emission, and therefore the analysis of this loop will concentrate on the radio emission. Conversely, the shortage of radio data covering the entirety of the Loop I region necessitates that much of the discussion of Loop I and Loop IV will be restricted to x-ray emission. The North Polar Spur is, however, sufficiently north of the celestial equator to be included in the radio surveys. Models will be constructed to fit the data, thus giving clues as to the nature of the loops, and as to how well they are in agreement with the idea that they are old, large supernova remnants.

5.2 RADIO EMISSION

The spectral index maps of the northern hemisphere shown in figure 4.7 indicate that the loop III radio spurs have a distinctly different spectral shape to their surroundings. The influence of loop III on the spectral index of the sky extends several degrees beyond its defined edge.

The 38/408MHz map shows the spurs to have a flatter than background spectral index of 2.5, with the inter-Loop-I/Loop-III region at 2.6. The flatter region associated with the loop III spur at l=96° is an arc roughly concentric with loop III but lies 2° outside it. The spectral index of this arc steepens rapidly towards 820MHz. Between 408 and 820MHz it has reached 2.8, whilst the inter-loop region remains at 2.6. The arc has now moved out to 8° outside the loop. In the individual radio maps the spurs fade towards higher galactic latitudes, and although discernible it is not obvious that there is enhanced radio emission joining the two spurs together. However, the 408/820 spectral index map shows clearly that the two spurs are connected, the arc of higher spectral index extending from the western spur up to the highest loop III galactic latitude; ie. $20^h > \alpha > 12^h$. The eastern spur is less obvious in this map. For $5^h < \alpha < 8^h$ it is just visible against a varying background, however, at higher galactic latitude it becomes clearly distinguishable from the background. It stretches round

from $\alpha=8^h$ to $\alpha=12^h$ to join with the aforementioned section of the western arc. Whereas the western spectral index arc is of steeper than background spectral index, this section is clearly flatter at 2.4.

It is unfortunate that this arc lies close to a potential source of contamination that could give rise to a similarly arced feature. This near coincidence requires some explanation, and justification as to why the observed spectral index arc is thought to be genuine.

The polar cap region, $\delta>45°$, was examined with the Jodrell Bank Mark 1A telescope, whilst the surrounding lower declinations were covered at an earlier date by the Jodrell Bank Mark 1 telescope, $0^h<\alpha<12^h$ (Haslam et al 1970), and by the Effelsberg 100m telescope, $12^h<\alpha<24^h$ (Haslam et al., 1974). In examining the spectral index maps it was found necessary to subtract 1.7K from the polar cap region of the 408MHz data in order to give the smoothest transition across the line of 45° declination. The by eye fit was done using a 408/1420 spectral index map (Lawson et al., 1987). Although every effort was thus made in order to minimise any chance of a spurious feature being present, it is possible that there may be some residual miscalibration at the join of the different sections of the 408MHz map. Despite this uncertainty, it is likely that this is only a second order effect on top of a genuine spectral index ridge. The arc has a fairly well defined edge at the 45° declination but is several

degrees wide, extending to higher declinations which are well inside the northern part of the survey. Had this feature been more closely confined to the join of the different sections then perhaps its genuineness might be more in question.

At the higher frequencies the effect of the loop is still clearly visible. The 820/1420 spectral index of the western loop III spur rises steeply to 3.1, still above that of the inter-loop region, though this too has climbed rapidly, reaching 3.0. The eastern spur at low galactic latitudes is now virtually indistinguishable from its background spectral index at 2.8. The two spurs are even more clearly joined than at the mid-frequencies. The ridge of high spectral index is now traceable from α=19^h round to α=8^h where it falls to as low as 2.9, though this is above background at this point. The spectral index arc is more sharply defined than at lower frequencies, and now lies on or very close to the loop edge, rather than several degrees outside it.

The region within loop III shows no obvious difference in spectral index from that of the background outside the loop, though the galactic plane confuses much of this area. The NPS shows a similar trend to that of the nearest loop III spur. It has the same flattish spectral index of 2.5 at the lower frequencies, is relatively flatter at 2.7 between 408 and 820MHz, but rises sharply to the same high spectral index of 3.1

between 820 and 1420MHz. Only a small tangential region is visible on the highest spectral index map. The relative positions of the spectral index ridges also show a similar trend, in that the 408/820 ridge lies further from the loop centre than does the 38/408 ridge. The actual positions of these ridges relative to the circle of the loop are slightly different in that the loop I ridges lie relatively closer to the centre of the loop than those at the corresponding frequencies for loop III, the 38/408 spectral index ridge actually lying inside the defined loop.

5.2.1 Varying the Background Contribution and Calibration

The spectral index maps of figure 4.7 probably represent the best that can be achieved from the available data to show the nature of the galactic emission in the northern celestial hemisphere. However, this will be the integrated emission along the complete line of sight of the Galaxy, and for the study of the loops it would be desirable to subtract any extraneous foreground/background emission. Because of the large angular size of the loops and the relative small size of the galactic fluctuations it is not possible to do this for the entirety of loop III. However, this might be possible for selected points on the loop with a suitably nearby region that can be considered close enough to represent a background but far enough away not to be influenced by the loop.

Table 5.1 gives the emission at 7 selected points, after subtraction of the extragalactic emission and recalibration as described above. The first two points are from the western spur of loop III, the next two from the eastern spur, the 5th from loop I, the 6th from the inter-loop region and the 7th from the 'sky minimum'. Table 5.2 gives the spectral indices over each frequency range at these points for different subtractions. For each range the 1st spectral index corresponds directly with the maps in figure 4.7. The 2nd column for each frequency range gives the error that is obtained if the 38 and 408MHz values are set to the opposite extremes allowed by their quoted base level errors, prior to the correction of the higher frequencies using the sky minimum. The 3rd column is the spectral index after subtraction of a nearby background.

The temperatures in the 1st columns of table 5.2 are plotted in figure 5.1, which is also reproduced as an over-lay at the rear of this thesis for comparison with the model spectra produced later in this chapter. The temperatures have been converted into intensities in units of kJy/sr, since this shallower gradient gives a clearer graphical distinction between the different spectra. With the exception of point 7, which is very close to the sky minimum normalised to have a constant spectral index, all of the selected areas show varying degrees of spectral steepening at higher frequencies. This would be true for any sampled region from figure 4.7.

	RA	dec	l	b	38	408	820	1420
	(deg)				K			
1	287	56	87	20	9775	29.8	4.44	0.80
2	265	63	92	32	7825	21.9	3.31	0.58
3	108	58	159	26	7590	20.3	3.26	0.70
4	134	65	150	38	6620	17.4	2.91	0.58
5	235	20	32	50	13395	37.1	5.41	0.99
6	242	47	73	47	6565	14.1	2.16	0.42
7	148	36	189	52	3303	7.94	1.36	0.35

Table 5.1

Coordinates of 7 sample points with the temperatures after extragalactic background subtraction and base level normalization.

	38/408			408/820			820/1420		
1	2.44	0.06	2.24	2.73	0.09	2.77	3.12	0.22	3.26
2	2.48	0.08	2.14	2.71	0.12	2.74	3.15	0.32	3.50
3	2.50	0.08	2.15	2.62	0.11	2.47	2.80	0.17	2.49
4	2.50	0.10	2.47	2.56	0.11	2.59	2.94	0.26	3.47
5	2.48	0.05	2.46	2.76	0.08	2.83	3.16	0.17	3.46
6	2.59	0.12	2.64	2.69	0.16	2.93	2.98	0.45	4.44
7	2.54	0.23	----	2.53	0.23	----	2.47	0.25	----

Table 5.2

The spectral index at the 7 points as defined in table 5.1
Each frequency range has three columns of numbers.
The 1st column gives spectral index as shown in the maps of figure 4.8. The 2nd gives an error estimate on this, defined by the quoted base level errors of the 38 and 408MHz maps. Column 3 gives the spectral index obtained if a local sky background is removed from each point, ie The temperatures at point 7 are subtracted from points 3 and 4, and those at point 6 from the other three.

Figure 5.2 re-plots two of these spectra, but additionally shows some of the associated errors. The dotted lines bracketing each spectrum represent the flattest and steepest spectra that could have been obtained if the sky minimum normalization had been carried out with the extreme values of the 38 and 408MHz . The error bars at 820 and 1420MHz show the magnitude of the quoted base level errors at these frequencies (table 4.2). The open symbols show the intensities at the higher two frequencies prior to correction of the base levels. The adjustment at 820MHz is greater than the quoted error would have suggested possible, but the obvious resultant 'kink' in the spectra is not acceptable for synchrotron emission. The corrections of 1.41 and 0.93K at these frequencies convert to 20 and 7.8kJy/sr in figure 5.2. The figure demonstrates the effectiveness of the procedure for equating the base levels, as it imposes far more stringent limits on the 1420MHz intensity than do the quoted errors.

As indicated in the previous chapter, imposing a constant spectral index on the sky minimum region is merely a limiting case, and a spectral steepening towards higher frequencies would also be possible. In order to

Figures 5.1-5.5

Figure 5.1 Radio spectra for 7 sample regions. Co-ordinates for curves 1 to 7 are given in table 5.1

Figure 5.2 Radio spectra of regions 3 and 5 showing the related uncertainties. Dotted lines indicate the flattest and steepest spectra attainable if the extreme 38 and 408MHz allowed by the errors in table 4.2 were used in the normalization of the higher frequency maps. The error bars are also from table 4.2. The dash-dot lines are the spectra obtained if the sky minium has the arbitrary spectral steepening described in the text.

Figure 5.3 Synchrotron spectra from an $N_{SS} \propto E^{-2}$ electron spectrum with the cut-offs given in figure 5.4

Figure 5.4 Simple electron spectrum cut-off functions of the form $\exp(-(E/10)^{\beta})$

Figure 5.5 As figure 5.3, but with $N_{SS} \propto E^{-1.7}$

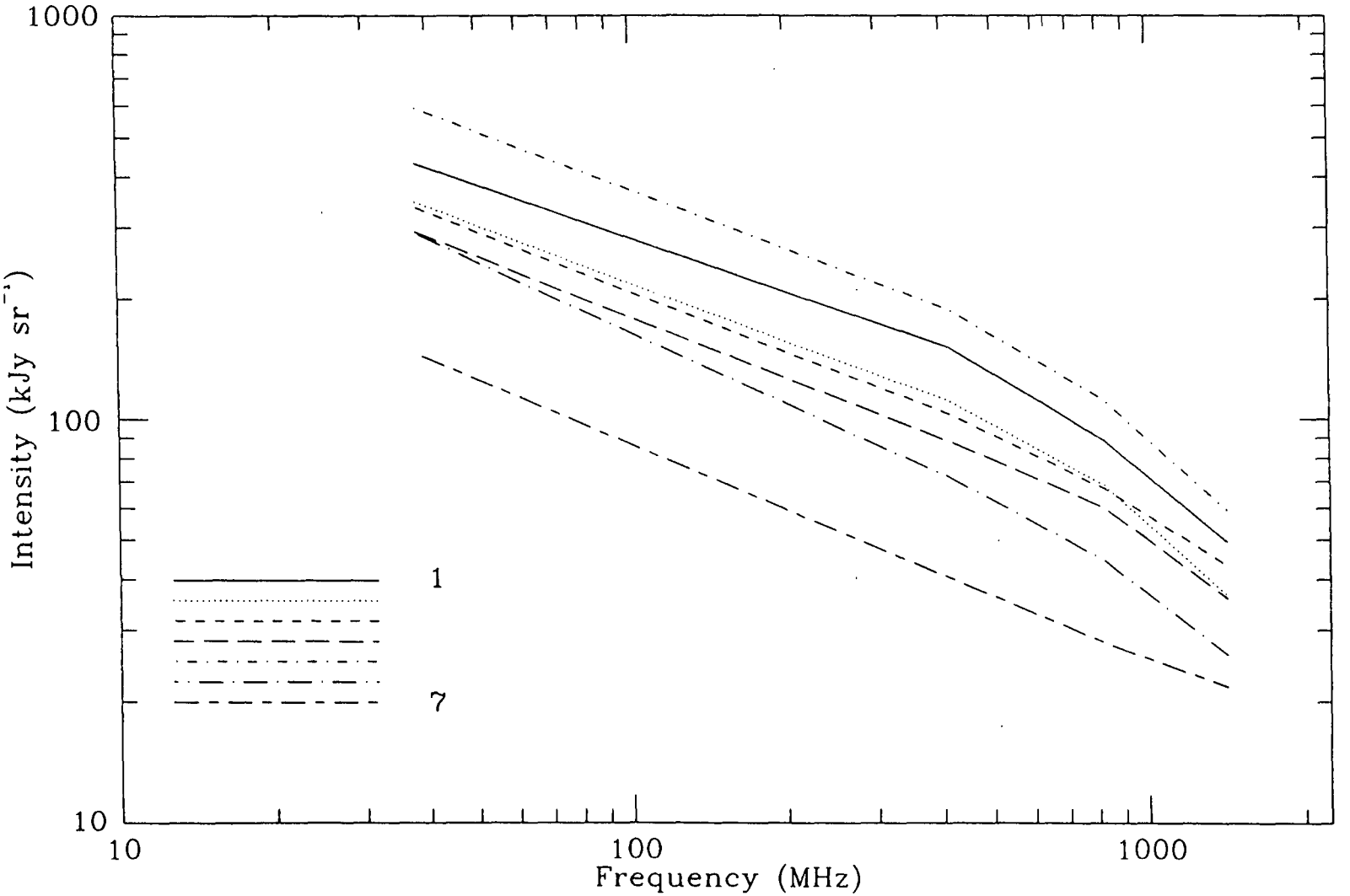

Figure 5.1

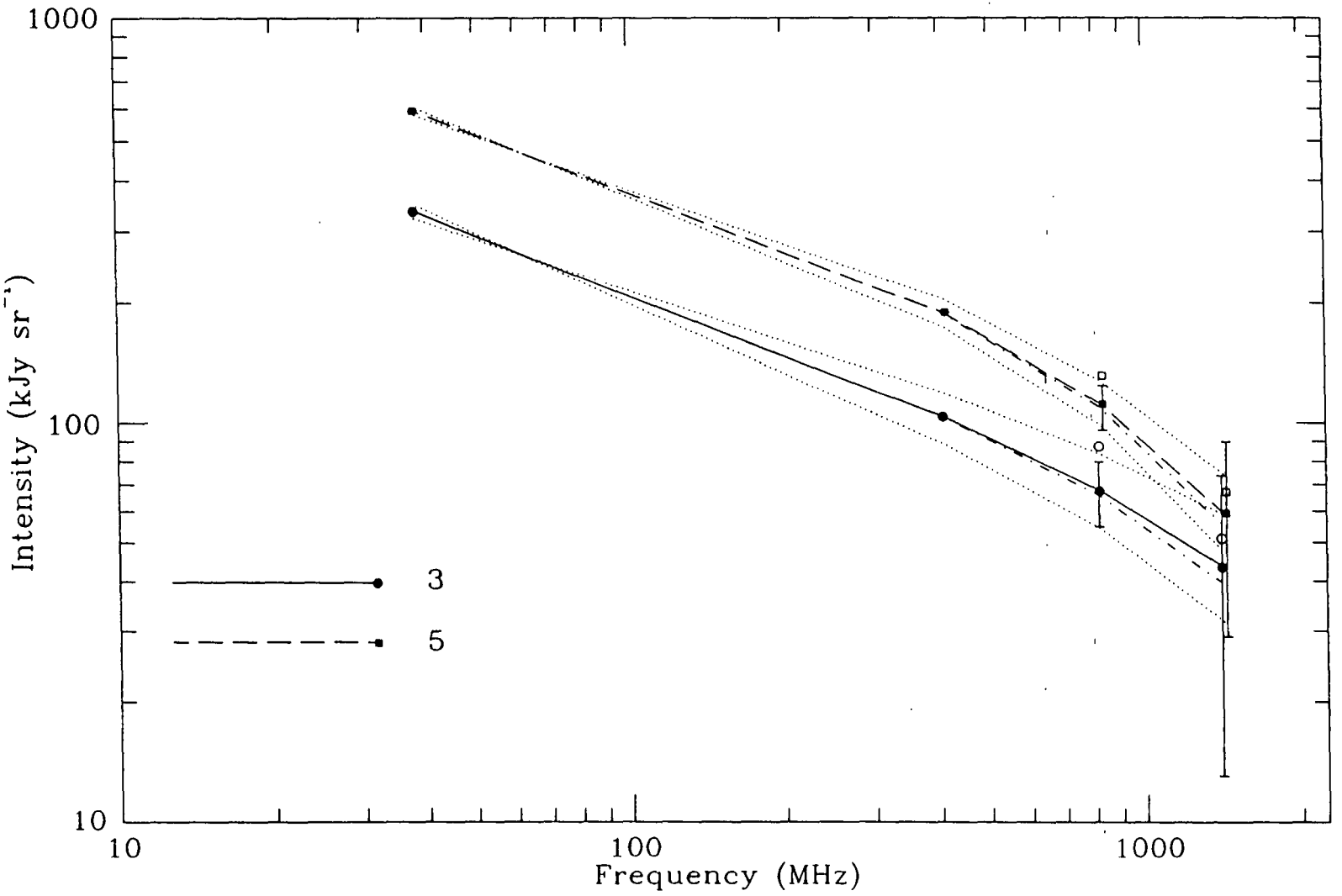

Figure 5.2

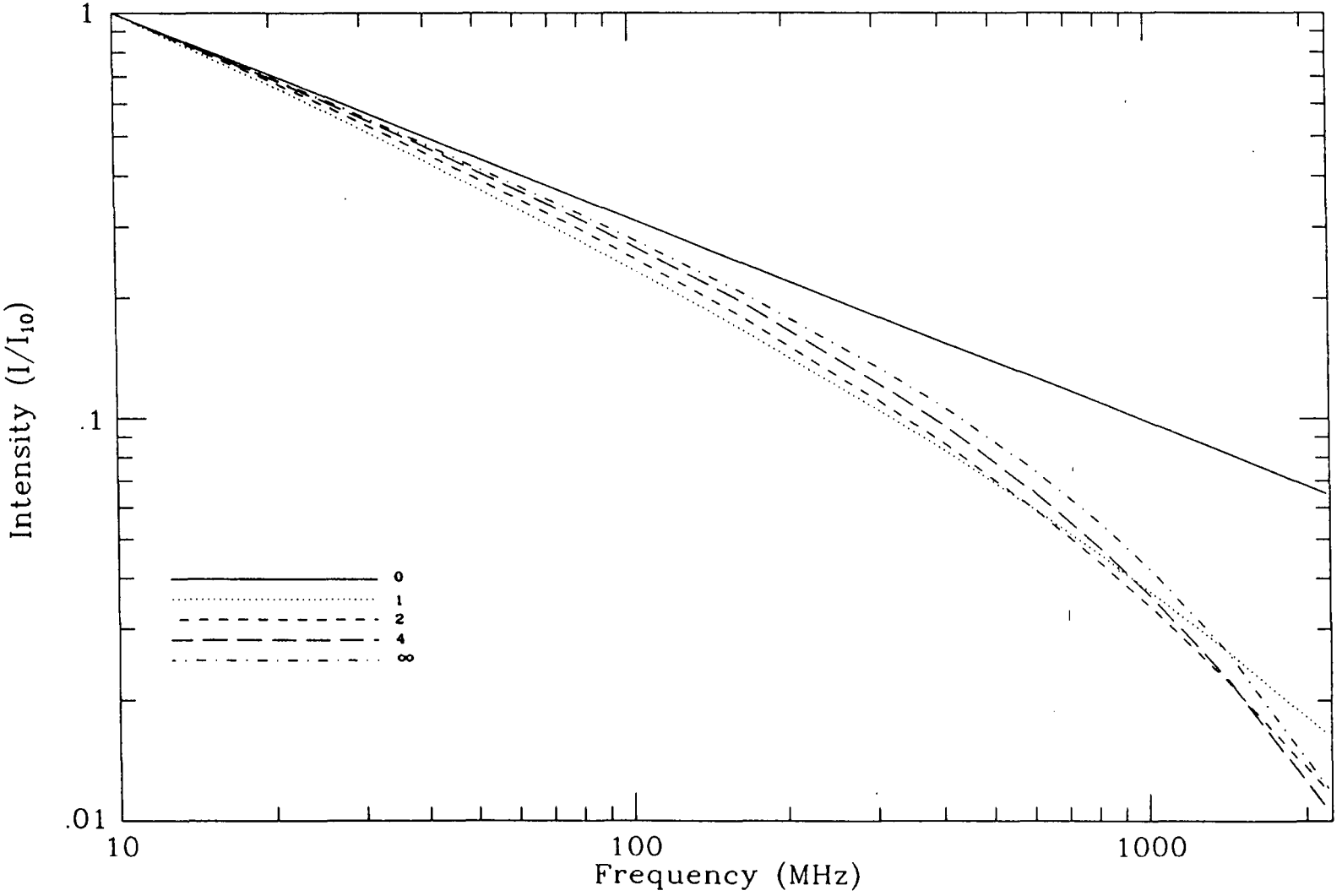

Figure 5.3

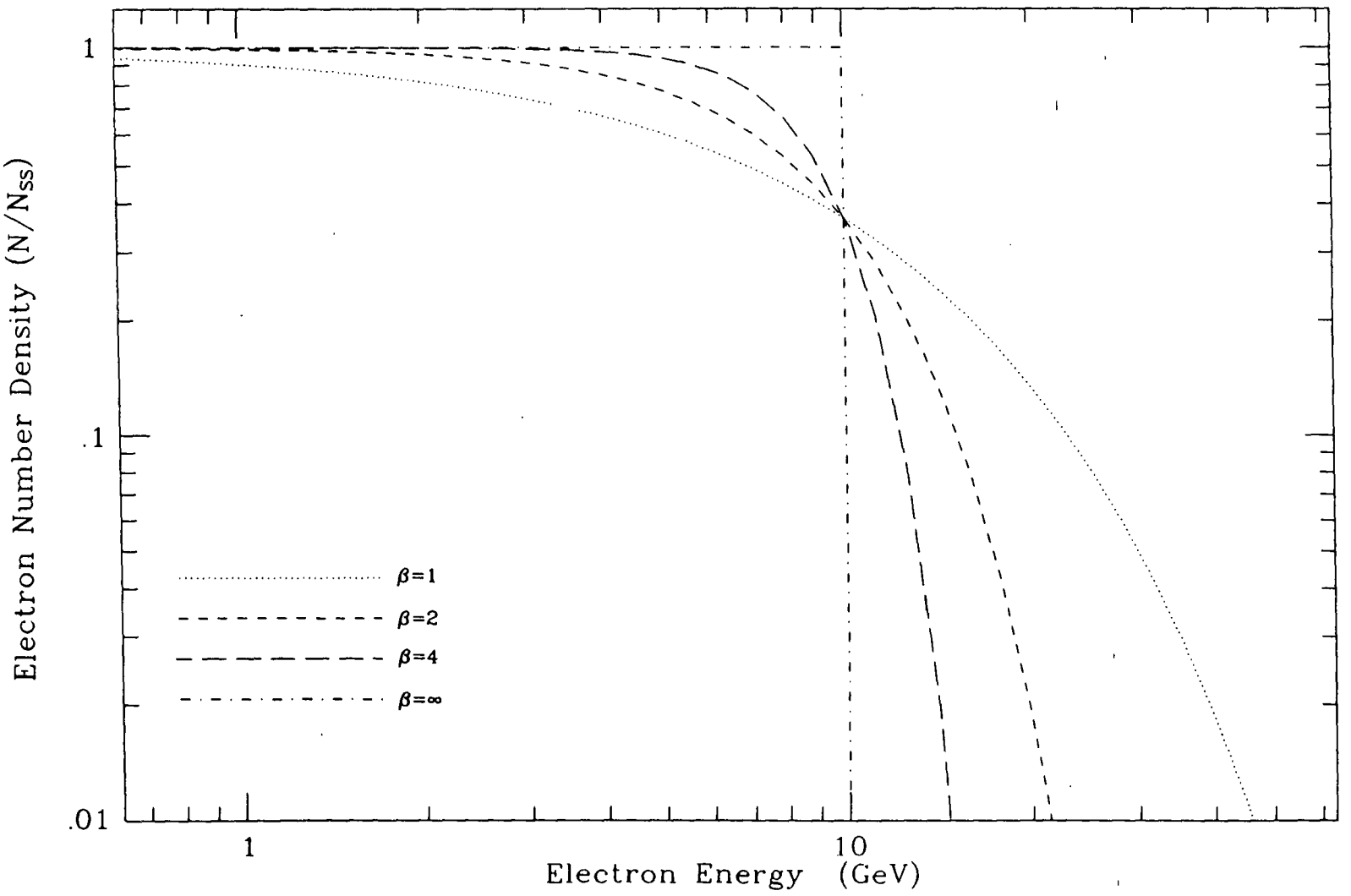
1
.1
.01
1
10
Electron Energy (GeV)
Electron Number Density (N/Nss)
β=1
β=2
β=4
β=∞

Figure 5.4

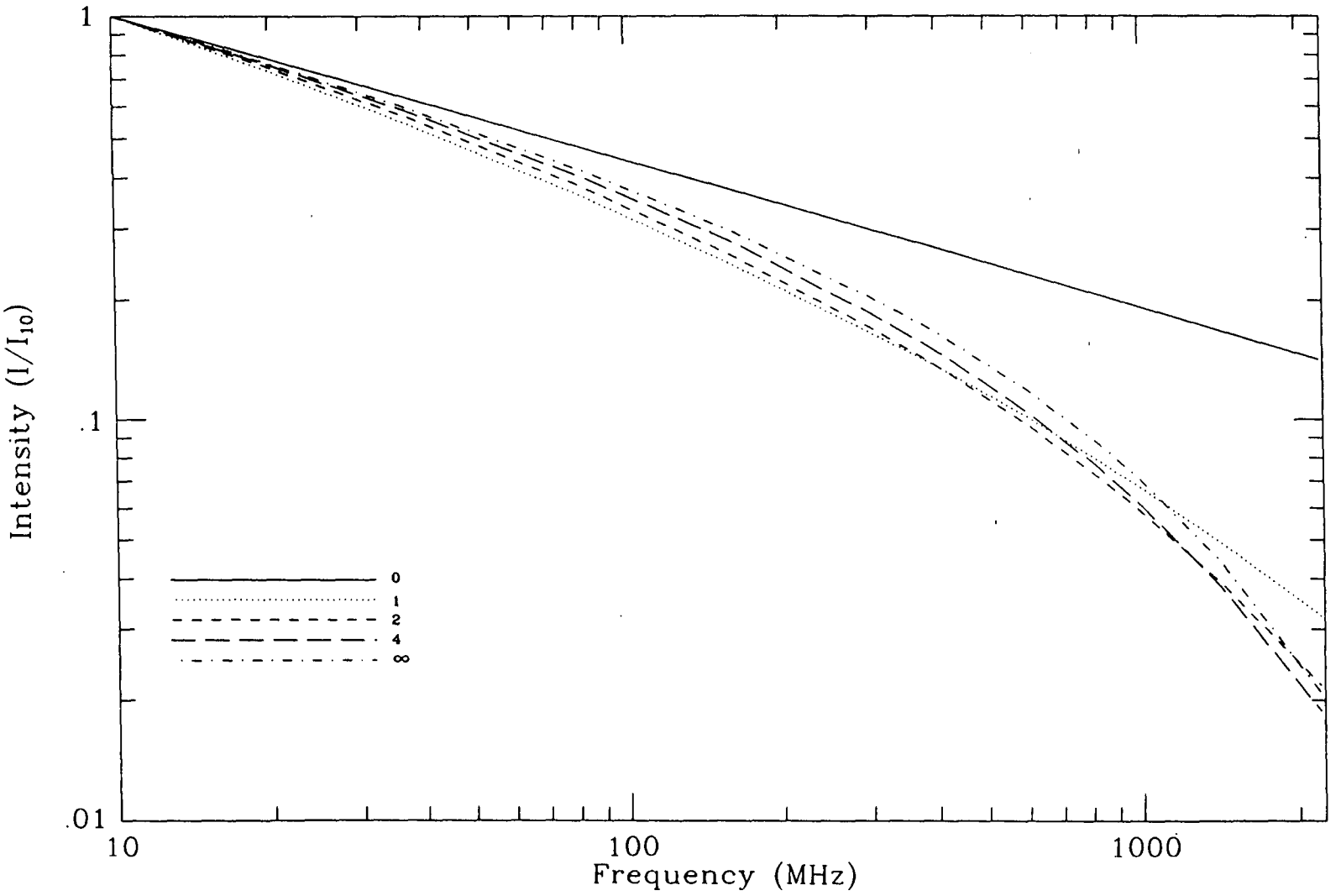

Figure 5.5

show the sensitivity of the sample points to any such deviation from a constant spectral index, also drawn in figure 5.2 are curves showing the effect of allowing such a steepening. The dot-dash line in each of the sample spectra are for assuming the sky minimum to have α38/408=2.51, α408/820=2.6, α820/1420=2.7. The former is defined by the observations, but the later two are arbitrary. It is unlikely that the sky minimum can steepen much more than this, since the resulting enhanced steepening over the rest of the sky would be too dramatic to have resulted from synchrotron radiation. As the next section will show, there are already very tight requirements on a model of the cosmic ray energy spectrum imposed by the very broad-band emission of the synchrotron process.

5.2.2 Modelling the Spectra.

The temperature and spectral index of the radio emission in this frequency range requires that the emission mechanism for the radio loops is synchrotron. If the required cosmic ray electrons are the result of shock acceleration at the remnant/ISM interface then equations 3.16 and 3.17 give the expected distribution of the electron number density with respect to energy. For a strong shock this would predict that the resultant electron spectrum should be a power-law of index γ=-2. This in turn leads to a brightness temperature spectral index of $\alpha_{T_b}=(\gamma+3)/2=2.5$, or equivalently, an intensity

spectral index of $\alpha_I=(\gamma-1)/2=0.5$. Unless otherwise mentioned, references to the spectral index, α, refer to α_{Tb}. If this electron power-law distribution should extend up to infinite energies, then so too should the emission power-law, up to infinite frequencies. In order to explain the reduction of emission at higher frequencies it is necessary to reduce the number of electrons at higher energies, or truncate them at some upper limit.

Before attempting to model a reduction in high energy electrons via some acceptable physical process, it is worth examining the effect on the emission spectra of relatively simple mathematical cut-offs. Figure 5.3 shows the emission spectra resulting from exponential type cut-offs applied to an $N_{ee}=KE^{-2}$ (K=constant) electron energy distribution, and figure 5.4 shows the corresponding cut-off functions. The electron spectra are of the form

$$N\ dE=KE^{-\gamma}\exp[-(E/E_o)^{\beta}]\ dE \qquad 5.1$$

with $\beta=0,\ 1,\ 2,\ 4,\ \infty$; $\beta=0$ implying no cut-off, and $\beta=\infty$ an instantaneous truncation. E_o has been set to 10GeV, and the frequency scale in figure 5.3 is correct for this value of E_o and an interstellar magnetic field, B, of $1\mu G$. The intensity scale has been normalised to unity at 10MHz for each curve. The frequency of synchrotron emission is proportional to BE_o^2. Therefore, in comparing the model spectra of figure 5.3 with the observations in figures 5.1 and 5.2, the model frequency can be scaled by

a factor of $BE_o^2/100\mu G.GeV^2$.

Overlaying the two sets of graphs and comparing by eye reveals that it is not possible to get a good fit for any of the five spectra associated with spurs. Even with the $\beta=\infty$ model, the resultant emission spectrum does not appear to have a sufficiently sudden turn-down. It is possible to get close to the high frequency spectrum, ie. from 408 to 1420MHz, for regions 1, 2, 3 and 5 with BE_o^2 ranging from 160 to 350 with $\beta>4$, except for the less curved spectrum from region 3 when $\beta=2$ is sufficient. Unfortunately, $\alpha 38/408$ is required to be close to 2.5 and unaffected by the cut-off in the electron spectrum, and these fits to the higher frequencies 'predict' an intensity at 38MHz twice that observed. The problem lies in the extremely broad-band emission of the synchrotron process. It is not possible to have a cut-off energy that can sufficiently reduce the higher frequency emission without also affecting frequencies below 10MHz. The high frequency synchrotron spectrum will be determined by the energy of the cut-off, whilst the low energy spectrum will reflect the electron power-law spectrum. If 820 and 1420MHz are in the former domain then 38 and 408MHz would appear to be in the transition region. By starting with a flatter electron spectrum it was hoped that the modelled 38/408 spectral index could be brought down without greatly affecting the emission at higher frequencies. Trials showed that setting $\gamma=1.7$ had the desired effect, and the resulting spectra using the same cut-off functions

are shown in figure 5.5. It is found that with similar scaling factors, reasonable agreement is found at all four observed frequencies for the same four regions. Region 4 does not fit any of the trial models well, the 820MHz intensity appearing to be anomalously large. Later in this chapter, the problems of inferring an electron spectrum flatter than $\gamma=2$ will be examined.

In order to give the relative intensity scale of figures 5.3 and 5.5 the same units as figures 5.1 and 5.2, the constant K in equation 5.1 needs to be of the order $10^5\,cm^{-2}$. For $\beta=0$ and $\gamma=1.7$; $K=10^6\,cm^{-2}$, but for $\beta=\infty$ and $\gamma=1.7$; $K=3.8\ 10^5\,cm^{-2}$.

5.2.3 Production of the Electron Energy Spectrum

Shock acceleration (equations 3.15-3.17) provides a ready explanation of how electrons can achieve high enough energies to radiate at several MHz in a magnetic field of only a few microgauss, the energy distribution being power-law of $\gamma=2$ or greater. The problem is to find a mechanism that will produce the electron spectrum required to give the observed synchrotron emission. The previous section suggests $\gamma<2$ and a very rapid truncation at an upper energy limit. In the next two sections a physical explanation for the cut-off is sought, and a discussion of the flat spectrum is given in the following section.

5.2.3.1 Energy Losses -

Electrons lose energy via synchrotron radiation at a rate $dE/dt \simeq -10^{-4} B^2 E^2$ GeV/Myr, with B in μG and E in GeV. The energy dependence is such that the higher energy electrons loose energy much more rapidly, but the loss rate in a few microgauss field is far too low for energies less than 100GeV to have been significantly affected in the lifetime of a supernova remnant. As an example, a 20GeV electron in a 3μG field would take 400Myr to fall to the required cut-off energy of around 10GeV. A 50μG field would be required for there to be significant impact.

Inverse Compton losses with background radiation give $dE/dt \simeq -7.10^{-4} E^2$, which is less significant than synchrotron in a 3μG field. Both have the same energy dependence, but together they do not provide a suitable mechanism.

Adiabatic losses appear to provide the greatest potential for energy loss. A 100pc sphere expanding at 400km.s^{-1} gives $dE/dt \simeq 3E$ GeV/Myr. Although the energy losses at 10GeV are considerably greater than synchrotron or inverse Compton losses, the energy dependence is not sufficiently strong to give the required turn-down to a power-law spectrum.

Bremsstrahlung and ionization losses are much less important than adiabatic losses, and both also lack a sufficiently strong energy dependence. Loss mechanisms, therefore, would not appear to be responsible for a termination of the electron spectrum.

5.2.3.2 Finite Acceleration Time -

Particles injected into the shock at low energies will require a finite time to cross the shock a sufficient number of times to be accelerated up to a given energy (equation 3.17). The higher the energy the longer the time required. Thus, for a shock such as in an old supernova remnant which has existed for 10^5 years say, there will be a maximum energy above which no electron has yet been able to reach.

The minimum time required to accelerate a particle from momentum p_o to p is given by

$$t=3/(V_1-V_2)\int_{p_o}^{p}[(D_1/V_1)+(D_2/V_2)]dp'/p' \qquad 5.2$$

(Axford, 1981) with D and V are the diffusion coefficient and the velocity with respect to the shock. Subscripts have the usual meaning, referring to the upstream and downstream sides of the shock.

Forman and Dury (1983) have calculated a time dependent solution for a simple plane shock, of the form $f_{ss}I(x,t)$, where f_{ss} is the steady state spectrum at the shock, and I(x,t) is a temporal and spatial dependent

component. They have solved I(x,t) for the case when the diffusion coefficient is a power-law function of momentum, and have also found a more usable approximation to the exact solution. It is this approximation that we have used here to generate trial electron spectra to compare with the observations of the radio loops.

Concerning ourselves only with the electron distribution at the shock, moments of t become

$$\bar{t}=3/(V_1-V_2)\int_{\sim o}^{\mathcal{E}}[(D_1/V_1)+(D_2/V_2)]dE'/E' \qquad 5.3$$

$$\overline{\delta t^2}=6/(V_1-V_2)\int_{\sim o}^{\mathcal{E}}[(D_1^2/V_1^3)+(D_2^2/V_2^3)]dE'/E' \qquad 5.4$$

the terms that are a function of distance ahead of the shock having been dropped. Since we are dealing only with electrons and with energies well in excess of their rest mass, the momentum terms have been replaced by energy. The time dependent component is given by

$$I_{(t)}=0.5[\exp(\bar{t}^2/\overline{\delta t^2}).\mathrm{erfc}(A+B)+\mathrm{erfc}(A-B)] \qquad 5.5$$

where 'erfc' is the complementary error function, $\mathrm{erfc}(x)=\int_o^x \exp(-x^2)\,dx$, and $A=\sqrt{[\bar{t}^3/(2t\overline{\delta t^2})]}$ and $B=\sqrt{[\bar{t}t/(2\overline{\delta t^2})]}$.

Taking equations 5.3 and 5.4, putting $V_1=\eta V_2=V$, $D_1=mD_2=D=C(E/E_o)^{\omega}$ (implying $\omega_1=\omega_2$) and integrating gives,

$$\bar{t}=\frac{3\eta(\eta+m)C}{\omega m(\eta-1)V^2}(E/E_o)^{\omega} \qquad 5.6$$

$$\overline{\delta t^2}=\frac{3\eta}{\omega m^2}\frac{(\eta^3+m^2)}{(\eta-1)}\frac{C^2}{V^2}(E/E_o)^{2\omega} \qquad 5.7$$

A typical value for the shock velocity of an old remnant is a few hundred $km.s^{-1}$. Axford (1981) gives $D=2.10^{26}(E/3(Gev))^{0.35}\,cm^2\,s^{-1}$, deduced from the escape of cosmic rays from the confinement volume of the galaxy.

In order to obtain numerical solutions to equation 5.5, all the following trials have been solved for $V=400km.s^{-1}$, $C=2.10^{26}\,cm^2\,s^{-1}$, and $E_o=3GeV$, and in the first examples η and m have been held constant. Assuming the shock to be strong and the diffusion coefficient to be unaffected by the shock (the same power-law for each having already been assumed in equations 5.6 and 5.7), $\eta=4$ and $m=1$.

Evaluating equation 5.5 with these parameters gives the graphs shown in figure 5.6, with $\omega=0.35$ (Axford 1981), 1.0 and 2.0. All three of these curves are drawn for $t=2.10^5$ years, though the energy axis can be scaled as $(V^2t/C)^{1/\omega}$. For V, C and t as above $V^2t/C=50$. Figures 5.7 and 5.8 plot the synchrotron spectrum resulting from these cut-offs superimposed on an $E^{-\gamma}$ electron spectrum with $\gamma=2.0$ and 1.7 respectively. Again, the former has been chosen as being the theoretical result of a strong shock, and the latter as being a better fit to the observations. The frequency axis can now be scaled by $B(V^2t/C)^{2/\omega}$ (B in μG). The obvious result is that the

Figures 5.6-5.11

Figure 5.6 Electron cut-off functions for equations 5.6 and 5.7. $V^2 t/C=50$

Figure 5.7 Synchrotron spectra for electron spectra cut-offs given figure 5.6, with $B=1\mu G$ and $N_{SS} \propto E^{-2}$

Figure 5.8 As figure 5.7, but with $N_{SS} \propto E^{-1.7}$

Figure 5.9 Electron cut-offs for various parameters in equations 5.6 and 5.7.

Figure 5.10 Suddenness of the cut-off function wrt m and η.

Figure 5.11 Change in cut-off function wrt ω

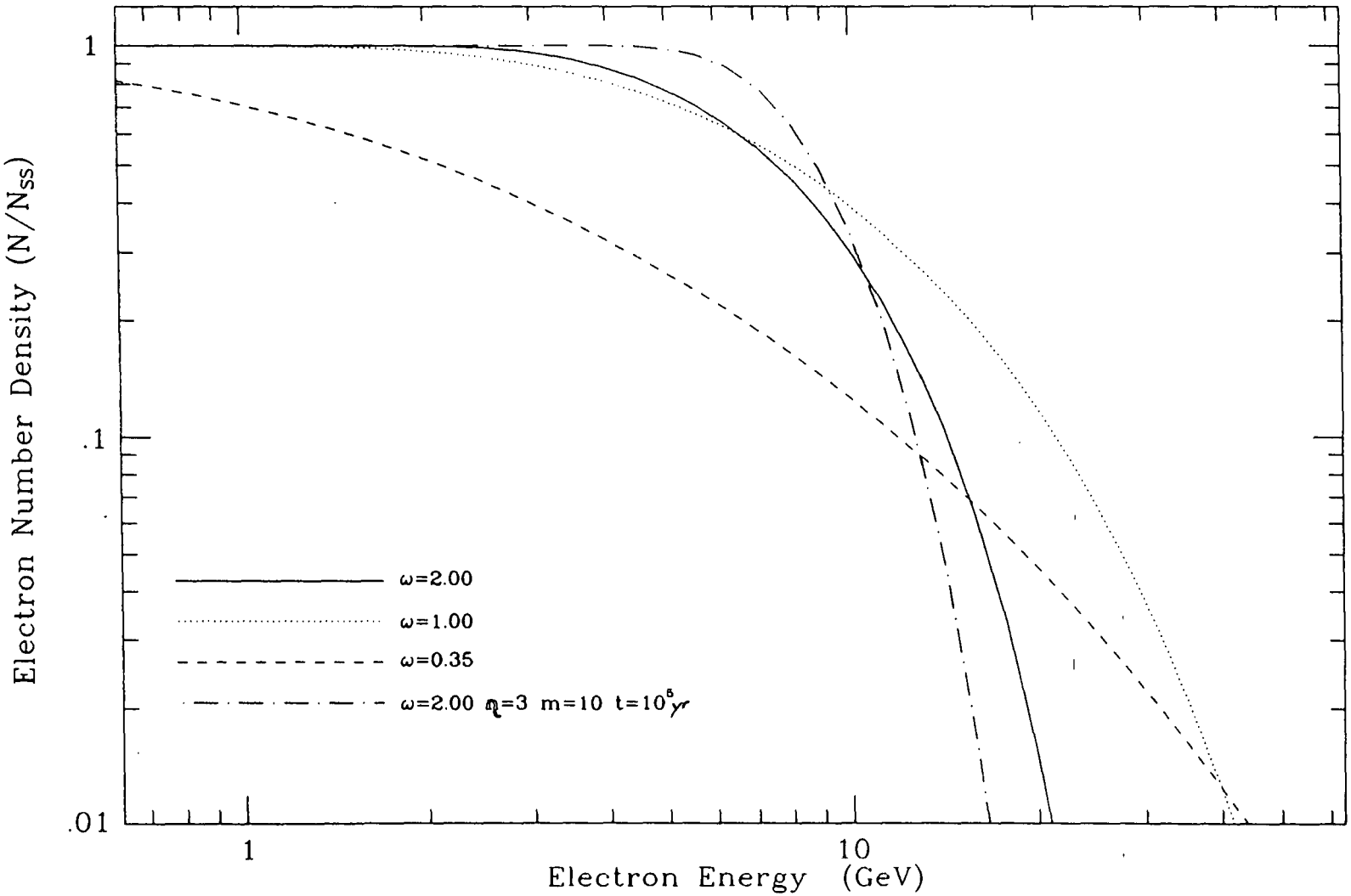
1
.1
.01
1
10
Electron Number Density (N/Nss)
Electron Energy (GeV)
ω=2.00
ω=1.00
ω=0.35
ω=2.00 η=3 m=10 t=10^5 yr

Figure 5.6

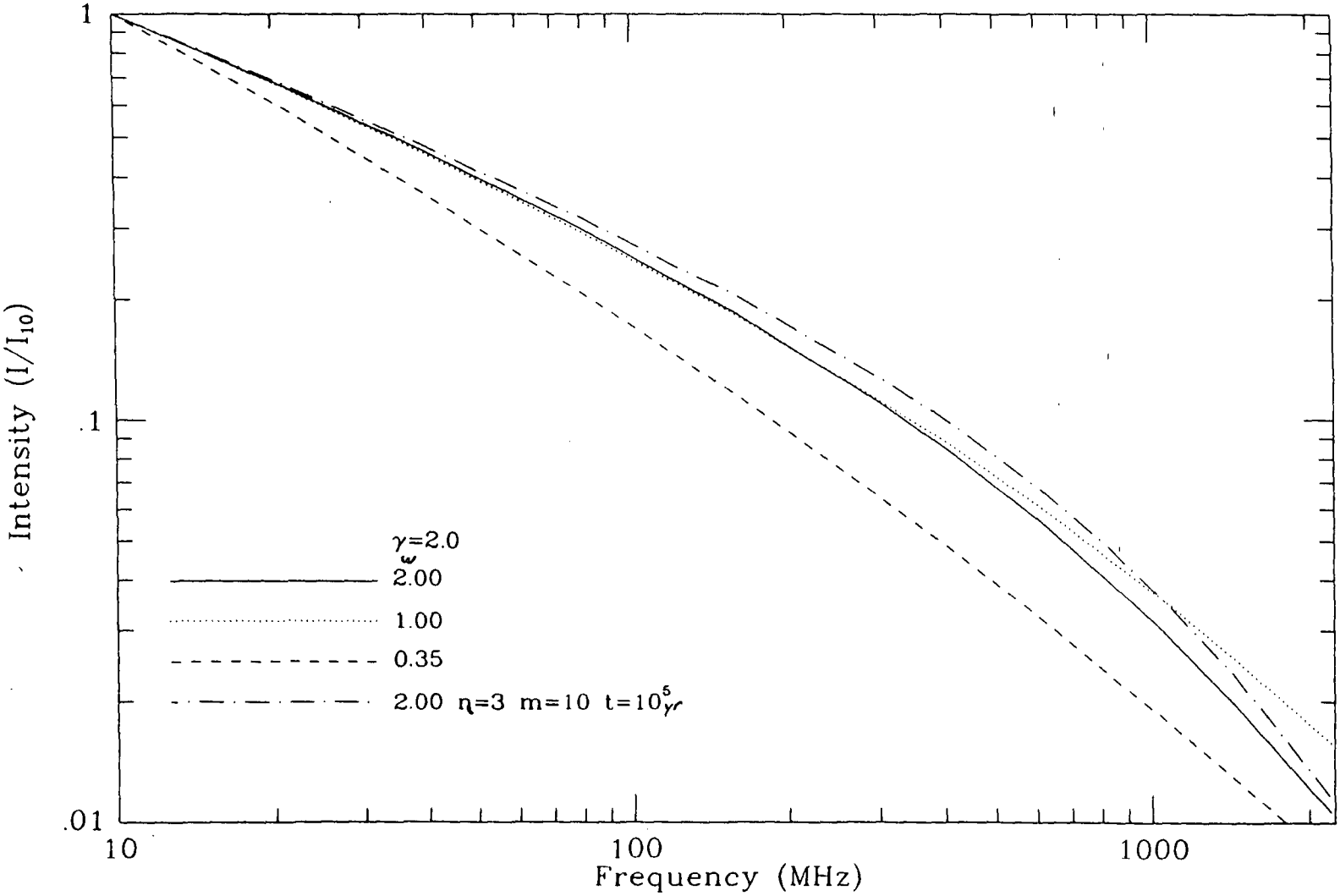
1
.1
.01
Intensity (I/I10)
10
100
1000
Frequency (MHz)
γe=2.0
2.00
1.00
0.35
2.00 η=3 m=10 t=10^5 yr

Figure 5.7

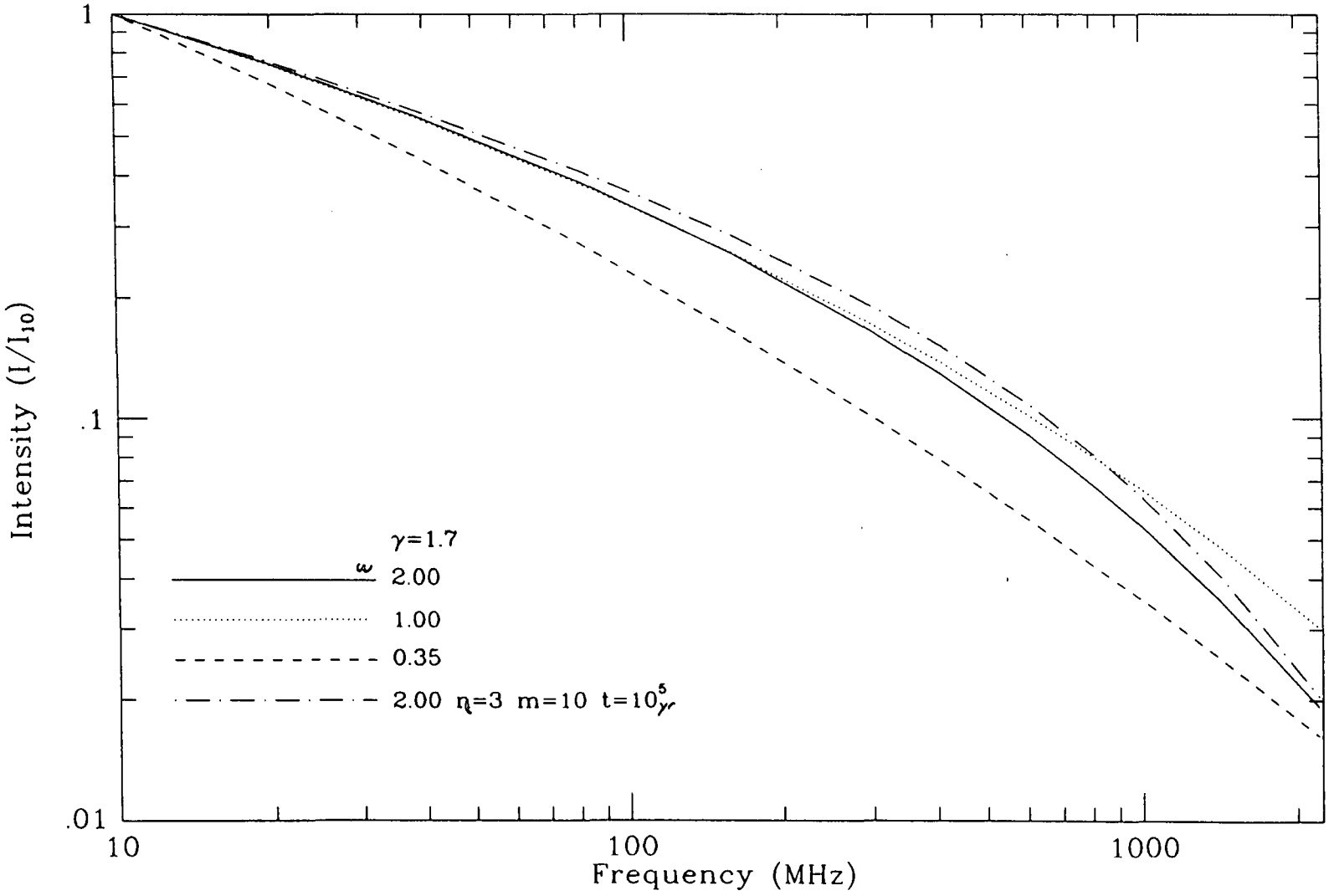
1
.1
.01
10
100
1000
Intensity (I/I10)
Frequency (MHz)
γ=1.7
ω
2.00
1.00
0.35
2.00 η=3 m=10 t=10^5 yr

Figure 5.8

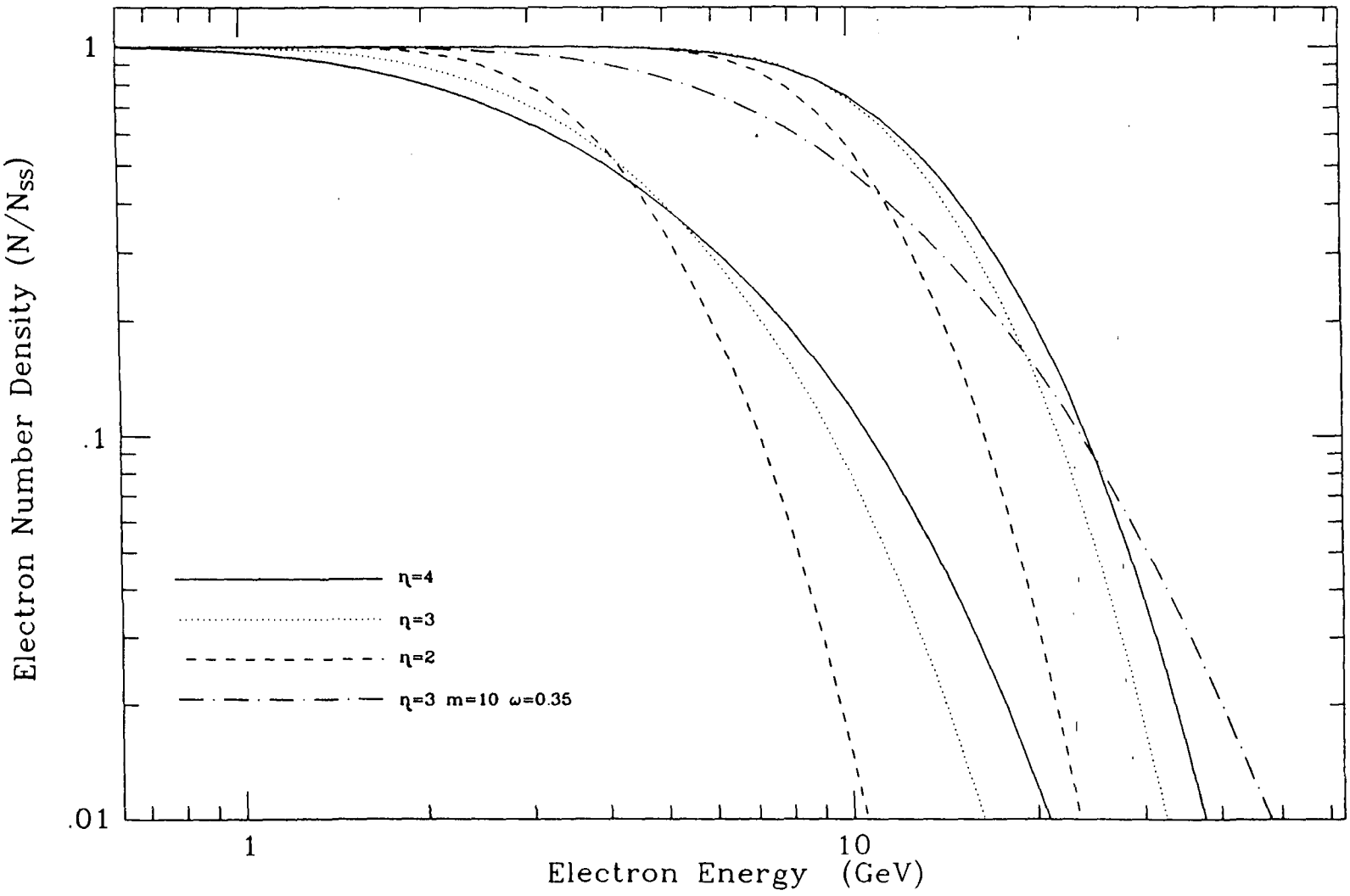
Electron Number Density (N/Nss)
1
.1
.01
1
10
Electron Energy (GeV)
η=4
η=3
η=2
η=3 m=10 ω=0.35

Figure 5.9

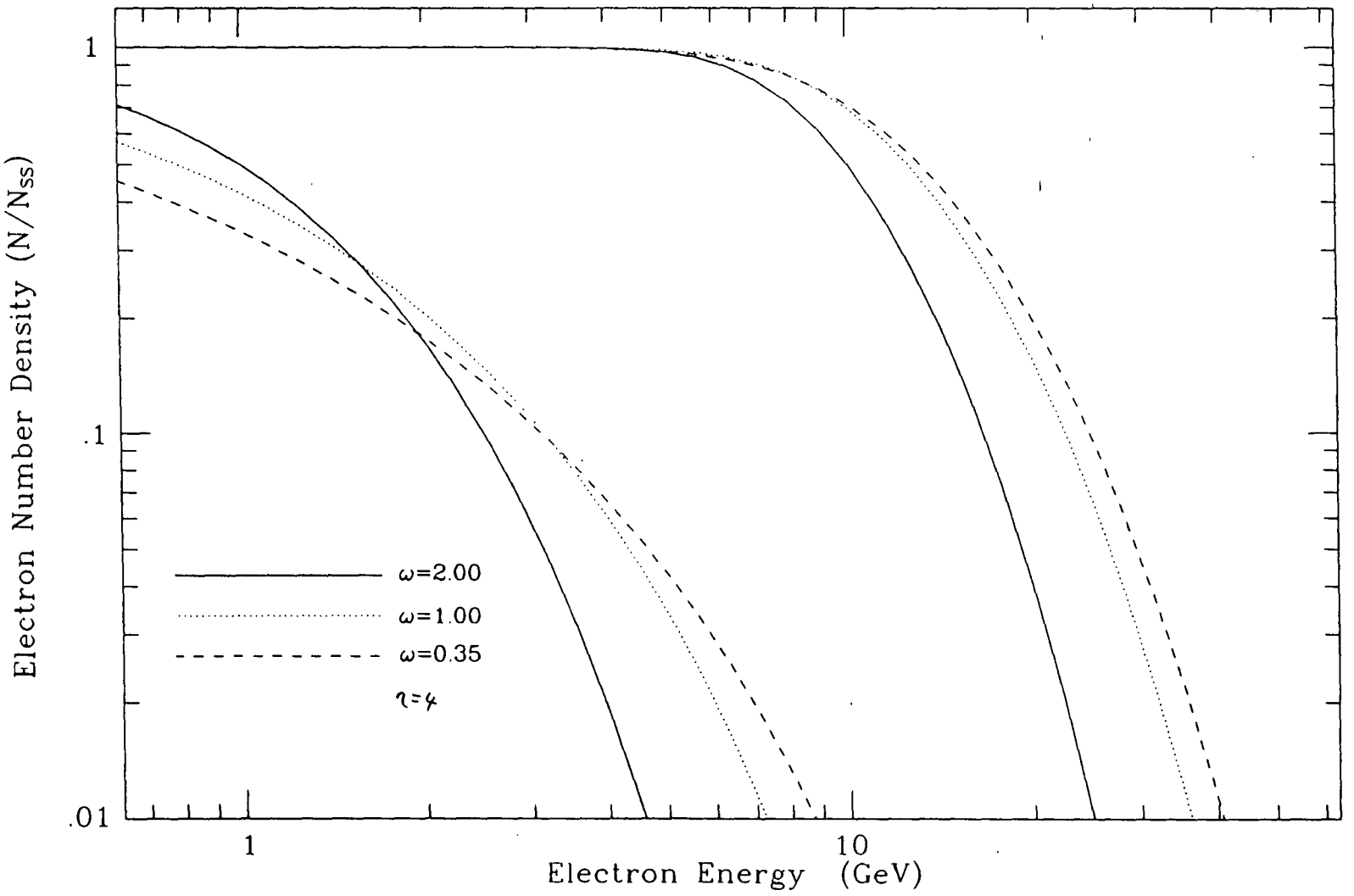
1
.1
.01
Electron Number Density (N/Nss)
1
10
Electron Energy (GeV)
ω=2.00
ω=1.00
ω=0.35
η=4

Figure 5.11

steepening of the cut-off is a function of the diffusion coefficient's power-law. The greater the value of ω, the more sudden the turn-down. Axford's value of ω=0.35 is clearly insufficient to produce a suitable cut-off. However, it need not be the case that the local medium has a substantially different energy dependence from that suggested by Axford. The Forman and Dury model is concerned with a plane shock, yet a supernova shock is spherical. Once the cosmic ray energies are sufficiently large that the distance they diffuse ahead of the shock is appreciable when compared to the size of the remnant then they may start to 'see' the spherical nature of the shock. This will result in a reduced probability of re-encountering the shock, causing an effective increase in the diffusion coefficient. For a shock velocity of a few hundred $km.s^{-1}$ and $D \simeq 10^{27}$ $cm^2 s^{-1}$ the characteristic diffusion scale length, D/V, is of order 10pc, or roughly 10% of the radius of the radio loops.

Comparison of figures 5.7 and 5.8 with figure 5.1 reveals that it is necessary for a to have $\gamma<2$. Of the six curves γ=1.7 and ω=1 give the best fit to points 3 & 4, with $B(V^2 t/C)=8.2\mu G$. The other data, namely regions 1, 2, and 5, are best fit with γ=1.7 and ω=2, $B(V^2 t/C)$ between 125 and 160μG.

The parameters that have so far been fixed are η and m. It is found that for a reduction in the value of η and for moderate increase in m the suddenness of the electron

	ω	m	η	χ^2	K(10^3 cm^{-2})	B(V^2 t/C)
1	1	1	4	3.35	2.69	85
	2	1	4	2.38	2.54	162
	2	10	3	1.56	2.92	56
2	1	1	4	1.83	2.31	77
	2	1	4	1.02	2.19	131
	2	10	3	0.60	2.44	48
3	1	1	4	0.026	2.08	83
	2	1	4	0.07	1.92	162
	2	10	3	0.21	2.21	56
4	1	1	4	0.26	1.84	81
	2	1	4	0.27	1.73	152
	2	10	3	0.28	1.97	53
5	1	1	4	2.57	4.11	63
	2	1	4	1.22	3.80	126
	2	10	3	0.61	4.42	43

Table 5.3 Trial fits to the 5 sample regions.

cut-off is increased. As an example, also included in figures 5.6, 5.7, and 5.8 is a fourth curve, with ω=2, η=4 and m=10. This is drawn for V^2 t/C=25, since with m=10 the smaller diffusion coefficient behind the shock yields a greater efficiency of acceleration. These parameters give a much better fit to spectra 1; 2 and 5. Comparison with figure 5.2 shows that with the correct choice of parameter values it is possible for this mechanism to produce a cut-off more dramatic than for β=4.

As a guide to how well these curves fit the sample spectra from the spurs, table 5.3 gives the parameters used to obtain the fits and a χ^2 to evaluate the quality of the fit.

η	m	ω	Γ
4	1	1	1.33
3	1	1	1.09
2	1	1	0.74
4	10	1	0.82
3	10	1	0.74
2	10	1	0.65
3	10	0.35	1.25
4	1	2	0.89
3	10	2	0.57
	β		
	1		3.36
	2		1.67
	4		0.84

Table 5.4

Suddenness of cut-off wrt η, m, and ω

χ^2 can only be taken as a guide to a trend of the goodness of fit because of the large number of parameters. The small χ^2 for spectra 2 and 3 are merely a reflection of the fact that these show a much slower turn over than the other regions, and are therefore easier to fit. In order to show the relationship between the cut-off and the other parameters, figure 5.9 plots the electron cut-off

function for η=4,3,2 and m=1,10 for ω=1, though the corresponding synchrotron spectra are not shown here. Also plotted is the curve for m=10, η=3 and ω=0.35, demonstrating that it is difficult to produce the required cut-off whilst keeping the power-law dependence of the diffusion coefficient at that estimated by Axford. As an arbitrary measure of the suddenness of cut-off, table 5.4 gives, in dex, the increase in energy between N/N_{88}=0.999 and N/N_{88}=0.1, ie. from roughly the first onset of the cut-off to 10%. All seven curves in figure 5.9 are listed plus five others. The exponential cut-offs for β=1, 2 and 4 give relatively faster synchrotron steepening than these numbers would suggest, and this reflects the difference in 'shape' of the two types of curve. For identical values of these numbers in an exponential and a Forman and Dury cut-off, the former has a more gradual onset but the latter has the flatter high energy tail. Thus it is not simple to see from the electron spectrum the synchrotron turn-down without fully integrating the synchrotron process over all electron energies. However, if only curves of the same type are compared, this measure of the suddenness of cut-off is probably a fair reflection of the trend of the rate of turn over of the synchrotron spectrum. For the model of finite acceleration time any curve with a cut-off value of Γ=0.9 or less would be acceptable for most of the sample areas. Clearly there is no one set of parameters that will fit the observations, though there are minimum values for m and ω. The variations between

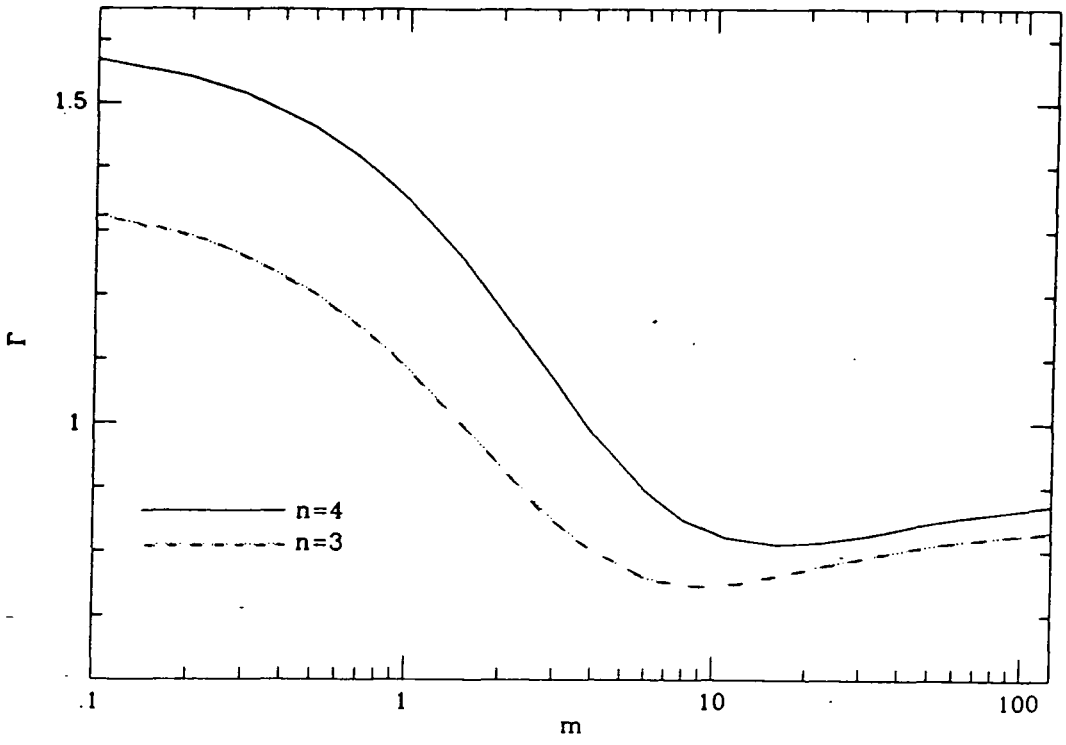

Figure 5.10

the sample areas and the still considerable errors associated with each preclude any precise statement regarding these values. However, from the approximate requirement of having $\Gamma<0.9\ \omega$ and m should at least be of the order of 1 and 10 respectively. Figure 5.10 shows Γ as a function of m for $\omega=1$. For a given value of ω, Γ is a minimum for $m=\eta^2$.

A simplification in the models given above has been to always assume the diffusion coefficient power-law dependence to have been the same on either side of the shock. In pointing out that it is the spherical nature of the shock that leads to an effective enhanced dependence, we are automatically noting an inherent asymmetry between the two sides of the shock. There may, in any case, be differences in the actual value of ω between the undisturbed medium and the turbulent, compressed

post-shock medium, but only on the outside of the shock will there be an effective increase due to curvature. It would, therefore, perhaps be more accurate to assume that the inner shock region has a lower value of ω. The result of this on the cut-off function is a little complex and is dependent on the value of m, and this can be seen by comparing figures 5.9 and 5.11. In the latter some of the curves shown in figure 5.9 have been reproduced, but ω_2 has been fixed at 0.35. For small values of m the cut-off is very slow, and the overall efficiency of the acceleration is clearly reduced. For larger values of m there is very little change to the spectrum. The cut-off takes place at around the same energy and there is only a marginal smoothing of the cut-off. The curves no longer have quite the same shape as when $\omega_1 = \omega_2$, so it is not possible to compare Γ. The smaller value for ω_2 appears to result in a very slow but small decrease from the steady state spectrum before the effect of ω_1 takes over with a rapid cut-off.

5.2.3.3 Flat Electron Spectra. -

A problem still exists with the above model in that the resultant spectra only approach the observations by assuming an $E^{-\Gamma}$ steady state spectrum that is flatter than that predicted for a strong shock. There is very little relief given by the observed line of sight projection of regions ahead of the shock onto the shock region. Axford (1981) shows that the energy spectrum is

only power-law at the shock and behind it. The spatial distribution of the electron spectrum is shown in figure 5.12, the curves taken from Axford (1981). Ahead of the shock, because the higher energy particles diffuse further upstream, the curves become peaked. Low energy electrons are absent, and the higher energy electrons have a slightly flatter spectrum. However, the effect of this even prior to considering the weaker field ahead of the shock is not significant.

A weakening of the shock to η=3 implies γ=2.5 and α=2.75, seriously exacerbates the problem, and η=2, γ=4, α=3.5 at first looks to be ruled out. Equation 2.17 would thus appear to put some restraint on the shock strength η, since any reduction from its maximum value of 4, helping to increase Γ, will steepen the expected spectra. However, this may not be so. If the initial injected cosmic ray spectrum is a power law that is flatter than the shock would produce then this initial spectrum will be maintained (Axford, 1981). How the initial particles achieved such a spectrum in the first place would then be the problem, since it is likely that they will have originally been produced by shock acceleration. This would at least allow a weak shock to be seen today as having a strong shock power-law spectrum. If much of the initial acceleration was done whilst the shock was strong then once the shock weakened the then existing power-law could be maintained at the higher energies. Only at the low energies, to which the newly injected particles have

had time to reach, would there be a power-law that reflected the present shock strength.

None of the above suggests that it is possible for a simple shock to produce a flatter spectrum than E^{-2}, and there is no evidence for such a pre-existing flat electron spectrum. If a flatter spectrum can be produced it must be produced in situ. The spectrum is governed by the ratio of the velocities either side of the shock in the shock frame (equation 3.16), and for a non relativistic gas the maximum compression that can be achieved is 4. Thus the maximum velocity ratio is 4. The cosmic rays 'see' the ISM on either side of the shock in terms of magnetic scattering centres, which if coupled to the thermal gas are limited to the same velocity as the gas. However, in the post-shock region there will be a great deal of turbulence. It could be considered that it is the bulk velocity that is one quarter of the velocity of the un-shocked gas, and that superimposed on this is a whole spectrum of velocities. Such a complex shock would have a continuous range of η, with electrons experiencing a different effective shock strength on each passage though the shock. For γ=1.7, equation 3.17 requires that $\eta = V_1 / V_2 = 5$. This could be achieved for some regions if the turbulent velocities were of the order 20% of the bulk velocity of the post shock gas, ie. 5% of the shock velocity. As with a simple shock which will flatten a steep electron spectrum but will maintain a flatter one, it may be that although electrons will often be scattered

by regions with effective sub-strong shock velocities their spectrum is governed by the super-strong shock encounters.

Shock-shock encounters might provide a means of producing flatter electron spectra. For two shocks approaching with equal velocities, when viewed in the rest frame of one the post-shock gas of the second will have a velocity 7 times that of the former. Electrons unaffected by the inter-shock region would thus behave as if η=7. There would be a similar effect if two shocks travel in the same direction, such as with successive supernova in the same region of space. If the inner-shock had the same velocity with respect to the outer's post-shock gas as the outer shock had to the ambient ISM, η=7 could be achieved if both shocks were strong. This may not even require a second supernova event. Observations of Cas A show that supernova ejecta can catch and overhaul the original blast wave as it is slowed by the ISM (Braun et al., 1987). In young SNR this could provide a source for faster secondary inner shocks. However, by the time the remnant reaches the age of the radio loops this flatter spectrum is likely to have been swamped by that due to more recent injection.

5.2.3.4 Relevance of the Model -

There are major differences between the model and reality. The model is for a plane shock, and the parameters have been fixed from zero time. For a real

supernova remnant the symmetry is spherical, and the shock velocity and strength are likely to decrease with time. Although the shock velocity reduces from several thousand $km.s^{-1}$ at its birth to a few hundred $km.s^{-1}$ in its old age, much of its time will be spent relatively close to its deduced present value. For a Sedov type expansion with $V \propto t^{-3/5}$, over 70% of a remnant's life will have been spent within a factor of 2 of its present shock velocity. With the McKee and Ostriker (1977) modification to account for cloud evaporation, $V \propto t^{-2/5}$, this figure rises to 80%.

As mentioned earlier, the spherical nature of the shock may be shown in the model by the need to have a relatively strong energy dependence for the effective diffusion coefficient. This parameter is, therefore, also likely to have some time dependence, its value changing with the curvature of the shock. As with velocity, the radius will have changed by only a factor of two in the last 70% to 80% of a remnant's life.

Although there are many approximations and assumptions made in applying this model of time dependent shock acceleration to a spherical blast wave, the results are quite favourable. As figures 5.3 and 5.4 suggest, the required electron spectrum cut-off is extremely sudden, and it is perhaps remarkable that this physical explanation is capable of producing such an effect. Three parameters as defined in equations 5.4 and 5.5 are found to affect the suddenness of the cut-off, namely η, m and

ω. Starting with nominal values of 4, 1, and 0.35 respectively, the direction in which the parameters need to be adjusted to sharpen the cut-off are all physically acceptable. One would expect that for a remnant at the end of its adiabatic phase the shock may have started to weaken, reducing η. The tangled and compressed magnetic field in the post-shock turbulence would result in a smaller diffusion coefficient than that ahead of the shock, thereby increasing m. The curvature of the shock will give rise to greater energy dependence of the diffusion coefficient, thereby increasing ω.

5.2.3.5 The Model for Electron Acceleration? -

It is not possible to produce a single model to fit the data. Each radio spur, indeed each position along a single spur, gives a slightly different spectrum, and furthermore the errors associated with each spectrum are considerable. Assuming a finite acceleration time to be the reason for the spectral steepening, there are too many free parameters which affect the rate of the cut-off to be able to give a reliable fit. All that can be said with confidence is that the model is capable of producing a sufficiently rapid cut-off, by assuming the loops to be SNR, and can do so by setting the free parameters to values that would fit our understanding of the likely nature of the ISM.

5.3 X-RAY EMISSION

5.3.1 Absorption by Neutral Hydrogen

In order to model the temperature of the x-ray gas by comparison of the counts seen in each band it is necessary to integrate model spectra (next sub-section) across the detector's pass bands. Some of the emitted x-rays will be absorbed by neutral interstellar matter before they can reach the solar system and thus affect the apparent spectra. Attenuation of the form

$$I_{(E)}=I_{o(E)}\exp(-\sigma_{(E)}N_H) \qquad 5.8$$

where $I_{(E)}$ is the source spectrum and N_H is the intervening column density of gas. The energy dependent absorption coefficient σ_E

can be represented by an approximation to the Brown-Gould absorbtion cross-section thus (Tanaka and Bleeker 1977)

$$\sigma_E=0.65*10^{-22}E^{-3} \qquad 0.1<E<0.53 \text{ keV} \qquad 5.9a$$

$$\sigma_E=2.0*10^{-22}E^{-2.5} \qquad 0.53<E<5 \text{ keV} \qquad 5.9b$$

Integrating equation 5.8 over the pass band of a particular filter, $Q_{(E)}$, gives

$$I=\int Q_{(E)} I_{o(E)}\exp(-\sigma_{(E)}N_H)dE \qquad 5.10$$

which represents the actual detected intensity in counts/second. If the source is a thermal spectrum, $I_{o(E)}$ is given by equations 5.11.

If the H_I is not uniform, then N_H should be replaced by an effective column density. This will be slightly smaller and will be dependent on the degree of clumping (Jakobson and Kahn 1986, and references therein).

5.3.2 Temperature Determination

Before the temperature can be deduced it is necessary to know the nature of the emission. Observations of the soft x-ray background are best fitted with a thermal spectrum. There are three causes of thermally produced x-rays; bremsstrahlung, recombination and line emission. Equations 5.11 were used in fitting the spectrum to the data and their relative importance in the total emission with respect to temperature is shown in figure 5.13. Below 10^7 K line emission is clearly the dominant process, with the total radiative power increasing with decreasing temperature.

$$dP_B/dE = 1.65.10^{-20}\Sigma N_e N_{z,z} Z^2 \langle g \rangle \exp(-E/KT)(T)^{1/2} \qquad 5.11a$$

$$dP_R/dE = 5.17.10^{-21} S_{>\nu} N_e N_H \exp(-E/KT)(T)^{1/2} \qquad 5.11b$$

$$P_L = (N_e^2/1.2)(N_{z,z}/N_z)(N_z/N_H)(C_{\theta,j})(B_{j,i})E \qquad 5.11c$$

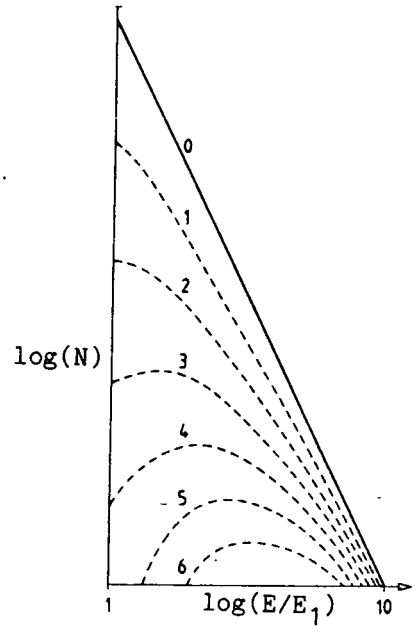

Figure 5.12
Electron spectra for xV_s/D, a distance x ahead of a plane, strong shock. Injection at E_1

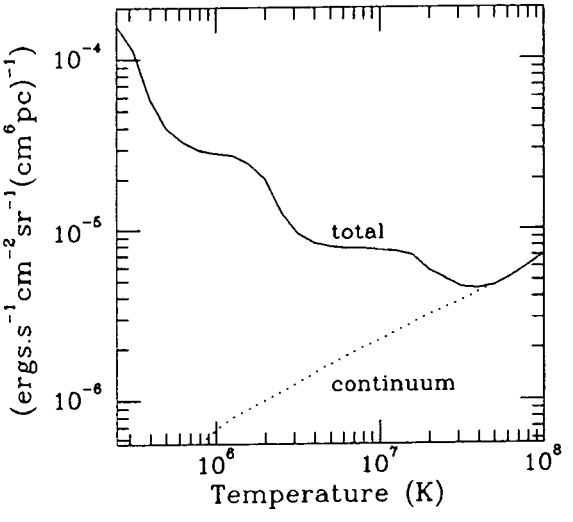

Figure 5.13

Relative contributions of continuum and line x-ray emission to the Flux per Emission Measure.

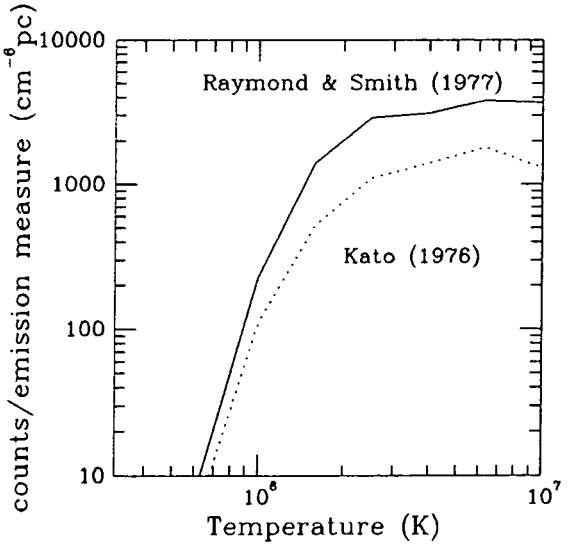

Figure 5.14

Discrepancy between the counts calculated for the M1-band using different line data.

P is the power emitted by each mechanism. N_e, N_H, N_z and $N_{z,z}$ are respectively the number densities of electrons, hydrogen atoms, atoms of atomic number z (Allen, 1973), and the number of such in ionization state z. $\langle g \rangle$ is the gaunt factor, E the photon energy, k the Boltzman constant, T the temperature, $S_{>\nu}$ is the strength of the recombination edges above frequency ν, and $C_{e,i}$ and $B_{i,e}$ are collisional probabilities and branching ratios for given lines.

Line strengths were taken from Raymond and Smith (1977), recombination edge data from Tucker & Koren (1971) and bremsstrahlung gaunt factors from Karzas and Latter (1961). The line data of Raymond and Smith is strictly for a plasma in equilibrium, ie. with electron and ion components at equal temperature. It is not clear that this is the case for an astrophysical plasma that has recently been shock-heated. One might hope that any deviations from an ideal plasma would only marginally alter the observed counts in the 7 Wisconsin x-ray bands. When not in equilibrium the individual line strengths may be totally different, but if a given line is suppressed from its value at equilibrium a nearby line tends to be excited, thus giving a similar broad-band averaged intensity. There is in any case, much difficulty in determining the line strength for equilibrium conditions. This is noticeable when comparing the data of Raymond and Smith, with that of Kato (1976). There are large discrepancies between individual line strengths, but when

integrated over an x-ray pass-band much of these differences are averaged out. Figure 5.14 shows the result of integrating over the M1-band. Kato's lines are consistently weaker than Raymond and Smith's at all energies and thus there is little difference between the two when temperatures are deduced from the counts ratio of two bands. An equally important source of error will be in choosing the correct abundance of the elements with respect to hydrogen. There are clearly many uncertainties in the modelling of the x-ray emission.

All calculations that follow have used this theoretical spectrum for the given temperature, and integrated it through the pass bands of the x-ray detectors. Appendix B gives the counts per emission measure in each band for a range of temperatures and absorbing column densities.

5.3.3 LOOP III

The lack of x-ray emission from Loop III is perhaps the most disconcerting aspect of this object for those that would like to explain Loop III as being the result of a supernova explosion. Berkhuijsen (1973) estimates that the loop's centre is only 150pc from us. The nearest edge is thus as little as 50pc away, and the tangential points where one would expect an x-ray maximum are 111pc. Paresce (1984) indicates that only $2.10^{20}\,cm^{-2}$ of H_I lie between us and this part of the loop. Table 5.5 shows

what fraction of the emitted x-rays fail to reach the detector for this absorbing column density. Since there is no evidence for any abnormally high neutral gas density in the line of sight to the tangential points, there can be little extra absorbtion above these values. Whilst the absence of B-band x-rays may thus be entirely due to absorbtion, for the other bands one must conclude that the gas within the hypothesised sphere is too cold or too diffuse to emit sufficient x-rays to be seen by the Wisconsin detectors.

log(T)	B	C	M2	I
5.6	99	92	-	-
6.0	95	83	13	1
6.4	89	66	10	1
Typ. cnts.	35	118	30	50
Stnd. dev.	8	27	5	8

TABLE 5.5

% of counts absorbed by $N_H = 2.10^{20} cm^{-2}$

Also given in table 5.5 are the typical count rates from the Loop III region and an indication of the size of the fluctuations. More precisely, the actual numbers given are the mean counts/sec and standard deviation for the region of sky enclosed by l=90°, 110°, and b=10°, 30° and can be considered typical of the surrounding area. If the gas was distributed in a shell structure as would be predicted from a spherical blast wave model, and was hot enough to radiate x-rays, this sample area would

be expected to be a region of high x-ray emission. Being just inside the arc of the western spur, the line of sight gas column density should be highest here. Assuming an H_I column density of 2.10^{20} and that a ridge of emission 2σ above background would be detected, table 5.6 gives upper limits to the emission measures for given temperatures (columns 1 and 2) such that 2σ above the background is not exceeded in any of the bands. Column 3 gives the mean density of the hot gas on the assumption of a line of sight through the sphere of 50pc. Columns 4-7 give the expected counts/sec in the respective bands.

log(T)	em	ρ	B	C	M2	I
log(K)	cm^{-5} pc	cm^{-3}	counts/sec			
5.6	0.33	0.08	16	46	0	0
5.8	0.033	0.025	11	54	0.1	0
6.0	0.0067	0.01	8	54	0.6	0.1
6.2	0.0031	0.008	4	54	2	0.6
6.4	0.0035	0.008	2	54	10	6

Table 5.6

Maximum emission measure at given gas temperatures such that 2σ is not exceeded in any band.

If a minimum density of 2.10^{-2} is assumed for the shell of the remnant , similar to that deduced for the NPS x-ray ridge (see section 5.3.4), then table 5.6 suggests a maximum shock temperature of only 8.10^5K. Equations 3.2b and 3.2c can be combined to give

$U_s^2 = (16/3)(p_s/\rho_s)(1+4M^2)(1-1/5M^2)$, where $M = U_s/a_o$ is the Mach number. Using $a_o^2 = \gamma p_o/\rho_o = \gamma kT_o/\langle m_h \rangle$ and equation 3.8c gives

$$U_s^2 = (3\eta^2 T_s/(4-\eta))(\gamma k/\langle m_H \rangle) \qquad 5.12$$

If the mean particle mass $\langle m_h \rangle$ is calculated assuming $n_{H^+}/n_H = 0.1$, then for a cold ISM this puts a limit on the shock velocity of 240km.s^{-1}. For a warm ISM the shock strength may be well below the strong shock limit. If the shock strength has fallen to 3 or 2, and thus the Mach number M to 3 or 1.73, the upper limits on the shock velocity are 211 and 276km.s^{-1} and the upper limits on the temperature of the ambient medium are 2.10^5K and 5.10^5K respectively. Alternatively, if the ISM is assumed to have a temperature similar to that deduced for Loop I (see section 5.3.4) then the shock, if present, must be very weak.

Dogiel et al. (1983) estimate an upper limit to the shock temperature of 1.6×10^6K. If Loop III is placed at the furthest limit allowed by Table 1.1 then the map of Paresce (1984) suggests that $N_H = 5.10^{20}$cm^{-2} would just be possible. Although the distribution of the absorbing gas might reduce its effective absorbtion column density, taking 5.10^{20}cm^{-2} as a maximum gives the upper limit shock temperature of Dogiel et al., and by equation 5.12 a maximum shock velocity of 340km.s^{-1}.

As is evident in the synchrotron emission, the supposed SNR clearly 'sees' the ISM as being non-isotropic. Just as the relativistic electron spectra must have evolved differently with respect to position on the loop in order to account for the variation in intensity, so also the kinematic evolution is likely to be non-spherically symmetric. Arriving at an upper limit to the shock velocity tells us nothing of such spatial variations. Any further deductions as to the nature of Loop III are thus best drawn from comparison with Loop I where there is much evidence as to the state of the non-relativistic gas. If both are considered to have a similar origin, as their radio emission might suggest, then one may extrapolate observations of Loop I to Loop III keeping as much as possible the same whilst still accounting for the observed differences.

5.3.4 LOOP I

Loop I appears to have much x-ray emission associated with it, and also some fairly low density filamentary neutral H_I clouds. The hot x-ray gas inside Loop I was once part of the ISM before being shock heated by the advancing blast wave. The observed neutral gas that forms part of the ISM ahead of the current shock position is perhaps indicative of the nature of the recently shocked volume.

The large area of emission mentioned in chapter 4 as being in the hemisphere of the galactic centre has a clear line of sight coincidence with Loop I, including areas south of the galactic equator where no loop radio emission is detected. Since the soft x-rays must be emitted fairly locally in order to have not been absorbed by neutral gas, this would suggest that the region of emission lies is at a similar distance to the loop. However, the most striking evidence for the x-rays to be associated with the radio loop is the similarity between the NPS and the bright x-ray ridge that lies a few degrees inside it.

This is most prominent in the M-bands. There is a notable correlation between the distribution of the M-band intensity and that of the radio emission that forms the North Polar Spur. The location of these two ridges of emission is not coincident. The x-ray ridge lies at a smaller galactic longitude, inside the arc of the radio NPS, and it does not curve on a similar small circle path. However, the two ridges both have their maxima at the same latitude of ~+20°. Both fade rapidly towards the plane and gradually to a similar high latitude. The B and C-bands shows signs of this ridge above b~+40°. Below this latitude there is little evidence for any enhancement in these bands, despite the fact that this is the region of the M-band maximum. Above b~+60° the ridge becomes confused with the latitude dependent emission which has become very intense, and also has suffered some contamination (McCammon et al., 1983). The I-band is not

too different from the M-bands, but the ridge has almost vanished from the J-band map. The 2-6keV map shows no sign of a ridge.

Behind this x-ray ridge there is the large area of sky with enhanced x-ray emission. Possibly because of the strong latitude dependence this is not seen in the B and C-band maps, but is noticeable on all of the other five maps, being most prominent in the M-band. The region extends from l~20° to l~300° and b~-30° to b~60°. Close to the galactic plane some of this may be explained by sources unconnected with the NPS, and there do appear to be some very bright 'knots' of emission in the plane. However, the bulk of the emission would tie in well with the idea that it was shock heated gas from within the cavity of Loop I. The 2-6keV band shows only a small and patchy enhancement over and above the background. In itself this might not be significant, but since the area enclosing these enhancements (which are not seen outside this region) is coincident with that from the lower energy bands it is likely they have the same origin. These hot spots within the cavity may be the result of reverse shocks from clouds, allowing extra heat dissipation locally and 'stopping' some of the advancing hot gas behind the cloud to give a density enhancement.

5.3.5 Loop I as a Single Supernova Remnant

Using the Sedov solution it is possible to deduce average parameter values that give a general description of Loop I as a SNR resulting from a single supernova exploding in a zero temperature, homogeneous medium. However, the ISM model of McKee and Ostriker (1977) predicts that much of the ISM is not cold, and the soft x-ray maps of figure 4.2 confirm that this is so for the local ISM. For old, large SNR with relatively low expansion velocities, the result of having such an ambient medium will be to greatly reduce the strength of the shock. In order to model Loop I we therefore adopt a similar procedure to Hayakawa et al. (1979) (equations 3.6 to 3.12) which will approximately account for weak shocks. The model assumes homogeneity of the ISM. The additional complications of inhomogeneity will not be modelled, but will be discussed in relation to the model.

Hayakawa et al. (1979) observed a single 8° wide x-ray scan through Loop I and attempted to model the x-ray profile. A substantial part of their fit can be summarised as choosing the shock strength that best matched the position of the x-ray maximum in their model to that of the observations. The scan was made approximately along the great circle at l=330° and thus cut the edges of the loop at b=80°, close to possible confusion with Loop IV, and well into the southern galactic hemisphere where the radio spur is not observed.

It would appear to be more reliable to repeat their model fit in the vicinity of the NPS where both the radio spur and the x-ray ridge are well defined. A critical requirement to this fit is to have a good knowledge of were the shock front is, since the distance between this and the x-ray ridge primarily determines the value of the parameters. This is not a simple problem. Even in the NPS region it is not obvious where to place the shock, but it must be considered even more unreliable to guess the position of the shock with only the extrapolation of the loop to rely on, as was done for part of the Hayakawa model. The shock has sometimes been taken as lying on the radio maximum (Davelaar, 1980), but this would appear to be a dubious assumption. Cosmic ray electrons streaming ahead of the shock confuse the issue as there will be some emission from this forward region, but the compression of the magnetic field will cause the bulk of the radio emission to emanate from behind the shock. Projection effects then result in the greatest emission measure appearing some distance behind the shell of maximum volume emissivity. Hayakawa et al. (1979) do not explicitly state where they choose to place the shock, but from diagrams of their model we deduce that the shock has been placed at the position of the loop as defined by Berkhuijsen (1971). We will later discuss how the results obtained from our model will be altered by a different choice for the position of the shock. We take the shock as lying 5° beyond the loop (table 1.1) where it is

coincident with the sharply defined outer edge of the NPS. The angular radius of the shock is thus 63°.

5.3.5.1 The Ridge to be Modelled -

We note that the x-ray ridge does not follow a concentric arc to the radio spur. Table 5.7 gives the angular distance from the loop centre of the x-ray ridge at various latitudes. Between b=20° and b=50° the ridge lies roughly on a straight line, ie. a great circle. Above b=50° the ridge does curve round, but soon reaches a region where some of the observed emission may be due to Loop IV. Table 5.7 gives an estimate of the angular distance of the ridge from the loop's centre at a number of positions.

Ridge latitude	Angular distance from l=329° b=17.5°		
degrees	C-band	M-band	I-band
+20	-	54.3	53.5
+30	47.9°	50.9	50.1
+40	54.0	50.2°	49.1°
+50	52.0	49.4	47.9
+60	50.2	47.9	45.3

Table 5.7 Angular distance from the centre of Loop I of the X-ray ridge at various latitudes as seen in the different bands. °estimated centre of a broad maxima rather than the absolute peak emission

Figure 5.15 shows the density profile for equations 3.11 with shock strengths of η=2, 3 and 4. Also shown for comparison is that for the Sedov solution, to which the

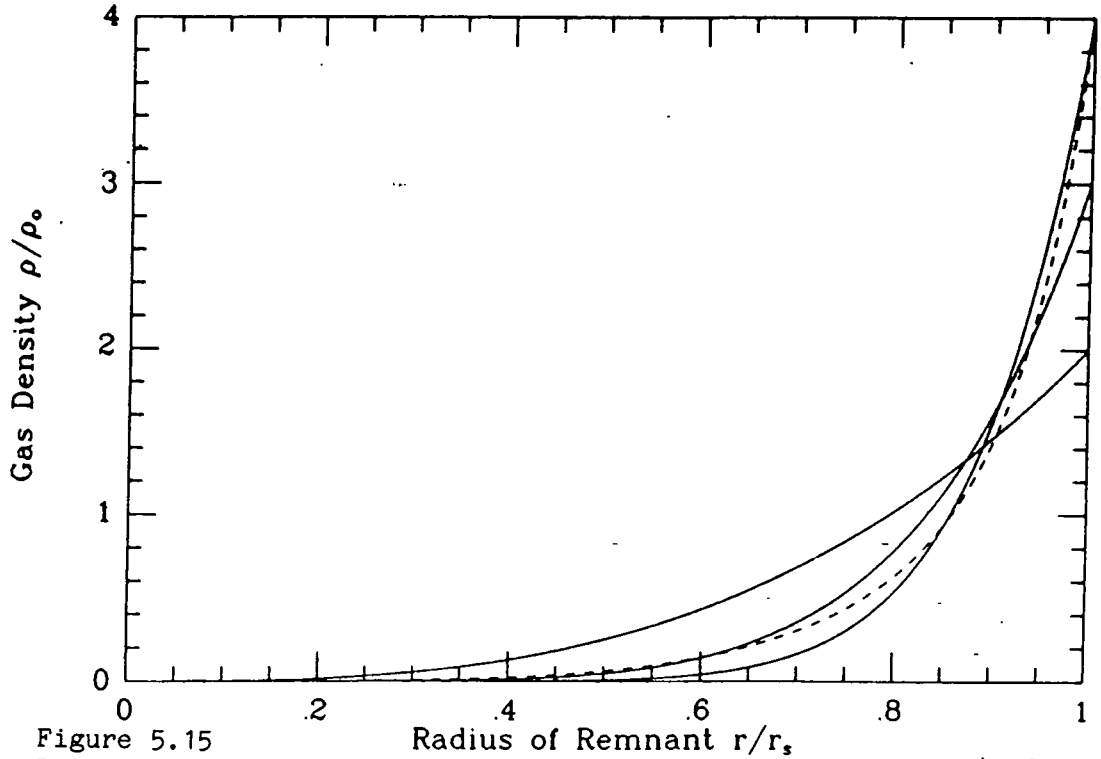

Figure 5.15
Density profiles for equation 3.11, for shock strengths of 4, 3, and 2. The Sedov solution is shown as a dashed line.

Figure 5.16
Projected emission measures for Loop I for different shock strength. (Note, the x-axis is not quite linear wrt the same axis in figure 5.15

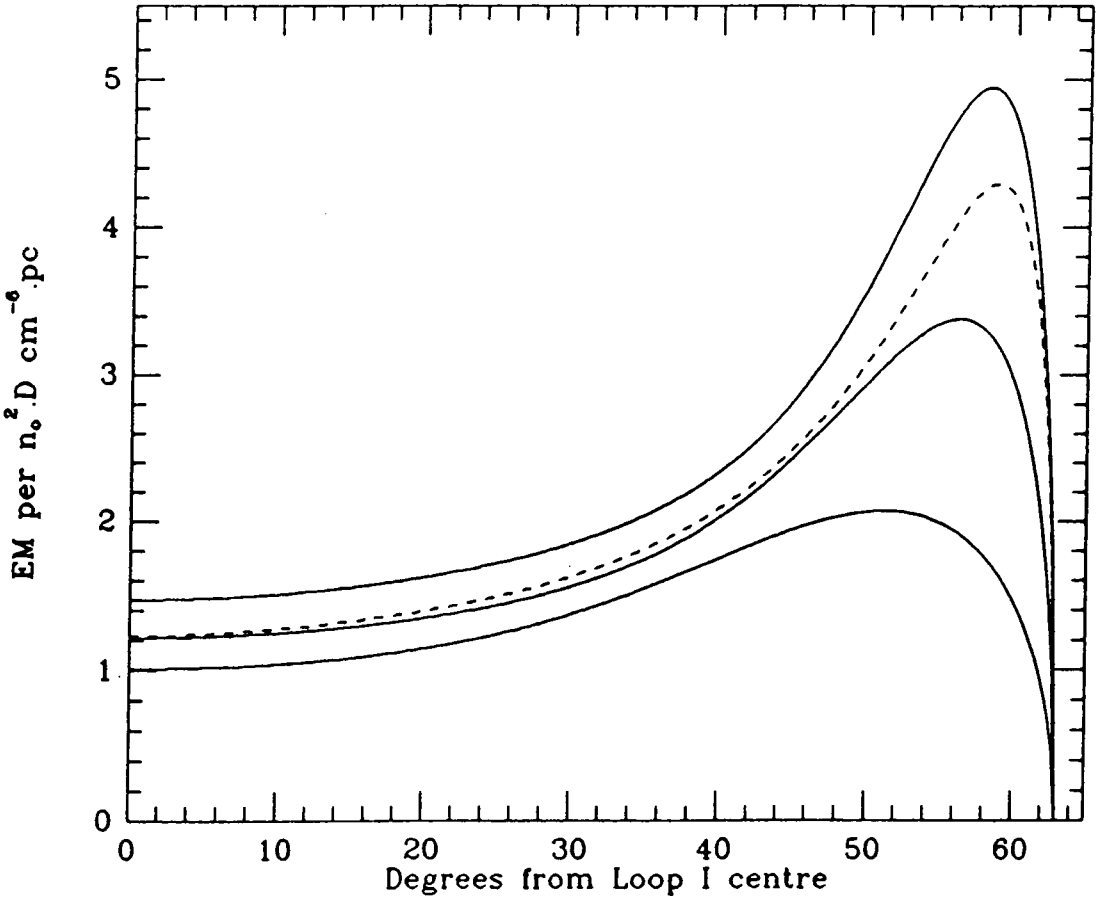

η=4 curve is the approximation. Integrating through the model SNR for all lines of sight gives the projected emission measures seen in figure 5.16. There are two points to note from figure 5.16. Firstly, as the shock weakens the x-ray maximum lies further from the shock, with the maximum emission measure lying at r/r_s=0.95, 0.93, 0.88 for η=4, 3, 2. Secondly, the relative intensity of the ridge maximum to that in the direction of the remnant's centre also falls with the strength of the shock, EM_{max}/EM_{centre}=3.3, 2.8, 2.1. These two points fit well with the observed x-ray ridge which in the M and I bands is faintest where it is furthest from the radio spur. We will therefore attempt to model Loop I as having a stronger shock at lower than at higher latitudes.

5.3.5.2 The Model -

In addition to the different choice of shock radius, there are some other less major differences between the model presented here and that of Hayakawa et al. (1979). Firstly, we note that the model emission of Hayakawa et al. (1979) have a very abrupt edge at the shock, in spite of the fact that the observations were made with a 'field of view' of $\simeq 3°$ (Hayakawa et al. 1977, 1978) in the direction of the scan. No mention is made of convolving their model to the resolution of the detector. The x-ray emission of McCammon et al. (1983) is of much lower resolution, and it is therefore more essential that our models be smoothed to the 7° resolution of the B and C

bands and the 6.2° of the higher energy bands. This was done with a one dimensional gaussian. We note that the smoothing has the effect of moving the x-ray maximum further from the shock.

Hayakawa et al. (1979) also assume a constant temperature with respect to radius. Although the Sedov solution suggests that there should be an appreciable temperature gradient, the justification for this isothermal model is that within a sufficiently thin shell, the variation in temperature is small. The modification of heat conduction in some models leads to a much more uniform temperature. However, many observers have noted signs of an increasing temperature towards the centre of the loop across the x-ray ridge. Even with a 6.2° resolution figure 4.3 shows that the ridge seen in the C, M1, M2 and I bands moves slightly towards a smaller radius with increasing energy (see table 5.7). To account for this a temperature gradient of the form

$$T_r = T_s (r/r_s)^{\phi} \qquad 5.13$$

was introduced into the model. With shock temperatures of 3.10^6 K this also has the slight effect of moving the M and I band ridges away from the shock, since these energy ranges have greater emissivity at higher temperatures.

By way of example as to how the convolution and temperature gradient affects the shock, for the isothermal strong shock the x-ray maximum of the M2 band lies at 56.25° angular radius after convolution to 6.2°. Adding a temperature gradient with ϕ=0.5 moves the maximum to 56°. The unconvolved maximum emission measure (figure 5.16) is at a radius of 58.25°. Both have a significant effect, the temperature gradient becoming more important and the convolution less so for weaker shocks.

The total x-ray emission in the direction of the loop consists of the summation of foreground and background emissions, and that from the SNR itself. The emission external to the SNR is not constant, since the Loop I cavity occupies a considerable fraction of any line of sight, and thus the column densities of the foreground and background regions vary greatly with angular radius. Hayakawa et al. effectively fit this region with a volume emissivity, and change the column length according to what fraction of the line of sight is occupied by the SNR cavity.

$$I_T = I_{SNR} + I_F + I_B \qquad 5.14$$

I_T is the total intensity, I_{SNR} that from the SNR model and I_F and I_B are the contributions from the foreground and background. The approach we adopt is slightly different in that we calculate the emissivity of the cavity prior to the presence of the remnant directly from the model parameters of the remnant. Since the model

deduces the initial ambient density and the temperature of that gas it should be correct to say that these two parameters determine the pre-SNR emissivity, and thus each line of sight intensity can be calculated. Although essentially the same equation, équation 5.14 becomes

$$I_T = I_{SNR} + I_o - I_c \qquad 5.15$$

I_o being the intensity observed outside the loop and I_c the intensity calculated for the pre-SNR volume.

Hayakawa et al. include in their model a parameter to account for cloud evaporation, such that the ambient density, n_o is replaced by $n_H = (1+f)n_o$, where f is the fraction of the gas in the model that is said to have been evaporated from clouds. They equate this evaporated fraction with that predicted by McKee and Ostriker (1977) for remnants of the loop's size and age to deduce that f=0.7. However, it is unlikely that all the evaporated material from McKee and Ostriker type clouds would simply behave as if it were part of the ambient gas and adopt the density profile of equation 3.11. Much of such evaporated material is likely to remain at smaller radii, occupying the centre of the cavity. The major consequence of introducing this parameter into their model is reduce the deduced ambient density. In our model it has the additional importance of altering the temperature of the pre-SNR hot gas, both temperature and density determining I_c in equation 5.15.

If the shock were considered to propagate in a 2-component diffuse medium rather than the cold component to have come from compact clouds or closely associated intermediate density halos then it might be considered to evolve as if in a medium whose temperature is an average of the hot component of density n_o and the cold component of density fn_o. The temperature, T_h, of the hot component would then be $T_o*(1+f)$. Allowing for a neutral gas fraction f alters the value of I_c in two ways. Reducing the x-ray emitting component of the ambient gas by (1+f) reduces the emission by $(1+f)^2$. A secondary effect is that the increase in its deduced temperature changes its emissivity. The inclusion of the parameter f is essential to the model. Without it the deduced value for I_c in the B and C bands exceeds the sum of I_{SNR} and I_o towards the centre of the loop, which is physically impossible. The value of the parameter f is thus deduced by fitting the central emission in the B and C bands.

The background I_o is set to a constant value for all but the B and C bands. In the two lower energy bands the strong latitude dependence requires that I_o increase with latitude. The only other input parameter is the intervening gas column density N_H. This has been assumed constant for all lines of sight. Although this is not realistic, any assumption, even with reference to H_I maps, would be too unreliable to put into a model. Possible H_I distributions are best discussed in relation to the results of the simpler model.

Figures 5.17-5.21

Figure 5.17 Radial cuts through the Loop I x-ray data, cutting the shock at b=20°, 30°, 40°, 50° and 60°

5.17a B-band

5.17b C-band

5.17c M1-band

5.17d M2-band

5.17e I-band

Figure 5.18 Radial cuts through the Loop I 408MHz data, cutting the shock at b=20°, 30°, 40°, 50° and 60°

Figure 5.19 Radial cuts through the Loop I x-ray data for the B, C, M1, M2 and I bands, cutting the shock at

5.19a 20°

5.19b 30°

5.19c 40°

5.19d 50°

5.19e 60°

Figure 5.20 Model A. A fit to figure 5.19a. For parameter values used see table 5.8

Figure 5.21 Model B. A fit to figure 5.19e. For parameter values used see table 5.8

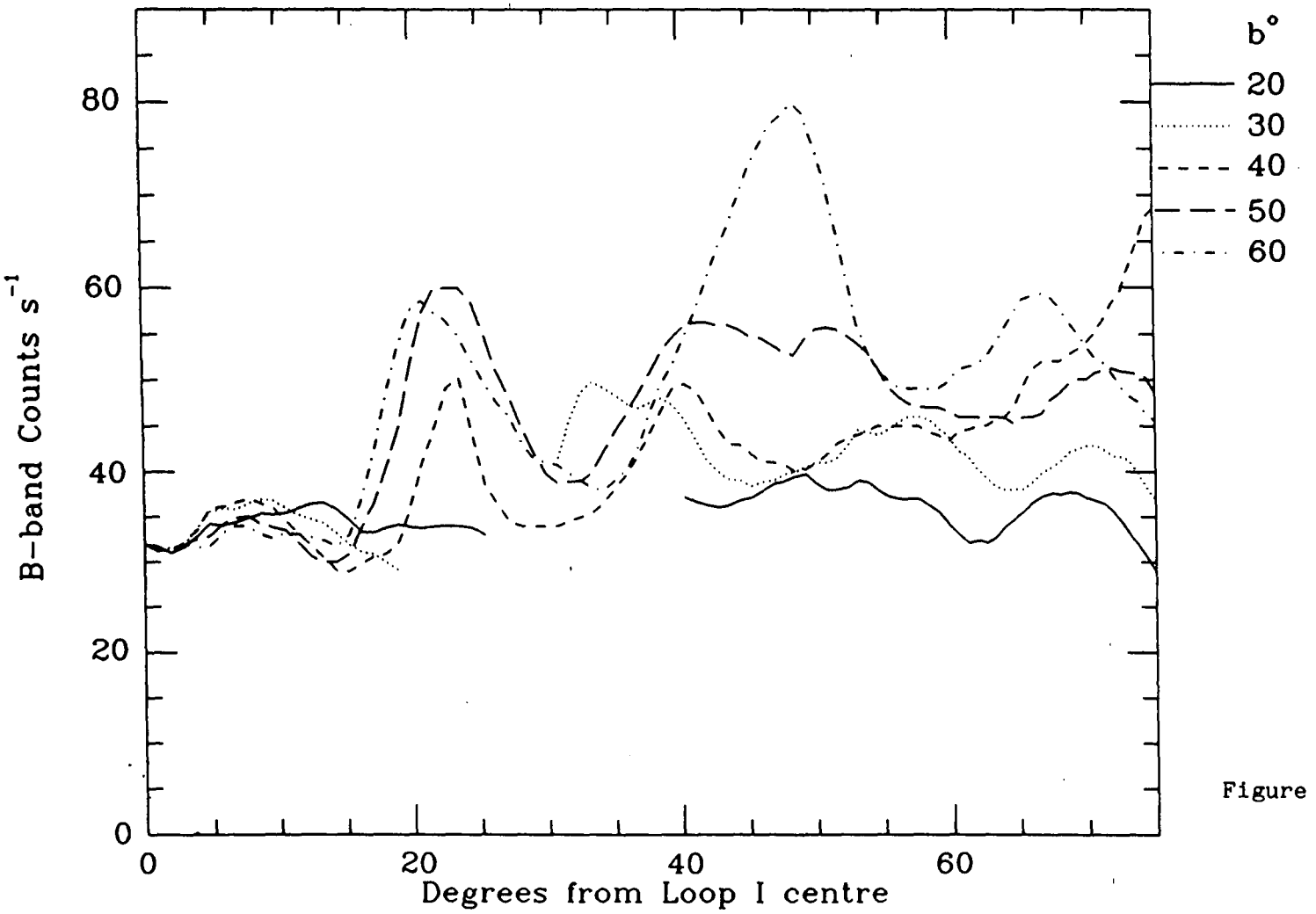
b°
20
30
40
50
60
B-band Counts s^{-1}
0
20
40
60
80
0
20
40
60
Degrees from Loop I centre

Figure 5.17a

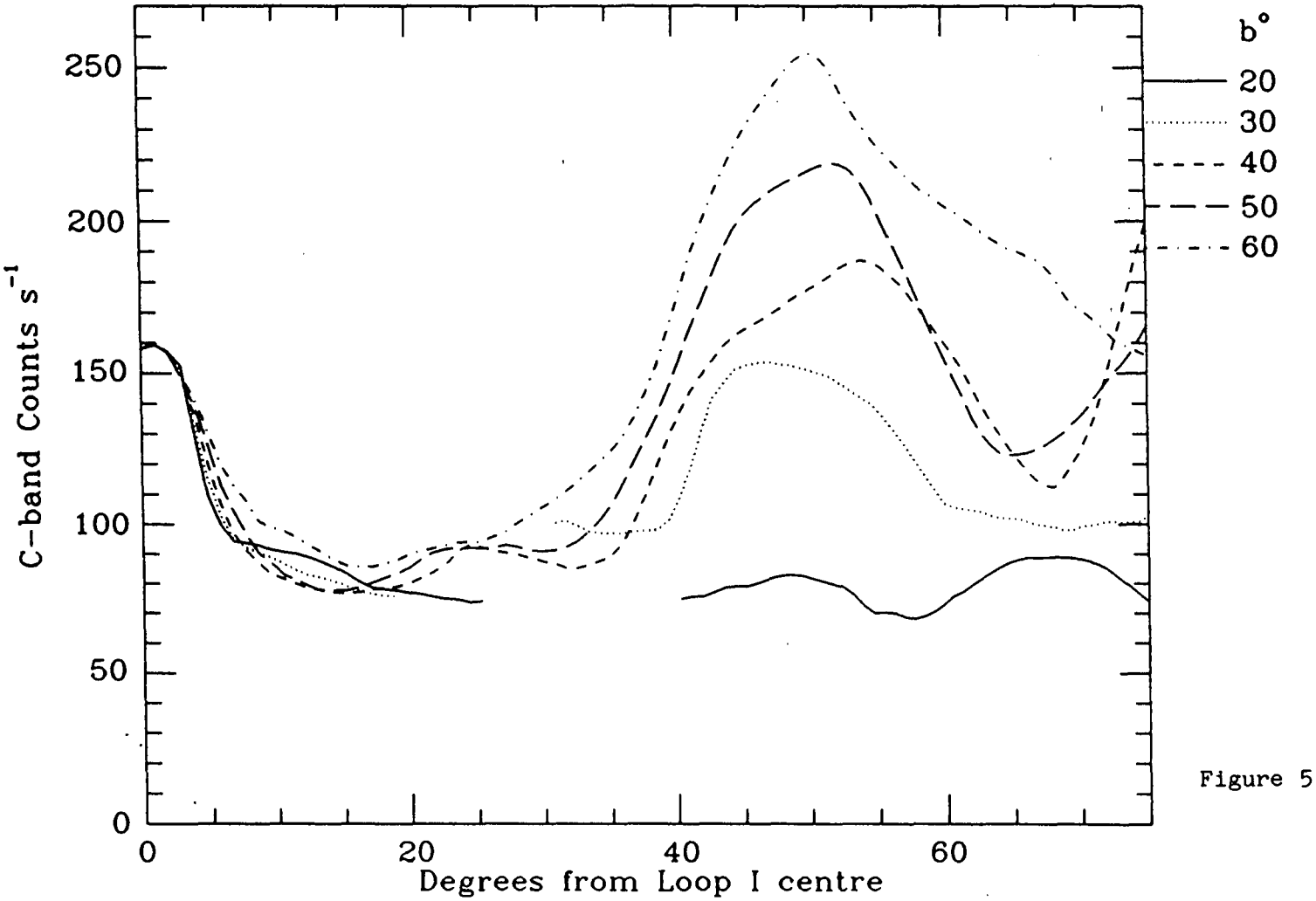
b°
20
30
40
50
60
C-band Counts s^{-1}
250
200
150
100
50
0
0
20
40
60
Degrees from Loop I centre

Figure 5.17b

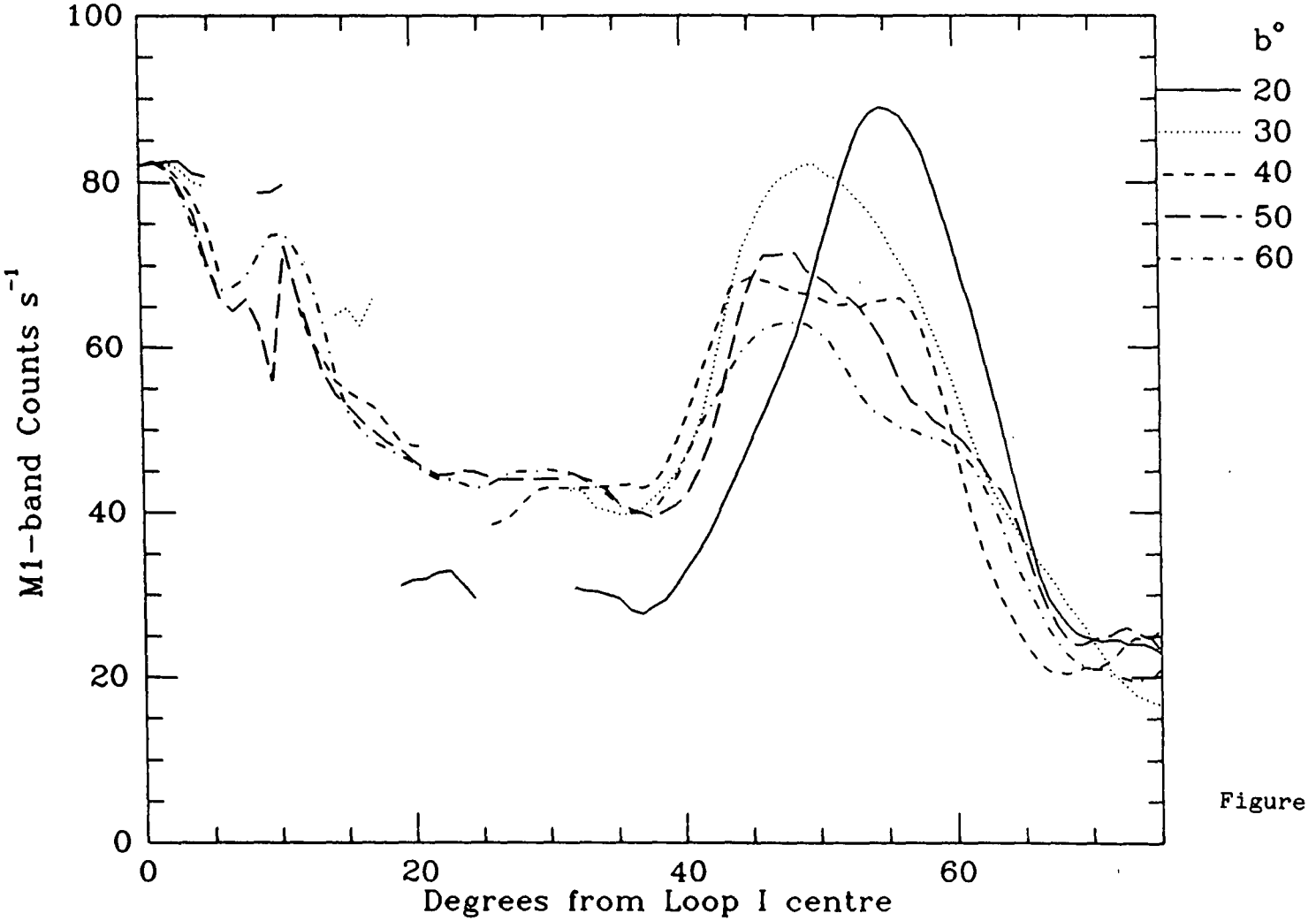
100
80
60
40
20
0
0
20
40
60
M1-band Counts s^{-1}
Degrees from Loop I centre
b°
20
30
40
50
60

Figure 5.17c

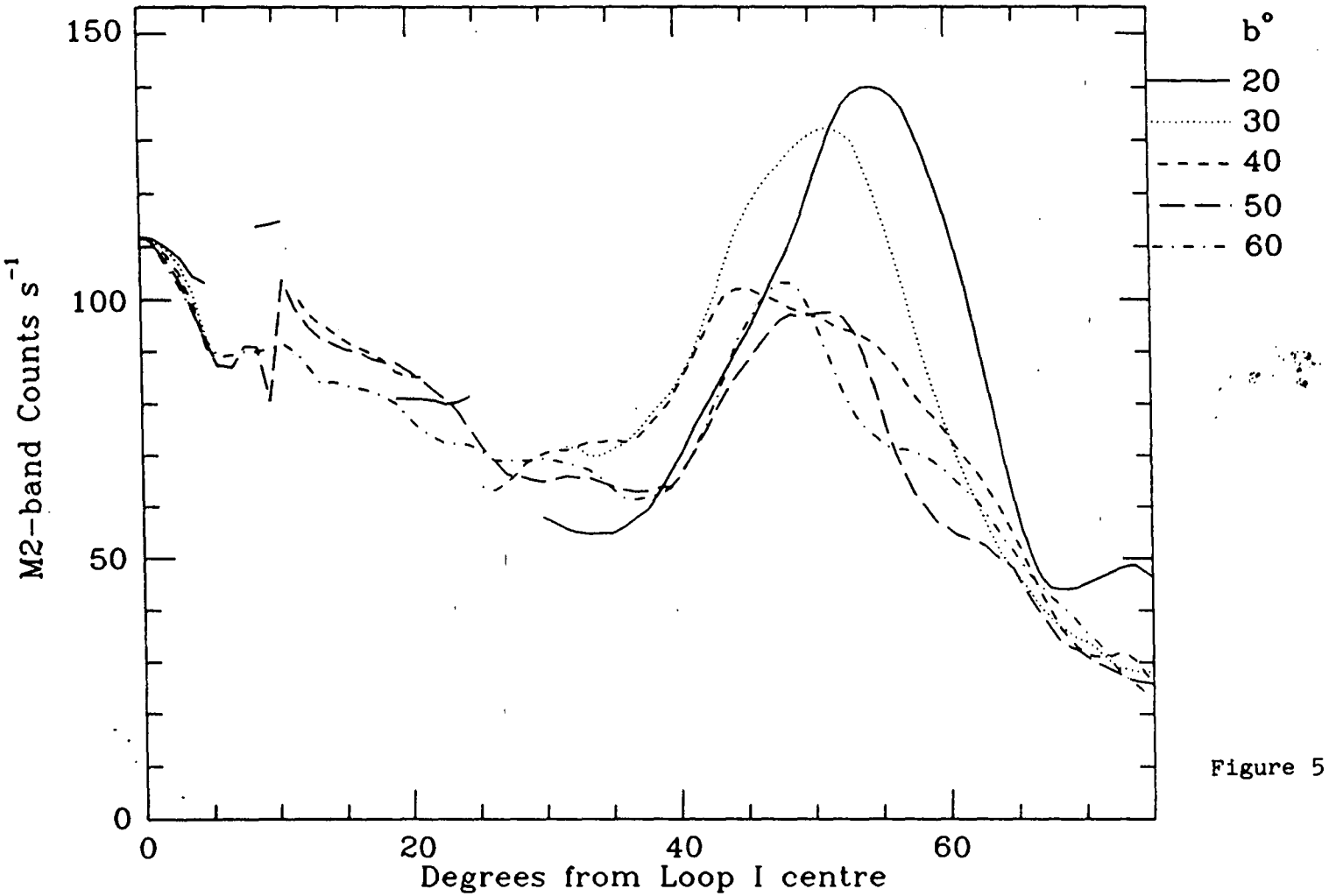
150
100
50
0
0
20
40
60
M2-band Counts s^{-1}
Degrees from Loop I centre
b°
20
30
40
50
60

Figure 5.17d

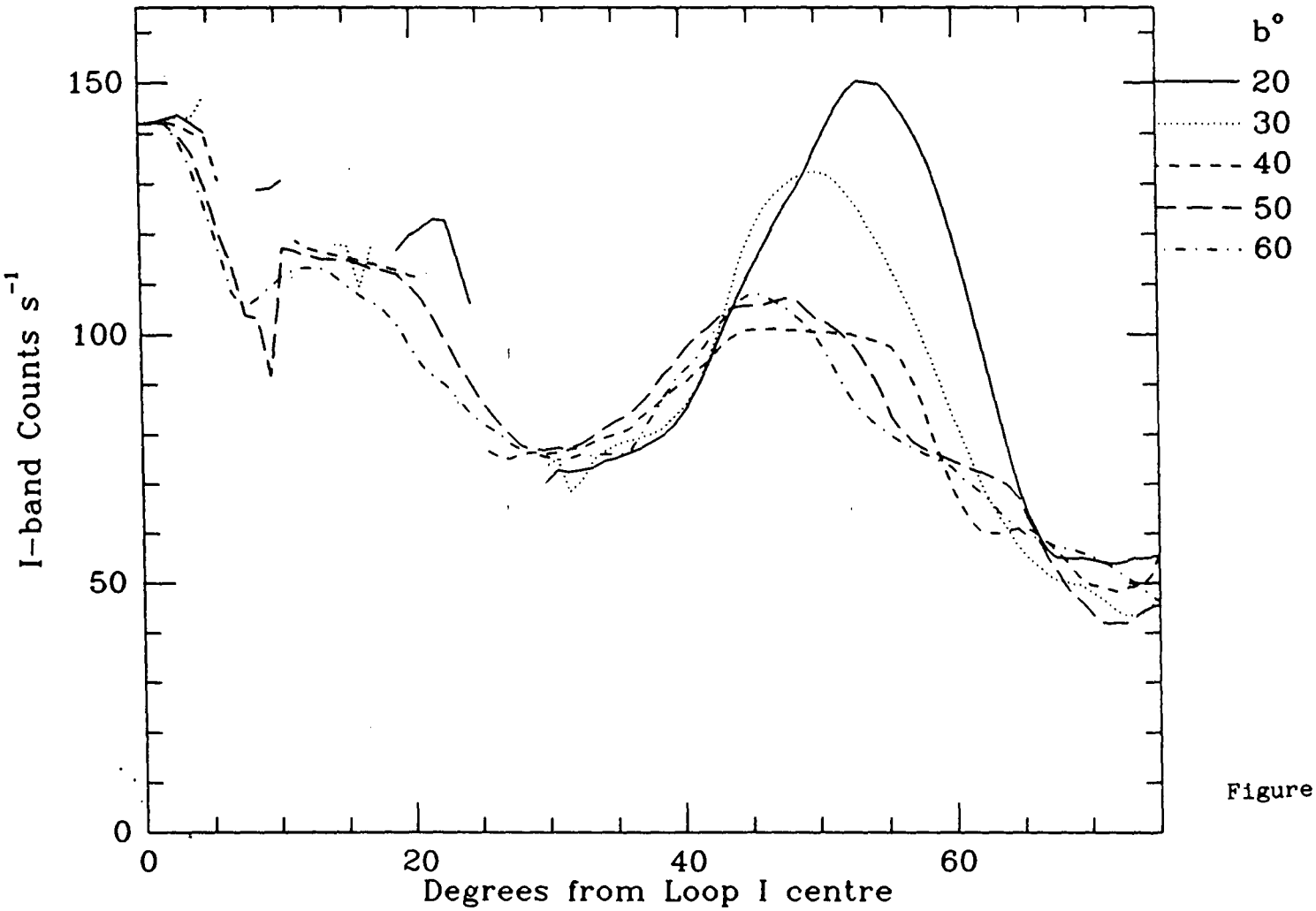
b°
20
30
40
50
60
150
100
50
0
I-band Counts s^{-1}
0
20
40
60
Degrees from Loop I centre

Figure 5.17e

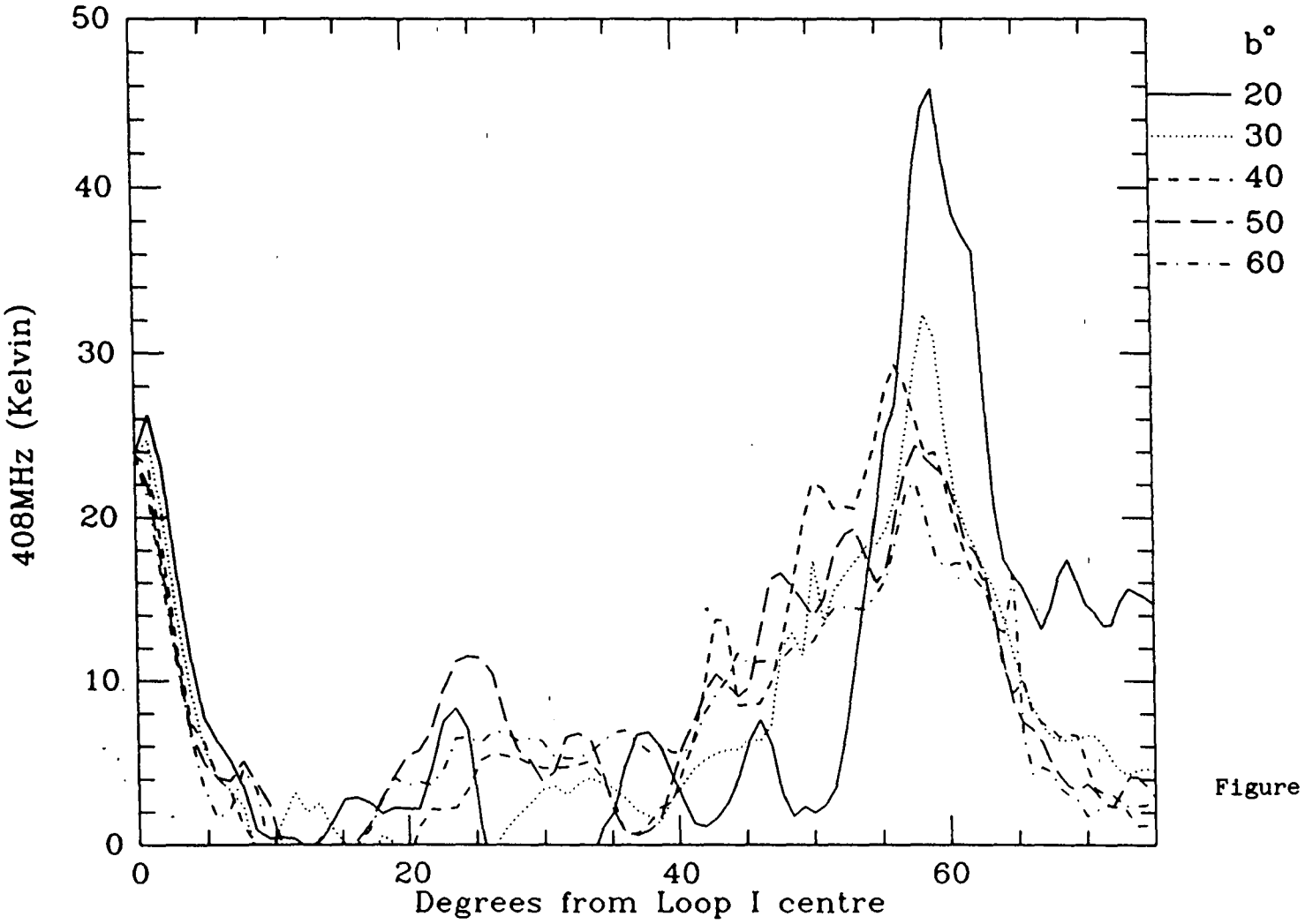
50
40
30
20
10
0
0
20
40
60
408MHz (Kelvin)
Degrees from Loop I centre
b°
20
30
40
50
60

Figure 5.18

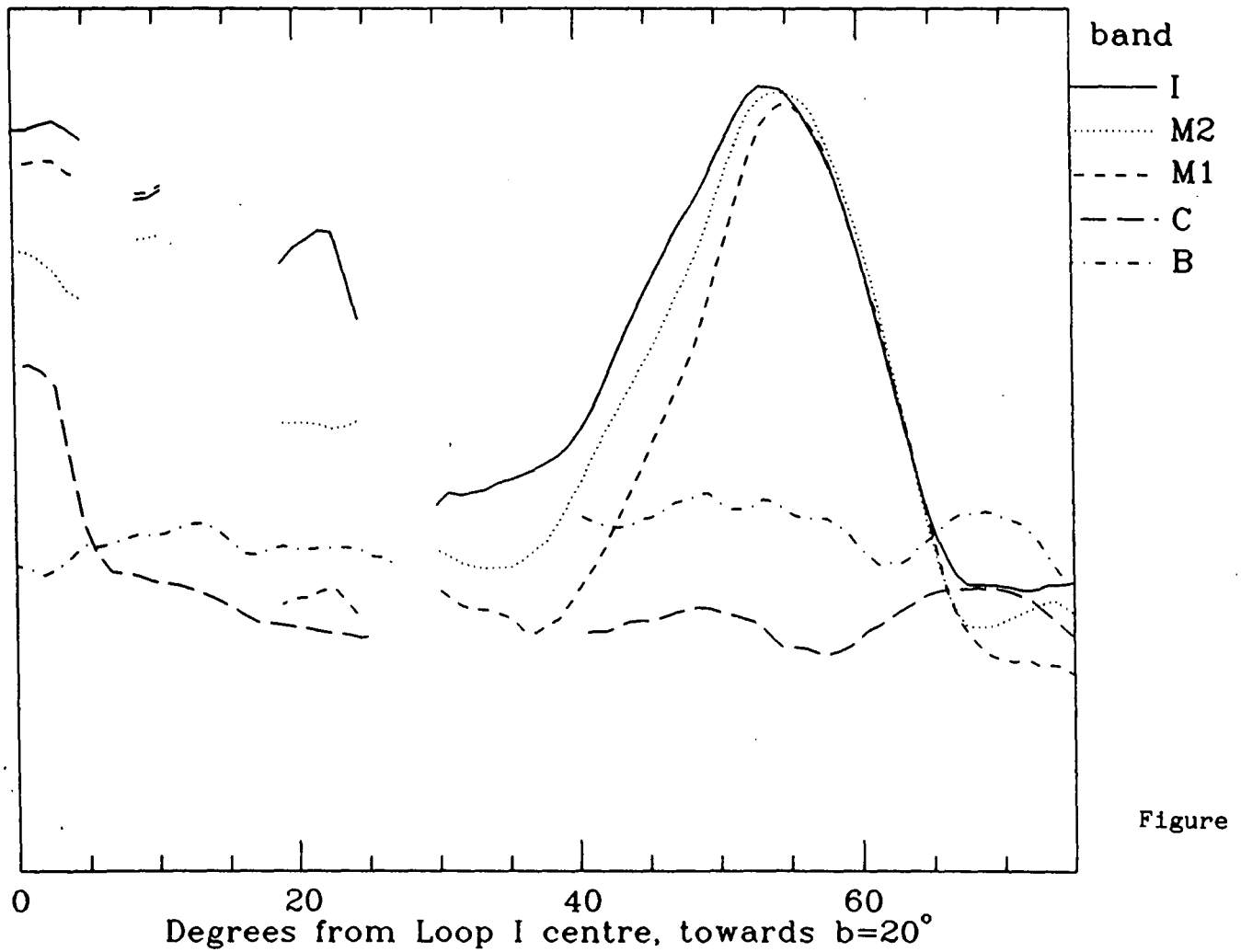
band
I
M2
M1
C
B
0
20
40
60
Degrees from Loop I centre, towards b=20°

Figure 5.19a

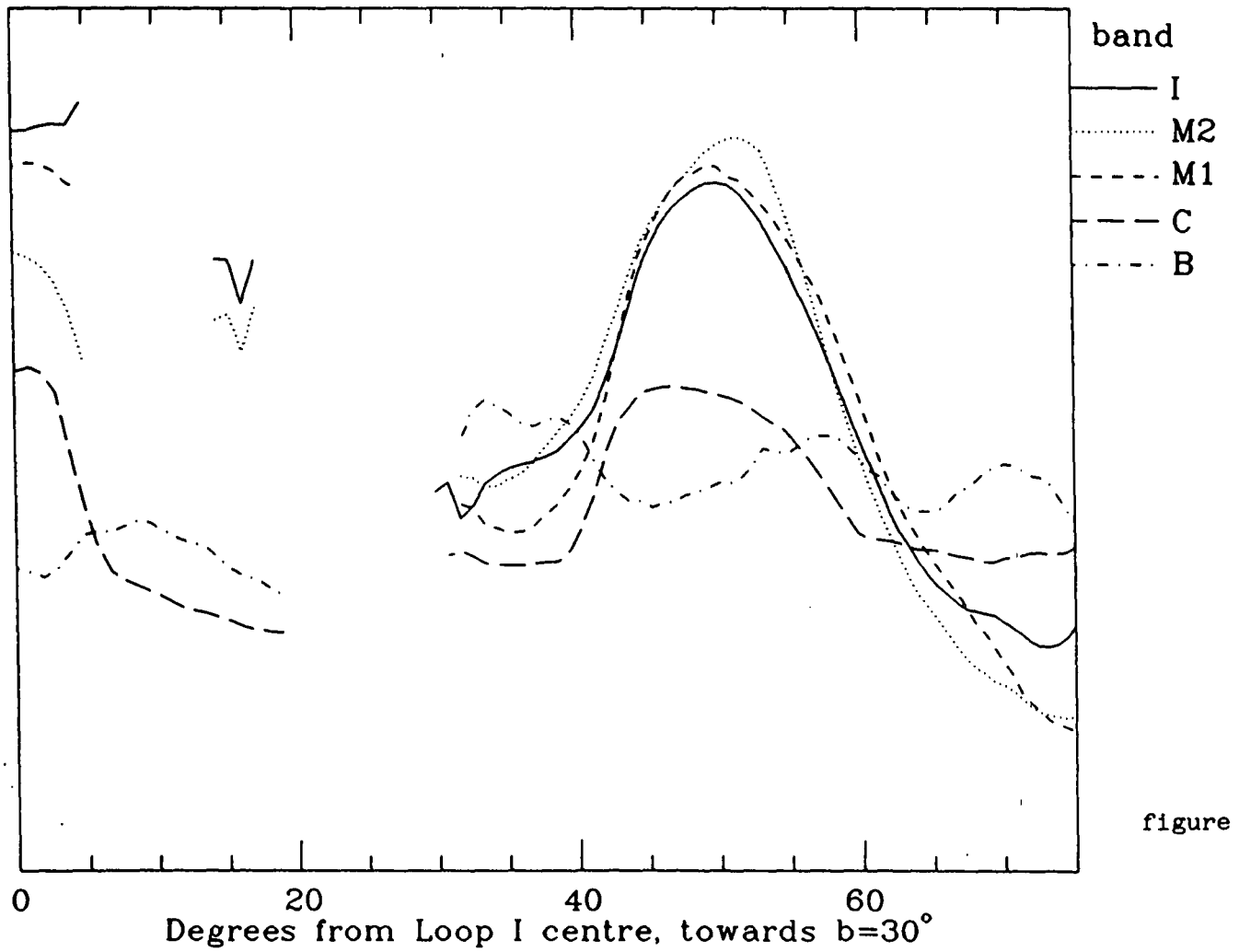
band
I
M2
M1
C
B
0
20
40
60
Degrees from Loop I centre, towards b=30°

figure 5.19b

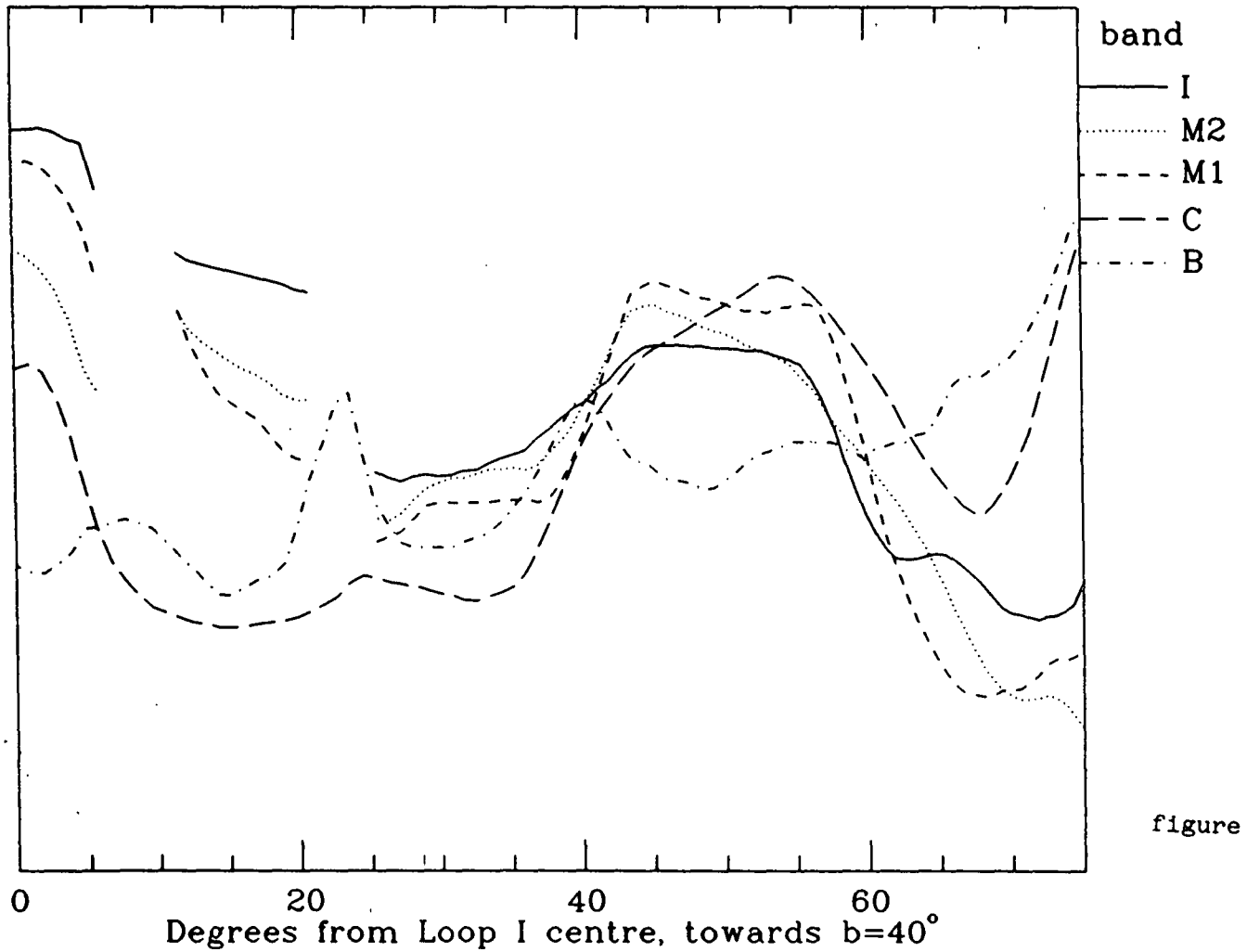
band
I
M2
M1
C
B
0
20
40
60
Degrees from Loop I centre, towards b=40°

figure 5.19c

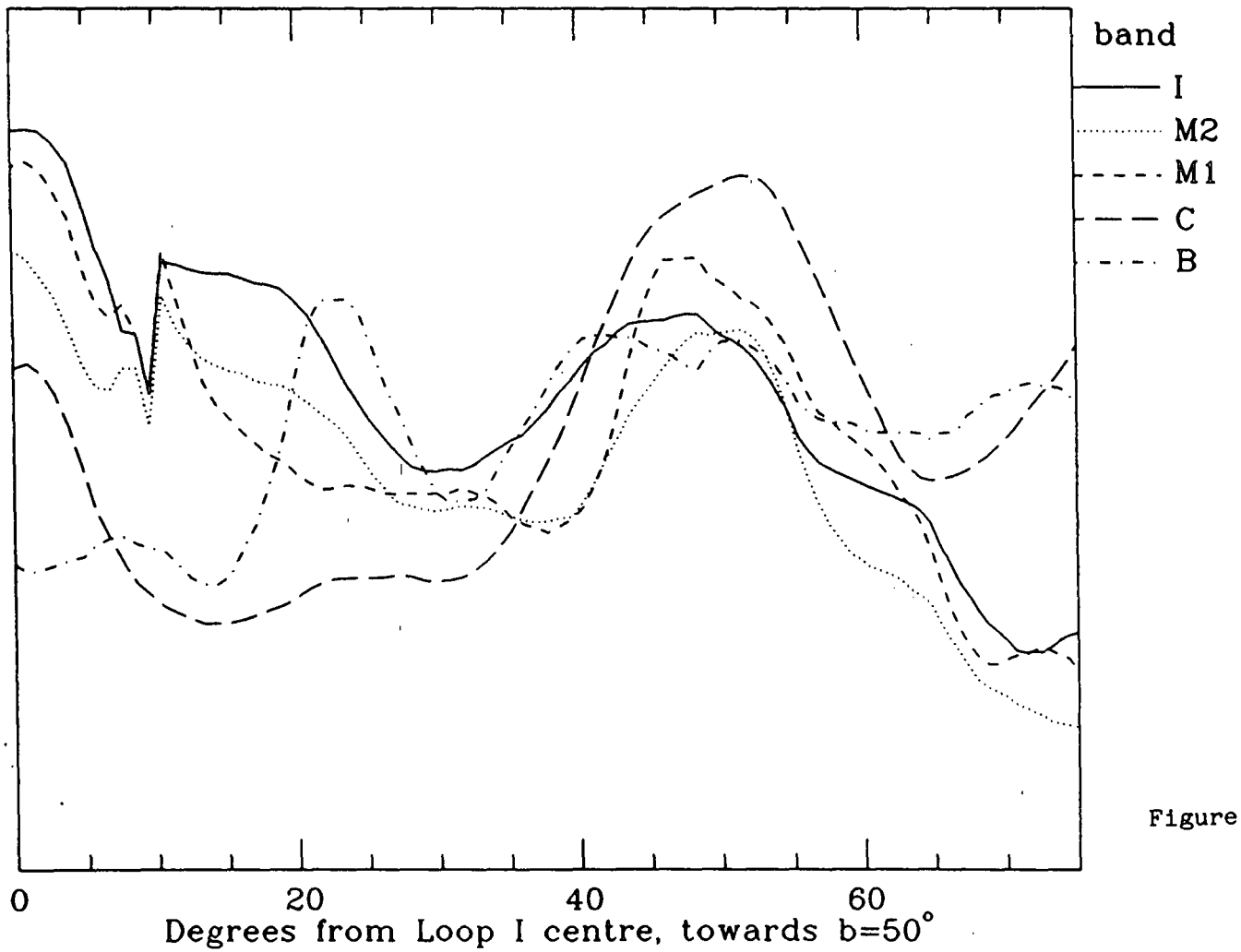
band
I
M2
M1
C
B
0
20
40
60
Degrees from Loop I centre, towards b=50°

Figure 5.19d

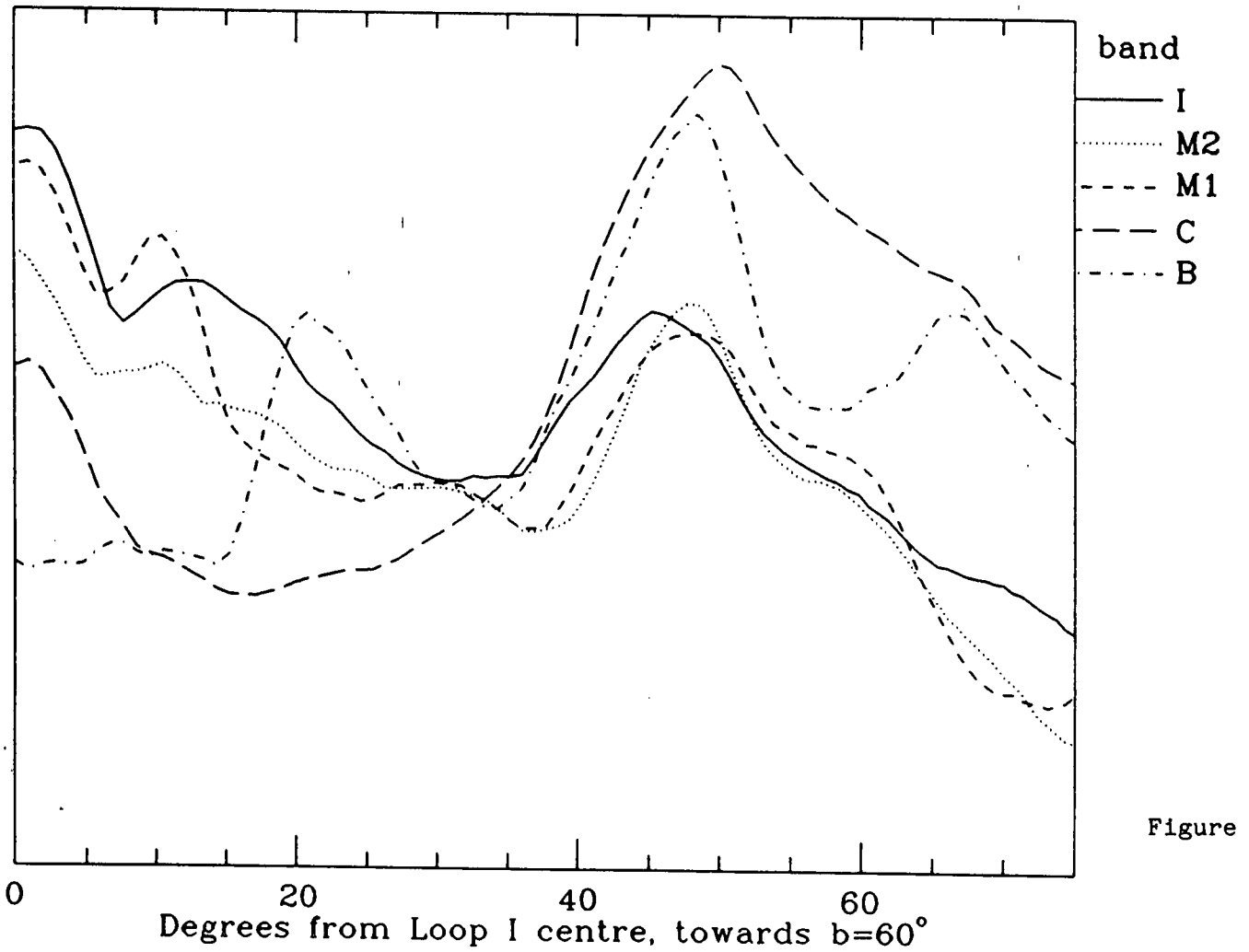
band
I
M2
M1
C
B
0
20
40
60
Degrees from Loop I centre, towards b=60°

Figure 5.19e

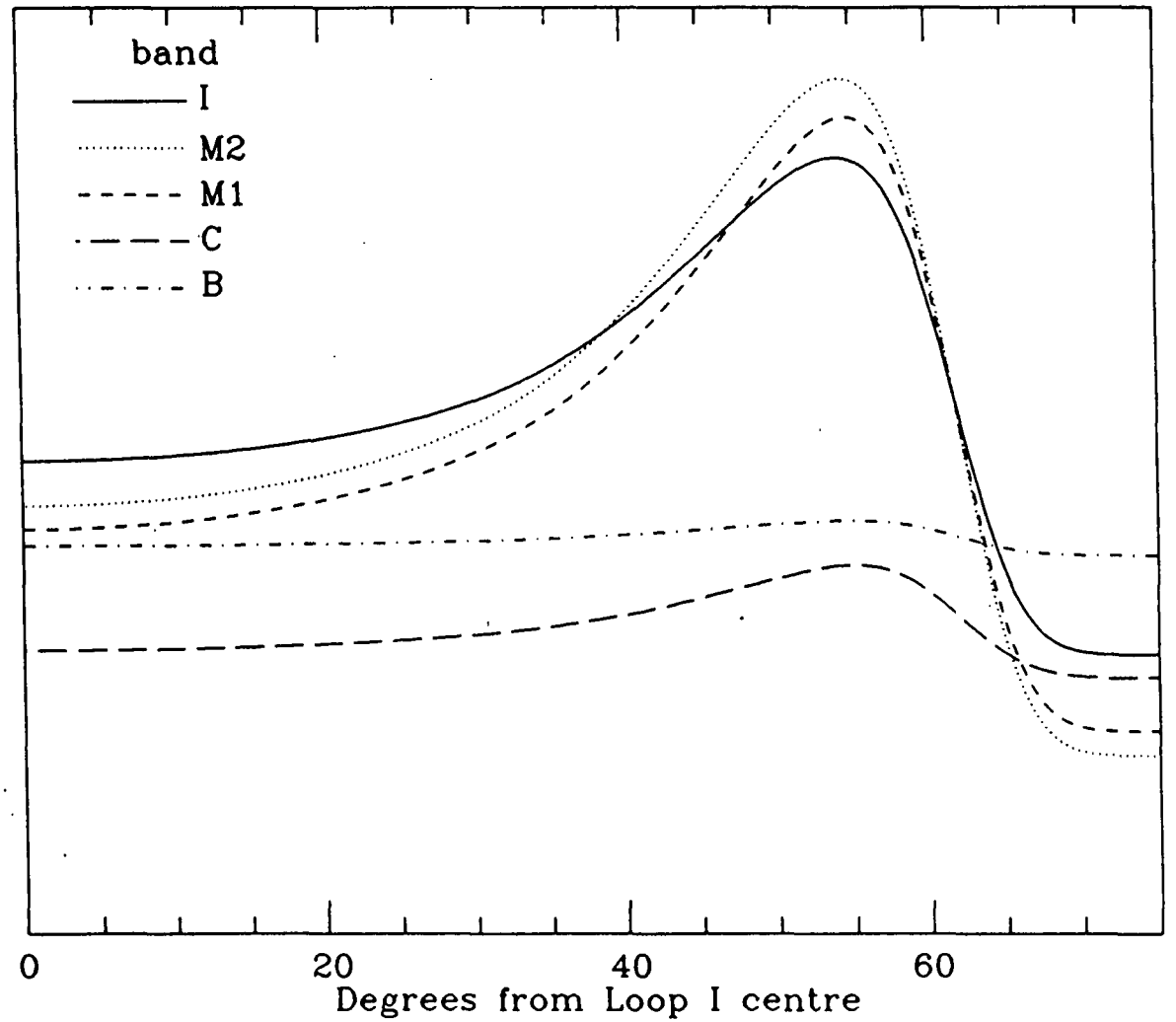

Model A

Figure 5.20

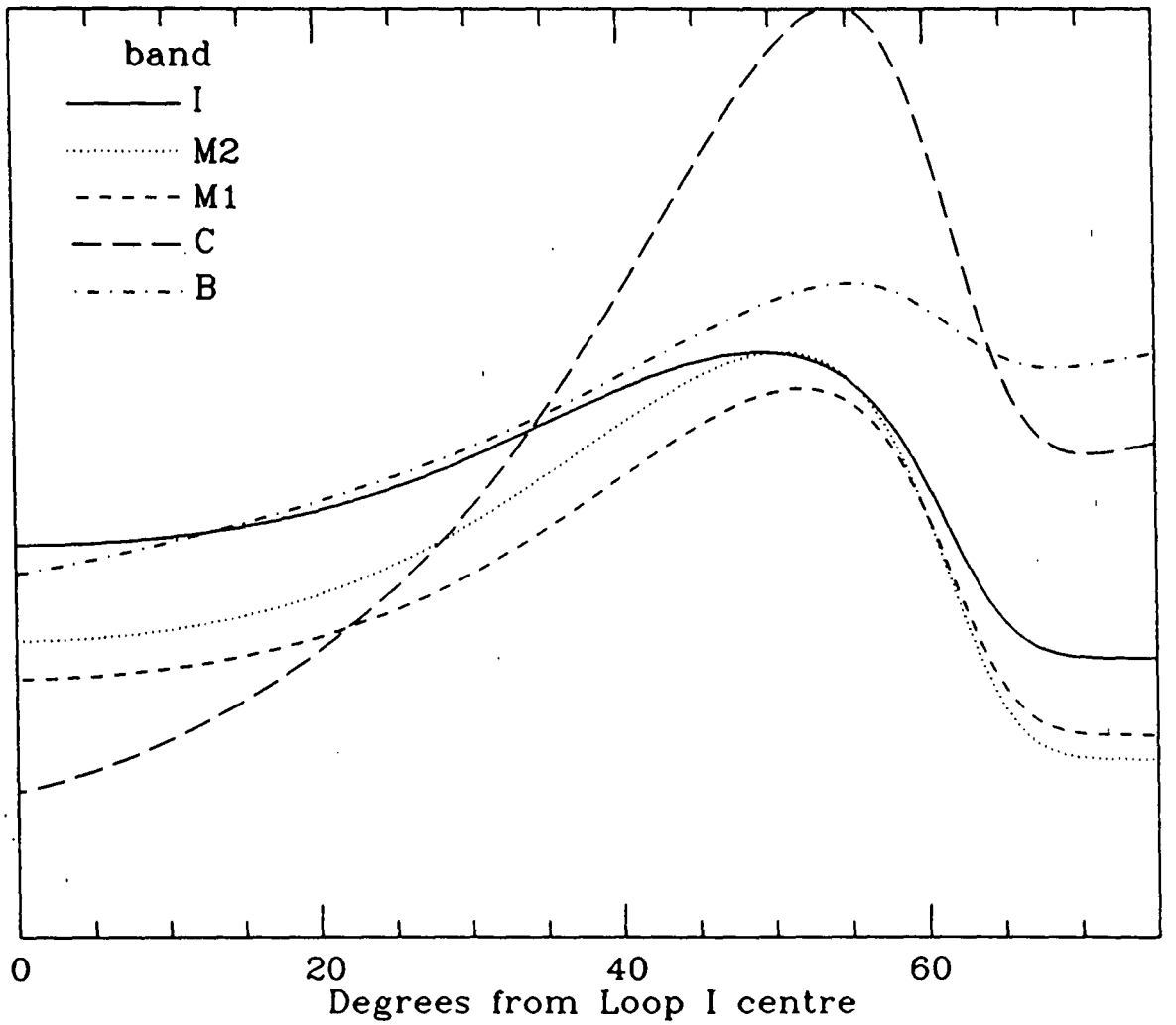

Model B

Figure 5.21

5.3.5.3 Fitting the Data -

In order to better see the radial distribution of the x-ray emission, figures 5.17a-e show arbitrary cuts through the maps of figure 4.3. Each cut starts at the loop centre, l=329°, b=17.5°, and radiates out in the direction of the NPS, crossing the loop between b=20° and b=60° at intervals of 10° of galactic latitude. Figure 5.18 plots cuts through the 408MHz data in figure 1.1 (Haslam et al. 1982). Figure 5.17 plots the cuts belonging to one band on a single graph, showing most clearly the trend of the x-ray ridge with respect to latitude. Figure 5.19 re-plots the same data, but orders the data by cut, showing the relationship between the bands at the same positions. Figures 5.20 and 5.21 (reproduced as over-lays on the inside rear cover) are approximate fits to figures 5.19a and 5.19e respectively, and shall be referred to as Model A and Model B. The parameters used to generate the models are given in table 5.8, along with the modelled ambient temperature and the temperature of the M-band ridge.

Discrepancies between values obtained in table 5.8 and those given in Parkinson and Osborne (1985) are due to slightly different assumptions and differences in the complexities of the models. The previous paper simply fitted the position of the M and I band ridges with respect to the shock and approximated the ridge temperature to 3.10^6 K. Parameters f and N_H were not included because the B and C bands were omitted from the

	Model A	Model B
T_s (K)	3.10^6	$3.2\ 10^6$
ϕ	0.5	0.5
η	3	2
$n_H=(1+f)n_e$ (cm^{-3})	0.0094	0.0078
f	0.5	0.5
N_H (cm^{-2})	8.10^{20}	1.10^{20}
T_e (K)	$0.8\ 10^6$	$1.8\ 10^6$
T_h (K)	$1.2\ 10^6$	$2.7\ 10^6$
T_H (K)	$3.1\ 10^6$	$3.4\ 10^6$

	B	C	M1	M2	I
I_e counts.s^{-1}	15	75	19	30	50

For Model B, I_e increased to 35 and 145s^{-1} at r=75° in the B and C bands respectively.

Table 5.8

Parameters used to construct models A and B.

fit.

The models do not predict the observed intensity of the medium energy x-rays towards the centre of the loop, and does not explain any of the enhancement in the J and 2-6keV bands. These require the existence of a hotter component. Although a temperature gradient is included in the models, and thus the temperature rises sufficiently high to produce harder x-rays, the density falls off to zero towards the SNR centre. Therefore the intensity is

insignificant and the density profile is not accurately represented by the model. There must be a second hotter gas component, probably provided by the evaporation of clouds, that is not accounted for in equation 3.11. It is for this reason that it is erroneous to assume that the factor f represents all the cloud evaporation. Our model requires the factor f to explain the B and C bands, but it is a fit to observations rather than any assumption as to where the cold component might come from. Hayakawa et al. (1979) assume this component to be the McKee and Ostriker (1977) evaporated gas, but some of this evaporation will take place after the passage of the shock and will not be swept up into the general gas distribution given by equation 3.11a.

The value of T_s is determined by the ratio of the ridge intensities in the M and I bands. The difference in the value of T_s between Models A and B is not significant, and can be accommodated by uncertainties in the background intensity I_o.

Agreement between the M and I band intensity ratios of the observed ridge and those in the model are not as good as one might hope. This may also be due to an inaccurate estimate of the background but other possibilities exist. The temperature gradient is small and thus the models have approximately only one temperature component. In reality, inhomogeneities will lead to clumps of hotter or colder than average gas, and

thus a model with two or more temperature components is needed to more accurately fit observations.

The intervening column density of H_I has been introduced in the model to give sufficient absorbtion to suppress the B and C band emission in the direction of the ridge. The values used in the models are thus thought to be representative of the ridge area only. The factor f was chosen as 0.5 to fit the B and C band intensities at the centre of the loop in model B only. The choice for model A was fairly arbitrary since most of these softer x-rays are absorbed by the large column density of H_I. Had the model restricted the H_I to the ridge only, then a similar value to model B would have been required.

A temperature gradient of ϕ=0.5 gave the required separation of the M and I bands of less than 1°, but for model B this increased to 2.5°. The latter is probably at the limit of what can be accommodated by the observations (some regions being consistent with ϕ=0), and thus gives a maximum allowable temperature gradient. If r_s=115pc and T_s=3.10^{6}K then at the shock $dT/dr<1.3.10^4 K.pc^{-1}$, compared to the Sedov solution which gives $dT/dr=10^5 K.pc^{-1}$.

The most significant parameters of the model are η and n_H. The latter determining the intensity of the projected x-ray maximum, and the former giving its position. The model suggests that the SNR must have evolved in a low density region comparable to the

$n_o = 0.0035 cm^{-3}$ predicted by McKee and Ostriker for the hot phase of the ISM. The low value of η shows that this gas is already at temperatures around 10^6 K

Comparison of models A and B suggests that the shock weakens at higher latitudes due to an increase in the ambient temperature. It is possible that this is evidence for a general increase in the temperature of the gas away from the plane. A reduction in the shock strength also results in less emission due to the lower densities behind the shock. However, the observed differences in intensity between b=20° and b=60° cannot be entirely explained by this, and thus model B requires a slightly smaller ambient density. This may be another indication of a variation in the local ISM with respect to z.

5.3.5.4 The Size of Loop I -

Some of the parameter fits in models A and B will be affected by discrepancies between the size of Loop I and the assumed size. We will split this uncertainty into two categories. The first source of error is the lack of knowledge as to the distance to the centre of the Loop (130±75pc) and the second is the unknown angular position of the shock. The former only affects the deduced ambient gas density, which will scale as $(D/130)^{-1/2}$. The effect of the latter is more complex. Increasing the angular radius of the shock reduces the value of η. The maximum allowable value of ϕ will then have to be reduced since

the effective width of the gas shell will have been increased. It will be necessary to increase n_o because of the reduced density within the shell. Since there will be more gas towards the centre of the loop, the increased emission here in the B and C bands reduces the required value of f. T_o would rise, whilst the shock temperature would remain at about 3.10^6 K and N_H would be unaffected. The non-linearity of each of these changes prevents a simple relation between each parameter and the angular separation of the shock from the x-ray ridge, though it is possible to estimate limits to the range of possible separation.

Figure 5.14 shows that the closest the ridge can be to the shock is in the case of a strong shock, the minimum separation being 5% of the remnants radius. The closest that the x-ray ridge gets to the NPS (which is assumed concentric with the shock) is at b=20°, with an angular radius of 56°. After convolution to the resolution of the data the minimum allowable radius of the shock is 61°, ie. 3° beyond the radio spur.

However, the changing separation of the ridge and shock with increasing latitude suggests that this may be too close. Although table 5.7 shows the separation increasing continually up to b=50°, most of this takes place below b=30°. This sudden change can be more readily explained if the shock is placed at a larger radius. Firstly, the relative change would then be less

dramatic. Secondly, the weaker the shock the more sensitive it is to changes of the ambient temperature.

An estimate of the maximum allowable angular radius of the shock comes from examination of the width of the ridge. As the shock becomes weaker the ridge becomes broader. Comparison of models A and B with the ridge in the medium energy bands suggests that although the fit is good at the outer edge, towards the loop centre the model intensities are slightly too high. With a shock radius of 63°, the models' ridges may therefore be a little wide, though a 64° radius shock cannot be ruled out. We therefore estimate that $61° < r_s < 64°$.

5.3.5.5 The N_H Distribution -

The value of N_H adopted in both models A and B is large in comparison to the observed column densities in the direction of the x-ray ridge. In the direction of l=30°, b=20°, the Leiden-Green Bank 21cm survey (Burton, 1985) indicates that there is only $4.10^{20}\,cm^{-2}$ in the entire line of sight. Even if all of this gas lay between us and the x-rays, this value falls short by a factor of two of that required in the model. Parkinson and Osborne (1985) suggested that $N_H = 4.10^{20}\,cm^{-2}$ could provide sufficient absorbtion, but we now believe that this can only be considered a minimum requirement, with a greater value giving a better fit. The model assumes the value of the absorbtion coefficient σ_E to be given by equation

5.9, which holds for the case of a uniform distribution of the absorbing gas. However, Jakobsen and Kahn (1986) show that clumping of the neutral gas reduces the effective value of σ_E. Jakobsen (1986) gives the reduction factor as

$$\sigma_E'/\sigma_E = (1-\exp(-\sigma_E N_{\bar{h}}))/\sigma_E N_{\bar{h}} \qquad 5.16$$

where $N_{\bar{h}}$ is the column density of the average cloud. For E=0.25keV, equation 5.10 gives $\sigma_E = 4.2.10^{21}$. Thus, if $N_{\bar{h}} = 10^{20}\,cm^{-2}$ is chosen as a typical cloud size, the absorbtion is be reduced to 0.8 of that for a uniform gas distribution. This puts the absolute minimum column density at $5.10^{20}\,cm^{-2}$, and model B then requires $N_H = 10^{21}\,cm^{-2}$. This now puts the required column density beyond the total amount of N_H observed, and it is necessary to assume that the x-rays emission is also unevenly distributed and is closely associated with the clouds. The effectiveness of the absorption would thus be increased. This clumping could exist in two possible forms. The first requires that most of the x-ray emitting gas resides close to clouds at the observed temperature of 3.10^6K. Away from the clouds the gas (also at 3.10^6K) is too diffuse to have a flux comparable to the denser component. The second possibility, and in our view more likely, is that x-rays are emitted with significant intensities from both the cloud halos and the inter-cloud region, but that the temperature of the gas away from the clouds is hotter. The model might thus be better

represented as having two components. The hotter one giving rise to a detectable fraction of the medium energy x-rays, whilst the remainder comes from cooler cloud halos from where most of the B and C band x-rays can be easily absorbed. By way of example, the ridge at b=30° can be reasonably well fitted by two components at 6.6×10^6 K and 2.6×10^6 K with emission measures of 0.0044 and 0.037 cm^{-6} pc respectively. The details of how cloud halos may be heated is discussed more fully later in the chapter.

5.3.5.6 Spherically Symmetric? -

The model is based on the assumption of spherical symmetry. However, as is evident from one glance at the radio and x-ray maps (shown numerically in the differences between models A and B) although Loop I may be spherical it is certainly not symmetric. The section of the blast wave that propagated along approximately constant latitude at b=20° may well have evolved in an ISM with roughly constant properties, but model B would then imply that as the remnant evolved in a direction away from the galactic plane the density fell and the temperature increased. We do not attempt to re-model for this additional complexity, but we discuss here some of the implications for model B.

The lower density and the increased pressure imply that the shock should travel more rapidly. Chevalier and Messina (1976) and Cox and Franco (1981) have analyzed

models where a supernova explodes at the centre of a spherical density gradient, $n_o = n_o' r^{-\xi}$. If the mass of swept up matter is equated with the integrated density profile of equation 3.11a then the value of n_o deduced from the model becomes the mean density, and the actual density immediately ahead of the shock is

$$n_o' = n_o (3-\xi)/3 \qquad 5.17$$

and equation 3.11b becomes

$$\nu = (3-\xi)\eta - 3 \qquad 5.18$$

This indicates that for ambient densities decreasing with radius ($\xi>0$) the radial distribution of gas within the remnant becomes flatter. In model B we require that $\eta=2$ in order to give the position of the x-ray ridge, but η merely determines ν, the parameter directly responsible for the projected maximum. With equation 3.11b replaced by 5.18 the required value of $\nu=3$ can be arrived at with say $\eta=3$, $\xi=1$. It would thus be possible to have little change in the strength of the shock over the arc of the NPS and yet a different density distribution. However, if we examine possible values of ξ more closely we find that the density gradient required by the model is too small to greatly affect the value of η or n_o. If we assume that model A has evolved in a medium of constant n_o then, in order to make the ambient density gradient compatible with model A at r=0, it is necessary to modify it at some small radius. If we set the density within $r_c = 0.1 r_s$ equal to

the ambient density predicted for model A (within this radius, for moderate values of ξ only 0.1% of the swept up mass will have been contained, and therefore the density profile unaffected) then we find that $\xi<0.1$. As $r_e \rightarrow 0$, $\xi \rightarrow 0.03$. Thus n_o' and η in equations 5.17 and 5.18 are virtually unaffected.

The above discussion assumed model A to have evolved in a constant gas density. We should also consider the possibility that the ambient gas between the loop centre and l=30°, b=20° was not constant. If the H_I shell outside the radio NPS is evidence that the SNR responsible for the x-ray emission evolved inside an old cavity (either a previous SNR or a bubble due to strong winds from the Sco-Cen O-B association) then it is possible that there existed a density gradient that can be approximately represented by $\xi<0$. There are now no constraints on the value of ξ, other than what one might consider to be 'reasonable' for an old large cavity. If the cavity were formed by a previous SNR then at one time the density distribution will have been described by equation 3.11a. At the death of an old remnant, as the shock velocity approaches the ambient sound speed, $\eta \rightarrow 0$ and equation 3.11b suggests that $\nu \rightarrow 0$. However, equation 3.11b only truly holds for a remnant the has evolved with η constant with time. The onset of the radiative cooling phase as the temperature falls below 10^6 K may radiate much energy away relatively rapidly, 'freezing' the gas distribution at say $\eta \sim 2$ and $\nu \sim 3$, the value of ν for the

earlier SNR becoming ξ for the later one we observe now. Although the further passage of time since then will have led to additional erosion of that profile via cloud evaporation and pressure equalization, ξ=-1 would not, therefore, seem an unreasonable possibility. With this value of ξ equation 5.18 shows it is now possible to maintain the required density profile of model A and its 63° shock radius with a weaker shock than originally deduced, ie. η=2.25. A similar ξ for model B would reduce η to 1.5. In our earlier consideration of the position of the shock front in relation to the x-ray ridge at b=20° it was suggested that it was not possible to reduce its radius below 61°. If we now allow ξ=-1, the same model allows a strong shock to lie only 4° from the ridge at 60° radius. This, however, will even more severely exacerbate the previously mentioned problem of the rapid change in the relative ridge position between b=20° and b=30°. Although it is always possible that the projected shock is not circular, and it also jumps rapidly to having a smaller radius, there is no evidence for such deviation in the radio NPS. Our belief that the outer edge of the radio spur marks the shock, and that the sudden change in the strength of the shock is best minimized, suggests to us that the shock probably lies between 62° and 63°. This implies that the only way ξ=-1 can be accommodated is by having the very low values for the shock strength given above.

5.3.5.7 Non-Continuous Evolution -

Models A and B assume a homogeneous ISM, and the discussed modifications to these models assume a smoothly varying medium. The SNR is not, therefore, considered to have suffered any sudden changes in its evolution, and the position of the x-ray maximum reflects the details of this steady evolution. However, we will now consider the possibility that the x-ray ridge owes its position more to local discontinuities in the ambient medium than to a SNR as modelled. The H_I shell outside the NPS is not only an example of such a discontinuity, but whatever the reason for its formation, any similar features formed during the same process may well be parallel/concentric with it.

In the ISM model of McKee and Ostriker, clouds are assumed spherical and are relatively small and isolated. Any advancing shock is thus able to pass through the inter-cloud medium around the sides of clouds almost unhindered. In reality, however, much diffuse cloudy material is seen to exist in filamentary or sheet-like structures (Heiles, 1979, 1984). A shock encountering such a gaseous wall will not be able to pass around it so easily. McKee and Cowie (1975) analyzed the effect of a shock on a cloud. They showed that for the shock driven into the cloud, $U_c^2 = U_s^2 \rho_o / \rho_c$ where the subscript c denotes the properties of the cloud. With the temperature of the shocked gas proportional to U_s^2, the temperature within a cloud of $n_h \simeq 1 cm^{-2}$ is likely to be a factor of

order 100 below the temperature of the shocked inter-cloud medium, and is therefore unlikely to radiate 1keV x-rays. There will, however, be some form of transitional halo around the cloud at an intermediate density. Shock heating and turbulent mixing with the inter-cloud gas may then produce halo temperatures more comparable with the low density gas. This region around the edge of a cloud may thus be responsible for a large fraction of the emitted x-rays. At temperatures of a few million Kelvin, a small reduction in temperature results in a slight reduction of x-rays with energies>1keV, but this is small compared to the increased emission due to the density enhancement. For example, if the low density inter-cloud medium had half the density and double the temperature (3.10^6K) of the cloud halo, the volume emissivity of the halo would be greater by a factor of 15 for the C-band and 1.6 in the M2-band, these ratios becoming greater with increasing relative density of the halo. The presence of the cloud also leads to greater heat dissipation locally. As indicated by McKee and Ostriker, the gas already swept up and following the shock will usually be travelling faster than its sound speed relative to the obstructing cloud, and therefore a reverse shock will be set up which becomes a bow shock. Gas crossing this will experience further heating in addition to that due to the passing of the initial shock. It is thus possible that through mixing, the slightly denser region around clouds need not be cooler in proportion to the increase in density, and

their relative M-band emissivity further enhanced.

If the clouds obstructing the shock were not compact spheres, but were sheet like and still dense compared with the inter-cloud medium, then in the limiting case the reverse shock would act as a reflected shock, which has a simple analytical solution. Bradley (1962) shows that if the incident shock is strong then the reflected shock will increase the temperature by a factor of 2.4. Weaker shocks will result in a reduced enhancement,

$$T_{s2}/T_s=(5\eta-2)(\eta+2)/(3(4\eta-1)) \qquad 5.19$$

where T_{s2} is the temperature of the gas that has been re-shocked by the reflection. The jump in the density with respect to the ambient density ahead of the primary shock is given by

$$\rho_{s2}/\rho_o=\eta(4\eta-1)/(\eta+2) \qquad 5.20$$

implying a possible density of $10n_o$.

In reality these maximum values will not be attained since the perfect reflection will not take place, the clouds not having a precisely defined boundary and infinite density. Neither will the clouds present a flat surface to the incident shock, and thus gas will tend to flow around the leading clouds. This, however, may still provide additional local heating. Whilst the clouds were considered isolated spheres the shock would simply join itself after passing around the sides of the cloud. Now,

however, with the clouds assumed to be grouped into the aforementioned filamentary sheets there will be a tendency for the primary shock to be focussed into the gaps between clouds. This leads to the possibility of shock-shock interactions. With two identical shocks approaching head on the effect would be equivalent to a perfect reflection, and equations 5.19 and 5.20 would apply.

From the above it would appear possible that a great deal of emission can arise from the interaction of the shock with an organised cloud formation. It is possible that the temperature of the region may not be greatly different from that which would result from the shock heating of the inter-cloud medium alone, but the resultant greater density leads to a much higher volume emissivity. However, the temperature may be enhanced or reduced with respect to the inter-cloud gas, depending on the ratio of the densities of the gas evaporated from the edge of the cloud to that of the inter-cloud medium, and the quantity of extra energy that is liberated as heat in turbulent shocks.

5.3.5.8 Loop IV and the Re-heating of the NPS -

The X-ray ridge associated with Loop I continues north into the region of sky occupied by Loop IV. Here the origin of the x-rays becomes ambiguous, either one or both of the loops contributing. At $l=330°$, $b=70°$, the ridge turns sharply south, towards the centre of Loop IV.

This may indicate that much of the emission is due to the presence of the smaller loop. The x-ray spectrum also changes from that of the main ridge. This region forms the brightest J-band emission seen anywhere in the sky away from the galactic plane, and some 2-6keV x-rays are also prominent. Although the location of this region and its low medium band intensity makes estimates of the intensity of the enhancement seen in each band even more difficult than for the main ridge, the emission in the I, J and 2-6keV bands suggest a temperature component in the range of 10^7 to 3.10^7K. However, there is also some M-band emission, which is not compatible with such a high temperature, and requires a second cooler component. On the assumption of a temperature of 2.10^7K for the source of the high energy x-rays an emission measure of $0.004 cm^{-6} pc$ is required. It is not possible to model this emission in the same manner as was done for Loop I since it does not form a discernible 'concentric' ridge with Loop IV, the brightest emission coming from the centre of the loop. The temperature suggests a shock velocity of order $1000 km.s^{-1}$, and age of under 8000yrs and a radius of only 68pc (assuming $E_o = 10^{51}$ ergs and $n_o = 0.0035$). This would put Loop IV at the lower limit of sizes suggested by table 1.1.

Loop IV has been suggested as a possible candidate for the re-heating of the Loop I cavity (Iwan, 1980), the latter having been excavated by a previous supernova event. Although the H_I shell beyond the NPS indicates

that there may well have been some previous event, the asymmetry of Loop I is not best explained by an explosion at the site of Loop IV. Both radio and x-ray emission indicate that the greatest energy input is in the region closest to the plane. Assuming that the Loop I emission comes from the tangential points on the sphere defined in table 1.1, and that the site of the Loop IV progenitor is also as given in the same table, then in order that Loop IV be responsible for the NPS the emission at l=30°, b=20° and at l=30°, b=60° would require a shock travelling 210 and 187pc respectively. Thus the shock which had traveled the furthest (slightly) would be responsible for by far the greatest activity. Also, the distances travelled are very large compared to the deduced Loop IV radius of 105pc. This can be partly accommodated by the fact that the shock within the cavity will have traveled faster due to the gas here being hotter and less dense than that outside. However, it would seem unlikely for twice the distance to have been covered, especially since Loop IV will have evolved to 25pc in size before encountering the edge of Loop I and will then have had to fight its way through whatever remains of a shell existed.

If Loop IV were only the 68pc across, as suggested above, then it would be easier to transport the blast energy to the observed x-ray and radio NPS since the distance would now be much reduced and the shock travelling in this direction would have evolved entirely within the cavity of Loop I. However, the distance to the

aforementioned regions of the NPS would now be 134 and 109pc. The relative differences between the two distances is now more discrepant with the observed intensity distribution.

There is also a problem with the distribution of the x-rays elsewhere within the Loop I cavity. As mentioned earlier, this more extended emission is concentrated towards the NPS edge of the loop, whereas Loop IV is 10% closer to the corresponding tangential point of Loop I at l=270°, b=20°, or 17% closer if Loop IV is only 68pc in radius.

Another indication that Loop IV may not be a suitable candidate for the re-activating of the NPS is contained in the details of the fine structure seen in the radio emission. Some of the narrow sub-arcs above b=40° have a greater curvature than the main spur. Their southern ends are within the NPS but their northern ends come in towards the centre of the loop (figure 4.3h). They would appear to indicate that the blast wave responsible discernibly travels from the lower latitudes towards the higher. Sub-shocks emanating from the direction of Loop IV would be traveling towards the galactic plane, albeit slightly. Although all this does not entirely rule out a model similar to that of Iwan(1980), we prefer to believe that any re-heating event of an old cavity has a different origin.

If the radio sub-arcs do indicate shocks moving in a direction perpendicular to the line of each arc then their inclination tends to suggest that some of the gas in the region of the NPS is not moving perpendicular to the main spur. The numerical analysis of Chevalier and Gardner (1974) indicates that for an ISM where density decreases with z, the centre of a still near spherical remnant may reside at a greater height above the galactic plane than the site of the progenitor star. In such a situation the gas velocity vectors will tend point slightly towards higher latitudes than does the plane of the shock. The sub-arcs could then still be explained by a single supernova explosion. However, it may simply indicate that the site of a re-heating explosion lies not at the centre of the Loop (l=329°, b=17.5°) but at a slightly lower latitude and/or greater longitude.

5.3.5.9 Sco-Cen Association -

The group of stars that form the Sco-Cen association lies in the same region of sky as Loop I. Forming part of Gould's Belt, the association extends from l=300°, b=10° to l=360°, b=20° in a band roughly 10° wide. Figure 5.22 gives a plot of all the stars in the hemisphere of Loop I of spectral classification B3 or earlier, within a distance range of 50 to 300pc from the Sun. Data for the figure was taken from the Combined Astronomic Catalogue prepared by the Royal Greenwich Observatory, and available on the UK Starlink computer, of stars in the SAO and AGK3

stellar catalogues. Distances to the stars were calculated on the assumption that they were main sequence dwarfs with the Luminosity-Class relation given in Allen (1973, p200) and $5\log(d\ (pc))=m_v-M_v+5$. Blaauw (1964) gives the distance to Sco-Cen as 170pc, ie. 40pc beyond the quoted Loop I centre (table 1.1) but well within its quoted uncertainty. Stellar winds from the Sco-Cen association have been proposed as the driving force behind the excavation of a cavity and the formation of the H_I shell, prior to a single supernova event that is responsible for Loop I. However, it is possible that the association could provide the site for the explosion of the proposed supernova explosion.

We thought that it might be possible to compare the spectrum of the observed spectral classification with an assumed initial mass function (Rana and Wilkinson, 1987, and references therein). There are, however, several difficulties. Firstly, the number of stars involved makes statistics poor. Secondly, there is considerable uncertainty in the initial mass function (IMF) at the high mass end, though most authors (Rana and Wilkinson, 1987) give similar number density gradients with respect to mass. Finally, the IMF is derived as a galactic average, and there is every reason to assume that the mass distribution of stars forming in a single region can vary widely from one region to another.

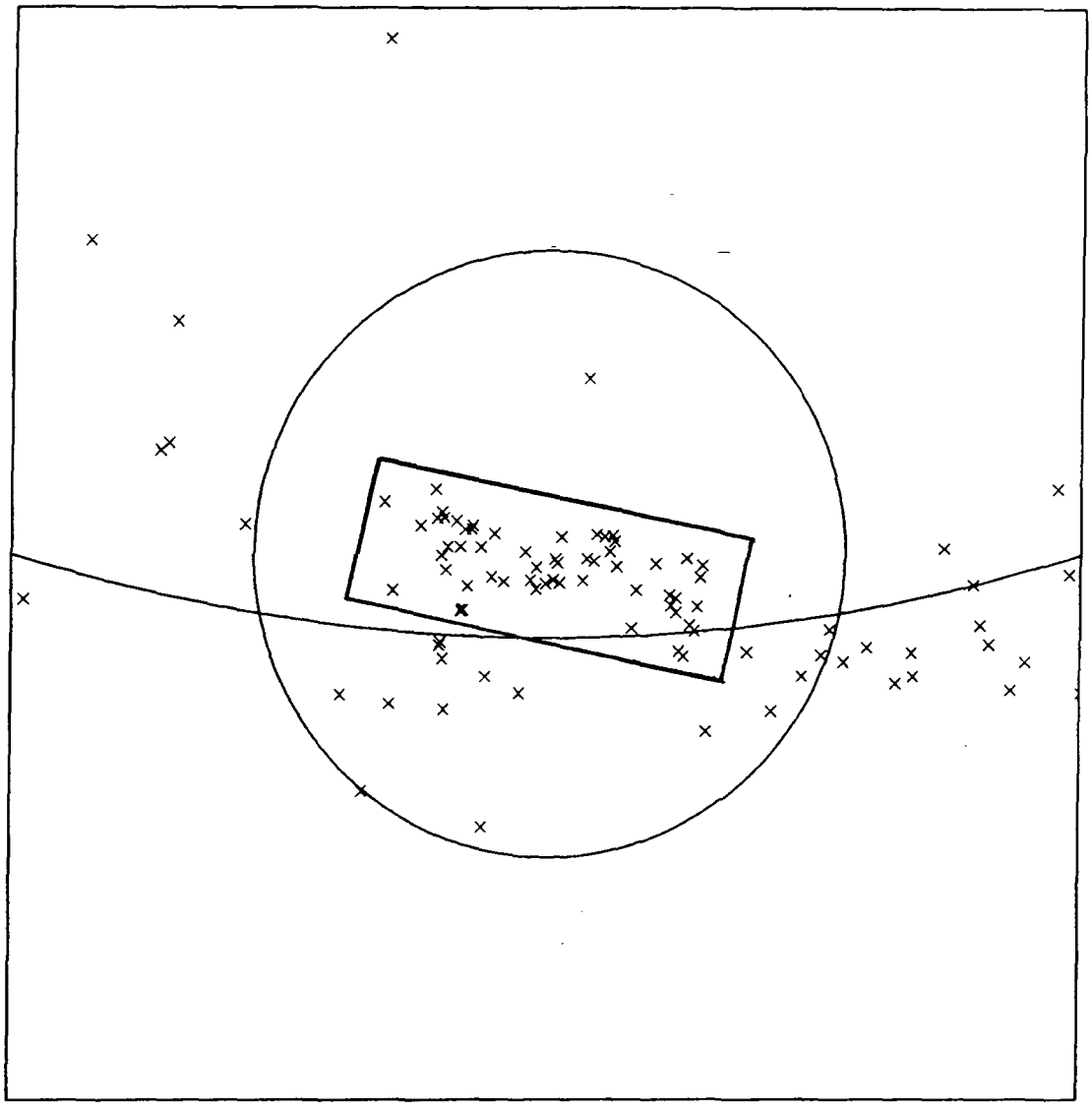

Figure 5.22 Stars of Spectral type B3 and earlier between 50pc and 300pc distant.

Blaauw (1964) gives the age of Sco-Cen to be between 10 and 20 million years, with the associated runaway star, ζ Oph, having a kinematic age with respect to Sco-Cen of 1 million years. The kinematic age of the group of stars may not directly correspond to the age of the individual stars, which may not even have formed at the same time (Wilkinson, 1987), but it should at least provide a reasonable guide to their ages. Table 5.9 gives the number of stars by spectral type in the direction of the main Sco-Cen region, ie. all the stars within the box in figure 5.22. Also given is an estimate of the expected life-times for such stars. The lifetimes are arrived at from the relation of Spectral-Class/Stellar-Mass (Allen, 1973, p209) and the relation between Stellar-Mass and Life-times (Miller and Scalo, 1979).

CLASS	NUMBER OF STARS	LIFETIME (Myr)
O9	0	5.6
B0	3	6.8
B1	6	8.4
B2	9	11
B3	37	16

Table 5.9. The number of stars of a given spectral type in the Sco-Cen association (defined by the box in figure 5.22).

Even if the stars have ages towards the lower age estimate for the association (Blaauw 1964) it is probable that one or more stars within the region have ended their lives and are no longer visible. If Sco-Cen is responsible for the Loop I progenitor(s) then the size estimated by Berkhuijsen (1973) is likely to be a lower limit, the near edge of the association being ~130pc away (Sco-Cen being ~80pc across).

The case against there having been multiple supernovae in the same volume of space is the estimated rate of such events occurring throughout the galaxy. The probability being that sufficient time will pass between supernovae in the same volume of space for the debris of an earlier SNR to have dispersed before the occurrence of the next supernova. The grouping of many young stars in the same volume, possibly all with similar ages, increases the probability of repeated Supernovae. McCray and Kaftos (1987) considers the case for repeated supernovae from associations, and concludes that for a typical IMF an association can inject energy into a 'super-shell' at a roughly constant rate for 5.10^7yrs. Evidence for this hypothesis comes from the number of large H_I shells seen throughout the galaxy (Heiles; 1979, 1984) , with radii between 100 an 1000pc, and the lack of observable SNR in comparison to the formation rate of pulsars. If associations form with about 20 would-be supernovae, McCray argues that only around 5% of of them will explode into a relatively dense ISM (n_o~$1cm^{-3}$). The remainder

evolve in a pre-existing low density cavity, thus having very low surface brightness and escaping detection. Could it be that Loop I is a very local example of this, with a radius of around 170pc?

By contrast to Loop I, Loop III shows no substantial number of young stars in its vicinity, and those that are, are generally close to, and south of, the galactic plane.

5.3.5.10 Dust and Loop I -

Although it is not the dust we are primarily interested in, but the associated gas, we make use here of the high resolution observations available from the IRAS survey. Figure 4.8 establishes the good correlation between the high latitude diffuse H_I and the IRAS 100μm maps. Verschuur (1974a,b) has studied regions of the NPS H_I (each about 100 square degrees) with resolution of 10arcmins, and the IRAS 100μm data shows a good detailed correlation here.

We had hoped to be able establish two results. The first was to be able to show whether or not the dust in the H_I NPS showed any sign of additional heating, either due to interaction with the supposed shock front had it advanced so far, or with an enhanced radiation field due to the proximity of the x-ray emitting shell. Secondly, the high resolution of the 100μm 'plates' might give better information as to the distance to the H_I shell. Absorbtion and polarization measurements of stars might

give improved results if the data-set was reduced to only those stars that were directly in line with brighter emission from the filamentary structure. Distant stars that had dust-free lines of sight would have previously confused the results.

The temperature of the dust can be calculated from the 60μm to 100μm intensity ratio (figure 4.9) once background sources have been subtracted. Unfortunately the low emission of the Infra-red emission in this shell made such a determination difficult, the 60μm intensity being only ~10% of the background subtracted. On top of this, the severe striping of the data due to the scanning of the satellite meant that it was not possible to get a good 'picture' of the entire region. Where reasonable 60/100μm ratios existed the temperature was not discrepant with that deduced generally for the high latitude dust. Any prior thoughts that a temperature difference might be detectable between the inner and outer edges of the dust (gas) shell could not be examined.

In fact, we would not really have expected to see any significant change in the dust temperature. In the previous sections we have made it clear that we do not believe the blast wave to have penetrated this region, and thus the gas here should not yet have been shock heated. Also, the increased radiation flux due to the proximity of the x-ray emitting shell is small in comparison to the general Interstellar Radiation Field (ISRF). The M-band

ridge suggests emission of order 10^{35} ergs.s^{-1}. If we assume the ridge as seen by the H_I shell to be approximated by a sheet 50*50pc^2

then the enhanced energy density is only ~4.10^{-6} ergs.s^{-1}cm^{-2}, well below the value for the ISRF. Mathis, Mezger and Panagia (1983) give the local ISRF as $2.7.10^{-2}$ ergs.s^{-1}cm^{-2}. For large grains this enhancement to the radiation field would not be significant, but with current theory now suggesting that the grain size spectrum continues down to polyatomic sizes (Draine and Anderson, 1985; Mathis, Rumpl and Nordsieck, 1977) the effects of single high energy photons or electrons on individual grains becomes important. The small grains being intermittently raised to high temperatures for short periods before cooling rapidly. A small mass fraction of the dust may thus be disproportionately influential on the detected temperature (Dêrert, Boulonger and Shore, 1986; Dweck, 1986). Eventually, the IRAS data should be available in a de-striped form, and the region could be re-examined for temperature variations.

Using the IRAS data to help clarify the distance to the H_I shell appeared a better prospect since only the 100μm band, where the diffuse clouds are proportionally brighter than in the 60μm band, needed to be used. An initial attempt was made using the Starlink on line stellar data-base. Information on spectral type and the B

and V magnitudes was available. It was thus possible to deduce a distance to each star and an E_{B-V}, on the assumption that all stars were main sequence. Expected values of main sequence absolute magnitudes and B-V colour temperatures were obtained from Allen (1973). Clearly, many non main sequence stars would confuse the data, but it was hoped that the majority of stars would highlight any trend. Unfortunately, the low absorbtion at high latitudes is insufficient to overcome the error due to uncertainties in the stellar type and the poor accuracy of the B and V magnitudes given in the catalogue. The deduced E_{B-V} showed predominantly only scatter about $E_{B-V}=0$. It was, therefore, not possible to obtain any relationship without use of a more accurate data-base, and this approach was not pursued further.

Dust also manifests itself in the presence of a magnetic field by the polarization of starlight. This method was used by Bingham (1967). He concluded that stars closer than 70pc did not show polarization parallel to the NPS, whereas those beyond 90pc clearly had this as a preferred direction of polarization. He thus placed the NPS at 110±20pc. Seymour (1969), using a sample of 500 stars concluded that those in the direction of the NPS only showed that the NPS was between 0 and 110pc. Axon and Ellis (1976) have produced a catalogue of stellar polarizations of over 5000 stars, combining the results of a number of observers. In order that the catalogue should not contain too many spurious stars they chose only those

stars with reliable distance estimates, taking account of stellar absorbtion. This data-base shows that many stars closer than the 70pc suggested by Bingham (1967) show signs of polarization parallel to the NPS. In figure 5.23 we reproduce part of that data-set (80-200 pc) in the form of the stereographic projection used previously (figure 4.4). The polarization vectors are clearly aligned with the edge of Loop I.

Figure 5.24 shows the polarization with respect to 100μm intensity for stars more distant than 100pc, and figure 5.25 gives the relationship of polarization with distance in the direction of the NPS. The 100μm intensities were taken from the IRAS 'sky-plates', each 16.5x16.5 degrees square. Plates 60-66 are centred on δ=30° and plates 84-90 on δ15°, each sequence running from RA=13hrs to RA=19hrs. The method of background subtraction was the simple fitting of an inclined plane of intensity across each plate. Where a 'Lune-band' occurred this procedure was repeated either side of the discontinuity.

There is just a hint in figure 5.25 of a slight jump in the magnitude of the polarization at a little under 100pc. With the exception of one star, there are no stars below 0.05% polarization beyond 100pc, and only 7 stars closer than 50pc have greater than 0.06% polarization. By careful selection of only those stars with lines of sight coincident with the 100μm filaments it was hoped to be

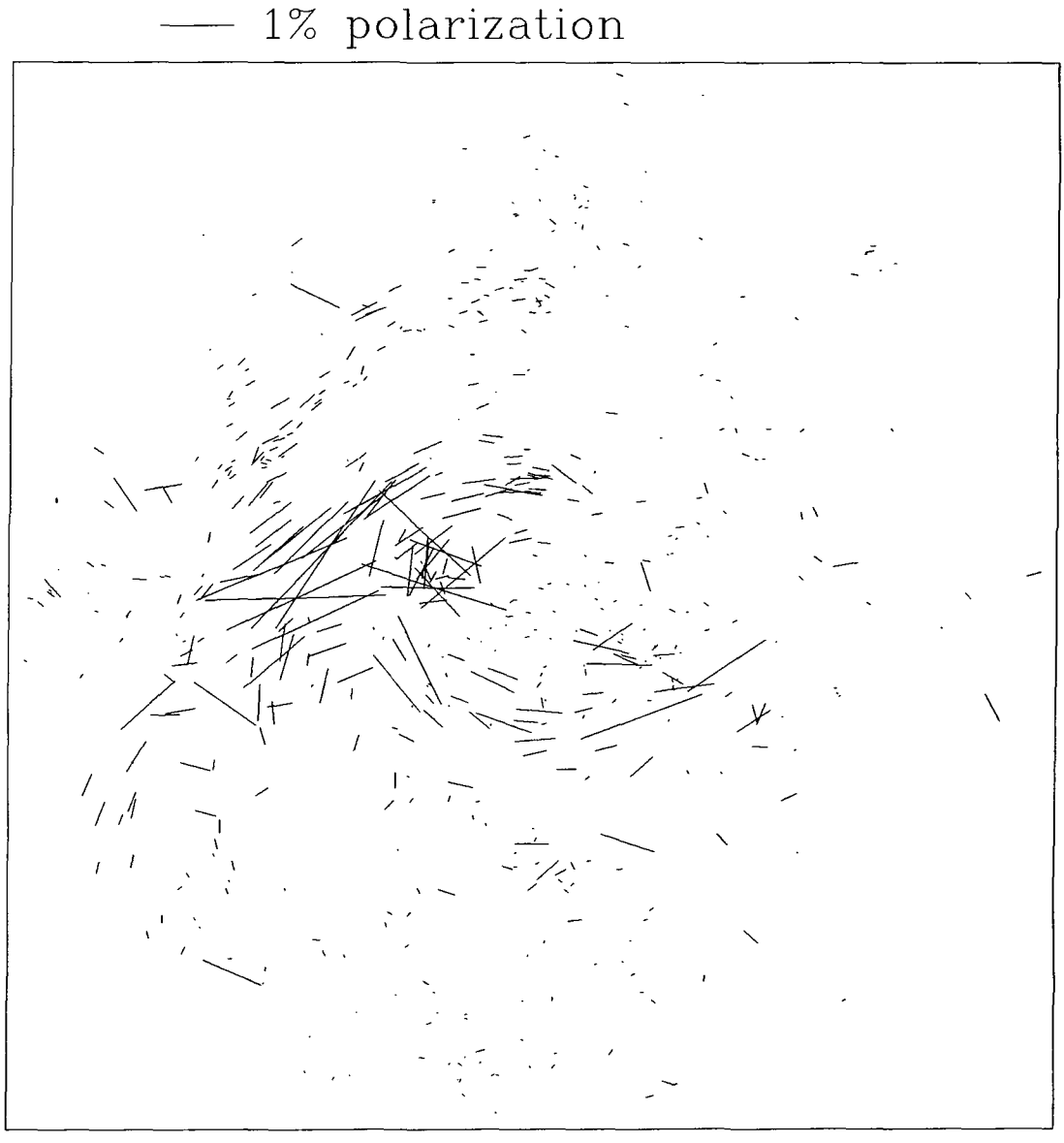

Figure 5.23 Polararization of stars between 80 & 200pc from the Sun in the direction of Loop I.

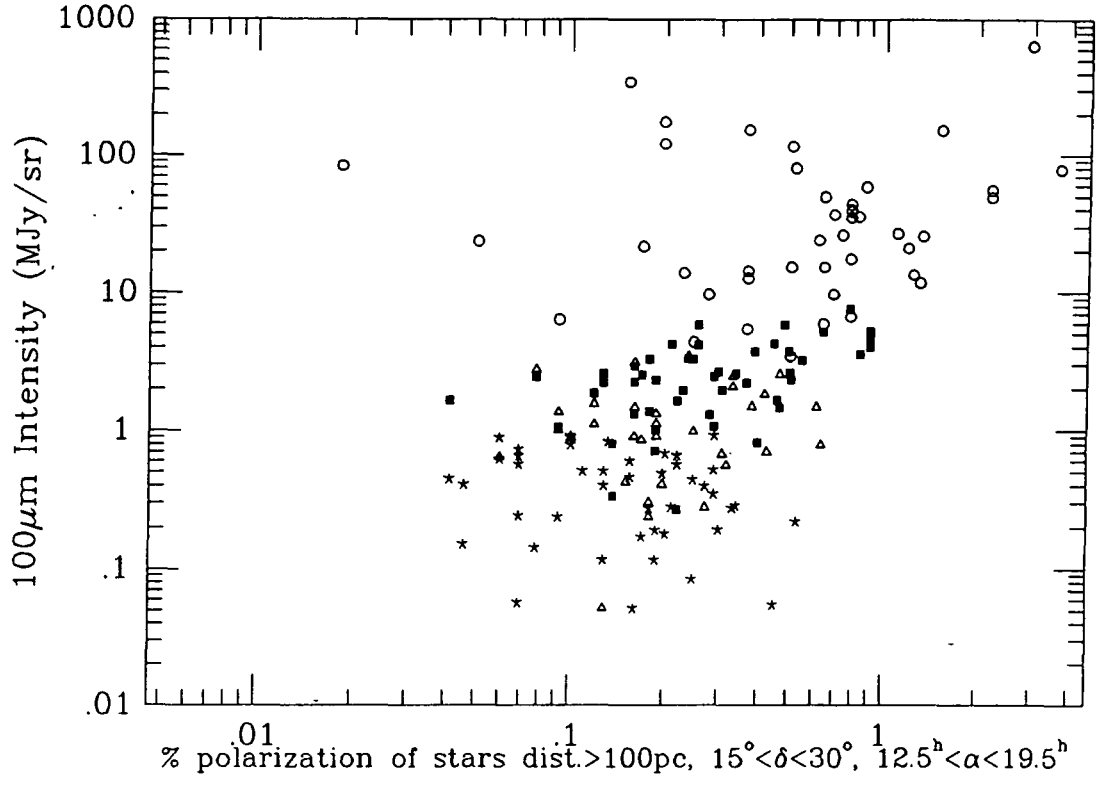

Figure 5.24

IRAS plate No.

★	60, 61, 84, 85
△	62, 63, 86, 87
■	64, 65, 88, 89
○	66, 90

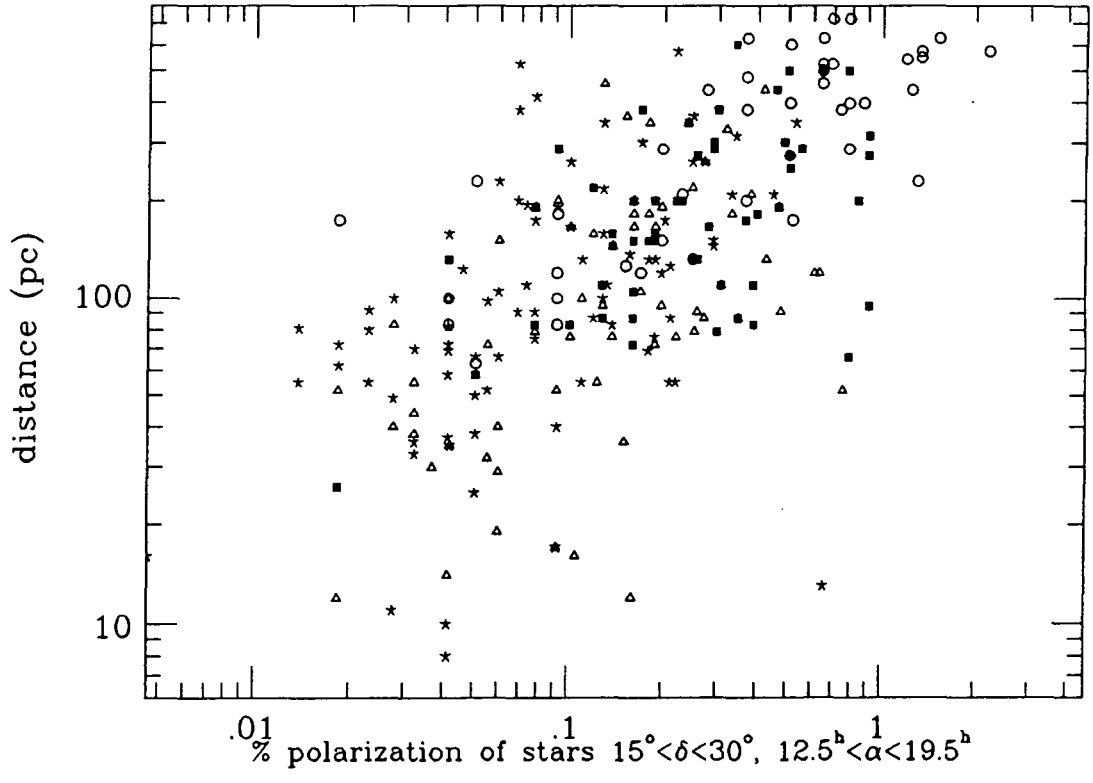

Figure 5.25

able to highlight any such jump in polarization that did exist. At first glance figure 5.24 shows a reasonable correlation between the 100μm intensities and polarization, and the above arguments would appear to be justified. However, closer examination reveals that this trend is almost exclusively a latitude dependence, both polarization and 100μm intensity increasing towards the galactic plane. It was thus not possible to 'improve' the polarization-distance plot via selection of the stars used, the lack of any genuine correlation being the downfall of the method.

An explanation for the failure of the method may come from Davis and Greenstein (1951). They describe a distribution parameter F,

$$F=1/3-\langle\cos^2\phi\rangle \qquad 5.21$$

where ϕ is the angle between the axis of symmetry of a prolate or oblate spheroid and that of the aligning magnetic field, and $\langle\cos^2\phi\rangle$ is the mean value for all grains. For a prolate spheroid they predict

$$F=6.3\times10^{6}B^2/(a.n_H T_d\sqrt{T_g}) \qquad 5.23$$

with F→1/3 for large B, implying the grains are fully aligned. B (μG) is the magnetic field strength, a (μm) is the mean grain radius, n_H (cm^{-3}) is the gas density, and T_g and T_d are the temperatures of the gas and dust. The amount of polarization is clearly dependent on the degree of alignment of the grains and the column

density of the absorbing region. If the latter is increased by having a large line of sight distance through a cloud then enhanced polarization might be expected. If the increase is due to increased dust density within clouds, without any enhancement in the magnetic field, then a constant gas-dust ratio would imply n_H in the [illegible]inator of equation 5.22 would increase [illegible]tionally, and the amount of collisional dealignment would increase. A possible explanation for the H_I is that it forms a uniform density spherical shell, and the filaments are simply caused by small scale ripples in the shell causing some regions to be seen edge on. If that were the case, and the preferred direction of polarization was exclusively due to the region of enhanced H_I then the [illegible]nts would have been expected to corelate with the polarization. The apparent lack of polarization-dust correlation could therefore well imply that the filaments are, at least in part, regions of greater physical density. [illegible]er than merely enhanced projected column densit[illegible]g the temperature of the dust and gas [illegible]fected by the increased density (the clouds are too thin for self shielding from the ISRF) then this implies no increase in the magnetic field to accompany the increased density.

Although noting that there may be a hint of increased polarization between 50 and 100pc from the Sun, we conclude that it has not been possible to be more precise than Seymour (1969), ie. the H_I lies somewhere within

110pc of the Sun.

We have attributed the polarization to the dust in the H_I shell, outside the NPS. This, therefore, does not necessarily have any bearing on the distance of the radio or x-ray emission, unless (as has been implied by some of the suggested models above) there is a physical relationship, the H_I shell influencing the formation of the NPS.

CHAPTER 6

OTHER GALACTIC REMNANTS

6.1 INTRODUCTION

In this chapter we will briefly examine observations of other SNR, and make comparisons between these and the observations of Loops I and III discussed in the previous chapters. Attention is paid to the general relationship between the gas distribution in and around the remnant and the relative position of the synchrotron emission. For a few large SNR where observations have been made at more than two radio frequencies the spectrum is compared to that of Loop III.

In a search for a radio object to identify with a known gamma-ray source a new SNR was discovered, and in and attempt to find x-ray evidence for the gamma-ray source (from the SNR or otherwise), low energy EXOSAT x-ray images of the same region were studied. We present here the results of this study, and the relationship between the gas and the radio emission from this object is also discussed.

6.2 COS-B SOURCE 2CG342-02

6.2.1 Introduction

The second COS-B catalogue (Swanenburg et al., 1981) contains a list of 25 γ-ray sources, only 4 of which have been confidently identified with a known object. Of the remaining 21 sources this one has appeared to be of interest for the following reasons, and we therefore considered this the most worthy of investigation at radio wavelengths, and at x-ray energies by EXOSAT.

The Einstein satellite has already looked for x-ray counterparts to 11 of the 21 sources. Several possible candidates have been discovered for some, but due to their proximity to the over-crowded galactic plane no positive identifications have been made. Of the remainder, 2CG342-02 is the second furthest away from the galactic plane, thus reducing the chances of ambiguous sources. Apart from those in complex regions, only one other COS-B source has strong radio emission from within the error circle.

The region was examined at 843MHz with a resolution of ~1arcmin using the Molonglo Observatory Synthesis Telescope (MOST). The shell of an apparent SNR 31arcmins in diameter was detected, and also several small sources, the brightest of which lies close to the centre of the remnant.

A study of a short observation made with the imaging low energy (0.03-2.0keV) experiment on EXOSAT showed that there was no sign of any soft x-ray emission coming from any of the sources seen on the MOST map.

6.2.2 Previous Data from the Region

Between August 1975 and December 1978, COS-B observed 2CG342-02 (RA=$17^h 04^m 36^s$, $\delta=-44° 28'$) on 5 occasions, the flux above 100MeV being 2.10^{-6} photons.$cm^{-2}s^{-1}$ if an E^{-2} photon spectrum is assumed. This was one of 25 sources detected, only 4 of which have been identified: Crab and Vela pulsars, the ρ Oph cloud and the quasar 3C273.

Strong radio emission has been detected at several frequencies within the 1° radius error circle of 2CG342-02. These detections, are shown in figure 6.1 and are listed in table 6.1.

Hill et al. (1968) have mapped this region at 1410MHz to a 14arcmin resolution with the Parkes 64m telescope. This shows an extended region of enhancement within the error circle, and this is the map reproduced in figure 6.1. A map made at 2300MHz has been supplied by A. Greybe (Jonas et al., 1985) This was made with the 26m telescope at Hartebeesthoek Observatory, R.S.A. with a 20arcmin resolution, and also shows a similar enhancement. Both maps suggest fluxes comparable with those in table 6.1, and the positions are compatible with MSH17-401 and KOM43.

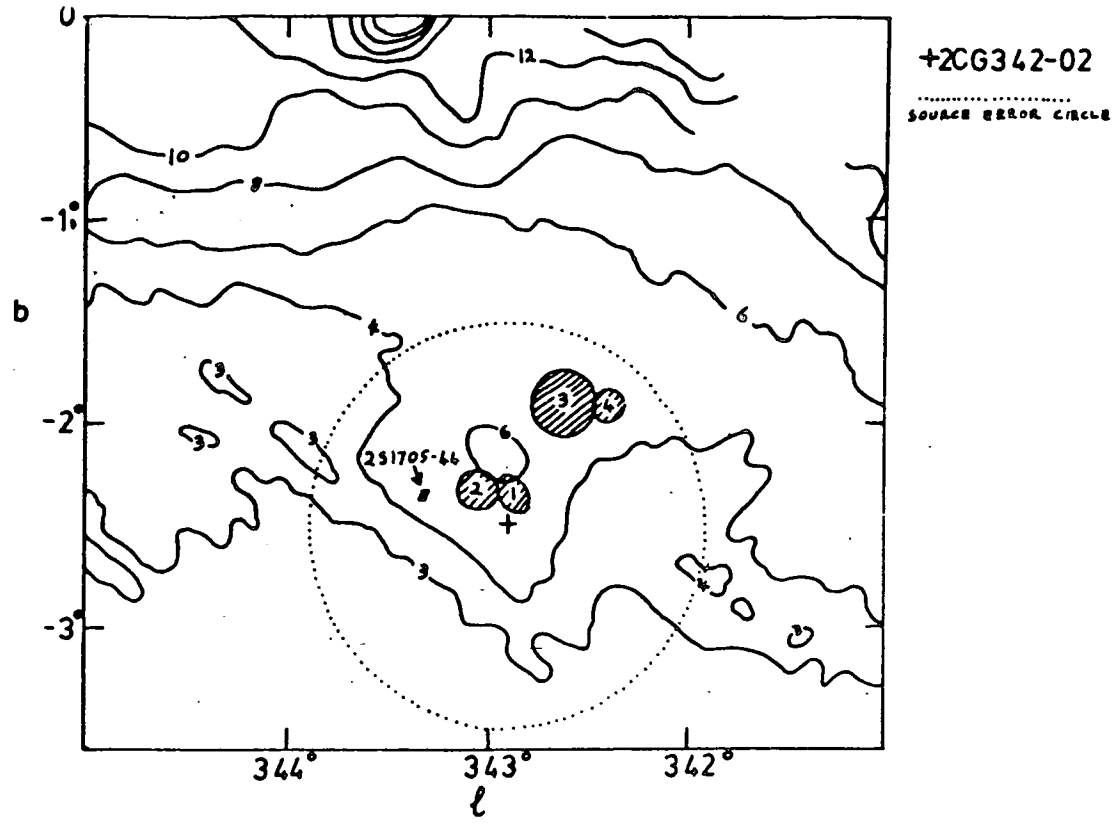

Figure 6.1 1410MHz map of Hill et al. Contours are in K. Sources in table 6.1 are shown.

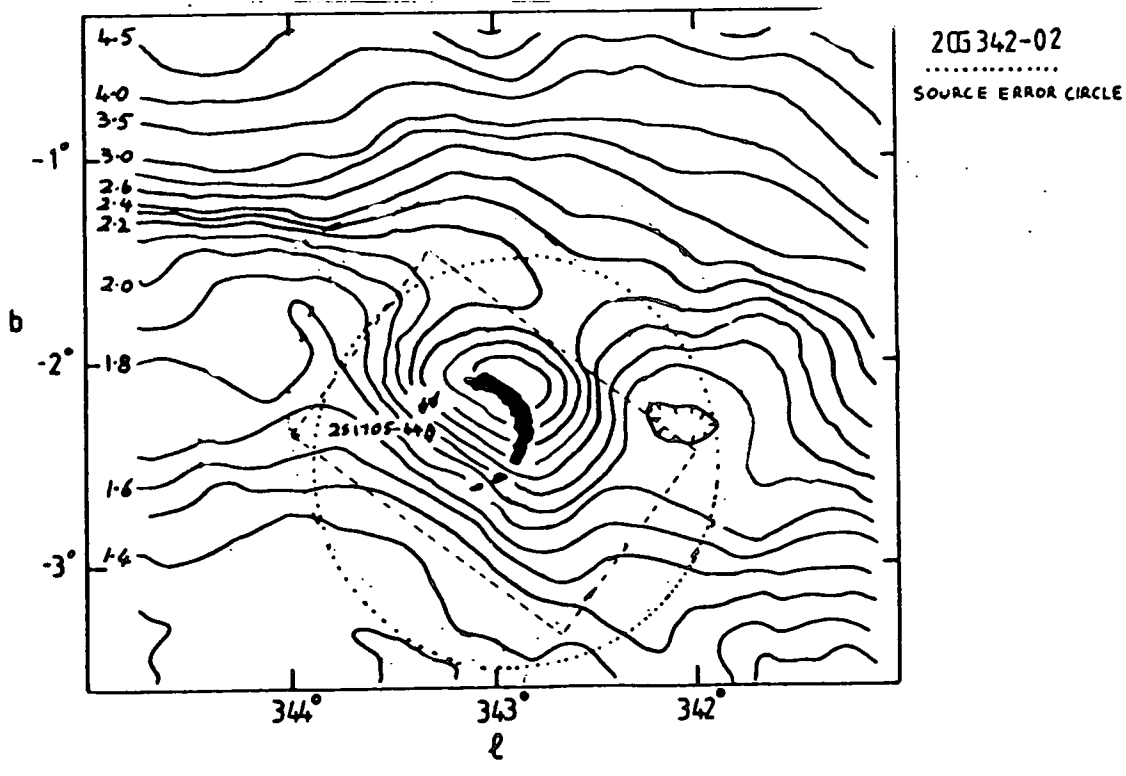

Figure 6.2 2300MHz map of Greybe. Contours are in Kelvin. The COS-B error circle, the field of view of figure 6.3 and a sketch of the MOST SNR are also shown.

	source name	frequency MHz	flux Jy	RA h m s	dec ° ′
1	MSH17-401	85	25	17 03 48	-44 24
2	KOM43	408	45	17 04 20	-44 14
3	CTB36	960	30	17 01 00	-44 20
4	MHR59	1440	15	17 00 30	-44 32

Table 6.1

Previously detected strong radio sources in the vicinity of 2CG342-02.

None of the 4 surveys listed in table 6.1, nor the two maps shown in figures 6.1 and 6.2 have detected two separate sources from this region. Such is the strength of the sources and the uncomplicated nature of the radio sky at this co-ordinate that is is unlikely that a source can have been missed. Therefore, although CTB36 and MHR59 have positions discrepant with respect to the other sources in excess of their quoted errors, it appears likely that all these source are the same one, and that this lies close to $17^h 04^m$, $-44° 20'$.

6.2.3 The MOST Observations

A 70arcmin by 100arcmin field centred on $17^h 04^m 30^s$, $-44° 06' 00"$ was covered by B. McAdam at the request of J.L.Osborne. The resultant map is shown in figure 6.3. This reveals the shell of a SNR, detectable almost continuously over a semi-circle centred on $17^h 04^m 34^s$, $-44° 13' 00"$. There is no evidence of emission from the opposite half circle. The arc reaches its brightest at

$17^h 03^m 22^s$, -44° 06' 30", its closest point to the galactic plane. This point is coincident with the expected radio source, but the total flux from the shell is estimated at only 0.95Jy. From table 6.1 we would have expected to see around 30Jy.

The surface brightness-Diameter (Σ-D) relationship of Clark and Caswell (1976) is given by $\Sigma_{408}=10^{-15}D^{-3}$ and $\Sigma_{408}=3.6.10^{-5}D^{-10}$ for surface brightness at 408Mhz (Σ_{408}) respectively above and below 3.20^{-20} $W.m^{-2}Hz^{-1}sr^{-1}$, The diameter, D, is in parsecs. Assuming an intensity spectral index of α=0.5, a flux of 0.95Jy at 843MHz and an angular diameter of 31arcmins gives $\Sigma_{408}=2.1.10^{-22}$ $W.m^{-2}Hz^{-1}sr^{-1}$. This yields a diameter of D=53pc and a distance of 6.1pc. Caswell and Lerche (1979) modified this relationship to include a z-dependence. At galactic latitude -2.43° this remnant is some considerable distance below the galactic plane, and the z dependence should perhaps be considered. Caswell and Lerche give $\Sigma_{408}=10^{-15}D^{-3}\exp(-|z|/175)$. This yields a diameter of D=80pc, and a location 9.2kpc from the Sun, 400pc below the plane of the galaxy. There have been more recent Σ-D calibrations, but at this point we shall take Caswell and Lerche (1979) and Clark and Caswell (1976) as the standard texts, and use the former as an upper limit to the distance. In the next section the question of the reliability of such a relationship will be briefly examined using the more recent works.

For a standard supernova of explosive energy 10^{51} ergs in a McKee and Ostriker (1977) hot phase density of $3.5.10^{-3}$, a Sedov model would suggest a moderately old remnant of under 4.10^{4} yrs. If at 6.1pc this would be about 3000 years old.

There are numerous small sources scattered around figure 6.3, and there is a suggestion that the brightest part of the shell may in fact be due to a superposition of such a source. One of these sources is much stronger than the others, peaking at 274mJy in the MOST beam. It is possibly just resolved, but its total flux is no more than 315mJy. Its location, $17^h 04^m 52^s$, $-44° 14' 30"$, is quite interesting in that it is near to the centre of the SNR. With so many small sources nearby this is quite possibly a positional coincidence. All the other small sources contribute less than 0.2Jy between them. Clearly, 1.5Jy in the entire field is and order of magnitude less than we would have expected if the source or sources responsible for the previous radio detections were within the observed field.

The absence of a 30Jy source may be due to the previous detections being of a strongly variable object that happened to be in a quiet state when this observation was made. This might explain the very peaked spectrum suggested by table 6.1, but as so many surveys have caught the source in its on state it might be considered more than coincidence that it should be in its off state when

we tried specifically to observe it. An alternative is that the source was in the field during the observation, but that it is a large region of very smoothly varying intensity and is invisible to such a high resolution array.

Up to this point we have assumed that it is the co-ordinates of CTB36 and MHR59 that are in error, and although we still believe this to be probable, we note that the quoted positions lie outside the area covered by figure 6.3. The short-fall in the detected flux makes it worthwhile mapping this adjacent field to the same high resolution. The whole of the COS-B error circle will not have been covered by this and the already observed field, but there appears to be no evidence of radio sources from within the remaining unobserved areas.

6.2.4 The EXOSAT Observation

The results from the MOST map meant two areas were of particular interest to us, the SNR shell; especially its brightest point, and the brightest small source near to its centre. It had been hoped that we would be allocated some observing time on EXOSAT in order to look for an x-ray counterpart to 2CG342-02, using the satellite's low energy imaging experiment. Although unable to do so, we are fortunate in that a short preliminary observation of the nearby galactic bulge source 2S1705-440 had been made during the setting up and testing of the satellite. The

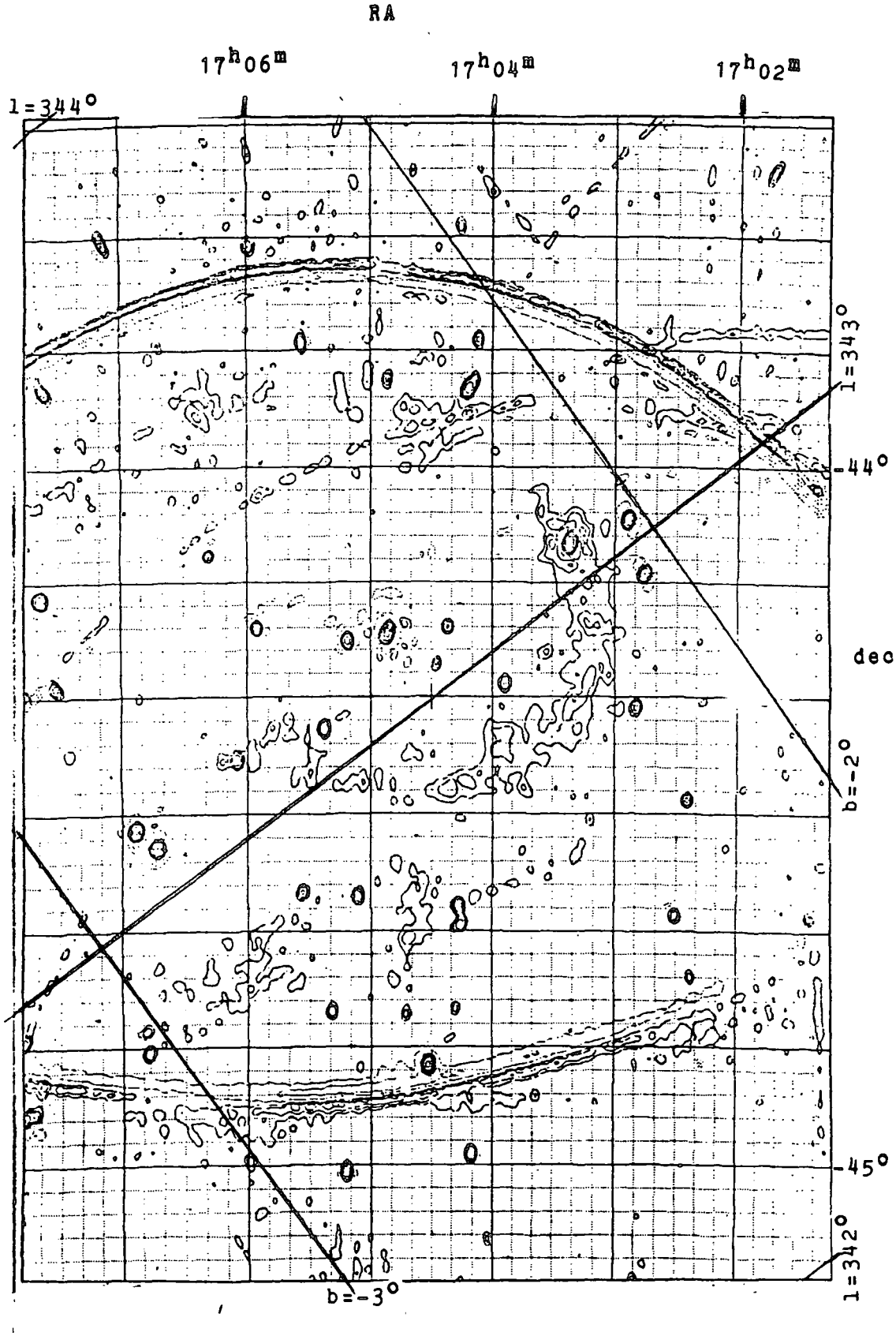

Figure 6.3 Uncleaned MOST 843MHz map. The lowest contours on the SNR are 3 and 6mJy

soft x-ray data from this experiment was made available to us by J. Heise. The experiment's 2.2° field of view included the entire remnant.

There were 4 usable observations. Two with the thin polypropylene filter totaling 9000seconds; one with aluminium/paraline, 6000seconds; and one with the boron filter, 12000seconds. The bulge source was clearly visible on all the images, but there appeared to be nothing that could be connected with anything seen in figure 6.3. The only other features on the x-ray images were of early type stars seen with the polypropylene filter, this being the most sensitive to UV contamination. Using these stars, the two points of interest were located on the EXOSAT images to an accuracy of 30arcsecs, ie. 8 of the detector's pixels. A 16'x16' area around each of the areas of interest was studied in detail to look for any hint of an enhancement. Two binnings were used, 15"x15" (4x4 pixels) and 77"x77" (20x20 pixels). The resolution of the detector for the off-axis positions of both potential sources was 50arcsecs. Thus the latter binning was large enough such that all the counts from a point source would fall into one bin.

There was no evidence of 1σ emission with any filter from the bright central source, and no more than 2σ from near the shell. With 5σ required before claiming evidence of detection (EXOSAT OBSERVERS' HANDBOOK) there is clearly no evidence of x-ray emission. Both areas

showed counts per bin distributions compatible with Poisson statistics.

6.2.4.1 A Limit to the X-ray Luminosity. -

As 2CG342-02 was not seen by this EXOSAT observation, it is only possible to put an upper limit to any x-ray emission. Tables given in the EXOSAT observers' handbook show the minimum detectable source strength (5σ) in units of milli-crabs (1 mCrab=$1.2.10^{-12}$ ergs.cm^{-2}s^{-1}) for various exposure times using the thin lexan filter. Of the filters used in the observations, the polypropylene most resembles the response curve of the thin lexan, so as an approximate guide we use these observations with the given tables.

Allowing for a 10% reduction in the sensitivity of the polypropylene filter with respect to to the lexan filter, we estimate that a 0.15mCrab source would have given a reliable detection. This assumes that the source has a Crab like spectrum, ie. E^{-2} photon spectrum, absorbed by 3.10^{21} cm^{-2} of H_I. The total column density in the direction of 2CG342-02 is 8.10^{21} cm^{-2}. Integrating an E^{-1} energy spectrum with this column density across the filter's pass band gives a loss of detected counts by a factor of 3 with respect to the crab column density. The Σ-D estimated distance of 6.1kpc and the appreciable distance from the galactic plane suggest that most of this gas will lie between us and the remnant.

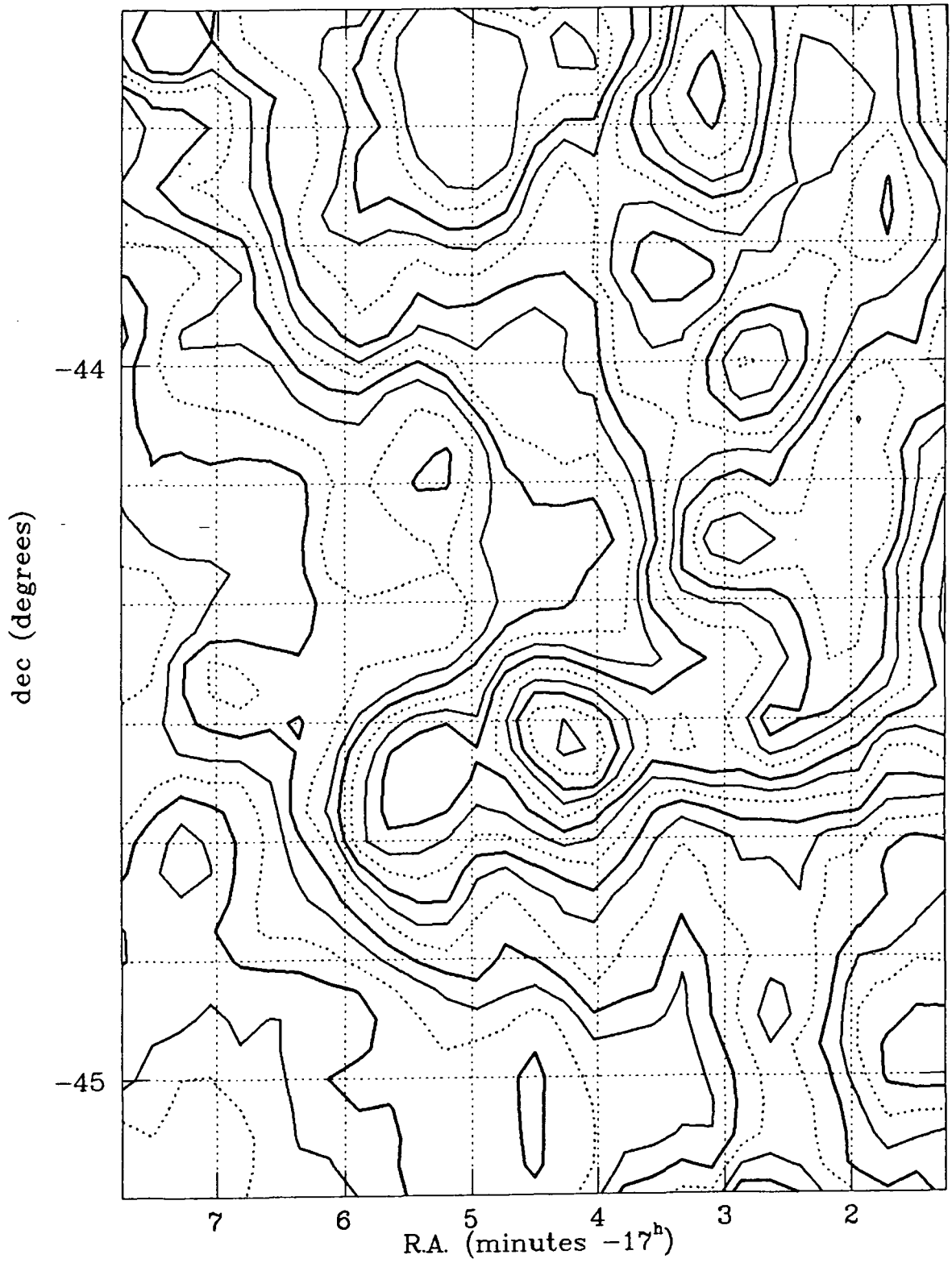

Fig. 6.4 IRAS 100μm (HCON1 uncleaned)

MJy/sr

..... 200, 230, 260, 290, 320, 350

——— 210, 240, 270, 300, 330, 360

——— 220, 250, 280, 310, 340

At three times the distance to the Crab the total luminosity of the x-ray source would have to be $0.0055L_{Crab}$ for a 5σ detection. Given that there is no evidence even at the 2σ level, we estimate the source luminosity to be below $0.002L_{Crab}$, ($L_{Crab}=6.10^{32}$ ergs.s^{-1} in x-rays). The spectrum of the Crab is unusually hard for SNRs. A remnant of the calculated size and age is likely to have a considerably softer spectrum. This will be more severely affected by absorbtion, and thus the actual limit luminosity could be slightly greater.

The luminosity limit suggested above is very small in comparison to that from the Crab, but if the COS-B source were associated with a central object in the remnant any associated x-ray luminosity should be compared to the source strength of the Crab pulsar, which is only 3% of the Crab nebula's luminosity at 1keV. In this context the minimum detectable luminosity is not so insignificant, and it would be feasible that a Crab like γ-ray source could have some associated x-rays that are below the detection limit of the observation.

6.2.5 A Concentric Outer Neutral Gas Shell?

We do not actually have 21cm observations of this region to a sufficiently high resolution, but once again we make use of an assumed approximately constant dust-gas ratio, and examine the IRAS 100μm sky plates covering

this region. A contour map is presented in figure 6.4, no background subtraction having been done. This shows clear evidence of a small ridge of higher 100μm intensity protruding from below the galactic plane. The length of the ridge is of the same order as the size of the remnant, it shows a tendency to be curved in the same sense and to the same degree as the arc of the remnant, and the intensity towards the centre of the remnant is slightly below that of its surroundings. The possibility of a positional coincidence cannot be ruled out, but it is tempting to see the dust distribution as representing a cavity with an outer perimeter shell of higher density gas. The lack of enhancement from the source itself confirms its non thermal nature (Haslam and Osborne, 1987).

Gamma-rays can be produced by the interaction of high-energy cosmic rays with gas. A source is therefore likely to consist either of a region of much enhanced cosmic-ray flux (as is likely for the Crab and Vela pulsars, 2CG184-05 and 2CG263-02), a region of very dense gas (such as the ρ-Oph cloud, 2CG353+16), or combination of both an increased number of cosmic-rays and higher gas densities. The latter is thought by Pollock (1985) to be the case in his probable identification of 2 COS-B sources, 2CG006-00 and 2CG078+01. Within the error circle of each source is a shell type SNR. Each remnant has at its brightest edge a dense cloud of gas with which it appears to be interacting. Synchrotron emission from SNRs

is an indication of the energy and density of cosmic-rays accelerated in the shock and of the strength of their interaction with the magnetic field whilst γ-rays show the strength of their interaction with the gas. Thus, using formula from Stecker (1977), Pollock (1985) gives an equation relating SNR radio flux at 1000MHz to the associated γ-ray flux above 300Mev. Transforming this to the frequency of 843MHz, used in the Molonglo observation of 2CG342-02, assuming an intensity spectral index of α=0.5 gives

$$F_{300}/S_{843} \sim 1.7.10^{-9}\eta^{-0.5}n_o B_o^{1.5} \text{ cm}^{-2}\text{s}^{-1}\text{Jy}^{-1} \quad 6.1$$

F_{300} is the γ-ray flux above 300MeV in $cm^{-2}s^{-1}$, S_{843} is the radio flux at 843MHz in Jy, n_o is the ambient H_I number density in cm^{-3}, and B_o is the ambient magnetic field strength in μG. The compression factor at the shock is represented by η. Pollock shows that for the two COS-B sources he considers and their nearby SNRs, acceptable choices of η, n_o and B_o give a theoretical γ-ray to radio flux ratio compatible with the observations.

The observations of 2CG342-02 and the MOST SNR give $F_{300}/S_{843}=7.6\text{x}10^{-7}\,\text{cm}^{-2}\text{s}^{-1}\text{Jy}^{-1}$. This assumes that the entire SNR shell is equally responsible for the production of γ-rays, whereas Pollock (1985) uses only that part of the radio emission coincident with the densest region of gas. Since, in this instance, the outer shell of gas which the remnant my be impacting upon shows

no region of exceptionally high density it is reasonable to include all the observed radio flux, but to note that this makes the above ratio a lower limit. We also note that the radio and gas ridges are not coincident, but are separated by a few degrees. Since the gas cloud will not have been fully engulfed by the shock its interaction with the remnant's cosmic rays will be much reduced, thus making the ratio and even stronger lower limit.

If we use the relationship between the 100μm intensity and H_I column density to be as given by the gradient of figure 4.8 (ie. $1.4.10^{18}\,cm^{-2}\,MJy^{-1}$), then figure 6.4 suggests $N_H \sim 10^{20}\,cm^{-2}$ for the shell. If at a distance of several kpc the line of sight thickness to the shell must be of the order 100pc, which implies a density enhancement above the surroundings of approximately $1cm^{-3}$. Assuming $n_o = 1cm^{-2}$, $\eta \sim 3$ and $B_o > 3\mu G$, equation 6.1 gives $F_{300}/S_{843} < 2.10^{-10}$ $cm^{-2}\,s^{-1}\,Jy^{-1}$. Thus the observed ratio is a minimum of 4000 times greater than the theoretical ratio. It would therefore appear unlikely that the enhanced cosmic ray density due to the shock and the outer neutral gas shell can account for the observed γ-rays.

6.2.6 Discussion

It is not possible to put forward a confident suggestion for a possible object that may be the source of the 2CG342-02 γ-ray emission.

The EXOSAT observations were unable to show either of the two radio sources as x-ray emitters. This may well be partly due to the high absorbing column density. If the remnant had the normal thermal x-rays of many shell like SNR then a temperature of below $2.5.10^6$K would probably not give a hard enough spectrum to be seen by the satellite. Were there to be a Crab like source then it should have been easily seen despite the absorbtion, even if only that few percent of the x-ray flux directly associated with the central object. If we were to expect some rough correlation between the COS-B γ-ray flux and that of associated x-rays then the object should be very x-ray bright. The γ-ray flux above 100MeV from 2CG342-02 is given (Swanenburg et al., 1981) as 2.10^{-6}photons.cm^{-2}s^{-1}, compared to the Crab, $3.7.10^{-6}$photons.cm^{-2}s^{-1}.

The bulge source 2S1705-440 has not been considered until now. This object is the most thermally energetic within the COS-B error circle, and the only object seen by the low energy experiment other than UV contamination from young stars. It therefore cannot be ruled out as a possible candidate. However, of the 14 bright bulge sources in the 3A catalogue (Warwick et al. 1981) only one, 2S811-171, falls within a γ-ray source error circle. Six of them lie close to the galactic centre were the γ-ray flux distribution is complex and thus sources could be missed, but the remaining seven are without any significant γ-ray flux. There thus appears to be no

evidence for such a source to emit γ-rays. Also, one might expect energetic particles to produce radio emission, and yet 2S1705-440 is totally invisible at 843MHz.

The MOST was unable to locate the expected strong, approximately 30Jy, source we were originally hoping to find, but it did reveal a well evolved SNR with a possible central object. The Crab and Vela pulsars are the central objects of remnants and have been seen by COS-B as strong γ-ray sources. Could this central 315mJy source produce γ-rays via a similar mechanism? If a spectral index of ν^{-1} is assumed for this object and the flux converted to the 400MHz of the pulsar catalogue of Taylor and Manchester (1975) it is seen that this source has a roughly similar flux to the majority of the 147 SNR listed. It will be interesting to discover if the MOST can discover pulsed emission from this or another source in a future observation.

If at 9.2kpc, the luminosity of 2CG342-02 is $4.6.10^{36}$ ergs.s^{-1} in photons above 100MeV, 10 times more γ-ray luminous than the Crab, which is closer at a distance of 2.3kpc. It would favour the chances of this remnant being the gamma-ray source if it were much closer. The discrepancy between observation and the estimated potential γ-ray flux from the synchrotron shell interacting with the observed outer gas shell would be very slightly reduced due to increasing the density of the

H_I shell, but not by any significant amount.

With regard to the central object, even if the remnant were at an extreme large distance, the large age accompanying this would not exclude the presence of a pulsar, Smith (1977) showing that most pulsars are older than any remnant shell at around 10^6 yrs. However, although there is little corelation between radio flux and and a pulsar's dynamical age, it may be that the high energy γ-rays are best produced in a younger object (Vela and the Crab are both young Pulsars). Thus the chances of a central pulsar producing measurable γ-rays as well as (the observed?) radio emission may be increased by having a younger, more energetic pulsar. It is thus worth briefly discussing the validity of the Σ-D relationship at this point.

6.2.7 Σ-D and the Distance to the New SNR (G343.3-2.4)

Several studies have shown, or attempted to show, that there is an observational relationship between the diameter of a SNR and its mean surface brightness, ie. the flux from the remnant divided by the total angular area that is enclosed by the outline, or extrapolation thereof, of the remnant. This can be approximated by $\Sigma_\nu(D)=A_\nu D^{-\beta}$ (Clark & Caswell, 1976; Milne, 1979; Green, 1984; Allakhverdiyev et al., 1986), where $\dot{\Sigma}$ is the mean surface brightness at frequency ν, D is the physical diameter, and A and B are constants that are fit to the

observations. On the not unreasonable assumption that the brightness of a remnant may be affected by its distance from the galactic plane, some relationships have included a z dependence, $\Sigma_\nu(D)=A_\nu D^{-\beta}\exp(-|z|/z_0)$ (Milne, 1979; Caswell and Lerche, 1979)

Intuitively, as a remnant expands the energy of cosmic rays that are present will be distributed throughout an ever increasing volume. Therefore, barring sufficiently rapid injection of energy into cosmic rays via shock acceleration or some other mechanism, one would expect the surface brightness of a remnant to decrease with its age and increasing diameter. Analytically, Duric and Seaquist (1986) derive a theoretical Σ-D relationship. The values of constants A and B being dependent on various parameters that describe the nature of the remnant and its environment. Since these parameters will vary from one remnant to another their theoretical equation predicts much scatter, and observationally the Σ-D relationship is far from reliable.

Green (1984) goes so far as to say that it is totally useless for predicting the diameter of an individual remnant and even its use for statistical purposes is questioned. However, in the absence of any additional data such as a measurable galactic rotation velocity from some associated H_I or a precise knowledge of the remnant's age from historical records, the Σ-D

relationship is the only means of estimating the distance to, and size of, many remnants. There is, therefore, a great need for such a relationship to exist, and it is common practice to use a Σ-D relationship despite the very large uncertainties. Figure 6.5 plots the Σ-D data used by Green (1984) and by Allakhverdiyev et al. (1986). It is clear from this why the two papers come to very different conclusions as to the existence of a Σ-D relationship. Both papers reject the idea of a z-dependence, Green claiming that this has largely been deduced from the fit to the anomalous positions of 2 remnants, ie. the Crab and 1006. Green's sole criteria for the selection of calibration sources is that they should have well defined distances. This is rightly criticised by Allakhverdiyev et al. (1986). Their Σ-D calibrators were chosen by relaxing the reliability of the distance estimates, but they chose only shell type remnants and those they believed to come from similar interstellar environments. A relationship now becomes quite clear, with a similar break in the fit for low surface brightness remnants as deduced previously by Clark and Caswell (1976). They then (strangely) go on to list distances and diameters deduced from the fit to their calibrators for all known SNR, including plerions in spite of their earlier criticism of Green (1984).

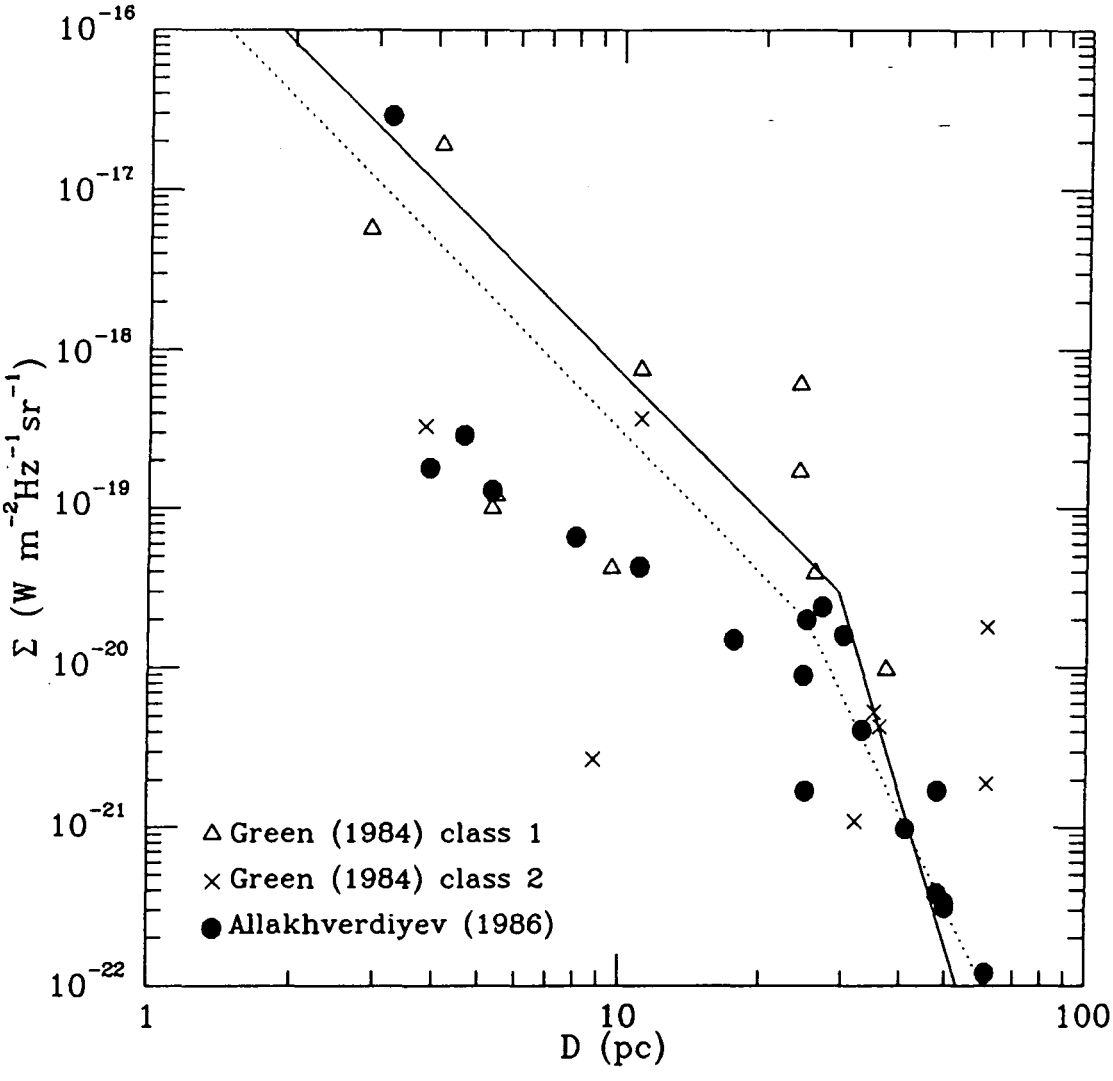

Figure 6.5 Recent calibrations of the Σ–D relationship showing the fit by Allakhverdiyev (dotted line) and that (to older data) of Clark and Caswell (1976) (solid line).

Considering the new SNR of figure 6.3 once more, this would appear to be an ideal object to fit the Σ-D relationship of Allakhverdiyev et al. (1986), since it is a well defined classic shell type remnant of the type used in the construction of the Σ-D diagram. Their relationship for $\Sigma<2.10^{-20}W.m^{-2}s^{-1}sr^{-1}$ at 1000MHz is $\Sigma=5.10^{-12}D^{-6}$, suggesting a distance of 6.4 kpc and D=58pc. (Their fit above $\Sigma=2.10^{-20}W.m^{-2}s^{-1}sr^{-1}$ is placed to the right of the calibrators for reasons of selection effects noted in Allakhverdiyev et al. (1983)) This is similar to that deduced from Clark and Caswell (1976), 52pc, but lower than the 80pc deduced earlier from Caswell and Lerche (1979). Although this remnant may well be of precisely the correct type to be used in conjunction with the fit of Allakhverdiyev et al. (1986) there is considerable scatter in figure 6.5 suggesting that the true diameter could be anything from from half to twice the deduced size.

6.2.8 Observational Evidence for a Distance?

If the IRAS 100μm ridge (figure 6.4) is associated with the remnant, the latter's distance could perhaps be better determined by the observation of the ridge at 21cm. The Durham-Parkes survey (Strong et al., 1982) has a resolution of 15arcmins, and covered the galactic plane for $-10° < b < +10°$ with a velocity resolution of just under $1km.s^{-1}$. The survey was under-sampled, the region of 2CG342-02 being covered at 0.5° intervals in longitude

and 1° intervals in latitude. Unfortunately, figure 6.4 suggests that the best place to have observed the ridge would have been l=342.8, b=-2.5 (α=17^{h}04^m, δ=-44°30′), where the ridge is brightest with respect to the background. This is almost equi-distant between 4 sampled points. The sample points along b=-3° pass too far below the ridge, but at b=-2° the ridge may still be present, though the background here is much brighter.

Examination of the survey shows that at l=342.5°, 343.0°, 343.5° , b=-2° (between α=17^{h}01^{m}00^s, δ=-44°29′00" and α=17^{h}04^{m}23^s, δ=-43°41′22") there exists a velocity component at -32km.s^{-1} which is much less evident at adjacent sampled positions. The corresponding distances for this velocity, assuming the rotation curve used by Burton and Gordon (1978) are 3.2 and 15.9kpc, ($R_\odot$=10kpc). The SNR at these distances would have a diameter of 29pc and 143pc respectively. If the scatter of the calibrators used by Allakhverdiyev et al. (1986) is typical for classic shell type remnants then D=29pc (for Σ=1.4.10^{-22}W.m^{-2}s^{-1}sr^{-1} at 1000MHz) would be acceptable, but D=143pc appears to be too large. A distance of 3.2kpc would place the remnant satisfactorally in the Norma spiral arm. Searching the catalogue of OB stars and associations (Humphreys, 1978) reveals no obvious association from which a remnant could have come. There are 4 listed associations within 5° of the remnant; SCO OB1, at 1.91kpc; NGC6206, 2.51kpc; ARA OB1a, 1.38kpc; and ARA OB1b, 3.47kpc. The first 2 are the closest,

centred on l=344, b=+1.5 and l=338.3, b=-1.2 but are very compact. The centres of the ARA associations are slightly more distant, but their members are widely dispersed. Between them they cover an area of sky from l=335° to 341° and from b=+3° to -3°. The SNR is only separated from either by an angular distance comparable to their dimensions, but this also is probably too great a distance to attempt to link either to the remnant. ARA OB1b is at a similar distance to that obtained via the kinematic observation of H_1, however, at this distance the remnant is separated from the association by over 300pc. Although no association exists that might indicate a distance to the remnant, the catalogue of Humphreys extends only to 4kpc. Since the remnant may well be more distant than this, the possibility of an OB association being responsible for the observed outer gas shell is not excluded.

From the available evidence it is not possible to be more precise about the size of the remnant than to put its diameter at 58±30pc, and only then if the Σ-D relationship is in any way reliable for this remnant. If associated with the gas (100μm) ridge of figure 6.4, and if the gas velocity component seen at l=342.5°→343.5°, b=-2° is a measure of that, and if there is no anomalous velocity of this gas, the size of the remnant is probably at the lower end of this Σ-D estimate, ie. D=29pc.

At this much closer distance there would be less discrepancy between the age of the remnant and the possibility that there is a highly active pulsar near the remnant's centre. At 29pc diameter for an initial energy of 10^{51} ergs and n_0=0.0035 (McKee and Ostriker, 1977), the Sedov solution gives an age of only 800yrs. At D=80pc the remnant's age would be 4.10^4 yrs.

There still remains the mystery of the missing radio flux. It may be revealed in the observation of an adjacent field, or if strongly variable, be visible in a later observation. If still absent at 1arcmin resolution then it would be worthwhile attempting to locate the missing 30Jy at a sightly poorer resolution in order to check against the smooth nature of the emission making the source invisible to the detector.

6.3 THE ASYMMETRY OF SHELL REMNANTS

Both this new SNR and Loop I are fairly typical of shell type remnants in that they are not detected over a complete circle. Those SNR that do have a shell detectable over 360° usually have one or two sections of arc that are far brighter than the rest. Supernova explosions can be far from symmetrical, as witnessed by the high velocities of many pulsars, velocities attained as a reaction to the explosive forces. However, the orientation of SNR shells is not random. Caswell (1977) noted that shell type remnants were, statistically,

preferentially brighter in the semi-circle that is towards the galactic plane. It was with this evidence that Caswell and Lerche (1979) justified the inclusion of a z-dependence in the Σ-D relationship. Their suggested explanation for a preferred direction of asymmetry and the z-dependence was a galactic magnetic field with a scale height of 260pc. For Loop I, Loop III and the new Molonglo SNR the radio emission is greatest towards the galactic plane. Also present with Loop I, and possibly near the MOST SNR, is an outer shell of higher density gas. In each case the partial shells of synchrotron emission are adjacent to the partial shells of gas. There are other examples of such 'coincidences'. Reich and Braunsfurth (1981) present 21cm maps showing that G116.9+0.2 (CTB1) is surrounded by an expanding shell of H_I at approximately twice the remnant's diameter. The H_I shell is present where the radio emission is brightest. In all these cases the H_I shell is beyond the region of radio emission, and is therefore not yet interacting with the SNR blast wave. Nevertheless, there appears to be a definite association between the positions of each. Routledge, Landecker and Vaneldik (1986) present H_I velocity maps in the direction of G166.2+2.5 (OA184). This remnant (deduced from their observations to be 175pc in diameter) is marginally brighter towards the H_I they have associated with it. This is not towards the galactic plane. Similarly with the two SNR that Pollock (1985) has identified as potential COS-B sources. Both remnants,

G78.2+2.1 (Higgs et al., 1977; Baars et al., 1978) and W28 (Kundu and Velusamy, 1972) have radio shells brightest where Pollock proposes they interact with dense clouds. For these sources the clouds have probably been impacted by the shock, but since they have not been completely engulfed this indicates that they were present prior to the remnant.

Blandford and Cowie (1982) developed a theoretical model of radio emission from shocks impacting with clouds. The model predicts that much of the radio emission should come from crushed clouds, or more accurately the crushed warm halos around the clouds. In chapter 5 it was suggested that clouds could enhance radio emission by breaking up the shock, deflecting and focusing sub-shocks and causing reverse shocks. These processes actively encouraging the acceleration of the cosmic rays and increasing the dissipation of heat. Both processes may be at work in the shell of SNR. Some of the examples given here show that it is features of the ISM local to each remnant that determines which section of the shell shall be brightest, specifically, the gas distribution. The fact that a majority of SNR are brighter towards the galactic plane simply reflects the most probable gas distribution. Caswell and Lerche (1979) may be partially correct in attributing this to the scale height of the galactic magnetic field. Where there are local gas density enhancements there may also be enhanced magnetic fields. However, for the lower density neutral clouds

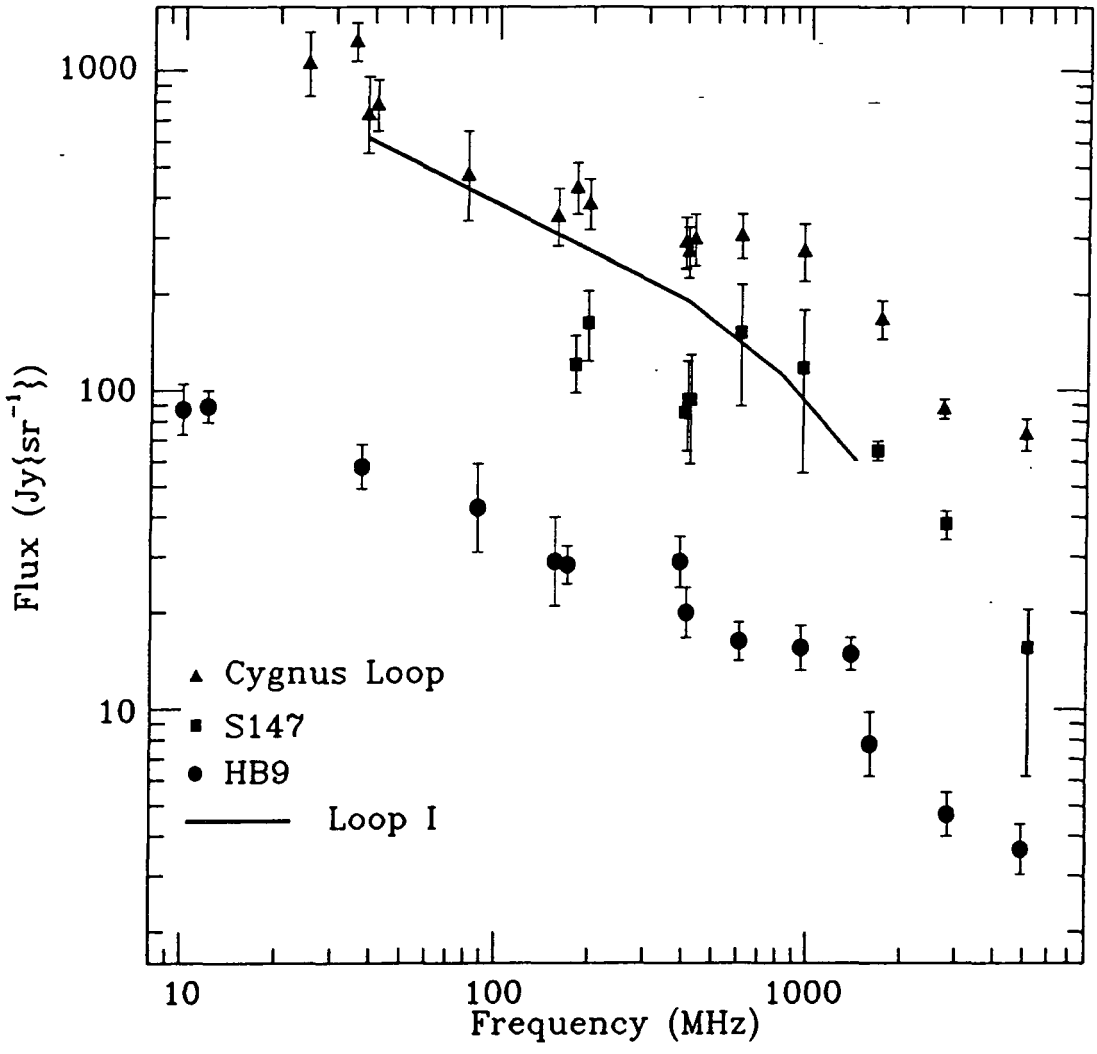

Figure 6.6 Possible spectral breaks in galactic SNR.

Data from Shastry et al. (1981), Kundu et al. (1980)
& DeNoyer (1974) for Cygnus, S147 & HB9 respectively.
Loop 1 intensities taken from figure 5.2.
True flux for HB9 is 10 times the scale.

such as seen in front of the shocks of Loop I and the MOST SNR this may not be so. There is no reason to suppose that diffuse non-ionized clouds will hold onto a magnetic field proportional to their density. In chapter 5 we examined the polarization of stars in relation to the IRAS dust filaments outside Loop I. Had there been increased magnetic field strengths as well as an increase in the gas and dust one would have expected to see a good corelation between the IRAS emission and the polarization, and none was observed. We therefore believe that in many remnants it is the gas distribution that determines the relative intensity distribution of both radio and x-ray emission.

6.4 SPECTRAL STEEPENING OF GALACTIC REMNANTS

In chapter 5 it was shown that Loops I and III show signs of spectral steepening. Of large diameter SNR the 5 listed here also appear to have steeper spectra at higher frequencies G126.2+1.6 (J.L. Osborne, private communication), G74.0-8.6 (Cygnus Loop; DeNoyer, 1974; Sastry et al., 1981), G160.9+2.6 (HB9; DeNoyer, 1974; Willis, 1973), G180.0-1.7 (S147; Kundu et al., 1980) and G33.2-0.6 (Reich, 1982). All the remnants are shell type, though the identification of G126.2+1.6 as such is only probable (Green, 1987). Whereas chapters 4 and 5 presented and analysed the giant radio loops as having a gradually increasing spectral index with frequency, the spectra of the remnants listed above have generally been represented by a power law with a break at around 1000MHz.

The spectra of 3 of these sources is shown in figure 6.6. The spectrum for the Cygnus Loop is for the entire object, but the different regions of the loop show different behaviour (Willis, 1973). The brightest Southern region does not show a spectral break. The North Eastern section is responsible for the steepening around 1000MHz seen in figure 6.6, but the much less intense North Western region the spectral break occurs at 400MHz. Not all remnants, of any diameter, show such a spectral steepening, though the majority have not been observed at a sufficient number of well separated frequencies to get a detailed spectrum. The above 5 remnants would thus appear to indicate that the steepening spectral index of loops I and III is compatible with their identification as SNR.

CHAPTER 7

CONCLUSIONS

7.1 INTRODUCTION

In this thesis a number of different possibilities have been discussed and suggested for the origin and evolution of the giant radio loops I and III, with the belief that the Loop IV (briefly examined) and Loop II are possibly similar features. The realistic conclusion that has to be drawn from this work is that of a number of possible models none is significantly preferable. The idea that each loop is due to a Supernova or Supernovae has for some time been the generally accepted view. This work has been approached with this assumption, and the most confident statement that can be made is that all the evidence examined here would tend to suggest that the loops are indeed Supernova Remnants. Their detailed evolution is more problematical. The difficulty with mathematically modelling such objects has always been the impossibility of producing a model of manageable simplicity that is still able to account for all the

observed details of an individual remnant. The ISM is too variable and unpredictable on scale sizes comparable with the size of a remnant to produce a perfect uniformly spherical shell desirable from the point of view of modelling. It was for this reason that of all the SNR models reviewed in Chapter 3 a simplistic and unrealistic model of the gas distribution was chosen as the starting point and the additional known complexities discussed in relation to the model. The model of Hayakawa et al. (1979) which was chosen for the examination of the thermal gas component of Loop I is sufficiently uncomplicated to provide an easy analysis, but included the essential fact, omitted in the Sedov solution, that the ISM into which the remnant is expanding is not necessarily cold. The model allows for the simple inclusion of weak shocks.

This introduction begins this final chapter in order to set the results into a context of a good deal of uncertainty. Many previous papers examining the evolution and nature of SNRs and the Radio Loops have concentrated on one aspect or region, and have arrived at reasonable conclusions for the assumptions and the data they have used. In order to give a more complete picture, this thesis has attempted to bring together different aspects, namely the x-ray and radio emission, and has looked at the loops on the scales of the overall distribution of emission and the finest scale structure unresolved in the data, and the results are not definitive.

7.2 LOOPS I AND III

The Loop I x-ray emitting gas is evidence of possible shock heating from a SNR blast wave, and the M and I band ridge appears to be explainable by the gas distribution given by equations 3.11a and 3.11b. The model presented in sections 5.3.5.2→4 adopted a single shock front of 63° angular radius from l=329°, b=17.5°, and we deduce that it is possible, with suitable choices for other parameters (primarily the shock strength), that the shock could exist within the range 61° to 64° and still match the position of the observed ridge maximum. If Loop I evolved in a cavity of density distribution given by equations 5.18 and 5.19, with ξ=1 then an angular radius of 60° cannot be ruled out. If the width of the ridge is also taken into account then this would favour a shock in the range of 62° to 63°.

The assumption that the projection of the shock is circular leads to the conclusion that the shock weakens away from the galactic plane. For the modelled regions at b=20° and b=60° (ie. models A and B) shock strengths of η=3 and η=2 are estimated respectively. This implies that there is a z-dependent change in the temperature (and density from the observed intensity) in the Loop I ISM. The greater the distance above the plane in the northern galactic hemisphere the higher the temperature and the lower the density. The apparent scale height of the gas is thus estimated at z_0=170pc. This value is large

compared to the neutral gas scale height, and is therefore additional evidence that the evolution of a blast wave preferentially takes place in a low density medium between clouds. However, this is considerably less than estimates for the scale height of the hot phase, and this probably reflects the fact that substantial emission comes from the evaporation of the neutral component.

If the x-ray emission can be approximately explained by this z-dependence in the gas distribution and temperature, then since the radio NPS follows a similar trend to the x-ray ridge in its intensity variation (ie. both fade towards high latitudes) it is possible that the radio may also be affected by the changes in these parameters. By extrapolation to Loop III, which shows a similar latitude dependence in its radio intensity, the z-dependence of temperature and density may be extended to the whole of the local ISM in the northern galactic hemisphere.

Further extrapolation to more distant interstellar space provides an alternative explanation for the statistical orientation of asymmetry observed in SNR (Caswell, 1977) to that that proposed by Caswell and Lerche (1979). SNR are generally brighter towards the galactic plane either because the gas temperature is lower here, allowing for stronger shocks with greater compression of the ambient magnetic field, or the greater density gives more opportunities for enhanced emission via

the crushed cloud mechanism proposed by Blandford and Cowie (1982). This does not exclude a contribution from the higher magnetic field strengths proposed by Caswell and Lerche (1979) to exist towards the galactic plane.

The degree to which these smaller scale shocks can be produced is probably also affected by the aforementioned density gradient, and it may be the combination of increasing (or decreasing) ambient hot phase with corresponding changes in the cloud density and complexity that leads to the enhancement (or lack of it) in the observed emission. The ability of cloud complexes to focus and reflect shocks will be dependent on the density contrast between the clouds and the advancing gas in the shock. Expansion from a high density region to a lower density region with proportionally less dense clouds will give a poor density contrast, and result in less turbulence. It is also possible that the lower density regions will have less complex, more isolated clouds. In the case of Loop I, figure 2.1 (Paresce, 1984) suggests the visible spur at l=30° has evolved into a region of increasing density, whilst the missing corresponding spur at l=270° evolved into a relatively less dense region, though not necessarily as far as the H_I hole. Maps at 21cm show the region around l=30° to be relatively cloudy, the H_I shell being one such feature in the area.

It is thus the gas density distribution that this work suggests may be the link between the x-ray and radio components of Loop I. A shock expanding into a complex cloudy medium may result in a greater conversion of energy from kinetic to thermal via focusing, reverse shocks and turbulence, heating the denser cloud halos to x-ray temperatures not attainable from the simple main shock driven into the cloud. These same factors enhance the radio synchrotron emission, by increasing the number of sites for shock acceleration of cosmic ray electrons and by giving greater compression within the ambient low density gas.

The fits to the radio spectra from loops I and III suggest that the steady state electron spectrum is slightly flatter than the γ=2 prediction of the Bell (1978) model. It was suggested in section 5.2.3.3 that turbulence behind the shock could result in regions where cosmic rays might see effective super-strong shocks. This and cloudiness produce increased post-shock turbulence and small shock-shock interactions, providing sites for the production of a flatter electron spectrum.

The Forman and Dury (1983) model for a finite acceleration time gives acceptable fits to the spectral steepening in loops I and III. Reasonable estimates for parameter values yield an age comparable with the loops' ages estimated from their x-ray temperatures and size. Similar spectral steepening is observed in other SNR.

Depending on which spur or part thereof is examined, the best choice of parameters will be slightly different, but all areas examined in loops I and III roughly fit an electron power law spectrum of γ=1.7, and effective energy dependence of the diffusion coefficient of $\omega \geq 1$, and $B(V^2 t/C) \sim 100 \mu G$. A shock velocity of $V=400 km.s^{-1}$, a magnetic field strength of $B=3 \mu G$ and a diffusion coefficient $D=C(E/3GeV)^{\omega}$ with $C=2.10^{26} cm^2 s^{-1}$ gives ages for loops I and III of order 10^5 years.

Chapter 5 suggested that both loops I and III may be more distant than given in table 1.1. If at its quoted distance, Loop III has to be relatively cold ($T<8.10^5 K$) in order to explain the lack of observed x-ray emission. If placed at the distance limit of the stated range of uncertainty then the extra intervening column density would allow a higher temperature, $T<1.6.10^6 K$. The higher temperature may be more compatible with the remnant being still in its adiabatic phase. If it is much below the lower temperature, rapid cooling should lead the formation of H_I behind the shock, and this is not seen at 21cm.

The possibility of Loop I being more distant comes about by its possible connection with the Sco-Cen Association. The H_I shell outside the NPS suggests the possibility of one or more previous SNR. O-B associations may be connected with multiple supernovae. This, along with stellar winds, has often been put forward as an explanation for the H_I shell. It seems reasonable to

extend this possibility to the currently visible remnant, which would put its centre around 170pc, and give it a diameter of 150pc. The greater distance to Loop I would also help to ensure that as much as possible of the $4.10^{20}\,cm^{-2}$ column density of H_I lies between us and the brightest part of the x-ray ridge. This, however, would still be insufficient to explain the amount of absorbtion of the very soft x-rays. This is further evidence that the x-ray emission is concentrated around clouds, as this will then give a much greater effective absorbing column density than should be possible for a uniform distribution of both emitting and absorbing components.

7.3 2CG342-02

The discovery of a SNR at 843MHz in the error circle provides a promising candidate for the identification of this COS-B γ-ray source. The presence of an outer H_I shell (as well as providing additional evidence for the influence of gas distribution on SNR evolution) could have given an acceptable explanation for the production of γ-rays. That is, an enhanced cosmic ray flux from shock acceleration interacting with a high density cloud. However, the synchrotron flux and the gas shell density are too small to account for the total γ-ray flux. The only remaining possibility from the same radio observation is the small source near to the centre of the remnant. Pure speculation, but could this be an associated pulsar?

7.4 FUTURE OBSERVATIONS

This thesis has primarily been concerned with the origin and nature of radio Loops I and III. Many previous papers have modelled Loop I in particular as a SNR using much the same data. The various models that have been proposed are largely dependent on the assumptions made as to the nature of the ISM, its density and the energy of the initial explosion. Aware of the fact that conclusions more detailed than "the loops are Supernova Remnants" are dependent on the assumptions, no one model has been proposed here, rather a number of possible variations to account for different conditions. Other authors have arrived at equally valid, often similar, possibilities. The conclusions here have therefore not been precise, and it appears that further observations need to be made if further theoretical work is not to amount to further speculation.

The main possibilities discussed in this thesis have been the steady evolution of a remnant (in the models treated as taking place in a uniform medium) and the non-continuous evolution, whereby localized cloud formations greatly influence the degree of emission. The North Polar Spur is almost certainly a Supernova Remnant, and its proximity gives a unique opportunity to examine the emission of old shell remnants in detail. The x-ray emission, and the ridge in particular, should ideally be surveyed as completely as the data of McCammon et al.

(1983) which was used here, but with a much higher resolution. Clumped x-ray emission substantially below the scale of 1pc (1°) would be strong evidence for hot halos around clouds. EXOSAT's low energy detectors had exceptionally high resolution, but was not a survey instrument and did not attempt to examine the ridge. It will be interesting to see if ROSAT, the next major x-ray satellite, can see the x-rays from Loop I.

The single observation at 843MHz of the COS-B source 2CG342-02 was inconclusive, and further observations need to be made. The absence of 30Jy is a puzzle that needs to be resolved. There should be a re-observation of the same field to look for variability, and of adjacent fields. The region of the sources CTB36 and MHR59, whose positions were initially assumed spurious, is of particular interest. Timed observations of the small source at the centre of the remnant would also be of interest in order to search for a pulsed periodicity.

APPENDIX A

Intensity (erg.s^{-1}cm^{-2}sr^{-1}) between energy limits given in table 4.1 per count rate within that band.

log10(TEMP)	NH cm^{-2}	B	C	M1	M2	I	J	2-6
5.20	0.00E+00	1.29E-11	9.23E-12	2.49E-15	0.00E+00	0.00E+00	0.00E+00	0.00E+00
5.40	0.00E+00	4.26E-11	2.92E-11	1.48E-12	8.84E-12	0.00E+00	0.00E+00	0.00E+00
5.60	0.00E+00	5.35E-11	5.75E-11	6.05E-11	6.04E-11	2.30E-11	1.36E-12	0.00E+00
5.80	0.00E+00	9.39E-11	7.71E-11	5.76E-10	1.28E-10	2.87E-11	2.48E-11	0.00E+00
6.00	0.00E+00	1.44E-10	9.32E-11	8.68E-10	2.14E-10	9.75E-11	7.67E-11	7.07E-11
6.20	0.00E+00	1.54E-10	9.81E-11	1.01E-09	3.29E-10	1.77E-10	1.36E-10	1.86E-10
6.40	0.00E+00	1.46E-10	9.03E-11	1.06E-09	5.06E-10	3.07E-10	1.74E-10	3.78E-10
6.60	0.00E+00	1.43E-10	8.86E-11	1.26E-09	5.12E-10	3.32E-10	1.97E-10	4.59E-10
6.80	0.00E+00	1.38E-10	8.62E-11	1.36E-09	5.03E-10	3.23E-10	2.06E-10	4.49E-10
7.00	0.00E+00	1.22E-10	8.46E-11	1.48E-09	5.17E-10	3.16E-10	2.03E-10	4.25E-10
7.20	0.00E+00	9.45E-11	8.27E-11	1.64E-09	5.59E-10	3.08E-10	2.01E-10	4.06E-10
7.40	0.00E+00	1.50E-10	8.70E-11	1.26E-09	6.62E-10	3.08E-10	2.23E-10	4.06E-10
7.60	0.00E+00	1.50E-10	8.71E-11	1.16E-09	5.97E-10	3.26E-10	2.47E-10	4.19E-10
7.80	0.00E+00	1.49E-10	8.68E-11	1.18E-09	5.73E-10	3.39E-10	2.46E-10	4.33E-10
8.00	0.00E+00	1.48E-10	8.64E-11	1.18E-09	5.61E-10	3.50E-10	2.45E-10	4.66E-10
5.20	4.00E+20	1.58E-10	1.08E-10	0.00E+00	0.00E+00	0.00E+00	0.00E+00	0.00E+00
5.40	4.00E+20	1.58E-10	1.02E-10	6.23E-11	9.19E-12	0.00E+00	0.00E+00	0.00E+00
5.60	4.00E+20	1.42E-10	9.30E-11	1.64E-10	6.36E-11	2.58E-11	1.47E-12	0.00E+00
5.80	4.00E+20	1.16E-10	9.00E-11	6.84E-10	1.38E-10	3.24E-11	2.63E-11	0.00E+00
6.00	4.00E+20	9.20E-11	8.86E-11	9.04E-10	2.29E-10	1.06E-10	7.91E-11	7.14E-11
6.20	4.00E+20	6.21E-11	8.50E-11	1.02E-09	3.46E-10	1.86E-10	1.39E-10	1.87E-10
6.40	4.00E+20	2.28E-11	8.02E-11	1.08E-09	5.13E-10	3.12E-10	1.76E-10	3.78E-10
6.60	4.00E+20	1.30E-11	7.55E-11	1.29E-09	5.12E-10	3.33E-10	1.99E-10	4.59E-10
6.80	4.00E+20	1.23E-11	7.02E-11	1.38E-09	5.05E-10	3.24E-10	2.07E-10	4.49E-10
7.00	4.00E+20	1.41E-11	6.74E-11	1.50E-09	5.20E-10	3.16E-10	2.05E-10	4.25E-10
7.20	4.00E+20	1.42E-11	6.66E-11	1.67E-09	5.63E-10	3.08E-10	2.03E-10	4.06E-10
7.40	4.00E+20	1.43E-11	7.05E-11	1.28E-09	6.68E-10	3.09E-10	2.24E-10	4.07E-10
7.60	4.00E+20	1.40E-11	7.04E-11	1.18E-09	6.01E-10	3.28E-10	2.47E-10	4.20E-10
7.80	4.00E+20	1.33E-11	6.99E-11	1.19E-09	5.76E-10	3.41E-10	2.46E-10	4.33E-10
8.00	4.00E+20	1.18E-11	6.75E-11	1.19E-09	5.64E-10	3.53E-10	2.45E-10	4.67E-10

Intensity (erg.s^{-1}cm^{-2}sr^{-1}) between 0.01 and 10keV
per count rate within the given band.

log10(TEMP)	NH cm^{-2}	B	C	M1	M2	I	J	2-6
5.20	0.00E+00	2.65E-09	1.66E-08	1.33E-03	1.57E+03	4.55E+06	0.00E+00	0.00E+00
5.40	0.00E+00	1.66E-09	5.13E-09	1.33E-04	6.05E-01	9.65E+01	1.42E+06	0.00E+00
5.60	0.00E+00	2.70E-09	5.55E-09	4.31E-05	2.43E-03	1.20E-01	8.26E+01	2.93E+09
5.80	0.00E+00	1.08E-09	1.15E-09	1.36E-06	5.54E-06	6.63E-05	1.98E-02	2.38E+03
6.00	0.00E+00	8.44E-10	4.80E-10	9.75E-08	2.25E-07	1.52E-06	5.70E-05	2.40E-01
6.20	0.00E+00	1.20E-09	3.24E-10	1.67E-08	2.60E-08	1.02E-07	1.31E-06	4.30E-04
6.40	0.00E+00	2.28E-09	3.10E-10	4.87E-09	4.36E-09	8.05E-09	5.90E-08	3.13E-06
6.60	0.00E+00	3.47E-09	6.05E-10	2.73E-09	1.23E-09	1.30E-09	6.19E-09	1.16E-07
6.80	0.00E+00	6.27E-09	1.24E-09	2.22E-09	7.73E-10	6.91E-10	2.37E-09	2.03E-08
7.00	0.00E+00	8.35E-09	2.37E-09	2.51E-09	7.34E-10	5.50E-10	1.61E-09	7.88E-09
7.20	0.00E+00	7.80E-09	3.42E-09	3.69E-09	8.79E-10	4.76E-10	1.18E-09	5.08E-09
7.40	0.00E+00	6.60E-09	2.03E-09	7.16E-09	1.99E-09	6.50E-10	7.68E-10	1.88E-09
7.60	0.00E+00	6.08E-09	1.83E-09	8.75E-09	4.00E-09	1.35E-09	9.59E-10	1.26E-09
7.80	0.00E+00	7.42E-09	2.20E-09	1.05E-08	5.14E-09	2.04E-09	1.21E-09	1.16E-09
8.00	0.00E+00	1.41E-08	4.18E-09	1.86E-08	9.12E-09	3.88E-09	1.90E-09	1.11E-09
5.20	4.00E+20	2.93E-10	1.23E-10	5.86E-07	1.55E-02	3.83E+01	0.00E+00	0.00E+00
5.40	4.00E+20	4.65E-10	1.12E-10	7.29E-07	8.14E-05	1.25E-02	1.68E+02	0.00E+00
5.60	4.00E+20	2.12E-09	2.17E-10	1.05E-07	2.28E-06	1.07E-04	6.60E-02	2.10E+06
5.80	4.00E+20	4.51E-09	3.12E-10	2.02E-08	6.92E-08	7.94E-07	2.06E-04	2.28E+01
6.00	4.00E+20	5.64E-09	3.56E-10	4.83E-09	1.05E-08	6.58E-08	2.19E-06	8.70E-03
6.20	4.00E+20	1.02E-08	4.22E-10	2.25E-09	3.34E-09	1.19E-08	1.40E-07	4.37E-05
6.40	4.00E+20	1.75E-08	6.54E-10	1.92E-09	1.62E-09	2.78E-09	1.89E-08	9.62E-07
6.60	4.00E+20	3.21E-08	2.32E-09	1.90E-09	8.12E-10	8.24E-10	3.70E-09	6.65E-08
6.80	4.00E+20	7.97E-08	5.96E-09	1.97E-09	6.65E-10	5.73E-10	1.85E-09	1.53E-08
7.00	4.00E+20	1.62E-07	1.24E-08	2.39E-09	6.81E-10	4.92E-10	1.37E-09	6.43E-09
7.20	4.00E+20	2.16E-07	1.93E-08	3.52E-09	8.14E-10	4.26E-10	1.01E-09	4.18E-09
7.40	4.00E+20	1.22E-07	1.20E-08	7.29E-09	1.87E-09	5.89E-10	6.70E-10	1.58E-09
7.60	4.00E+20	1.10E-07	1.09E-08	9.21E-09	3.88E-09	1.23E-09	8.40E-10	1.07E-09
7.80	4.00E+20	1.32E-07	1.34E-08	1.14E-08	5.18E-09	1.92E-09	1.09E-09	1.02E-09
8.00	4.00E+20	2.38E-07	2.63E-08	2.15E-08	9.80E-09	3.90E-09	1.83E-09	1.04E-09

APPENDIX B

Counts/second per emission measure ($s^{-1} cm^{-6} pc$) in each of the Wisconsin x-ray bands.

log10(TEMP)	NH cm^{-2}	B	C	M1	M2	I	J	2-6
5.20	0.00E+00	1.39E+01	2.22E+00	2.77E-05	2.35E-11	8.09E-15	0.00E+00	0.00E+00
5.40	0.00E+00	4.63E+02	1.50E+02	5.77E-03	1.27E-06	7.96E-09	5.41E-13	0.00E+00
5.60	0.00E+00	3.70E+03	1.80E+03	2.31E-01	4.11E-03	8.31E-05	1.21E-07	3.41E-15
5.80	0.00E+00	1.33E+04	1.25E+04	1.05E+01	2.57E+00	2.15E-01	7.21E-04	6.00E-09
6.00	0.00E+00	2.62E+04	4.61E+04	2.27E+02	9.84E+01	1.45E+01	3.88E-01	9.22E-05
6.20	0.00E+00	1.96E+04	7.29E+04	1.41E+03	9.08E+02	2.31E+02	1.80E+01	5.49E-02
6.40	0.00E+00	6.11E+03	4.50E+04	2.86E+03	3.20E+03	1.73E+03	2.37E+02	4.46E+00
6.60	0.00E+00	2.45E+03	1.41E+04	3.12E+03	6.94E+03	6.56E+03	1.37E+03	7.36E+01
6.80	0.00E+00	1.35E+03	6.86E+03	3.82E+03	1.10E+04	1.23E+04	3.58E+03	4.17E+02
7.00	0.00E+00	1.12E+03	3.94E+03	3.71E+03	1.27E+04	1.69E+04	5.78E+03	1.18E+03
7.20	0.00E+00	1.14E+03	2.60E+03	2.41E+03	1.01E+04	1.87E+04	7.53E+03	1.75E+03
7.40	0.00E+00	6.51E+02	2.12E+03	6.00E+02	2.16E+03	6.61E+03	5.60E+03	2.29E+03
7.60	0.00E+00	5.85E+02	1.94E+03	4.07E+02	8.91E+02	2.63E+03	3.71E+03	2.83E+03
7.80	0.00E+00	5.13E+02	1.73E+03	3.63E+02	7.41E+02	1.87E+03	3.15E+03	3.29E+03
8.00	0.00E+00	4.64E+02	1.57E+03	3.53E+02	7.17E+02	1.69E+03	3.44E+03	5.89E+03
5.20	1.00E+20	1.50E-01	9.07E-02	9.32E-06	2.12E-11	7.61E-15	0.00E+00	0.00E+00
5.40	1.00E+20	2.05E+01	1.87E+01	1.79E-03	1.17E-06	7.44E-09	5.18E-13	0.00E+00
5.60	1.00E+20	2.56E+02	3.79E+02	1.35E-01	3.81E-03	7.80E-05	1.16E-07	3.38E-15
5.80	1.00E+20	1.58E+03	3.83E+03	8.98E+00	2.39E+00	2.02E-01	7.01E-04	5.95E-09
6.00	1.00E+20	4.84E+03	1.76E+04	2.07E+02	9.18E+01	1.38E+01	3.80E-01	9.16E-05
6.20	1.00E+20	4.63E+03	3.38E+04	1.31E+03	8.52E+02	2.22E+02	1.77E+01	5.46E-02
6.40	1.00E+20	1.77E+03	2.55E+04	2.68E+03	3.04E+03	1.68E+03	2.33E+02	4.44E+00
6.60	1.00E+20	7.18E+02	7.97E+03	2.96E+03	6.67E+03	6.37E+03	1.36E+03	7.33E+01
6.80	1.00E+20	3.62E+02	3.89E+03	3.66E+03	1.06E+04	1.19E+04	3.53E+03	4.16E+02
7.00	1.00E+20	2.41E+02	2.17E+03	3.56E+03	1.22E+04	1.65E+04	5.71E+03	1.18E+03
7.20	1.00E+20	1.85E+02	1.36E+03	2.32E+03	9.80E+03	1.83E+04	7.44E+03	1.75E+03
7.40	1.00E+20	1.59E+02	1.13E+03	5.71E+02	2.10E+03	6.48E+03	5.54E+03	2.29E+03
7.60	1.00E+20	1.44E+02	1.04E+03	3.85E+02	8.60E+02	2.58E+03	3.68E+03	2.83E+03
7.80	1.00E+20	1.27E+02	9.28E+02	3.43E+02	7.14E+02	1.83E+03	3.12E+03	3.28E+03
8.00	1.00E+20	1.18E+02	8.45E+02	3.34E+02	6.92E+02	1.65E+03	3.42E+03	5.88E+03

log10(TEMP)	NH cm^{-2}	B	C	M1	M2	I	J	2-6
5.20	2.00E+20	1.61E-02	1.82E-02	3.20E-06	1.92E-11	7.17E-15	0.00E+00	0.00E+00
5.40	2.00E+20	3.15E+00	4.73E+00	6.00E-04	1.09E-06	6.95E-09	4.95E-13	0.00E+00
5.60	2.00E+20	4.82E+01	1.39E+02	9.69E-02	3.53E-03	7.32E-05	1.12E-07	3.34E-15
5.80	2.00E+20	3.43E+02	1.63E+03	7.99E+00	2.22E+00	1.89E-01	6.81E-04	5.90E-09
6.00	2.00E+20	1.22E+03	8.05E+03	1.90E+02	8.56E+01	1.31E+01	3.72E-01	9.10E-05
6.20	2.00E+20	1.36E+03	1.74E+04	1.21E+03	7.99E+02	2.13E+02	1.74E+01	5.43E-02
6.40	2.00E+20	6.99E+02	1.55E+04	2.51E+03	2.89E+03	1.62E+03	2.30E+02	4.42E+00
6.60	2.00E+20	3.25E+02	4.87E+03	2.81E+03	6.42E+03	6.19E+03	1.34E+03	7.30E+01
6.80	2.00E+20	1.64E+02	2.41E+03	3.50E+03	1.02E+04	1.16E+04	3.49E+03	4.15E+02
7.00	2.00E+20	1.02E+02	1.34E+03	3.42E+03	1.18E+04	1.61E+04	5.64E+03	1.18E+03
7.20	2.00E+20	7.44E+01	8.31E+02	2.23E+03	9.50E+03	1.78E+04	7.35E+03	1.74E+03
7.40	2.00E+20	6.54E+01	6.82E+02	5.44E+02	2.04E+03	6.36E+03	5.48E+03	2.28E+03
7.60	2.00E+20	6.00E+01	6.28E+02	3.64E+02	8.31E+02	2.53E+03	3.65E+03	2.82E+03
7.80	2.00E+20	5.38E+01	5.64E+02	3.25E+02	6.89E+02	1.80E+03	3.10E+03	3.28E+03
8.00	2.00E+20	5.16E+01	5.16E+02	3.16E+02	6.68E+02	1.62E+03	3.39E+03	5.87E+03
5.20	4.00E+20	8.32E-04	1.98E-03	4.16E-07	1.57E-11	6.36E-15	0.00E+00	0.00E+00
5.40	4.00E+20	1.64E-01	6.81E-01	1.05E-04	9.36E-07	6.08E-09	4.54E-13	0.00E+00
5.60	4.00E+20	3.26E+00	3.17E+01	6.57E-02	3.03E-03	6.46E-05	1.05E-07	3.28E-15
5.80	4.00E+20	2.94E+01	4.25E+02	6.56E+00	1.92E+00	1.67E-01	6.43E-04	5.81E-09
6.00	4.00E+20	1.39E+02	2.20E+03	1.62E+02	7.46E+01	1.19E+01	3.57E-01	8.98E-05
6.20	4.00E+20	2.30E+02	5.56E+03	1.05E+03	7.04E+02	1.97E+02	1.68E+01	5.37E-02
6.40	4.00E+20	2.41E+02	6.45E+03	2.20E+03	2.61E+03	1.52E+03	2.23E+02	4.38E+00
6.60	4.00E+20	1.50E+02	2.08E+03	2.54E+03	5.94E+03	5.85E+03	1.30E+03	7.25E+01
6.80	4.00E+20	7.92E+01	1.06E+03	3.20E+03	9.49E+03	1.10E+04	3.41E+03	4.12E+02
7.00	4.00E+20	4.63E+01	6.08E+02	3.15E+03	1.10E+04	1.53E+04	5.51E+03	1.17E+03
7.20	4.00E+20	3.37E+01	3.75E+02	2.06E+03	8.92E+03	1.70E+04	7.18E+03	1.74E+03
7.40	4.00E+20	2.95E+01	2.99E+02	4.94E+02	1.92E+03	6.12E+03	5.37E+03	2.27E+03
7.60	4.00E+20	2.74E+01	2.75E+02	3.27E+02	7.76E+02	2.44E+03	3.58E+03	2.81E+03
7.80	4.00E+20	2.52E+01	2.49E+02	2.91E+02	6.42E+02	1.73E+03	3.05E+03	3.27E+03
8.00	4.00E+20	2.56E+01	2.32E+02	2.84E+02	6.23E+02	1.56E+03	3.34E+03	5.86E+03

log10(TEMP)	NH cm^{-2}	B	C	M1	M2	I	J	2-6
5.20	8.00E+20	7.08E-06	1.00E-04	1.85E-08	1.06E-11	5.03E-15	0.00E+00	0.00E+00
5.40	8.00E+20	1.22E-03	4.58E-02	2.28E-05	6.96E-07	4.67E-09	3.81E-13	0.00E+00
5.60	8.00E+20	1.28E-01	3.55E+00	3.84E-02	2.25E-03	5.04E-05	9.09E-08	3.16E-15
5.80	8.00E+20	3.46E+00	5.31E+01	4.60E+00	1.43E+00	1.30E-01	5.74E-04	5.63E-09
6.00	8.00E+20	3.07E+01	2.99E+02	1.19E+02	5.67E+01	9.79E+00	3.28E-01	8.75E-05
6.20	8.00E+20	7.60E+01	9.62E+02	7.81E+02	5.48E+02	1.68E+02	1.57E+01	5.26E-02
6.40	8.00E+20	1.12E+02	1.53E+03	1.70E+03	2.14E+03	1.34E+03	2.11E+02	4.31E+00
6.60	8.00E+20	8.44E+01	5.45E+02	2.08E+03	5.09E+03	5.22E+03	1.24E+03	7.14E+01
6.80	8.00E+20	4.81E+01	3.11E+02	2.69E+03	8.21E+03	9.89E+03	3.25E+03	4.07E+02
7.00	8.00E+20	2.77E+01	1.95E+02	2.68E+03	9.63E+03	1.38E+04	5.25E+03	1.16E+03
7.20	8.00E+20	2.05E+01	1.23E+02	1.77E+03	7.88E+03	1.56E+04	6.84E+03	1.72E+03
7.40	8.00E+20	1.81E+01	8.90E+01	4.10E+02	1.71E+03	5.66E+03	5.16E+03	2.26E+03
7.60	8.00E+20	1.71E+01	8.24E+01	2.64E+02	6.79E+02	2.27E+03	3.46E+03	2.79E+03
7.80	8.00E+20	1.59E+01	7.57E+01	2.36E+02	5.59E+02	1.61E+03	2.95E+03	3.25E+03
8.00	8.00E+20	1.70E+01	7.57E+01	2.31E+02	5.43E+02	1.45E+03	3.24E+03	5.83E+03
5.20	1.60E+21	1.55E-08	1.86E-06	1.07E-09	4.98E-12	3.19E-15	0.00E+00	0.00E+00
5.40	1.60E+21	1.91E-05	1.10E-03	6.51E-06	3.93E-07	2.80E-09	2.69E-13	0.00E+00
5.60	1.60E+21	2.47E-02	1.17E-01	1.59E-02	1.27E-03	3.11E-05	6.87E-08	2.93E-15
5.80	1.60E+21	9.99E-01	2.42E+00	2.38E+00	8.09E-01	8.06E-02	4.60E-04	5.28E-09
6.00	1.60E+21	1.17E+01	2.41E+01	6.47E+01	3.33E+01	6.76E+00	2.78E-01	8.31E-05
6.20	1.60E+21	3.15E+01	1.06E+02	4.42E+02	3.38E+02	1.25E+02	1.37E+01	5.04E-02
6.40	1.60E+21	4.49E+01	1.95E+02	1.04E+03	1.46E+03	1.04E+03	1.88E+02	4.16E+00
6.60	1.60E+21	3.82E+01	1.14E+02	1.41E+03	3.76E+03	4.19E+03	1.12E+03	6.93E+01
6.80	1.60E+21	2.45E+01	9.41E+01	1.91E+03	6.18E+03	8.03E+03	2.95E+03	3.97E+02
7.00	1.60E+21	1.40E+01	6.77E+01	1.95E+03	7.35E+03	1.14E+04	4.79E+03	1.13E+03
7.20	1.60E+21	1.07E+01	4.42E+01	1.31E+03	6.17E+03	1.30E+04	6.22E+03	1.69E+03
7.40	1.60E+21	9.72E+00	2.69E+01	2.88E+02	1.37E+03	4.87E+03	4.77E+03	2.22E+03
7.60	1.60E+21	9.48E+00	2.57E+01	1.76E+02	5.26E+02	1.97E+03	3.23E+03	2.76E+03
7.80	1.60E+21	9.01E+00	2.46E+01	1.57E+02	4.28E+02	1.39E+03	2.77E+03	3.21E+03
8.00	1.60E+21	1.04E+01	2.91E+01	1.57E+02	4.17E+02	1.25E+03	3.06E+03	5.77E+03

REFERENCES

Allakhverdiyev, A.O., Guseinov, O.H., Kasumov, F.K. & Yusifov, I.M., 1983. Astroph. & Sp. Sci., **97**, 287.

Allakhverdiyev, A.O., Guseinov, O.H., Kasumov, F.K. & Yusifov, I.M., 1986. Astroph. & Sp. Sci., **121**, 21.

Allen, C.W., 1973. Astrophysical Quantities (3rd Edition), The Athlone Press, London.

Axon, D.F. & Ellis, R.S., 1976. M.N.R.A.S., **177**, 499.

Axford, W.I., 1981. Proc. 17th ICRC, Paris, **12**, 155.

Baars, J.W.M., Dickel, H.R. & Wendker, H.J., 1978. A&A, **62**, 13.

Bell., A.R., 1978. M.N.R.A.S., **182**, 147.

Berkhuijsen, E.M., 1971. Astr. Astrophys., **14**, 359.

Berkhuijsen, E.M., 1972. Astr. Astrophys. Suppl. Ser., **5**, 263.

Berkhuijsen, E.M., 1973. A&A, **24**, 143.

Bhat, C.L., Issa, M.R., Houston, B.P., Mayer, C.J. & Wolfendale, A.W., 1985a. Nature, **314**, 511.

Bhat, C.L., Issa, M.R., Mayer, C.J. & Wolfendale, A.W., 1985b. Nature, **314**, 515.

Blaauw, A., 1964. Ann. Rev. Astr. Ap., **2**, 217.

Bingham, R.G., 1967. M.N.R.A.S., **137**, 157.

Blandford, R.D. & Cowie, L.L., 1982. Ap.J., **260**, 625.

Borken, R.J. & Iwan, D.C., 1977. Ap.J., **218**, 511.

Bradley, J.N., 1962. in: Shock Waves in Chemistry and Physics, Methuen & Co. Ltd., London; John Wiley & Sons Inc., New York.

Braun, C.R., Gull, S.F. & Perley, R.A., 1987. Nature, **327**, 395.

Brindle, A.H., 1967. M.N.R.A.S., 136, 219.

Brown, R.H., Davis, R.D. & Hazzard, C., 1960. Observatory, 80, 191.

Bunner, A.N., Coleman, P.C., Kraushaar, W.C. & McCammon, D., 1972. Ap.J., 172, L67.

Burrows, D.N., 1982. PhD. Thesis, 'Spacial Structure of the Diffuse Soft X-ray Background.', University of Wisconsin, Madison, U.S.A.

Burton, W.B. & Gordon, M.A., 1978. A&A, 63, 7.

Burton, W.B., 1985. A&A. Sup. Ser., 62, 365.

Burton, W.B., Beal, E.R., Walker, H.J. & Jangeneelen, A.A.W., 1987, in: Light on Dark Matter, Proc. of the 1st IRAS Conf., ed. Israel, F.P., Reidel, Dortrecht, Holland.

Caswell, J.L., 1977. Proc. Astr. Soc. Aust., 3, 130.

Caswell, J.L. & Lerche, I., 1979. M.N.R.A.S., 187, 201.

Chevalier, R.A. & Gardner, J., 1974. Ap.J., 192, 457.

Chevalier, R.A. & Messina, A., 1976. Ap.J., 209, 424.

Chevalier, R.A., 1974. Ap.J., 188, 501.

Clark, D.H. & Caswell, J.L., 1976. M.N.R.A.S., 174, 267.

Cleary, M.N., Heiles, C. and Haslam, C.G.T., 1979. A&A. Sup. Ser., 36, 95.

Cowie, L.L., McKee, C.F. & Ostriker, J.P., 1980. Ap.J., 247, 908.

Cox, D.P. & Anderson, P.R., 1982. Ap.J., 189, L105.

Cox, D.P. & Franco, J., 1981. Ap.J., 251, 687.

Cox, D.P. & Smith, B.W., 1974. Ap.J., 189, L105.

Cox, P., Krugel, E. and Mezger, P.G., 1985. A&A, 155, 380.

Cruddace, R.G., Friedman, H., Fritz, G. & Shulman, S., 1976. Ap.J., 207, 888.

Davis, J. & Greenstein, J.L., 1951. Ap.J., 114, 206.

Davelaar, J., Bleeker, J.A.M. & Deerenberg, A.J.M., 1980. A&A, 92, 231.

DeNoyer, L.K., 1974. A.J., **79**, 1253.

Deert, F.X., Boulonger, F. & Shore, S.N., 1986. A&A, **160**, 295

Dogiel, V.A., Mayer, C.J. & Osborne, J.L., 1983. 18th International Cosmic Ray Conference, (Bangalore), Late Papers, XG.OG.T Vol.9, p231.

Draine, B.T. & Anderson, N., 1985. Ap.J., **292**, 494.

Duric, N. & Seaquist, E.R., 1986. Ap.J., **301**, 308.

Dwek, E., 1986. Ap.J. **302**, 363.

Ferlet, R., Lallement, R. and Vidal-Madjar, A., 1986. A&A, **163**, 204.

Forman, M.A. & Dury, L.O'C., 1983. Proc. 18th ICRC, Bangalore TIFR, Bombay, **2**, 267.

Forman, W., Jones, C., Cominsky, L., Julien, P., Murray, S., Peters, G., Tananbaum, H. & Giacconi, R., 1978. Ap. J. Sup., **38**, 357.

Frisch, P.C. & York, D.G., 1983. Ap.J., **271**, L59.

Gaffet, B., 1978. Ap.J., **225**, 442.

Giacconi, R. & Zamorani, G., 1987. Ap.J. **313**, 20.

Green, D.A., 1984. M.N.R.A.S., **209**, 449.

Green, D.A., 1987. preprint.

Greisen, E.W. & List, H.S., 1986. Ap.J., **303**, 702.

Hamilton, T.T & Helfand, D.J., 1987. Ap.J., **318**, 93.

Harwit, M., Houck, J.R., & Stacey, G.J., 1986. Nature, **319**, 646.

Haslam, C.T.G., Large, M.I. & Quigley, M.J.S., 1964. M.N.R.A.S., **124**, 273.

Haslam, C.G.T., Quigley, M.J.S. and Salter, C.J., 1970. M.N.R.A.S., **147**, 405.

Haslam, C.G.T., Salter, C.J., Stoffel, H. & Wilson, W.E., 1982. Astr. Astrophys. Suppl. Ser., **47**, 1.

Haslam, C.G.T., Wilson, W.E., Graham, D.A. & Hunt, G.C., 1974. A&A Sup. Ser., **13**, 369.

Haslam, C.G.T. & Osborne, J.L., 1985. Nature, 327, 211.

Hauser, M.G., Gillett, F.C., Low, F.J., Gautier, T.N., Beichman, C.A., Neughebauer, G., Aumann, H.H., Baud, B., Boggess, N., Emmeson, J.P., Houck, J.R., Soifer, B.T. & Walker, R.G., 1984. Ap.J., 278, L15.

Hayakawa. S., Kato, T., Nagase, F., Yamashito, K., MARAKAMI, T. & Tanaka, Y., 1977. Ap.J.Let., 213, L109.

Hayakawa. S., Kato, T., Nagase, F., Yamashito, K. & Tanaka, Y., 1978. A&A, 62, 21.

Hayakawa. S., Kato, T., Nagase, F., Yamashito, K. & Tanaka, Y., 1979. Publ. Astron. Soc. Japan., 31, 71.

Heiles, C., 1979. Ap.J., 229, 533.

Heiles, C., 1984. Ap.J., 55, 585.

Heiles, C. & Habing, H.J., 1974. A&A. Sup. Ser., 14, 1.

Heiles, C., Chu, Y-H., Reynolds, R.J., Yegingil, I. & Troland, T.H., 1980. Ap.J., 242, 533.

Higgs, L.A., Landecker, T.L. & Roger, R.S., 1977. A.J., 82, 718.

Hill, E.R., 1968, Aust.J. Phys., 21, 735.

Holberg, J.B., 1987. Ap.J., in press.

Holden, D.J., 1969. M.N.R.A.S., 145, 67.

Humphreys, R.M., 1978. Ap.J. Sup. 38, 309.

Innes, D.E. & Harquist, T.W., 1984. M.N.R.A.S., 209, 7.

Iwan, D.C., 1980. Ap.J., 239, 316.

Jakobson, P., 1987. Advances in Space Research, in press. COSPAR XXVI, Symposium 7, 4-5 July 1986, Talouse, France.

Jakobson, P., & Kahn, S.M., 1986. Ap.J., 309, 682.

Jenkins, E.B., 1987. Ap.J., 219, 845.

Johnson, H.M., 1957. Publ. Astr. Soc. Pacific., 69, 130.

Jonas, J.L., de Jager, G. & Baart, E.E., 1985. A&A Sup., 62, 105.

Karzas, W.J. & Latter, R., 1961. Ap. J. Sup., 6, 167.

Kato, T., 1976. Ap.J. Sup., 30, 397.

de Korte, P.A.J., Bleeker, J.A.M., Deerenburg, A.J.M., Tanaka, Y. & Yamashita, K., 1974. Ap.J., 190, L5.

Kundu, M.R. & Velusamy, T., 1972. A&A, 20, 237.

Kundu, M.R., Angerhofer, P.E., Furst, E. & Hirth, W., 1980. A&A, 92, 225.

Large, M.I., Quigley, M.J.S. & Haslam, C.G.T., 1966. M.N.R.A.S., 131, 335.

Lawson, K.D., Mayer, C.J., Osborne, J.L. & Parkinson, M.L., 1987. M.N.R.A.S., 225, 307.

Mathewson, D.S., 1968. Ap.J., 153, L47.

Mathis, J.S., Mezger, P.G. & Panagia, N., 1983. A&A, 128, 212.

Mathis, J.S., Rumple, W. Nordsieck, K.H., 1977. Ap.J., 217, 425.

McCammon, Burrows, Sanders, W.T. and Krausher., 1983. Ap.J., 269, 107.

McCray, R. & Kaftos, M. 1987. Ap.J., in press.

McKee, C.F. & Cowie L.L., 1975. Ap.J., 195, 715.

McKee, C.F. & Ostriker, C.P., 1977. Ap. J., 218, 148.

Miller, G.E. & Scalo, J.M., 1979. Ap.J. Sup. Ser., 41, 513.

Milne, D.K., 1979. Australian J. Phys., 32, 83.

Milogradov-Turin, J. and Smith, F.G., 1973. M.N.R.A.S., 161, 269.

Milogradov-Turin, J., 1984. M.N.R.A.S., 208, 379.

Nugent, J.J., Jensen, K.A., Nousek, J.A., Garmire, G.P., Mason, K.O., Walter, F.M., Bowyer, C.S., Stern, R.A. & Riegler, G.R., 1983. Ap.J. Sup., 51, 1.

Osborne, J.L., 1987. Private communication.

Paresce, F., 1984. A.J., **89**, 1022

Parkinson, M.L. & Osborne, J.L., 1985. Space Science reviews, **40**, 503.

Parker, E.N., 1965. Ap.J., **142**, 584.

Pauliny-Toth, I.I.K. & Shakeshaft, J.R., 1962. M.N.R.A.S., **124**, 61.

Pollock, A.M.T., 1985. A&A, **150**, 339.

Rana, N.C. & Wilkinson, D.A., 1987. M.N.R.A.S., **226**, 395.

Raymond, J.C. and Smith, B.W., 1977. Ap.J. Sup., **35**, 419

Reich, W. & Braunsfurth, E., 1981. A&A, **99**, 17.

Reich, W., 1982. A&A Sup. Ser., **48**, 219.

Rougoor 1966. Ap.J., **144**, 852.

Routledge, D., Landecker, T.L. & Vaneldik, J.F., 1986. M.N.R.A.S., **221**, 809.

Salter, C.J., 1983. Bull. Astr. Soc. India, **11**, 1.

Sastry, Ch.,V., Dwarakanath, K.S. & Shevgaonkar, R.K., 1981. J. Astrophys. Astr., **2**, 339.

Sedov, L.I., 1959. Similarity and Dimensional Methods in Mechanics. (New York, Academic)

Seymour, P.A.H., 1969. M.N.R.A.S., **142**, 33.

Smith, F.G., 1977. :in Pulsars, Cambridge University Press.

Sofue, Y, 1973. Publ. Ast. Soc. Japan., **25**, 207.

Sofue, Y, 1976. A&A, **48**, 1.

Spoelstra, T.A.Th., 1971. A&A, **13**, 237.

Spoelstra, T.A.Th., 1972. A&A, **21**, 61.

Stecker, F.W., 1977. Ap.J., **212**, 60.

Strong, A.W., Reily, P.A., Osborne, J.L. & Murray, J.D., 1982. M.N.R.A.S., **210**, 495.

Swanenburg, B.N., Bennett, K., Bignami, G.F., Buccheri, R., Caraceo, P., Hermsen, W., Kanbach, G., Licheti, G.G., Masnou, J.C., Mayer-Hasselwander, H.A., Paul, J.A., Sacco, B., Scarsi, C. & Wills, R.D., 1981. Ap.J. Let., **243**, L69.

Tanaka, Y. & Bleeker, J.A.M., 1977. Space Science Reviews, 20, 815.

Taylor, J.H. & Manchester, R.N., 1975. A.J., 80, 794.

Tucker, W.H. & Koren, M., 1971. Ap.J. 168, 283.

Turtle, A.J. & Baldwin, J.E., 1962. M.N.R.A.S., 124, 36.

Van-der-Laan, H., 1962. M.N.R.A.S., 124, 125.

Verschuur, G.L., 1974a. Ap.J. Sup. 27, 65.

Verschuur, G.L., 1974b. Ap.J. Sup. 27, 283.

Vidal-Madjar, A., Laurent, C., Bruston, P. & Audouze, J., 1978. Ap.J., 223, 589.

Webb, G.M., Dury, L.O'C. & Volk, H.J., 1986. A&A., 160, 335.

Webb, G.M., Forman, M.A. & Axford, W.I., 1985. Ap.J., 298, 684.

Weiss, D., 1980. Ann. Rev. Astr. Astrophys., 18, 489.

Wilkinson, D.A., 1987. private communication.

Willis, A.G., 1973. A&A, 26, 237.

Willis, A.G., Oosterbaan, C.E., Le Poole, R.S., de Ruiter, H.R., Strom, R.G., Valentijn, E.A., Katgert, P. & Katgert-Merkelijen, J.K., 1977. In: IAU Symp. No. 74, Radio Astronomy and Cosmology, p.39, ed. Jauncey, D.L., Reidel, Dordr

Yaglom, I.M., 1979. A Simple Non-Euclidean Geometry and its Physical Basis, p142, Springer-Verlag, New York.

York, D.G., & Frisch, P.C. 1984 IAU Colloquium No. 81 on: Local Interstellar Medium, NASA Conference Publication 2345, 51.

ACKNOWLEDGEMENTS

Whilst at Durham I have received a great deal of help and assistance from many people, from within the field of astrophysics and outside it. I would particularly like to acknowledge my academic supervisor, John Osborne, for his guidance, and his tolerance at allowing me to trundle on at my own pace.

I especially wish to thank those people with whom I have shared an office: Chris (a truly great physicist) Mayer, for his encyclopedic knowledge of all things astronomical, giving me an understanding of some of the problems I was supposed to be examining, and for his invitation of a free holiday visiting him and Wendy out in La Palma. David Wilkinson, for his constant good humour and numerous appalling jokes, and for the many illicit cups of coffee in the library, over which were discussed matters both astrophysical and ecumenical, though I would like to remind him that the answer is still 0.81parsecs. Alison Broadbent, for tolerating David and myself during our final year, and for consistently lending me pens, rulers and calculator without a single complaint.

I thank Alan Lotts for keeping the Starlink VAX running whilst I used and abused it, Maria Giler for her brief discussion on shock acceleration, Ken Richardson for his 'fatherly' advice, and other members of the theoretical astrophysics group and Durham physics department generally, including Brian Houston, Iain MacLaren and David Mannion.

Away from the department I wish to thank all those who have helped me to survive with at least half my sanity intact. June Rapson and Jenny Collier for their care and understanding, Vicky Augustynek for a hundred free meals. All of the people that have been involved in my sporting activities: Andrew Ratcliffe, Bohdan Kurpita, Kate Kingston, Pete Hoare, Phil Wilkes, Simon Miles, Simon Mawson and many more.

The Science and Engineering Research Council helped to fund this work, and I therefore acknowledge the financial assistance given to me by the British tax payer, enabling me to indulge in a subject of interest to me within the privileged environs of academia.

I am grateful to all those that provided data that has been used in this thesis: the University of Wisconsin for the x-ray data, Dr. C.G.T. Haslam of for the 408MHz data, W. Reich for the 1420MHz data, J. Heise for his preliminary EXOSAT data, and A. Greybe for the 2300MHz map.

Finally, thanks to my parents and sisters and all old friends for not complaining at my lack of communication. - I will write soon.

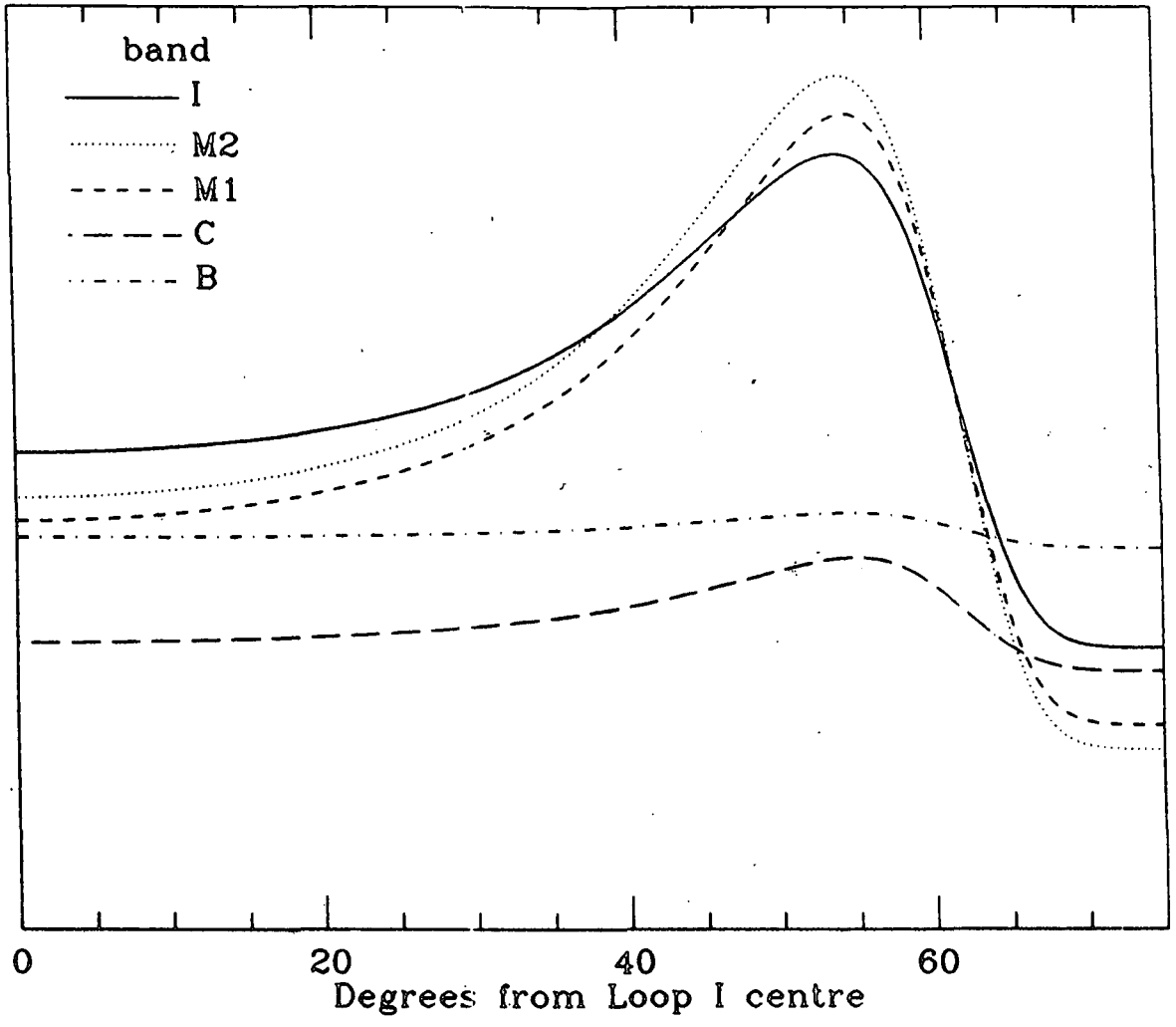

Model A

Figure 5.20

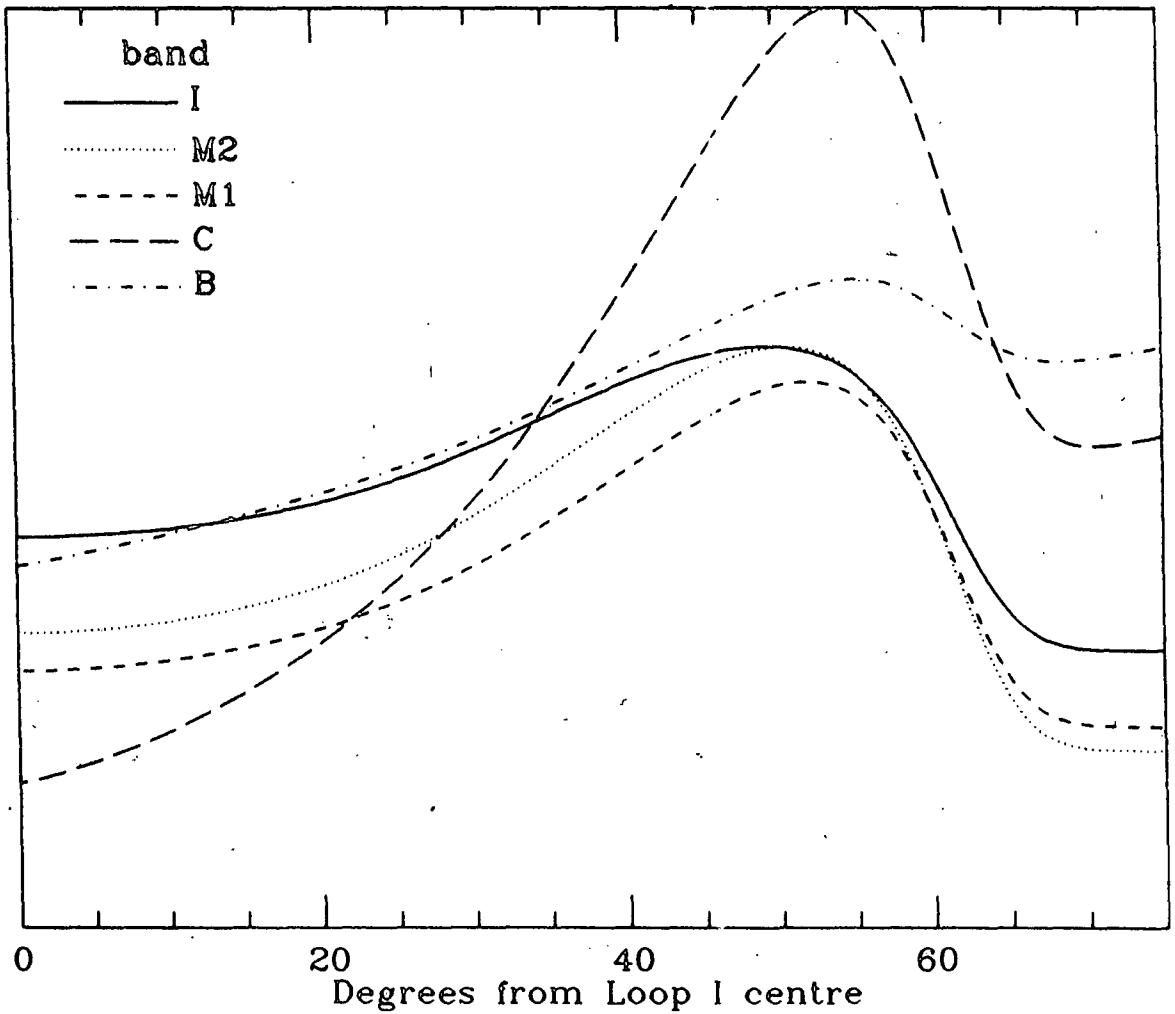

Model B

Figure 5.21

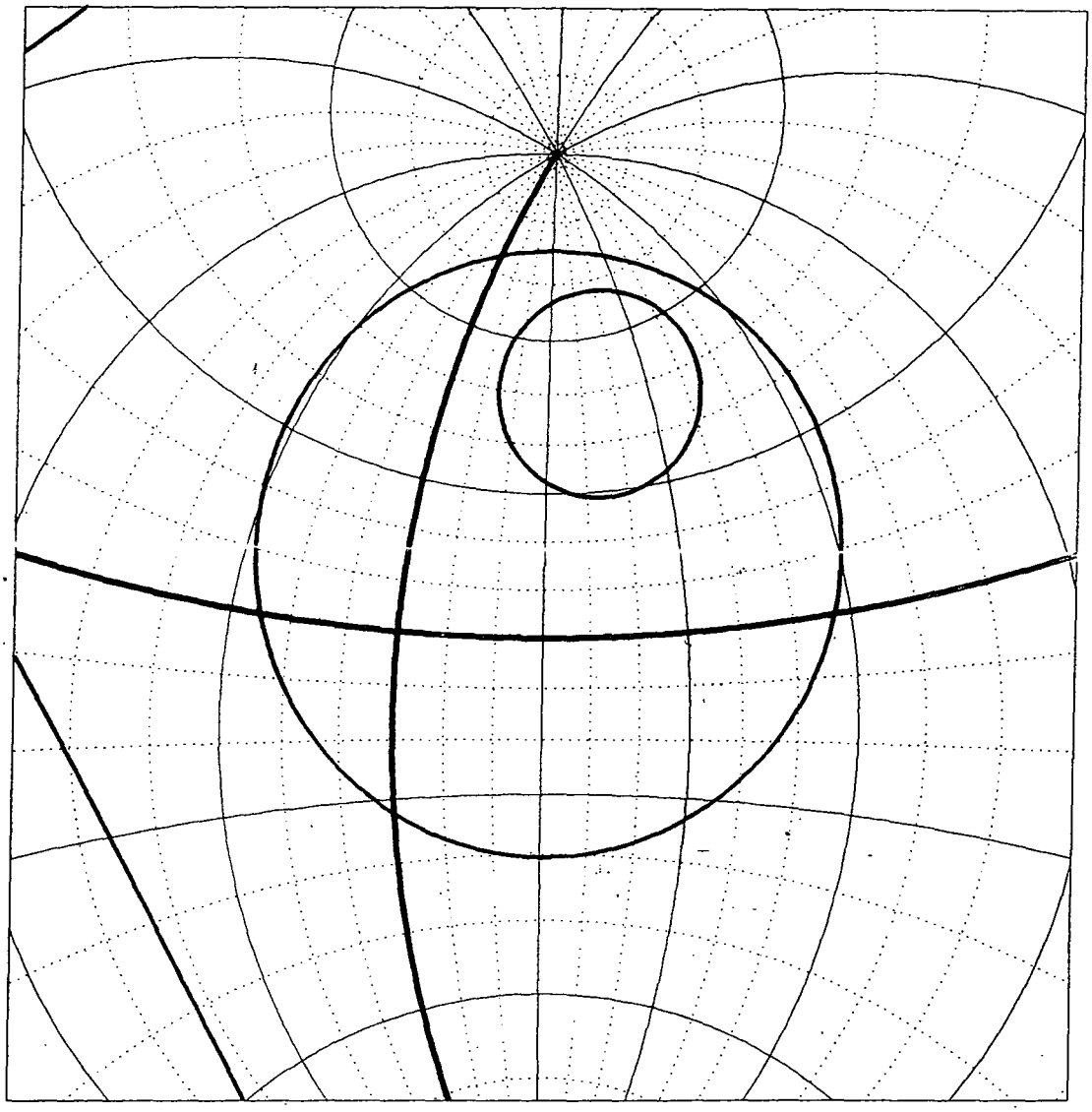

Figure 4.4 Co-ordinates for fig. 4.3 with the
the radio loops as defined by Berkuijsen (1971).
l=0 and b=0 are shown as bold lines.

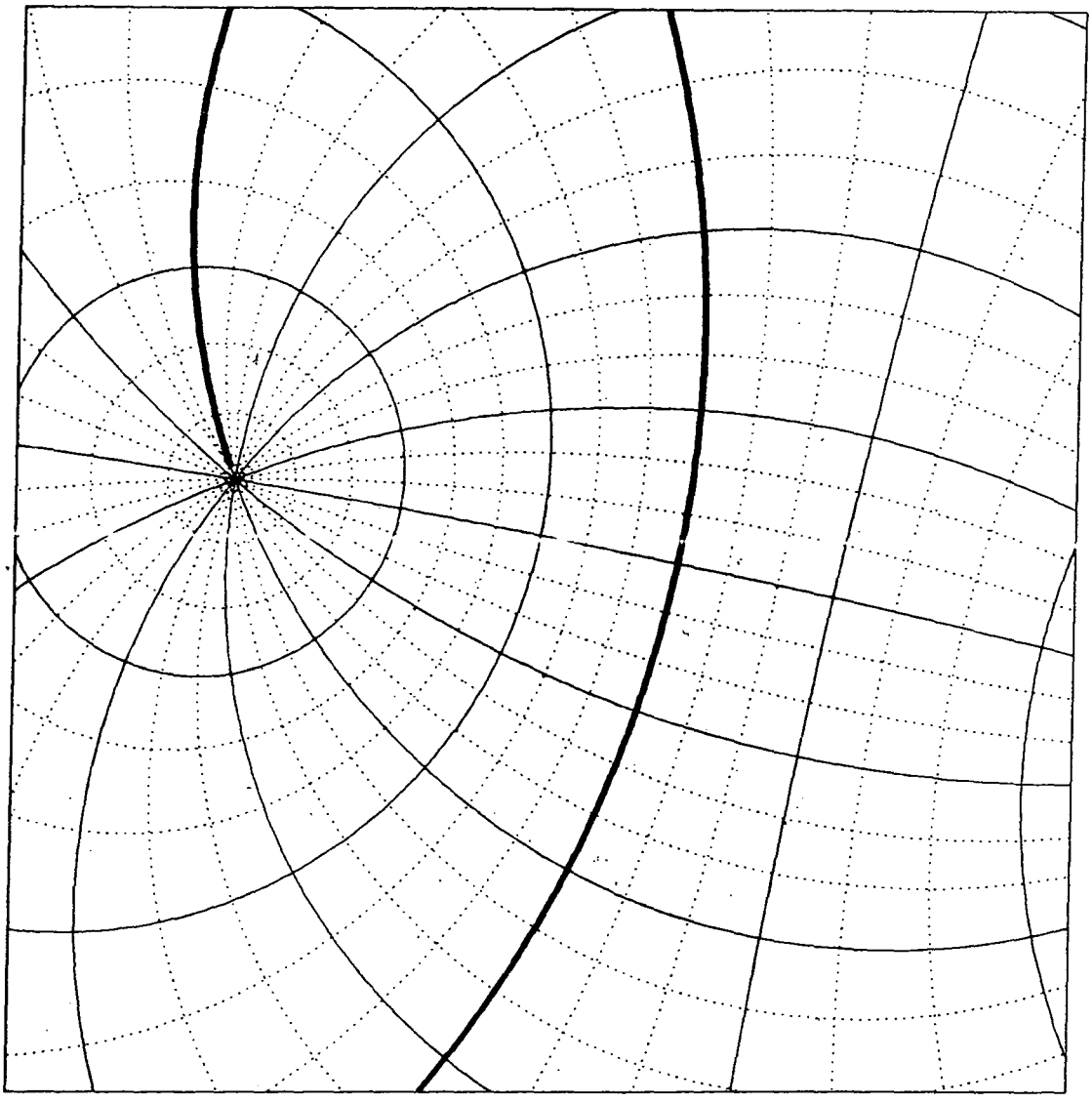

Fig. 4.6b Galactic co-ordinates for figs. 4.5 & 4.7
l and b marked every 10°. l runs clockwise about the N. Galactic Pole. l=0° and b=0° are bold.

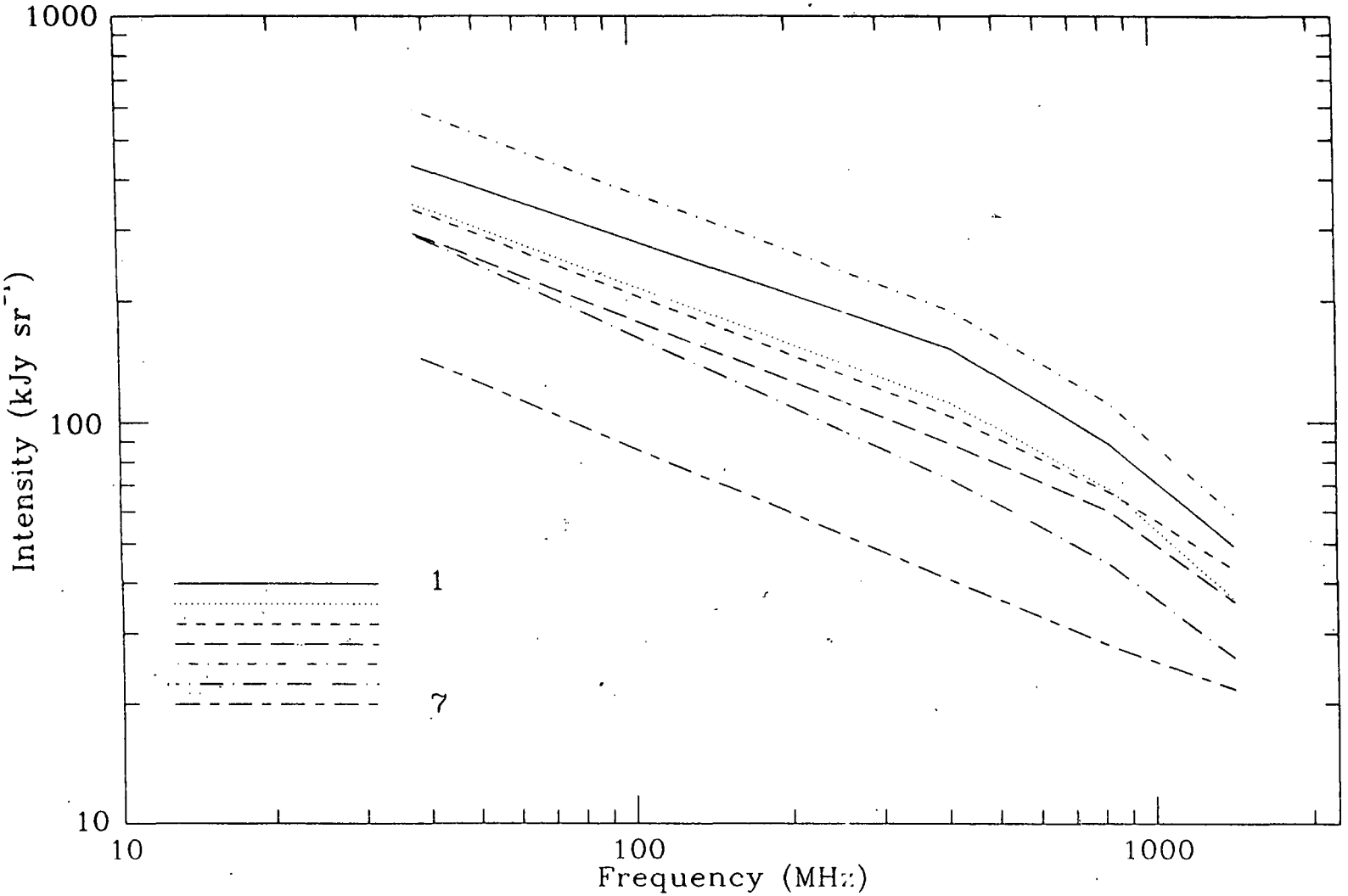

Figure 5.1